Imperial College London
Department of Earth Science and Engineering

Insights in variability of global subduction zones from 2D and 3D numerical models and plate motion data

Lior Suchoy

Supervised by Saskia Goes

Submitted in part fulfilment of the requirements for the degree of

Doctor of Philosophy (Ph.D.) in Geophysics of Imperial College London

and the Diploma of Imperial College London, June 2022

Abstract

Subduction of cold oceanic plates is a key driver of plate tectonics on Earth and has a wide range of surface expressions. The mechanisms governing subduction diversity are still debated. In this thesis, I investigate several key mechanisms using observations and numerical models of single plate subduction. First, I compile global subduction parameters along trenches from the last 120 Myr using recent global plate reconstruction models. The compilation highlights that trench motions generally contribute less than 20% to plate convergence, which has been attributed to low drag force at the base of the subducting plate. I investigate the role of basal drag using 2-D models of long and short plates including composite rheology. I show that even if basal drag force is low, it is expected to modify plate velocity significantly and that, in the Cenozoic record, its effect on velocity is masked because large-area plates experiencing significant basal drag have also been the ones with the highest driving slab pull. In particular for major subduction zones, some observed variability correlates with age-dependent variations of buoyancy and strength of the downgoing plate. Using a set of mechanical 3-D models, I show that to study Earth-like 'sinking' modes of subduction, the representation of plate buoyancy and strength needs to be carefully chosen. Next, I use these 3-D models to investigate the effect of lateral variations in plate buoyancy. Depending on the position of a buoyant ridge and whether the underlying plate is relatively old or young, the subduction of such a ridge modifies trench geometry and can either reduce or increase the shallow dip angle of the slab. These factors can explain why the impact of buoyant features is often different in West and East Pacific subduction zones. Thus variable plate strength and buoyancy and mantle drag significantly contribute to subduction diversity.

Statement of Originality

The author declares this thesis is the result of the author's work, unless stated otherwise in the text.

The copyright of this thesis rests with the author. Unless otherwise indicated, its contents are licensed under a Creative Commons Attribution-Non Commercial 4.0 International Licence (CC BY-NC).

Under this licence, you may copy and redistribute the material in any medium or format. You may also create and distribute modified versions of the work. This is on the condition that: you credit the author and do not use it, or any derivative works, for a commercial purpose.

When reusing or sharing this work, ensure you make the licence terms clear to others by naming the licence and linking to the licence text. Where a work has been adapted, you should indicate that the work has been changed and describe those changes.

Please seek permission from the copyright holder for uses of this work that are not included in this licence or permitted under UK Copyright Law.

Acknowledgements

I would like to thank my supervisor Saskia Goes for the continuous support and guidance throughout my PhD. Thank you for pushing me to expand my skills in every aspect. I could not have achieved half of what I did without your support. Thank you for kindness and patience in this journey.

I would like to thank all those who collaborated with me during these past years. To Ben Maunder, for being patient with my (sometimes basic) questions and for coming out with brilliant solutions to impossible problems. To Rhodri Davies and Fangqin Chen for their help with all things Fluidity, for constant feedback on my results and thoughts and for running the models which I couldn't. To Fanny Garrel and Loic Fourel for creating the models which were the basis for my own work.

I would like to thank my family. To my wife, Adi, for always being there. Your support is the reason I was able to reach this point. You were there in every step of the way, encouraging me to be the best I can. To my son, Mikhael, for being the inspiration for my work. To my parents, Eitan and Margalit, and my sisters, Hila and Maya, for pushing me forward and supporting me.

I want to thank my friends at Imperial. To all the great people I met here: Rid, Felipe, Andrea, Danny, Kartik, Sam, Kajetan and Waw. You made my time here the best it can be. Special thanks to Sam who took me hiking in the French Alps under the pretence of "field work".

Finally, I would like to thank the Engineering and Physical Sciences Research Council (EPSRC) for funding this work.

Dedication

לעדי ומיכאל

For Adi and Mikhael

Contents

Abstract **3**

Statement of Originality **5**

Acknowledgements **7**

1 Introduction **33**

1.1 Motivation and background 33

1.2 Thesis outline 41

1.3 Acknowledgement of contributions 43

2 Compilation of global subduction parameters **46**

2.1 Summary 46

2.2 Introduction 47

2.3 Methods and Uncertainties 49

2.3.1 Subduction parameter compilation overview 49

2.3.2 Workflow 51

2.3.3 Uncertainties 53

2.3.4 Differences between the reconstructions 57

2.4 Overview of subduction evolution based on the compilations 60

2.4.1 Global overview 60

2.4.2 Comparison of the evolution of the main trenches 64

2.4.3 Velocity and age trends 69

2.5 Tour of regional evolution of the main trenches 75

2.6 Conclusions 83

2.7 Files and access 85

3 Effects of basal drag on subduction dynamics from 2D numerical models 87

3.1 Summary 87

3.2 Introduction 88

3.3 Modelling methods 92

3.3.1 Governing equations and rheology 93

3.3.2 Model set up 95

3.4 Results 100

3.4.1 Reference model 100

3.4.2 Weak asthenosphere 105

3.4.3 Strong lithosphere effect (factor 2 and 10) 106

3.4.4 Self-consistent rheology 108

3.4.5 Models with extended domain 111

3.5 Discussion 112

3.5.1 Trench motion 112

3.5.2 Model limitations 113

3.5.3 The role of basal drag on Earth 114

3.6 Conclusions 120

4 3-D subduction regimes and choice of reference model 123

4.1 Summary 123

4.2 Introduction 124

4.3 Modelling methods 128

4.3.1 Modelling system and setup 128

4.3.2 Model Cases 131

4.4 Results 134

4.4.1 Reference: Case Ea 134

4.4.2 Effects of plate viscosity: Cases V1-V4 136

4.4.3 Effects of plate density: Cases D1, VD and D2 140

4.4.4 Effects of plate dimensions: Cases T, TD and N 141

4.5 Discussion 145

4.5.1 Model modes 145

4.5.2 Mode changes with plate parameters 149

4.5.3 Modelling Earth subduction 151

4.6 Conclusions 154

5 How buoyant features modify the dynamics of free subduction 156

5.1 Summary 156

5.2 Introduction 157

5.3 Methods 161

5.3.1 Modelling system and reference setup 161

5.3.2 Cases with ridges 164

5.4 Results 167

5.4.1 No ridge behaviour 167

5.4.2 Ridge buoyancy effects 172

5.4.3 Ridge location effects 173

5.5 Discussion 175

5.5.1 Buoyant feature subduction and the morphology of the trench and slab 175

5.5.2 Buoyant ridges and low-angle subduction 178

5.5.3 Buoyant feature subduction styles on Earth 179

5.6 Conclusions 185

6 Conclusions **187**

6.1 Overview 187

6.2 Future Work 191

Bibliography **194**

List of Tables

2.1 Subduction-zone parameters in the compilation 50

2.2 Large plates and main trenches IDs 53

3.1 Physical and rheological parameters of all models 98

3.2 Slab pull and basal drag forces in the Pacific and Cocos plates 115

4.1 All models variables 132

4.2 Parameters common to all simulations 133

4.3 Summary table of subduction modes for each simulation 145

4.4 Modified model variables 154

5.1 Parameters for all model cases 162

5.2 Parameters common to all simulations 164

5.3 Properties of buoyant features in the Pacific and Indian oceans 166

5.4 Isostatic calculation for 1 and 2 km bathymetric rise 167

5.5 Properties of buoyant features discussed in the main text 181

List of Figures

1.1 Cartoon of typical sub-oceanic (left) and sub-continental (right) subduction zones. Elements in the model are marked by circled numbers and forces are marked by coloured lines and arrows. After Goes, pers. comm. (2018) 34

1.2 A) Global subduction trench segments (multiple colours) with examples of slab morphologies (red) based on seismic tomographic images, with horizontal lines indicating the upper-lower mantle boundary. The dashed lines mark the India-Asia collision front. B) Global variations in trench velocity and C) lithospheric age at the trench. Note that trench age is not available where continental lithosphere is subducting along some segments. Landmass and plate boundaries are drawn in the background. Trench data from Müller et al. (2019), plate boundaries from Bird (2003) and slab shapes after Goes et al. (2017) and references therein. 35

2.1 Histograms of the lengths of trench segments at 0, 60 and 120 Myr, from the reconstruction of Müller et al. (2016b). 51

2.2 Plate boundaries through time: at 120 Myr, 60 Myr and the present day, from the reconstruction of Müller et al. (2019). Names of the main subducting plates in the Pacific, Indian and Tethys Oceans appear as abbreviations on the maps. Reconstructed landmass is shown as grey polygons in the background. Active trenches are shown in green, and other plate boundaries in bold black lines. Some minor deformation zones and plates boundaries were removed for clarification. 59

2.3 Global ocean floor age through time in 10 Myr intervals from 120 Myr ago to present, from the reconstruction of Müller et al. (2019). Black polygons mark plate boundaries, with subducting trenches overlain in bright green. Red arrows mark velocity vectors. Reconstructed landmass is shown as grey polygons in the background. 62

2.4 Global ocean floor age through time in 10 Myr intervals from 120 Myr ago to present, from the reconstruction of Müller et al. (2016b). Black polygons mark plate boundaries, with subducting trenches overlain in bright green. Red arrows mark velocity vectors. Reconstructed landmass is shown as grey polygons in the background. 63

2.5 Evolution of eastern and northern trenches in the Pacific Ocean through time from S06, M16 and M19. Reconstruction time is marked by colours. Present land mass is plotted in background. Abbreviations: ALE – Aleutian, J-K – Japan-Kuril, NAM – North America, SAM – South America. . . 66

2.6 Evolution of western and southern trenches in the Pacific Ocean and in the Indian Ocean through time from S06, M16 and M19. Reconstruction time is marked by colours. Present land mass is plotted in background. Abbreviations: IBM – Izu-Bonin-Mariana, R-N – Ryukyu-Nankai, S-J – Sunda-Java, T-K – Tonga-Kermadec. 67

2.7 Histograms of frequency along the main trenches after 60 Myr (purple) and of all trench segments after 120 Myr (red outlines) with median (solid lines) and mean (dashed lines) values. A) and B) show angle between trench strike and subducting plate motion direction, where 0° and 180° indicate motion parallel to the trench. C) and D) show the ratio of subducting plate to convergence velocity. Points with values >2 are summed in the last bar. E) and F) show the ratio of trench to subducting plate velocity. Points with values <-2 and >2 are summed in the first and last bars. Statistics from M16 are shown in the left panels (A, C and E) and from M19 in the right panels (B, D and F). Points with values below 30° and above 150° in A and B were excluded in C-F. Factor multipliers for the number of points are shown above the y axes on either side of the graphs. 71

2.8 Age trends illustrated by: A) and B) subducting plate velocity versus subducting plate age, C) and D) trench velocity versus subducting plate age. Parameters from the main trenches after 60 Myr are shown in colour (warm colours indicate West Pacific trenches and cold colours indicate East Pacific trenches) and those from all trench segments after 120 Myr are shown in the background in grey. Information from M16 in left panels (A and C) and from M19 in right panels (B and D). 73

2.9 Evolution of South America and North America trenches during the Cenozoic, with age grid and reconstructed landmasses, based on Müller et al. (2019). 76

2.10 Evolution of Aleutian and Japan-Kuril trenches during the Cenozoic, with age grid and reconstructed landmasses, based on Müller et al. (2019). . . 78

2.11 Evolution of Izu-Bonin-Mariana and Ryukyu-Nankai trenches during the Cenozoic, with age grid and reconstructed landmasses, based on Müller et al. (2019). 80

2.12 Evolution of South Pacific (including Tonga-Kermadec, New Hebrides and New Britain trenches) and Sunda-Java trenches during the Cenozoic, with age grid and reconstructed landmass, based on Müller et al. (2019). Directional triangles are shown where trench segments have different subduction polarity. 82

3.1 Present-day subducting plate velocities, measured at the trench in a lower mantle (plume) reference frame (O'Neill et al., 2005), as a function of plate size, in terms of a typical plate length. Typical plate length is a measure of plate size calculated as the age at the trench (Age_{trench}) multiplied by plate velocity (U_{plate}) (x markers) or as the square root of the plate surface area (S_{plate}, o markers). Velocities data from Sdrolias and Müller (2006) and Schellart et al. (2007) and plate size data from Conrad and Hager (1999). 91

3.2 Model set up illustrated with the initial viscosity field of the reference long-plate model, with text indicating parameters for the reference short-plate model. Initial trench ages are indicated for the overriding and subducting plates, which have linear age variations between the ridges and the trench. Initial plate temperature is set according to half space cooling (Turcotte and Schubert, 2002). See text for boundary conditions and further information. (a) Full model view, (b) Zoom of initial slab, (c) Zoom of trench and decoupling layer. The irregular adaptive mesh is presented on the right side of each panel. White lines mark the initial location of the trench (vertical line), the ULMB at 660 km, the bottom of the asthenosphere (chosen at 220 km) and the bottom of the lithosphere (at the 1100°C isotherm). 96

3.3 Viscosity field evolution at various times for the reference long-plate model (top row) and reference short-plate model (bottom row). White contour marks the 1100°C isotherm as the outline of the lithosphere. The vertical and horizontal spatial scales are identical and only part of the full model domain is shown. Note each model presents a distinct evolution of the slab and trench, which is the result of a difference in basal drag. 101

3.4 (a) Temporal evolution of parameters used for the calculation of basal drag for the long- (left panels) and short- (right panels) plate reference model. Top panel shows the velocities of the lithosphere (red line) and asthenosphere (blue line) (measured along the dashed and dotted lines in the bottom panel, respectively). Middle panel shows the magnitude of the viscosity of the asthenosphere (green line, measured along the dotted line in the bottom panel). Bottom panel shows a vertical profile (0-660 km depth) through the magnitude of the effective viscosity field. White lines mark the base of the lithosphere (1100°C isotherm) and asthenosphere (constant depth of 220 km). Parameters for the lithosphere were measured at 20 km depth (black dashed line) and parameters for the asthenosphere at 160 km depth (black dotted line). Time before $t660$ is shaded and is not shown in Figs. 3.5 and 3.7-3.9. (b) Location of the vertical profile location along which the quantities in (a) are measured (brown line), marked on an outline of the lithosphere at the initial condition of the long- (magenta line) and the short- (green line) plate reference model. The vertical and horizontal spatial scales are identical and only part of the full model domain is shown. Grey lines mark 220 km, 660 km (ULMB) and 1000 km depths. 103

3.5 Temporal evolution of the long-plate reference model (full lines) and the short-plate reference model (dashed lines). $t - t_{660}$ indicates the time since the initial interaction of the slab with the ULMB. (a) Velocity of the subducting plate (positive towards the upper plate, red) and the trench (positive away from the upper plate, yellow), measured at 2000 km distance from the initial subducting plate ridge. (b) Displacement of the subducting plate (red) and the trench (yellow) relative to the initial condition. (c) Percent of plate convergence (calculated as the sum of trench retreat and plate displacement) achieved by trench retreat. (d) Upper mantle slab pull and basal drag below the subducting plate, calculated as described in the main text. (e) Basal drag force from (d). (f) Ratio of basal drag to upper mantle slab pull force. This shows that basal drag is of a similar magnitude as effective slab pull (i.e. the difference between gravitational pull and the viscous mantle resistance on the slab sides) which is 10% of the upper-mantle slab pull force. 104

3.6 Comparison of final slab shapes for different models shown as a snapshot of the viscosity field. Long-plate (top row, (a)–(d)) and short-plate (bottom row, (e)–(h)) cases of Reference models ((a) and (e)), Weak Asthenosphere models ((b) and (f)), and Strong Lithosphere models with strength scaling factors of 2 ((c) and (g)) and 10 ((d) and (h)). White contour marks the 1100°C isotherm as the outline of the lithosphere. The vertical and horizontal spatial scales are identical, with grey lines to mark depths of 220 km, 660 km and 1000 km. For every type of model, the subducting slab in the short-plate model has more buckles and has undergone less trench retreat than in the long-plate model. 105

3.7 Temporal evolution of the long-plate (full lines) and short-plate (dashed lines) models. Rows of graphs are for different types of models, where (a)–(d) are Weak Asthenosphere models, (e)–(h) are Strong Lithosphere (factor 2) models and (i)–(l) are Strong Lithosphere (factor 10) models. The first column, (a), (e) and (i), shows the displacement of the subducting plate from the initial state, the second column, (b), (f), and (j), the amount of trench retreat, the third column, (c), (g) and (k), shows trench retreat significance as percentage of the total material converged, the fourth column, (d), (h) and (l), shows the ratio of basal drag to upper mantle slab pull force. All models are compared with the reference models, shown in light red. 108

3.8 Temporal evolution of the long-plate case (full lines) and the short-plate case (dashed lines) for the self-consistent rheology model. Lines and symbols are the same as in Fig. 3.5. 109

3.9 Temporal evolution of the long-plate (full lines) and short-plate (dashed lines) extended domain (grey) and reference (light red) models. (a) displacement of the subducting plate from the initial state. (b) amount of trench retreat. (c) trench retreat significance as percentage of the total material converged, (d) ratio of basal drag to upper mantle slab pull force. 110

3.10 Evolution of velocities and ages along the trenches considered in the global analysis of Cenozoic subduction systems, in intervals of 10 Myr. 3 maps are shown for each time interval, displaying the trenches used for the analysis (left), absolute subducting plate velocity in hotspot reference frame (O'Neill et al., 2005, middle) and age at the trench (right). Grey lines represent other boundaries of the subducting plates. The background light grey shows present day global coastlines for reference. Data following Müller et al. (2016b) and processed using GPlates (Müller et al., 2018) and Cartopy (Met Office, 2015). 118

3.11 (a) Velocity of subducting plates from Müller et al. (2016b) in lower mantle (plume) reference frame (O'Neill et al., 2005) throughout the Cenozoic, as a function of characteristic plate size (measured as the square root of plate surface area). (b) Plate size as a function of age at the trench for subducting plates throughout the Cenozoic. Maps showing the subduction zones at each time are shown in Fig. 3.10. Blue bold circles represent data from present-day subducting plates. Linear regression fits (black lines) show that there is no resolvable trend of velocity with plate size (p-value 0.351, R^2 0.03) while there is a trend of size with age (p value $<$ 0.05 and R^2 of 0.52). 119

4.1 (A) outline of subducting plate, coloured by normalised value of the second invariant of the strain rate tensor, $\dot{\varepsilon}_{II}$. Main forces are marked by blue, black and red arrows. (B) Schematic regime diagram of slab shapes (black) in various subduction modes. Orange background indicates 'bending' regime and blue background indicates 'sinking' regime (modified after Goes et al., 2017). (C) Global subduction trench segments sorted by subduction mode based on previous compilation of shapes from seismic tomography and seismicity by Goes et al. (2017). Subduction mode abbreviations (black): A - advance, F - folding, SR - strong retreat, VF - vertical folding and WR - weak retreat. Trench abbreviations (red): Ala - Alaska, Ale - Aleutians, An - Antilles, Ch - Chile, Cl - Calabria, Co - Cocos, Cs - Cascadia, He - Hellenic, Ho - Honshu, In - India, Iz - Izu, Ja - Java, Ka - Kamchatka, Ke - Kermadec, Ku - Kuril, Ma - Mariana, Pe - Peru, Ry - Ryukyu, Sc - Scotia, Su - Sumatra, To - Tonga. 127

4.2 Initial condition of (A) model domain and (B) subducting half-plate with geometry and boundary conditions. See table 4.1 for material properties (viscosity and density) of the plate and the mantle. Dimensions modified between models shown in parentheses. 129

4.3 Examples of grid cell geometry in (A) full model domain, (B) the front of the plate and (C) at the top of the edge of the trench. The mesh is refined during the evolution of the model to increase resolution in areas of high velocity and viscosity gradients to increase computational efficiency (see also Davies et al., 2007, 2011). The smallest and largest edges of the grid cells, shown in (C) and (A), respectively, are 1 km and 450 km long. 131

4.4 Slab geometries at the end of the simulation for all model cases, coloured according to the pressure. Case name and simulation time are shown for each panel. Cell length of the grid cells is 400 km. The symmetry boundary is to the right of the plate in each panel. 134

4.5 Temporal evolution of reference model Ea. (A)-(C) Trench retreat, plate advance and ratio of retreat to convergence, respectively, as a function of time. Red lines are for measurements at the symmetry boundary (i.e. at the centre of the plate), blue lines are for measurements in the middle of the half-plate and black lines for measurements at the edge of the plate. Vertical green lines mark the time that the slab reaches the bottom of the domain (i.e. *t660*). (D)-(F) Evolution of trench shape (top down view), slab shape at the symmetry (cross-section view) and slab shape at the edge, respectively. Red diamonds on (D) mark the location where slab and trench position, motion and velocity were measured, with results displayed in the other panels. Horizontal and vertical axes in (D)-(F) are scaled the same. 135

4.6 Trench retreat, plate advance and ratio of retreat to convergence (left, centre and right columns, respectively), as a function of time for models V1-V4, at the locations marked on Fig. 4.7. Lines styles are the same as in Fig. 4.5A-C. 138

4.7 Evolution of trench shape (top down view), slab shape at the symmetry (cross-section view) and slab shape at the edge (left, centre and right columns, respectively), for models V1-V4. Markings are the same as in Fig. 4.5D-F. Red diamonds on left column mark the location of measurements, with results displayed in the other columns and in Fig. 4.6. 139

4.8 Trench retreat, plate advance and ratio of retreat to convergence (left, centre and right columns, respectively), as a function of time for models D1, VD and D2, at the locations marked on Fig. 4.9. Lines styles are the same as in Fig. 4.5A-C. 141

4.9 Evolution of trench shape (top down view), slab shape at the symmetry (cross-section view) and slab shape at the edge (left, centre and right columns, respectively), for models D1, VD and D2. Markings are the same as in Fig. 4.5D-F. Red diamonds on left column mark the location of measurements, with results displayed in the other columns and in Fig. 4.8. 142

4.10 Trench retreat, plate advance and ratio of retreat to convergence (left, centre and right columns, respectively), as a function of time for models T, TD and N, at the locations marked on Fig. 4.11. Lines styles are the same as in Fig. 4.5A-C. 143

4.11 Evolution of trench shape (top down view), slab shape at the symmetry (cross-section view) and slab shape at the edge (left, centre and right columns, respectively), for models T, TD and N. Markings are the same as in Fig. 4.5D-F. Red diamonds on left column mark the location of measurements, with results displayed in the other columns and in Fig. 4.10. 144

4.12 All model cases plotted on subduction regime diagram (A) in ratio of plate and mantle thickness to the ratio of plate and mantle viscosity following Li and Ribe (2012) and (B) in plate stiffness to slab negative buoyancy force following Stegman et al. (2010b). Plate stiffness is calculated as $S = \eta_P/\eta_M \cdot (h/H)^3$ and slab buoyancy as $F_B = \Delta\rho \cdot h \cdot g/\eta_M$. Regime abbreviations (in circled black font) are the same as in Fig. 4.1, where our Folding ('F'), Advance ('A'), and Retreat ('R') regimes correspond to regimes V, III and a combined I, II and IV in Stegman et al. (2010b), respectively. Case names are coloured by subduction mode. See Table 4.1 and 4.4 for specific case parameters and Table 4.3 for our mode classification for each model. 146

4.13 Trench retreat, plate advance and ratio of retreat to convergence (left, centre and right columns, respectively), as a function of time for layered models with old, moderate and young plates, at the locations marked on Fig. 4.14. Lines styles are the same as in Fig. 4.5A-C. 152

4.14 Evolution of trench shape (top down view), slab shape at the symmetry (cross-section view) and slab shape at the edge (left, centre and right columns, respectively), for layered models with old, moderate and young plates. Markings are the same as in Fig. 4.5D-F. Red diamonds on left column mark the location of measurements, with results displayed in the other columns and in Fig. 4.13. The lower mantle is depicted on the centre and right columns by yellow semi-transparent rectangle. 153

5.1 Initial conditions of (A) our computational domain and (B) the subducting plate. See text and Table 5.1 and 5.2 for material properties and dimensions. We apply a free-surface boundary condition at the top of the domain, and free-slip boundary conditions elsewhere. 163

5.2 Representative slab geometries after plates start interacting with the ULMB for all model cases. Old plate cases are presented in panels (A)-(D) at 10 Myr and young plate cases in panels (E)-(H) at 30 Myr. The lower mantle is depicted by green semi-transparent box. For scale, grey grid cells of 400 km by 400 km are shown on domain boundaries. The ridges are located at the left side (symmetry boundary) of the half-plate in (B)-(C) and (F)-(G) and at the centre of the half-plate (i.e. half way between the symmetry plane and edge of the plate) in (D) and (H). 168

5.3 Temporal evolution of trench shape, corresponding to the front of the plate measured at 20 km depth, for all models. Dashed lines in panels (B)-(D) and (F)-(H) represent the location of the trench in the corresponding reference models without a ridge (cases NR_Old and NR_Young). Red diamonds mark the location where motion of the trench and slab were measured, with results displayed in Figs. 5.4 and 5.5. Note that the X and Z axes are differently scaled. 169

5.4 Slab depth as a function of time for old plate models in panels (A)-(C) and young plate models in panels (D)-(F). Dashed lines represent motions of the corresponding reference model without a ridge (cases NR_Old and NR_Young). Red lines are for measurements at the symmetry boundary (also ridge location in (A), (B), (D) and (E)), blue lines are for measurements in the middle of the half-plate (also ridge location in (C) and (F)) and black lines for measurements at the edge of the plate. Z-positions (along strike) where sinking was measured are marked on Fig. 5.3. Vertical lines mark the time that the slab reaches ULMB (i.e. $t660$) for the ridge model (light green) and the reference cases (dark green). Solid horizontal black line corresponds to the initial depth of the slab tip at 200 km. 170

5.5 Trench motion evolution for old plate models in panels (A)-(C) and young plate models in panels (D)-(F), at the locations marked on Fig. 5.3. Lines styles are as in Fig. 5.4, i.e., solid lines are for the ridge models, and dashed lines for the corresponding reference cases. Vertical lines mark $t660$ for the ridge (light green) and no-ridge (dark green) cases. The initial location of the trench, i.e. 0 km, is marked with solid black horizontal lines. 171

5.6 Top-down view of final plate top surface depth above 250 km of all models, coloured by depth, thereby providing an illustration of the along-strike variations in slab dip. Note that the X and Z axes are scaled differently. 177

5.7 Map of buoyant features (white outlined polygons) interacting with subduction zones in the Pacific and Indian oceans. Maroon surfaces indicate oceanic large igneous provinces (LIPs) and volcanic island chains. Slab depth contours are marked in RBG colours. Black lines indicate plate boundaries. Abbreviations for buoyant features discussed in the main text (white text): C - Caroline ridge, Ca - Carnegie ridge, Co - Cocos ridge, Em - Emperor ridge, H - Hikurangi plateau, Iq - Iquique ridge, JF - Juan-Fernandez ridge, Lo - Louisville ridge, Nz - Nazca ridge, OJ - Ontong Java plateau, Og - Ogasawara plateau, PK - Palau-Kyushu ridge, R - Roo rise, T - Tehuantepec ridge, Ya - Yakutat block. Other features (italic grey text): D - Daito ridge, M - Manihiki plateau, Ni - Ninetyeast ridge. Data from Coffin et al. (2006); Skinner and Clayton (2011); Tetreault and Buiter (2014), plate boundaries after Bird (2003), bathymetric data from Amante and Eakins (2008) and slab depth data from Hayes et al. (2018). 179

Chapter 1

Introduction

1.1 Motivation and background

Subduction zones are locations where one plate (usually oceanic) sinks below another, more buoyant, (either continental or oceanic) plate, immersing into the mantle. A "textbook" subduction zone includes a 3-D uniform plate subducting with a single bend at the trench to reach a dip angle $<$90° (Fig. 1.1 and e.g. Simkin et al., 2006). However, subduction zones on Earth are diverse, with a large variability in properties, including along-strike variations in age and thickness, trench curvature, stress regime, shallow and deep slab dip angles, the presence of tears and slab windows, or whether they exhibit local slab flattening (Uyeda and Kanamori, 1979; Jarrard, 1986; King, 2001; Govers and Wortel, 2005; Lallemand et al., 2005; Morra et al., 2006; Syracuse and Abers, 2006; Goes et al., 2011; Skinner and Clayton, 2013). Some of this variability in subduction characteristics may explain variations in surface expressions including whether island arcs and back arc basins or mountain belts are formed and whether subduction is accompanied by an active volcanic front or not (Fig. 1.2; Uyeda and Kanamori, 1979; Gutscher et al., 2000a; Heuret and Lallemand, 2005; Sdrolias and Müller, 2006). Different styles of subduction have been linked to variations in subduction-associated hazards such as the number and magnitude of earthquakes, the nature of volcanic

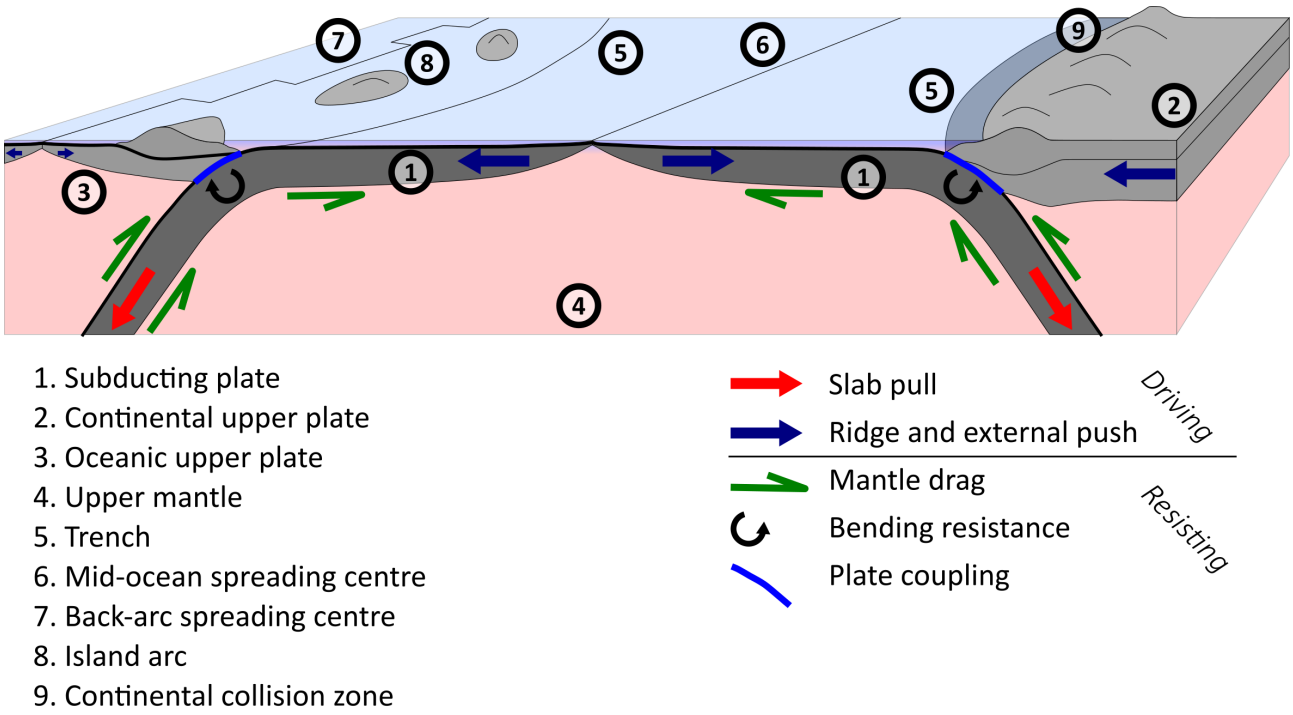


Figure 1.1: Cartoon of typical sub-oceanic (left) and sub-continental (right) subduction zones. Elements in the model are marked by circled numbers and forces are marked by coloured lines and arrows. After Goes, pers. comm. (2018)

eruptions and the rates of uplift, erosion and sedimentation (Uyeda and Kanamori, 1979; Ruff and Kanamori, 1980; Malinverno and Ryan, 1986; Meade and Jeanloz, 1991; Gutscher et al., 2000a; Dobson et al., 2002; Gutscher, 2002). It is therefore key to further understand the factors controlling variations in subduction zone behaviour.

This thesis explores how several key properties of the plate and underlying mantle may affect subduction variability. I will first evaluate observed variability in subduction velocities, trench shapes and incoming plate age structure by examining data from two recent GPlates global plate reconstructions (Müller et al., 2016b, 2018, 2019). Next, I will examine, using 2-D thermo-mechanical models, how drag of the mantle below the plates can modify subduction velocity and style. I will also explore, for the first time, the effect of the location of buoyant ridges on the subducting plate together with the age of the background plate on subduction dynamics. To build the 3-D mechanical models for this last study, I first examine how to best choose the parameters in the subduction model to ensure they represent an Earth-like subduction style. Together

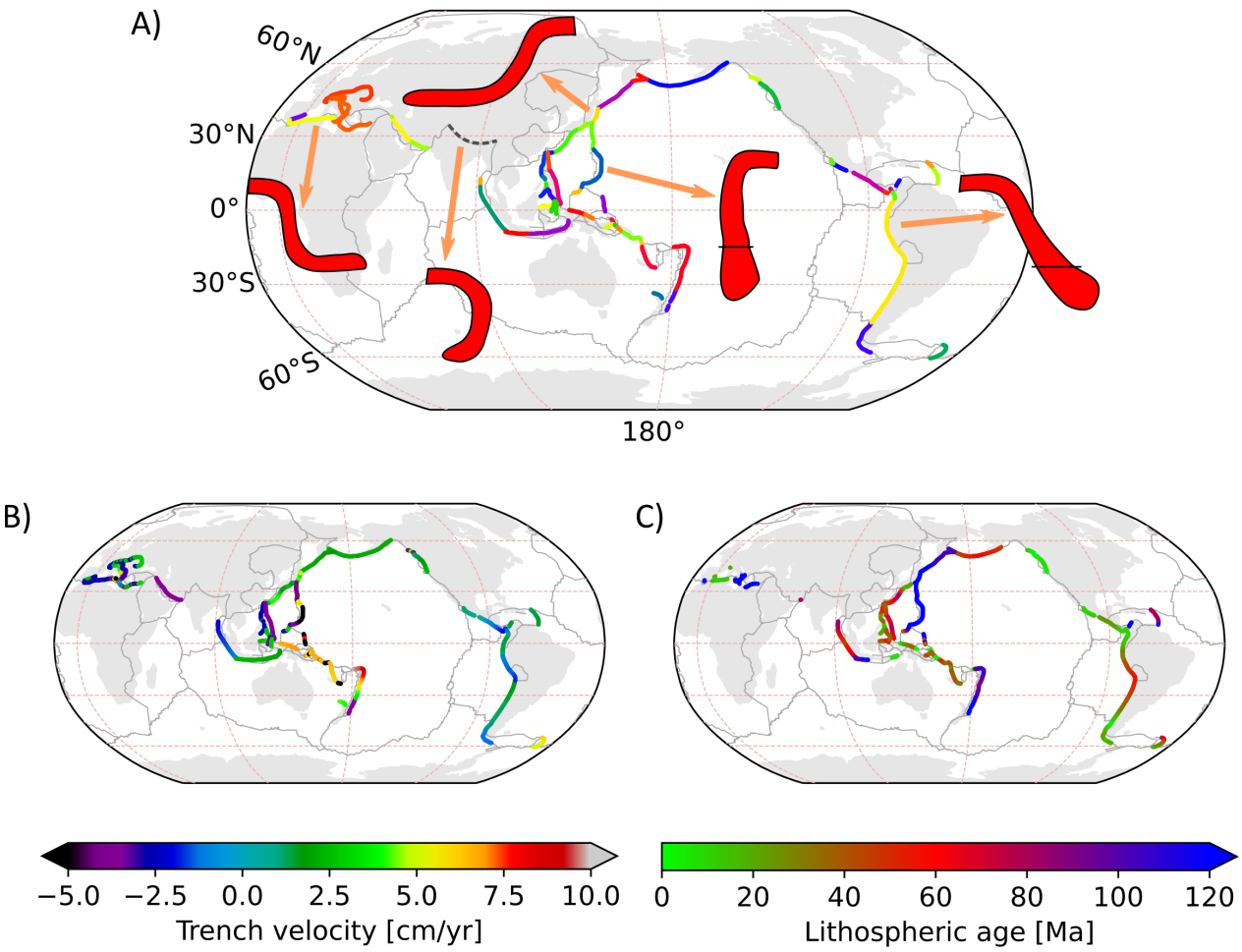


Figure 1.2: A) Global subduction trench segments (multiple colours) with examples of slab morphologies (red) based on seismic tomographic images, with horizontal lines indicating the upper-lower mantle boundary. The dashed lines mark the India-Asia collision front. B) Global variations in trench velocity and C) lithospheric age at the trench. Note that trench age is not available where continental lithosphere is subducting along some segments. Landmass and plate boundaries are drawn in the background. Trench data from Müller et al. (2019), plate boundaries from Bird (2003) and slab shapes after Goes et al. (2017) and references therein.

these studies provide new insights into some of the factors that govern the variability of subduction.

Subduction zones are diverse in many respects. Present-day convergence velocities between the subducting and upper plate range from ~0.5 cm/yr to ~10 cm/yr (Larson et al., 1997; Syracuse and Abers, 2006), and trench retreat rate between ~0.2-~15 cm/yr, with a few trenches advancing at up to ~3 cm/yr (Lallemand et al., 2005; Goes et al., 2011). Shallow slab dip angles (depths <125 km) range between 10-60°

and deep slab dip (>125 km) ranges between 20-90° (Lallemand et al., 2005; Syracuse and Abers, 2006; Hayes et al., 2012, Fig. 1.2). Other parameters which vary between subduction zones and laterally within a single subducting plate include lithospheric age (Jarrard, 1986; Sdrolias and Müller, 2006; Syracuse and Abers, 2006) and surface roughness and sediment thickness (Ruff, 1989; Rea and Ruff, 1996; Heuret et al., 2012; Scholl et al., 2015; Lallemand et al., 2018). Similarly diverse are the surface expressions of subduction, with most subduction zones around the Pacific producing large earthquakes (M8) while others, such as the Mariana subduction zone, do not have a history of large events (Kelleher et al., 1973; Lay and Kanamori, 1981; Ruff, 1989; Lay, 2015; Bilek and Lay, 2018). Most subduction zones are overlain by volcanic arcs, either oceanic or continental, which vary widely in composition and rate of volcanic activity (Nur and Ben-Avraham, 1983; McGeary et al., 1985; Peacock, 1996; Hilton et al., 2002; Stern, 2002). Finally, some upper plates are in extension which can result in new oceanic back-arc basins being formed, while others are in compression (Karig, 1970; Uyeda and Kanamori, 1979; Jarrard, 1986; Malinverno and Ryan, 1986; Lallemand et al., 2005; Heuret et al., 2012).

These variations in subduction style and expression are the result of multiple forces involved (Fig. 1.1; Forsyth and Uyeda, 1975). The main force driving subduction is the pull of the subducted slab due to the high density (as a result of its low temperatures) compared to the surrounding mantle. Slab pull has been shown to account for up to 90% of the driving force of subduction and plate motions, significantly exceeding other forces affecting plate motions (Elsasser, 1971; Forsyth and Uyeda, 1975; Becker and O'Connell, 2001; Conrad and Lithgow-Bertelloni, 2002). Although slab pull can be considered to be the main driver of plate tectonics, it alone does not explain the large variability in subduction zones globally (Jarrard, 1986; Conrad and Lithgow-Bertelloni, 2002; Schellart, 2004b; Lallemand et al., 2005; Cruciani et al., 2005). Some of the variation can be explained by different values of the lateral push force due to the gravitational potential that results from the increase in negative plate buoyancy with increasing age away from mid-ocean ridges, i.e. ridge push. Although ridge push

is an order of magnitude smaller than slab pull, it can affect subduction dynamics (Capitanio et al., 2007; Mahatsente, 2017). The driving forces are resisted by mantle drag which leads to viscous dissipation around the slab and below the plate (Forsyth and Uyeda, 1975; Dvorkin et al., 1993; Scholz and Campos, 1995; Conrad and Hager, 2001; Schellart, 2004b), the internal resistance of the (strong) plate to bending at the trench (Conrad and Hager, 1999; Schellart, 2004b), and coupling between the subducting and overriding plate (Scholz and Campos, 1995; Gutscher, 2002; De Franco et al., 2007; Pokorný et al., 2021). External forces by neighbouring plates (Tao and O'connell, 1992; Mishin et al., 2008; Yamato et al., 2009; Čížková and Bina, 2015; Király et al., 2016; Holt and Becker, 2017; Holt et al., 2018) and background mantle flow (Ricard et al., 1991; Boutelier and Cruden, 2008; Riguzzi et al., 2010; Rodríguez-González et al., 2014a; Ficini et al., 2017) may also contribute to the overall force balance.

All these forces can vary laterally and evolve as a function of time. Slab pull, ridge push and plate strength depend on plate age (Martinod et al., 2005; Capitanio et al., 2011; Mahatsente, 2017; Forsyth and Uyeda, 1975; Conrad and Hager, 1999). The magnitude and direction of mantle drag at the base of the plate and around the slab may vary with lateral variations of mantle flow and mantle viscosity as a function of temperature, hydration and strain rate and is less constrained than other forces (Boutelier and Cruden, 2008; Rodríguez-González et al., 2014a; Billen and Arredondo, 2018). Plate coupling, although localised at the trench, can have a key effect on subduction dynamics (De Franco et al., 2007; Běhounková and Čížková, 2008; Rodríguez-González et al., 2012; Pokorný et al., 2021) and depends on sediment and water influx to the trench, composition of the plate crust and surface roughness of the plate (e.g. Rea and Ruff, 1996; Lallemand et al., 2018). Slab pull can be additionally affected by variations in thickness of the magmatic crust on top (resulting in relatively buoyant features) (Cloos, 1993; Martinod et al., 2005).

The impact each factor has on subduction dynamics can be best investigated using numerical and analogue subduction models. Although subduction has been modelled

widely (e.g. Christensen and Yuen, 1984; Kincaid and Olson, 1987; Zhong and Gurnis, 1995; Conrad and Hager, 1999; Čížková et al., 2002; Funiciello et al., 2003a; van Hunen et al., 2004; Schellart, 2005; Capitanio et al., 2007; Gerya et al., 2009; Stegman et al., 2010b; Li and Ribe, 2012; Garel et al., 2014; Holt and Becker, 2017; Billen and Arredondo, 2018; Schellart, 2020; Pokorný et al., 2021) the main causes for the variability in subduction zone behaviour remain highly debated. The simplest subduction models investigate the dynamics of single slab subduction into the mantle (e.g. Christensen and Yuen, 1984; Conrad and Hager, 1999; Funiciello et al., 2003a; Schellart, 2005; Ribe, 2010). Other models introduce more complexity with additional factors such as an overriding plate (e.g. Capitanio et al., 2010; Rodríguez-González et al., 2014b; Manea et al., 2012; Taramón et al., 2015), heterogeneities in the plate (e.g. lateral variations in plate age, presence of buoyant features or transition from continental to oceanic lithosphere; Bellahsen et al., 2003; Martinod et al., 2005; Espurt et al., 2007; Capitanio et al., 2011; Magni et al., 2014; Menant et al., 2016), or adjacent plates (e.g. Mishin et al., 2008; Yamato et al., 2009; Čížková and Bina, 2015; Király et al., 2016; Holt and Becker, 2017; Holt et al., 2018), sometimes in a global setting (Stadler et al., 2010; Yanagisawa et al., 2010; Crameri et al., 2012; Mallard et al., 2016). The comparison of model behaviour with subduction observations, or trends between observed subduction parameters can help unravel what factors are key to explaining the variations in subduction, either in a specific setting or more globally (e.g. Forsyth and Uyeda, 1975; Lallemand et al., 2005; Sdrolias and Müller, 2006; Schellart et al., 2007; Goes et al., 2011; Capitanio and Morra, 2012).

Subduction models can be classified by their method (analogue or numerical), their driving force (kinematic or dynamic or a combination), whether they are regional or global and whether they consider a single plate, the presence of an overriding plate or include multiple plates. Models can be further classified according to whether they are mechanical or thermo-mechanical, and their rheology (viscous, plastic and elastic; linear or non-linear, single or multi-layered). Models in which a single plate is subducting into the mantle with no presence of an upper plate are termed ‘free sub-

duction' (e.g. Christensen and Yuen, 1984; Conrad and Hager, 1999; Funiciello et al., 2003a; Schellart, 2004a; Capitanio et al., 2007; Stegman et al., 2010b). Numerical free-subduction models are usually mechanical to avoid the spontaneous growth of the overriding plate that occurs in thermo-mechanical models (e.g. Garel et al., 2014).

Different model set-ups are suitable for addressing different questions. The choice of modelling system will depend on the objectives of the research, but also on the availability of computational resources or laboratory set-ups. Analogue models implicitly include physics that is challenging to model numerically (e.g. a free surface), but may not easily scale to Earth conditions due to the challenge of finding appropriate laboratory material properties. Numerical models, on the other hand, allow easier variation of input parameters and quantitative evaluation of the output but some physics are particularly challenging to implement. In all cases, models involve approximations and simplifications of the real Earth to (i) keep the models feasible and (ii) allow evaluation of the role of individual factors. Common simplifications include considering only a two dimensional (2-D) cross-section, implementing a free-slip rather than free-surface top boundary (Schmeling et al., 2008; Kaus et al., 2010; Quinquis et al., 2011), using linear viscosity and considering only mechanical evolution, choosing a viscous or visco-plastic rheology rather than full elasto-visco-plastic behaviour (Garfunkel et al., 1986; Tao and O'Connell, 1993; Davies, 1995; Zhong and Gurnis, 1995; Christensen, 1996; Funiciello et al., 2003b; Farrington et al., 2014; Fourel et al., 2014) and using simplified decoupling mechanisms between the subducting and overriding plates (De Franco et al., 2007; Běhounková and Čížková, 2008; Rodríguez-González et al., 2012; Pokorný et al., 2021).

Studies of subduction by numerical and analogue models had shown the relative significance of different aspects of the subduction system in determining subduction dynamics. Many studies showed that subducting plate age, which controls both slab buoyancy and plate bending resistance, is a key factor governing subduction behaviour and the associated subduction variability on Earth (Carlson et al., 1983; Funiciello

et al., 2003a; Schellart, 2008; Ribe, 2010; Stegman et al., 2010b). The exact nature of relations between these two main plate-buoyancy driven forces (slab pull and bending resistance) and resulting subduction evolution is debated, with different models producing different responses (Bellahsen et al., 2005; Stegman et al., 2006, 2010a,b; Capitanio et al., 2007; Schellart et al., 2007; Funiciello et al., 2008; Garel et al., 2014; Billen and Arredondo, 2018), a point which is discussed in Chapter 4.

Another main contribution of subduction modelling is to allow examination of single parameters in the subduction system. Present-day subduction on Earth is limited to only a few places, most of which concentrate around the Pacific Ocean (Stern, 2002, and references therein). In these locations, many elements of the subduction system change simultaneously. For example, in the western Pacific, older and larger subducting plates subduct below thin oceanic lithosphere, while in the eastern Pacific subducting plates are younger and smaller and subduct below thick continental plates (Sdrolias and Müller, 2006; Müller et al., 2008a; Di Giuseppe et al., 2009). Only by modelling subduction systems can the impact of each parameter, such as age, size and upper plate thickness, be investigated to evaluate their individual and joint effects. The models used in Chapter 3 examine one such parameter, i.e. plate size and the associated drag by the underlying asthenosphere.

Most of the studies of subduction models have so far focused on systematic investigation of systems without along-strike changes in properties. Only a few studies examined lateral variations in the subducting plate (Martinod et al., 2005, 2013; Espurt et al., 2008; Mason et al., 2010; Hu et al., 2016; Flórez-Rodríguez et al., 2019), mostly due to the high complexity and computational cost of 3-D models. With the insights from laterally-homogeneous models and improvements in modelling systems, the effect of lateral variations in the subducting plate can now be explored. Such lateral variations in the subducting plate include age variations and anomalous material properties (e.g. buoyant ridges, large igneous provinces or extinct spreading ridges), which are common in all present-day subduction zones (Tetreault and Buiter, 2014). These variations

are explored in Chapter 5.

1.2 Thesis outline

In order to examine how specific variations in plate properties affect subduction dynamics, I use 2-D and 3-D numerical models of mechanical and thermo-mechanical plates as well as comparative data from present and reconstructed subduction zones. Chapter 2 expands on the methodology used to extract present and reconstructed plate data, and which is referred to in the discussion in Chapters 3 and 5. Each of the Chapters 3, 4 and 5 assesses a different set of parameters and their effects on plate motion and slab morphology. These chapters are structured as stand-alone studies with relevant background and final discussion. The insights derived from the study in Chapter 4 are used to design the models in chapter 5. An outline of each main results chapter is given below, while the final Chapter 6 summarises the overall conclusions of the thesis.

Chapter 2 presents compilations of late Mesozoic–Cenozoic ($<$120 Myr) global subduction zone properties extracted from two recent plate reconstructions models (Müller et al., 2016b, 2019) implemented in GPlates (Müller et al., 2018). The resulting compilations include trench position, lithospheric age and plate velocities at points spaced 50 km along the trenches, for trench positions at a temporal intervals of 1 Myr. I compile more detailed information for nine major trenches in the Pacific and Indian Oceans during the Cenozoic, including average age and velocity. Apart from describing the compilation itself, this chapter describes the workflow used to generate the compilation and compares the subduction systematics with those from a previous compilation published by Sdrolias and Müller (2006). Lastly this chapter serves as an introduction and overview of the tectonic processes and history of each of the major trenches and how these were affected by the subducting-plate age distribution through time along each trench.

In Chapter 3, I evaluate how basal drag, or the traction between the mantle and the base of the plate, contributes to the overall force balance of subduction. Previous models of subduction concluded basal drag to be a minor force which, to first order, does not affect subduction dynamics. On the other hand, global mantle flow models concluded basal drag must be a substantial force. To understand this discrepancy, models of 2-D non-linear thermo-mechanical models with short and long plates were designed. The behaviour of the different length plates was examined using a range of asthenospheric and lithospheric rheologies. The results show how basal drag affects subduction dynamics in models which display Earth-like behaviour. These insights are then compared with a compilation of reconstructed Cenozoic plate motion data to reveal a positive correlation between slab age and plate size. This correlation indicates that, during the Cenozoic, the increased size of older plates moderates the added pull force and limits the range of velocities, thus masking the expression of basal drag.

Chapter 4 discusses how the choice of parameters for the reference case in a given subduction model set up affect the trends which arise from variations in plate density, viscosity and dimensions. It explores the subduction of a single 3-D mechanical plate model with typical Earth-like parameters and ten variations in plate properties, to determine how these parameter changes affect subduction regime and mode. It then compares the results with those of other studies of numerical and analogue models. This comparison shows similar variations in plate properties can result in different, and sometimes contradicting, trends. These differences can be usefully understood using a previously proposed classification of subduction as either occurring in 'bending' mode, where plates spend the majority of their potential energy on bending at the trench, or 'sinking' mode, where most of plate potential energy is used to overcome the viscous resistance to sinking through the mantle. It concludes by examining how these insights can be used to better design subduction models to ensure they reflect Earth-like 'sinking' mode behaviour and suggests simple modifications, such as implementing plates with a strong core, to overcome the shortcomings that arise in mechanical models with properties such as plate thickness, density and strength di-

rectly taken from measurements on Earth, which do not account for thermal effects and non-linear rheology.

In Chapter 5, the effects of localised lateral variations in plate buoyancy (i.e. buoyant ridges) on subduction dynamics is modelled and discussed. To examine this question, 3-D models of a single mechanical plate containing low buoyancy segments are designed. This chapter discusses the implications of ridge buoyancy, ridge location and background plate age on sinking patterns, trench shape and slab dip angle. The results of the models are compared with results from other modelling studies as well as the observed tectonic expressions from subduction of buoyant features on Earth. These comparisons highlight that there are three possible regimes of buoyant-feature subduction, depending on properties of both the subducting and overriding plate: (1) A 'trench deforming' regime in which subduction of the buoyant feature deforms the trench with minor slab steepening or contortion. (2) A 'slab deforming' regime in which subduction of a buoyant feature reduces slab dip locally whilst also deforming the trench. (3) A 'slab flattening' regime where the slab is flattened at shallow depth over a distance of up to several hundred kilometres where a buoyant feature subducts.

1.3 Acknowledgement of contributions

The design and execution of the models discussed in Chapters 3, 4 and 5 were done by the author using the computational modelling framework Fluidity. The development and coding of the database discussed in Chapter 2 was done by the author. The analysis of the results, and the compilation of data used in the discussion in each chapter was also done by the author.

The work presented here was made possible due to the generous help and contributions from Rhodri Davies (ANU, Australia), Fanny Garel (CNRS, France), Fangqin Chen (ANU, Australia), Ben Maunder (ICL, UK) and Saskia Goes (ICL, UK). Saskia Goes con-

tributed to each part of this work through discussion, direction and mentoring of the author. Saskia Goes also edited the text and commented on the figures. Rhodri Davis and Fangqin Chen helped design and run the models discussed in Chapters 3, 4 and 5. Rhodri Davis and Fangqin Chen also provided technical support for Fluidity, commented on the ongoing work for these chapters, and help evaluate and improve the models. Ben Maunder provided support on model set-up, design and interpretation for the models discussed in Chapter 3. Fanny Garel created the reference design of the model discussed in Chapter 3. Ben Maunder and Fanny Garel also commented on the text in Chapter 3. The MSci projects of Luke Jenkins (ICL, UK) and Kamile Rudaviciute (ICL, UK), in collaboration with Loic Fourel (U. Rennes, France), seeded the ideas developed in Chapter 5. Some numerical simulations were undertaken on the NCI National Facility in Canberra, Australia, which is supported by the Australian Commonwealth Government.

The Fluidity computational modelling framework, including source code and documentation, is available from `https://fluidityproject.github.io/`. The files for the compilations discussed in Chapter 2 are available at `https://github.com/lsuchoy/TrSubParametersCompilation`. The dataset used in Chapter 3 is available at `https://doi.org/10.5285/b3a75382-31db-428c-90bb-458fdf66d77a` as item number 139485. Initiation files used to generate the models in Chapter 5 are available at `https://doi.org/10.5281/zenodo.5833712`.

The results from Chapter 3 were published in:
Suchoy, L., Goes, S., Maunder, B., Garel, F., and Davies, R.: Effects of basal drag on subduction dynamics from 2D numerical models, Solid Earth, 12, 79–93, `https://doi.org/10.5194/se-12-79-2021`*, 2021*
The results from Chapter 5 were published in:
Suchoy, L., Goes, S., Chen, F., and Davies, D. R.: How Aseismic Ridges Modify the Dynamics of Free Subduction: A 3-D Numerical Investigation, Frontiers in Earth Science, 10, 1–16, `https://doi.org/10.3389/feart.2022.852742`*, 2022*

The results from Chapters 4 and 5 were used to create the models published in:
Fangqin, C., Davies, D. R., Goes, S., Suchoy, L., Kramer, S. C.: How Slab Age and Width Combine to Dictate the Dynamics and Evolution of Subduction Systems: A 3-D Spherical Study, Geochemistry, Geophysics, Geosystems, 23, 11, `https://doi.org/10.1029/2022GC010597`*, 2022*
And the models published in:
Fangqin, C., Davies, D. R., Goes, S., Suchoy, L., Kramer, S. C.: Comparing the Dynamics of Free Subduction in Cartesian and Spherical Domains, Geochemistry, Geophysics, Geosystems, 2022 [In print]

Chapter 2

Compilation of global subduction parameters

2.1 Summary

Surface expressions of subduction, including uplift and earthquake hazard, have often been correlated with the kinematics of subducting plates and the properties of subducting slabs. In this study, we compile a global set of subduction parameters at subduction trenches since 120 Myr from two recent GPlates plate reconstruction models by Müller et al. (2016b) and Müller et al. (2019). Our compilation includes trench position, subducting-plate, convergence and trench velocity and subducting plate age sampled at a spatial spacing of 50 km and temporal interval of 1 Myr. Comparison of the new compilation with a previous compilation by Sdrolias and Müller (2006) highlights the influence of key updates to the underlying plate reconstruction model particularly on the evolution of trench shapes and positions. Analysis of the compilation indicates that in the majority of sampled points along the trenches, subducting plates generally converge at a close to trench normal direction and trenches retreat, confirming that local slab pull is a significant force, in particular at the largest trenches. Yet,

subduction and trench velocities generally do not display any trend with local age at the trench, indicating that this age is not a good proxy of the magnitude of slab pull. Overall, the compilation indicates that there are significant influences from plate interaction on regional and sometimes even global scale.

2.2 Introduction

Tectonic plate reconstructions have been used extensively to examine a wide variety of questions that relate to changes in plate configurations through geologic time, including where mineral resources concentrate (Merdith et al., 2013), ancient water chemistry (Müller et al., 2013), effects of dynamic topography on surface evolution (Flament et al., 2015), the effect of mantle upwellings on mid-ocean ridge evolution (Whittaker et al., 2015) and the sequestration of deep-sea carbonates through time (Dutkiewicz et al., 2019). Another key application of plate reconstructions is to improve understanding of the dynamics of plate tectonics (e.g. Li et al., 2019) and plate-mantle interactions (e.g. Müller et al., 2016a). Subduction zones, as the main driver of plate tectonics (Forsyth and Uyeda, 1975; Vérard, 2019), play a key role in understanding the dynamics behind global plate motions and have been the focus of specific interests (e.g. Sdrolias and Müller, 2006; Wu et al., 2016; Braszus et al., 2021).

Many studies exploring trends and correlations in subduction parameters have done so based on present-day data (e.g. Jarrard, 1986; Lallemand et al., 2005; Schellart et al., 2007). Some studies examined subduction evolution in plate reconstructions (e.g. Pilger, 1981; Hall, 2002; Handy et al., 2010; Braszus et al., 2021) but only a few evaluated along-strike variations in plate properties (e.g. Sdrolias and Müller, 2006; Goes et al., 2011; Faccenna et al., 2018). One tool used to explore such variations through time is a compilation of subduction parameters along reconstructed trench positions. The most recent version of such a compilation, for the Cenozoic, was published by Sdrolias and Müller (2006) and included trench position, subducting-plate age and associated veloc-

ities for seven main trenches in the Pacific and Indian Oceans through the Cenozoic. This compilation, based on the available data at that time, facilitated and informed many follow-up studies (e.g. Schellart et al., 2007; Müller et al., 2008a,b; Goes et al., 2011; Seton et al., 2012). Subducting-plate age affects several key properties of the lithosphere, in particular plate thickness and slab buoyancy (e.g. Cloos, 1993; McKenzie et al., 2005). Such age-related properties have been shown to significantly affect plate and subduction evolution, for example affecting slab dip (directly and in combination with other parameters Cruciani et al., 2005; Capitanio et al., 2007; Irvine and Schellart, 2012), subduction and trench velocities (Forsyth and Uyeda, 1975; Jarrard, 1986; Bellahsen et al., 2005) and ocean and trench depth (Grellet and Dubois, 1982; Cloos, 1993).

Since the publication of the compilation by Sdrolias and Müller (2006), global plate reconstruction models have developed significantly, incorporating data from newer studies (e.g. Domeier and Torsvik, 2014; Wright et al., 2016) as well as adding algorithms to enforce certain rules of (dynamic) consistency, which reduce uncertainty in the reconstructions and their sampling through time where sufficient evidence is not available(e.g. Gurnis et al., 2012; Domeier and Torsvik, 2014; Müller et al., 2018). This, as well as the longer reconstruction time of recent reconstructions, motivated us to create an updated compilation of global subduction parameters through time.

A range of plate reconstruction models exist, with different emphases and different selections of available data sets (Vérard, 2019, and references therein). However, most plate reconstructions are either privately owned and are not accessible to the wider community (e.g. EarthModel owned by Halliburton Inc.; PaleoGIS owned by The Rothwell Group, L.P.; Globe owned by Getech Group plc; GeoVerse owned by CGG plc) or have not been updated in recent years (e.g. Stampfli and Borel, 2002; Lawver et al., 2015; Scotese and Schettino, 2017). The most commonly used community tool for plate reconstructions is GPlates (Müller et al., 2018). GPlates is a plate tectonic GIS system which is used for assembling local plate motion data into global plate reconstruction

models, and was built for easy use and modification. Its first use is to fit plate motion and velocities through time, to build models of global interaction between moving plates (e.g. Gurnis et al., 2012; Seton et al., 2012; Müller et al., 2016b; Matthews et al., 2016; Müller et al., 2019). It also allows for associating plate reconstruction models with other geographical data such as ocean floor age and models such as mantle tomography images through colour raster files (e.g. Müller et al., 2008b, 2013, 2016b, 2019). GPlates provides all the necessary tools to extract and analyse subduction parameters in space and time, and is therefore an ideal tool to create an updated subduction parameter compilation. Furthermore, it has been set up with the most recent and comprehensive global reconstruction models (Müller et al., 2016b; Matthews et al., 2016; Müller et al., 2019).

In this chapter, we create such compilation using these recent global reconstruction models of Müller et al. (2016b) and Müller et al. (2019). We extract subduction information and generate a global compilation of trench location, plate velocities and subducting plate age at spatial intervals of 50 km and temporal intervals of 1 Myr. We explore the parameters in this compilation since 120 Myr, and, for the most recent 60 Myr, compare it with the previous compilation by Sdrolias and Müller (2006). We conclude by examining the trends of trench evolution and age gradients in the main trenches in the Pacific and Indian Oceans.

2.3 Methods and Uncertainties

2.3.1 Subduction parameter compilation overview

Our subduction parameter compilation is constructed as a `.csv` (comma separated values) table where each row represents a point at a trench and each column represents a property. Table 2.1 shows the properties which can be extracted from the compilation for each point. These are divided into point parameters, which are unique for

Point parameters	Trench parameters
Reconstruction time [Myr]	Subduction zone length [km]
Location (latitude and longitude)[a]	IDs (GPlates sub. plate, GPlates sub. zone, main plate and main trench)
Age of the subducting plate [Ma]	Subducting plate surface area [km^2]
Trench azimuth[b] [°]	Age and velocity mean values and standard deviation along the trench
Convergence velocity[c]	
Trench velocity[c]	
Subducting plate velocity[c]	

Table 2.1: Subduction-zone parameters in the compilation. [a] Latitude ranges from ±90°, with 0° at the equator. Longitude is set to range from ±180°, with 0° at the prime meridian. [b] Trench azimuth is between 0° and 360°, with 0° set to North. [c] For each type of velocity, the compilation includes the angle to the trench [°] with 0° indicating trench-normal motion and ±90° indicating trench-parallel motion, magnitude [cm/yr], sign [Boolean], trench-normal velocity magnitude [cm/yr] and trench-parallel velocity magnitude [cm/yr]. Trench and subducting-plate velocities are in the absolute mantle reference frame of the reconstruction. For trench and subducting plate velocities, negative velocity is in the direction of the upper plate. For convergence velocity, negative velocity indicates divergence.

each point, and trench parameters, which are the same for all points of a given trench at a given time.

The values of the location, age, azimuth, velocity, reconstruction time and GPlates IDs are extracted directly from the GPlates plate reconstruction models and age rasters of Müller et al. (2016b) and Müller et al. (2019). The values are extracted for the last 120 Myr although the plate reconstruction models extend further back in time, to 230 and 240 Myr, respectively. The choice to exclude earlier data is due to the bias of the reconstruction to produce long trench segments in earlier periods, which is inconsistent with present-day trend (Fig. 2.1), as discussed further below.

Further analysis has been done for the main trenches in the Pacific and Indian Oceans, similar to Sdrolias and Müller (2006). We focused the analysis on the seven trenches analysed by Sdrolias and Müller (2006) and an additional two trenches: the South Pacific Trench and Ryukyu-Nankai Trench. These nine main trenches are where the nine largest plates are subducting (Table 2.2) during the Cenozoic (i.e. after 60 Myr) in the

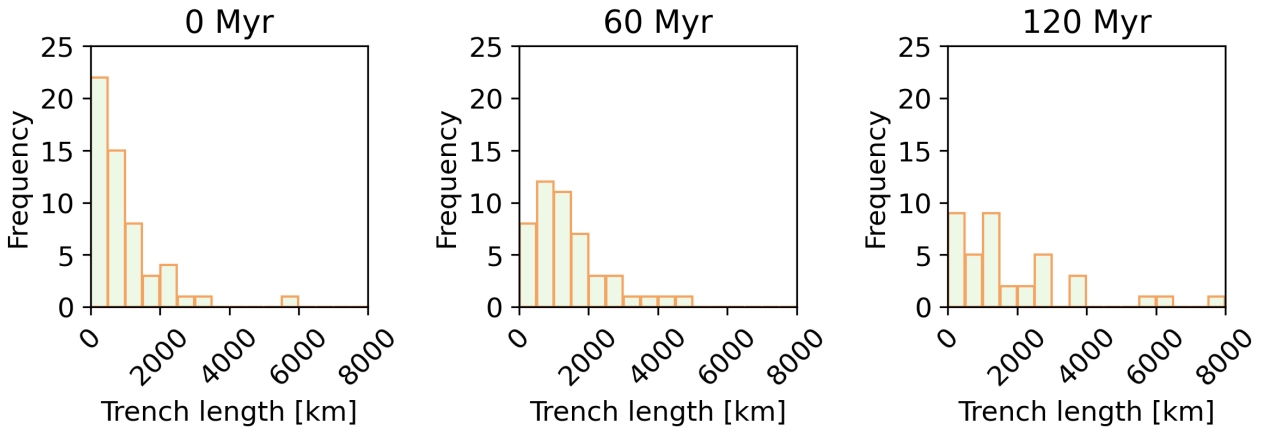


Figure 2.1: Histograms of the lengths of trench segments at 0, 60 and 120 Myr, from the reconstruction of Müller et al. (2016b).

Pacific and Indian Oceans. For these trenches, we calculate subduction zone length, subducting plate surface area and mean values and standard deviation of age and velocities. At each reconstruction time, we manually assign points to this set of main trenches and their associated plates based on sets of GPlates IDs. The final compilation includes both GPlates IDs and our main trench and subducting plate IDs, which makes it more versatile and useful for comparative analysis, as the analyses presented in Chapters 3 and 4 and in Chen et al. (2022b).

2.3.2 Workflow

The subduction zone parameter compilation is generated using a `Python3 Jupyter notebook` with the following workflow. Note that stage 6 is the only stage that is done manually by the user:

1. Load a GPlates plate reconstruction model (`.gpml` and `.rot` files and `netcdf` age grid files). This stage uses either the Müller et al. (2016b) or Müller et al. (2019) plate reconstruction models.
2. For each time step (i.e. 1 Myr), locate all the trench segments globally and sample them at intervals of 50 km to extract their location. Sample the corresponding

raster age file for the nearest value to each location and assign subducting-plate age.

3. Extract the subducting and overriding plate IDs at each trench point, and calculate their velocities.
4. Calculate trench obliquity and trench velocity.
5. Save the parameters as initial version of the compilation in `.csv` file format. This file does not include the association to main trenches and large plates.
6. The user manually assigns trench segments (`trench ID` and `plate ID` values) to each of the set of main trenches and each of the large subducting plates, respectively, in a separate supplementary file.
7. Load the initial compilation and the supplementary file, and add large plate IDs and main trench IDs accordingly.
8. Calculate for the set of main trenches, trench length, subducting plate surface area and mean values and standard deviation of subducting plate age and convergence, trench and plate velocities. Add these values to the compilation.
9. Save the extended set of parameters as the full subduction parameter compilation in `.csv` file format.

Although the workflow and associated code is designed specifically for the Müller et al. (2016b) and Müller et al. (2019) GPlates models, it can be adapted to other (e.g. future) GPlates models. The principles of the algorithm, as described above, can also be used to write a new code to extract data from non-GPlates plate reconstructions. However, the existing code relies heavily on the GPlates python interface (pyGPlates) and therefore cannot be used directly with non-GPlates models.

Other information, not included in our subduction parameter compilation, can be extracted from the GPlates models and integrated for analysis. This includes global seafloor age, plate polygon information and spreading rates around mid-ocean ridges.

Scripts for parameter extraction and some examples of plots are provided as part of the files that make up the compilation.

2.3.3 Uncertainties

Plate reconstruction uncertainties

The GPlates plate reconstruction models used for this study, as well as other plate reconstruction models, are inherently limited by the uncertainty in the underlying data (see review by Vérard, 2019).

The main source type of data used to evaluate plate position over the past 200 Myr is magnetic anomalies in the oceanic crust. Magnetic anomalies are used to derive Euler poles for plates near mid-ocean rides (e.g. Müller et al., 2008a). These anomalies constrain relative plate motions (RPM) well for most major plates, with larger uncertainties back in time (in particular before 120 Ma) and in some regions in the circum-Antarctic, West-Pacific and West-Australia (Domeier and Torsvik, 2014; Zahirovic et al.,

ID	Large plates	ID	Main trenches
1	Nazca	1	South America
2	Cocos	2	North America
3	Juan de Fuca	3	Aleutian
4	Pacific	4	Japan-Kuril
5	Philippine Sea	5	Izu-Bonin-Mariana
6	Indo-Australia	6	Ryukyu-Nankai
7	Farallon	7	Tonga-Kermadec
8	Kula	8	Sunda-Java
9	Izanagi	9	South Pacific$^{(*)}$
0	Other	0	Other

Table 2.2: IDs of large plates and IDs of main trenches in the Pacific and Indian Oceans, similar to Sdrolias and Müller (2006). $^{(*)}$ The South Pacific trench includes the present-day Tonga-Kermadec, New Hebrides and New Britain Trenches.

2014; Williams et al., 2015; Vérard, 2019). The RPM model can be constrained by including evidence of paleo-plate boundaries (e.g. volcanic arcs and orogenic regions) and of previously subducted slabs (Müller et al., 2019, and references therein).

RPM models can be fixed in space to create absolute plate motion (APM) models, which describe the motions of the plate relative to Earth's (fixed) deep interior. The most common source of data to anchor RPM models is palaeomagnetic data (Vérard, 2019). However, such data is biased in both space (towards the accessible part of the continents) and through time (with diminishing data for older periods; Williams et al., 2015; Vérard, 2019). Moreover, paleomagnetic data only provide information on the latitude and rotation relative to the north (Domeier and Torsvik, 2014). Other sources of data used to fix RPM models include hotspots relative position (e.g. Torsvik et al., 2008), seamount chains position and trend and models of net lithospheric rotation (NLR) (Conrad and Behn, 2010). However, such models are also debated and subject to uncertainty (Courtillot et al., 2003).

The other major uncertainty in reconstructions is on the position and shape of plate boundaries through time. Determining the plate boundary configuration and properties, requires the joint interpretation of a wide range of geophysical, geologic and petrological data, and is hence most dependent on the choices made by individual researchers. Paleomagnetic data, hotspots positional data and paleao-plate boundary data are all underpinned by radiometric dating methods (Williams et al., 2015; Vérard, 2019). Naturally, such methods are limited in accuracy (Best, 2002). Moreover, while the dating of rock samples depends on the dating method, associating each sample with a tectonic event is a matter of interpretation, and thus highly debated. In our regional tour (Section 2.5), we will discuss some of the literature and alternative interpretations of plate boundaries and how this affects the subduction parameters.

Uncertainties in the GPlates models of Müller et al. (2019) and Müller et al. (2016b)

The uncertainties in the subduction parameters compilations are inherited directly from the GPlates models they are extracted from. The extraction process itself does not add any further uncertainties, apart from deciding for the analysis of the main trenches, which trench segments to associate with any main trench. The accuracy of the GPlates models varies depending on the distribution and accuracy of the underlying data, the approximations used when processing the data and the choices of temporal and spatial interpolation between data points (Seton et al., 2012; Müller et al., 2016b, 2019).

One of the main uncertainties in the underlying model is due to the challenges of deriving rotation poles from seafloor spreading isochrons (Müller et al., 2016b). The average tectonic stage length is $\sim$5 Myr, but the models interpolate motion over 1 Myr periods, in order to facilitate continuous changes to plate boundaries. While extracting rotational poles from two sided symmetrical isochrons is straightforward, such data is partial, as it exists only in oceanic plates, and is often missing for periods in deep time. When only one-sided isochron data is available, the GPlates algorithm will use half-stage rotation and assume symmetry to reconstruct plate motion. While there are ways of reducing the uncertainty involved in such a method, it is still higher than cases where two-sided data is available (Müller et al., 2016b). When isochron data is not available, the reconstruction relies on other geological and geophysical data which varies in accuracy and certainty. The newer GPlates model of Müller et al. (2019) includes more evidence than the model of Müller et al. (2016b). While it is hard to quantify the difference in accuracy for the newer model (Vérard, 2019), the inclusion of more geological and geophysical data is likely to increase its accuracy. Moreover, the introduction of large deformation zones to the Müller et al. (2019) model emphasises the uncertainty in the location of the trenches within these regions. We note that trench locations within deformation areas were extracted directly from the Müller et al. (2019) model and not adjusted.

Another major uncertainty lies in determining plate boundary locations and geometries through time. The position of these boundaries is inferred from geological and geophysical information such as presence of arc magmatism, high-pressure metamorphism, ophiolite obduction and slab position derived by seismic tomography (Domeier and Torsvik, 2014; Tetley et al., 2019). Evidence of plate boundary locations back in time is not preserved everywhere, resulting in possible biases in the reconstruction. One example is the preservation of subduction boundaries on continental plates in the form of volcanic arcs, which are more likely to be preserved over time relative to their oceanic equivalent. When there is an absence of geological and geophysical evidence for separate block motions or internal deformation, the GPlates algorithm will use the smallest number of separate plates required to match the observations. It is therefore inevitable that the less evidence in earlier periods will lead to a smaller number of plates with increased average surface area and fewer short trenches (Fig. 2.1).

Other sources of uncertainty in the GPlates reconstructions are the smoothing of motions through time (i.e. constant motion rates are preferred when there is no contradicting evidence; Müller et al., 2016b) and optimisation of reconstructions towards low trench velocity and other plate tectonic constraints (Cox and Hart, 2009), following an 'Occam's razor' approach (Matthews et al., 2016). Finally, both the Müller et al. (2016b) and Müller et al. (2019) models use the reference frame of O'Neill et al. (2005) for plates motion younger than 70 Myr. For earlier periods, the absolute plate motion (APM) model used for reference frame differs. The Müller et al. (2016b) model uses the true polar wander (TPW)-corrected paleomagnetic model which tracks the changes to true north (Steinberger and Torsvik, 2008). The Müller et al. (2019) model uses a novel alternative reference frame which follows the method of Tetley et al. (2019). This method uses a joint global inversion to evaluate the contribution of TPW-corrected paleomagnetic data and other constraints such as age-progressive hotspot tracks, subduction zone migration, and rates of net lithospheric rotation, to derive a 'best-fit' reference frame model. While the two methods are mutually exclusive,

neither is necessarily better or more certain than the other. Moreover, the period between 70 and 105 Myr is used in both models to interpolate between reference frames, which adds uncertainty to the reconstruction in this period.

In conclusion, uncertainties of the reconstructions increase with earlier reconstruction time due to the decrease in available constraining evidence. It is hard to quantify the uncertainties of reconstruction at specific time (e.g. Torsvik et al., 2010; Zahirovic et al., 2014; Williams et al., 2015, and references therein), but it is possible to asses relative uncertainty. We consider variation in the extracted parameters over periods of 1 Myr as somewhat uncertain but ascribe higher certainty to variations over time intervals of 5 Myr and more. The certainty decreases somewhat prior to 70 Myr and significantly prior to 120 Myr, with any reconstructed plate motions and positions for periods before 120 Myr considered as highly uncertain. In spatial terms, the certainty of information for plates which exist today is considered higher than that of plates which have subducted fully. For example, the motion around the Pacific Ocean at 60 Myr is considered mostly certain, while the motion of the Kula Plate less certain. The reconstruction of the Tethys Ocean at this period is considered mostly uncertain.

2.3.4 Differences between the reconstructions

Our subduction parameter compilation is similar to, and could be considered an update of, the previously published compilation by Sdrolias and Müller (2006) which is based on the plate reconstruction model published by Müller et al. (2008b). Our subduction parameter compilation provides both extracted subduction-zone specific information for others to use, and a script to create future updates based on new GPlates models. In the following sections, we will refer to the compilation by Sdrolias and Müller (2006) as S06. The two parameter sets of the new compilations based on the plate reconstruction models of Müller et al. (2016b) and Müller et al. (2019) will be referred to collectively as M16-19 and separately as M16 and M19, respectively.

The M16-19 parameter compilations are more comprehensive than the S06 compilation in a few different ways. Firstly, S06 includes subduction parameters from the seven main trenches in the Pacific and Indian Oceans at ages younger than 50 Myr. M16-19 include subduction parameters of all the reconstructed trench segments on Earth at ages younger than 120 Myr, as well as a separate analysis of the parameters of the main trenches at ages younger than 60 Myr. M16-19 also include the Ryukyu-Nankai Trench, where the Philippine Sea Plate (PSP) subducts, and the South Pacific Trench as additional main trenches. The sampling rate of age and velocity along the trenches is increased to 50 km in M16-19 compared to 100 km in S06.

Other differences in the evolution of ages, motions and trench shapes are the result of the incorporation of data from newer studies in the underlying plate reconstruction models of M16-19. Particularly noteworthy differences are:

- The history of the Phoenix plate in M16-19 includes late Mesozoic fragmentation into several smaller plates (Hikurangi and Manihiki in the west and Chazca and Catequil evolving into the Aluk plate in the east; Fig. 2.2; Taylor, 2006; Seton et al., 2012) affecting the evolution of subducting plate ages along South American and South-West Pacific Trenches.

- More information about the evolution of PSP, South China Sea Plate and other south-east Asian basins (Zahirovic et al., 2014; Bai et al., 2015) led to changes to the IBM and Sunda-Banda subduction zone evolution.

- Updated insights into the interaction between the Caribbean, North America and South America plates (Boschman et al., 2014; Braz et al., 2018) affect Caribbean and Farallon Trench evolution.

- In the closing Tethys Ocean, new plate boundaries were added to reflect the fragmentation and later merging of continental blocks, like the larger Adria and Iberia blocks and the smaller Tisza and Dacia blocks in the western Tethys (Handy

et al., 2010). The convergence of the Greater India and Asia Plates is more complex in M16-19, with multiple subduction zones and back arc basins such as the Kohistan-Ladakh and Woyla basins (Gibbons et al., 2015, and references therein)

- Finally, newer data sheds more light on the evolution of the South Pacific Trench as an interlinked system.

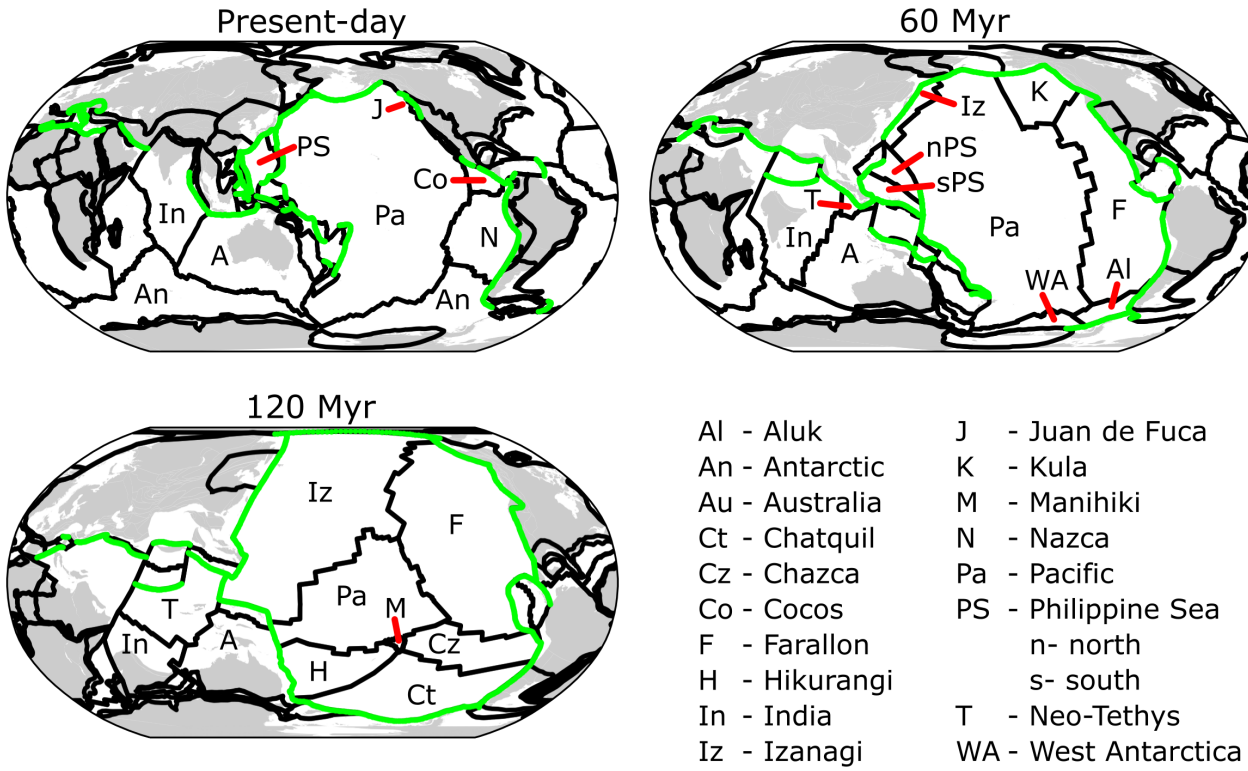


Figure 2.2: Plate boundaries through time: at 120 Myr, 60 Myr and the present day, from the reconstruction of Müller et al. (2019). Names of the main subducting plates in the Pacific, Indian and Tethys Oceans appear as abbreviations on the maps. Reconstructed landmass is shown as grey polygons in the background. Active trenches are shown in green, and other plate boundaries in bold black lines. Some minor deformation zones and plates boundaries were removed for clarification.

2.4 Overview of subduction evolution based on the compilations

In this section, we first give a brief overview of global subduction evolution during the late Mesozoic (after 120 Myr). Next, we compare the Cenozoic (after 60 Myr) evolution of the main trenches in the three reconstructions, highlighting the effects of uncertainties and updates. We conclude by examining the trends in velocity, and for the main trenches during the Cenozoic trends in velocity with age, to evaluate expressions of subduction forcing.

2.4.1 Global overview

In this section we present a global overview of the evolution of plates and trenches and of major tectonic events since 120 Myr. While some of these events and their causes are debated, we focus our overview on the plate reconstruction model of Müller et al. (2019) shown in M19 (Fig. 2.2 and Fig. 2.3). The evolution for M16 displays similar features and is presented in Fig. 2.4. The evolution of the model underlying S06 differs in a few ways as summarised above, and can be found in Müller et al. (2008b).

The last 120 Myr period covers the evolution of the subduction of the Pacific Plate from the early subduction beneath the Australian Plate, along the South Pacific Trench, to the present circum-Pacific subduction systems (Seton et al., 2012). The period is marked by several major global tectonic events including the closure of the Tethys Ocean and the subsequent collision of India and Arabia with Asia (Rowley, 1996), the ongoing opening and expansion of the Atlantic Ocean and the fragmentation of Gondwana into separate continents (e.g. Torsvik et al., 2009). It is also characterised by the disappearance by subduction of the Izanagi, Phoenix and Kula Plates (Seton et al., 2012). These events, which were interdependent, directly affected the organisation

of plates and trenches locations globally. The effect of these global events differs between S06 and M16-19, and to a lesser degree between the M16 and M19.

At 120 Myr, the Pacific Plate is only one of several plates in the Pacific Ocean. The main plates in the Pacific ocean at that time are the Izanagi (subducting below East Asia), Farallon (subducting below the Americas) and the fragments of the Phoenix Plate (subducting below Australia and Antarctica) (Fig. 2.3), with a growing Pacific plate at the triple junction of these three main plates. By the early Cenozoic, at 60 Myr, the Izanagi Plate and Phoenix fragments have almost fully subducted and the Farallon Plate started to fragment, resulting in a separate Kula Plate, subducting below Alaska and Canada (Fig. 2.3).

An event, called the global Eocene plate reorganisation event (EPRE) (Seton et al., 2015; Müller et al., 2016b), dated 50–40 Myr is apparent in many regions around the Pacific Ocean. While the reasons for this event are debated, most agree it is affected by the subduction of the Izanagi-Pacific Ridge (Vaes et al., 2019, and references therein) and the initiation of subduction along the IBM system (Seton et al., 2015; Müller et al., 2016b), as well as the India-Asia collision (Hall, 2002). the EPRE is commonly associated with a change in the direction of motion of the Pacific Plate held responsible for the change in orientation of the Hawaii-Emperor hotspot track (Sutherland et al., 2017; Vaes et al., 2019). It has also been associated with the merging of the Kula Plate, near Alaska, with the Pacific Plate (Madsen et al., 2006, and references therein), increased retreat of trenches subducting the southern part of the Pacific Plate (Seton et al., 2015; Whittaker et al., 2007) and the merging of the India and Australia Plates (Müller et al., 2016b).

In the last 30 Myr, both the Farallon and South Pacific Trenches segmented (Figs. 2.5 and 2.6). In North America, the interaction of the Farallon-Pacific Ridge with the North America Trench separated the Juan de Fuca Trench from the rest of the plate (Fig. 2.4; Riddihough, 1984). The later formation of the Cocos Ridge segmented the Farallon Plate and associated trenches further into the Cocos and South America (Nazca)

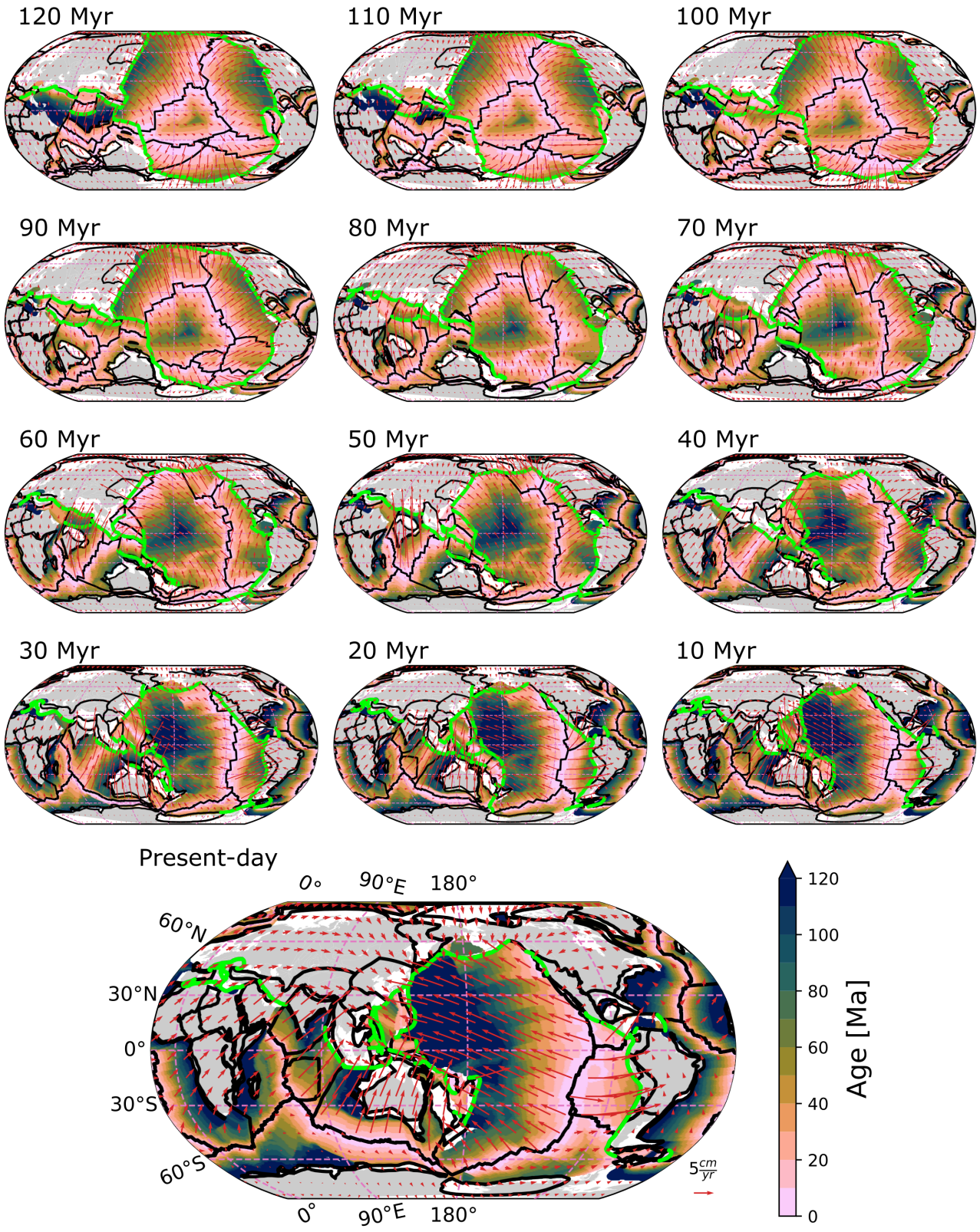


Figure 2.3: Global ocean floor age through time in 10 Myr intervals from 120 Myr ago to present, from the reconstruction of Müller et al. (2019). Black polygons mark plate boundaries, with subducting trenches overlain in bright green. Red arrows mark velocity vectors. Reconstructed landmass is shown as grey polygons in the background.

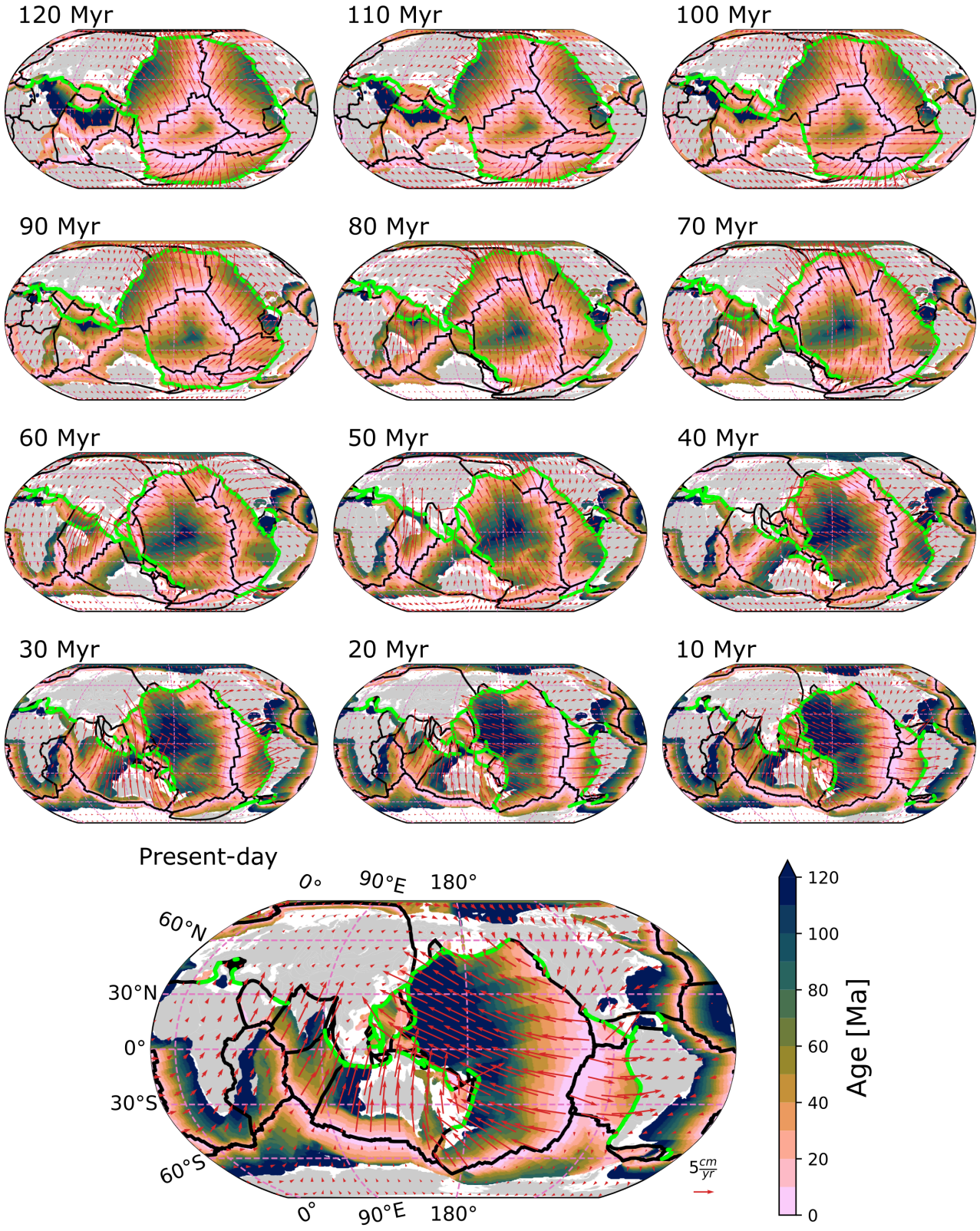


Figure 2.4: Global ocean floor age through time in 10 Myr intervals from 120 Myr ago to present, from the reconstruction of Müller et al. (2016b). Black polygons mark plate boundaries, with subducting trenches overlain in bright green. Red arrows mark velocity vectors. Reconstructed landmass is shown as grey polygons in the background.

Trenches (Lonsdale, 2005). The segmentation of the South Pacific Trench at the same time is not associated with ridge-trench interaction but with the arrival of major buoyant features to the trench, in particular the Ontong-Java Plateau (Mann and Taira, 2004).

The Indian Ocean-Tethys domain during the past 120 Myr is characterised by a more fragmented set of trenches, which evolved as the Tethys closed. Closure started in the late Mesozoic in the west where Africa and Europe or continental blocks between the two continents collided. In the early Cenozoic, at 60–50 Myr, the rapid northward motion of India led to the closure of the central Tethys, with collision of the first Indian arc system around 50 Myr (Hall, 2002). Subduction of the Tethys, Indian and Australian Plates was continuous since 120 Myr along the evolving Sunda-Java-Banda Trench. This subduction behaved increasingly as a coherent zone after spreading along the Wharton Ridge, which separated the Indian and Australian plates, ceased around 40 Myr (Zahirovic et al., 2014; Sutherland et al., 2017). The evolution of this trench system since 20 Myr is strongly influenced by collision with the Australia continental margin.

2.4.2 Comparison of the evolution of the main trenches

In this subsection we compare the evolution of the seven main trenches discussed in Sdrolias and Müller (2006) during the Cenozoic, to illustrate similarities as well as the implications of differences between the underlying reconstructions. The differences in part reflect improved insights and data in the newer reconstructions but in part different choices within the inherent uncertainties in the reconstructions. Figs. 2.5 and 2.6 show the trench evolution in M19, M16 and S06.

Figs. 2.5 and 2.6 shows that the overall trend of the eight main trenches is one of continuous trench retreat, apart from a few sections such as the Cocos trench (which is rotating) and the northern end of the Sumatra trench in the late Cenozoic. As a

result of this dominant trench retreat, the plates in the Pacific Ocean are diminishing in size. One exception is the PSP, which is consumed in the Philippine and Ryukyu-Nankai trenches but also expands westward (at diminishing rate) as the IBM trench retreats.

There are two main differences in the evolution of the South America trench in S06 and M19 (Fig. 2.5) . The velocity and position differ due to the introduction of deformation zones in Müller et al. (2019). The South America trench in M19 is less curved at 60 Myr due to subsequent oroclinal bending. This results in a lower trench retreat velocity in M19 relative to M16 and S06. In addition, the subducting-plate age distribution along the South America trench in M16-19 has changed because of the different history of Phoenix plate fragmentation. In S06, a ridge intersects the central trench in the Early Cenozoic, while in M16-19 this ridge is inactive and intersects the trench further north, resulting in subduction of older lithosphere at the centre of the trench (near the main bend) throughout the Cenozoic (Figs. 2.3 and 2.4).

The evolution of the Farallon Trench below Central and North America was updated in two ways. Firstly, in the early Cenozoic, the subduction below the Caribbean Plate is allowed to rotate (from approximately W-E to NW-SE; Fig. 2.5) independently from the main Farallon Trench that borders North America. Secondly, in M19, the Farallon-Kula spreading centre is inferred to initiate significantly further south than in S06. As a result the northern end of the North America trench is highly deformed in the early Cenozoic.

The evolution of the Aleutian-Alaskan Trench is largely similar in the three reconstructions, with a main phase of back arc extension between 50–45 Myr (Fig. 2.5), and the strongest retreat in the centre of the trench. However, the ages along the trench evolve differently, in particular in the east where in the early Cenozoic the Kula plate subducts, due to the updated evolution of the Kula plate in M16-19. In S06, the eastern, Alaskan, end of the trench coincides with the Izanagi-Farallon ridge up to 60 Myr and remains almost stagnant. By contrast, in M16-19, the eastern end of the trench

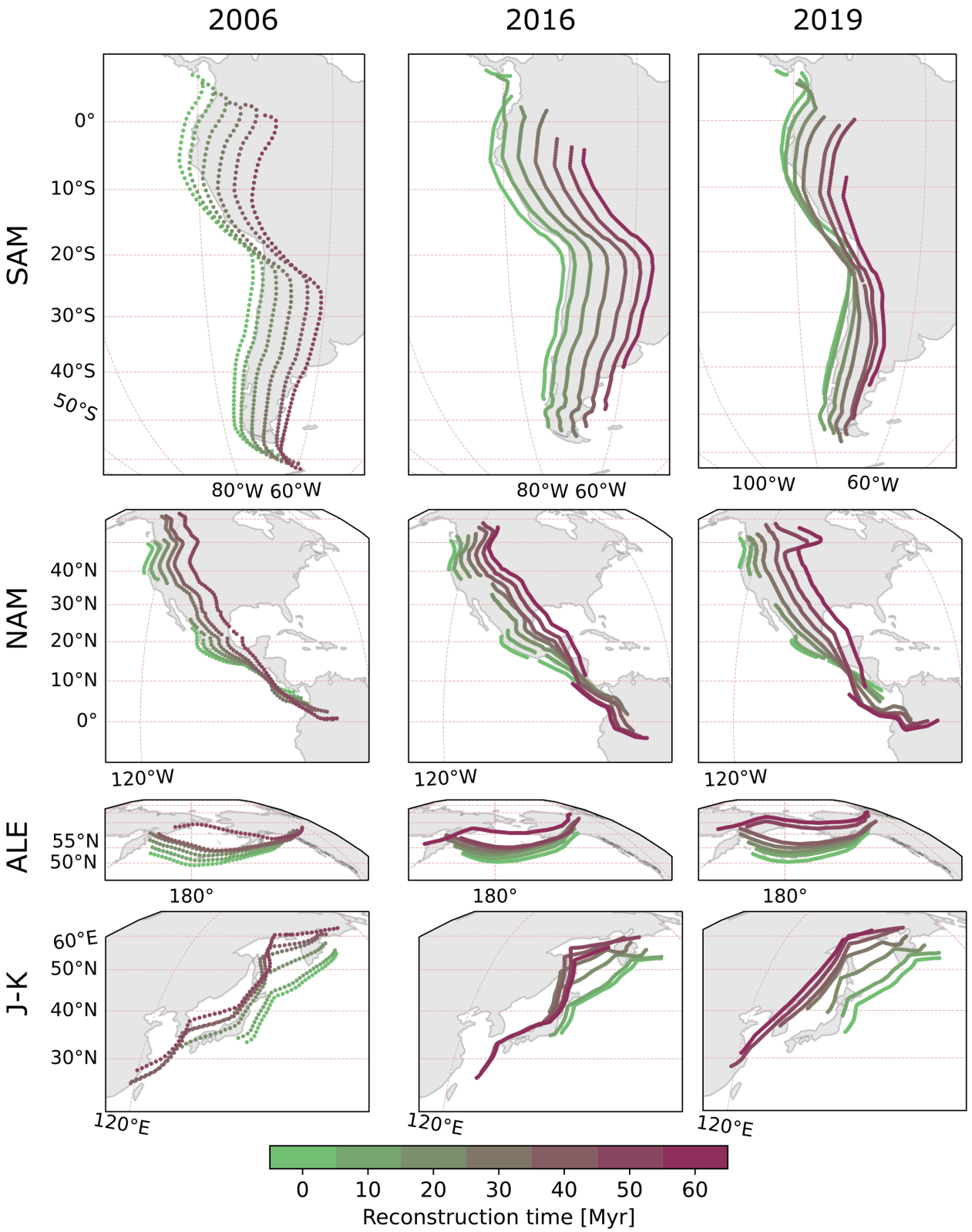


Figure 2.5: Evolution of eastern and northern trenches in the Pacific Ocean through time from S06, M16 and M19. Reconstruction time is marked by colours. Present land mass is plotted in background. Abbreviations: ALE – Aleutian, J-K – Japan-Kuril, NAM – North America, SAM – South America.

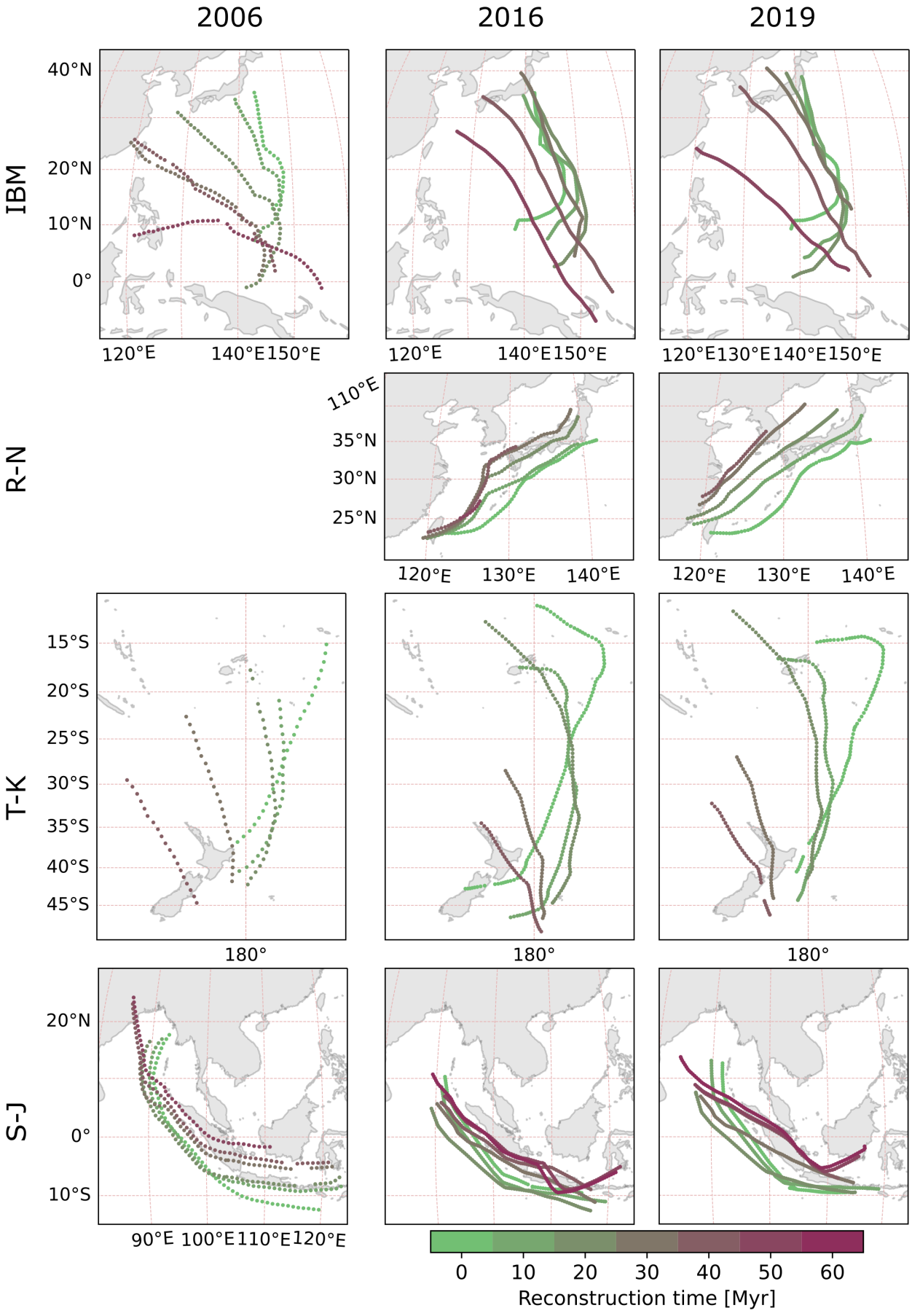


Figure 2.6: Evolution of western and southern trenches in the Pacific Ocean and in the Indian Ocean through time from S06, M16 and M19. Reconstruction time is marked by colours. Present land mass is plotted in background. Abbreviations: IBM – Izu-Bonin-Mariana, R-N – Ryukyu-Nankai, S-J – Sunda-Java, T-K – Tonga-Kermadec.

subducts Kula Plate at this time and is more mobile.

The evolution of the Japan-Kuril Trench during the Cenozoic begins with the final stages of subduction of Izanagi Plate, which subducts fully by ∼55 Myr. In M19, a large offset in the Izanagi-Pacific ridge is inferred to coincide with the kink in the Kamchatka-Kuril trench, while further south there is less variation in Izanagi age at the trench (Fig. 2.3), and hence in when the ridge reaches the trench, than in S06 (Fig. 2.5). The later evolution of the trench, from 45 Myr, is highly influenced by the subduction of the (North-)PSP along the Ryukyu-Nankai Trench and the fast retreat of the IBM Trench. As discussed below, in M16-19, the rotation of the IBM trench is much reduced and mostly accomplished between 50–30 Myr. As a result, the location of the Boso triple junction, where Nankai, Izu and Japan trenches intersect, already marks the southern end of the Pacific subduction system along the Japan-Kuril trench after 40 Myr in M16-19. By contrast, in S06, the Nankai segment is subducting Pacific lithosphere until about 20 Myr. In M19, this trench evolves from a relatively straight trench in the early Cenozoic to its current curved arc with two kinks.

The evolution of the IBM Trench is strongly linked with the evolution of the Ryukyu-Nankai Trench and the formation of the (North- and South-)PSP, for which new data has provided better constraints since S06. Initiation of the IBM Trench has now been dated at ∼50 Myr. In M16-19, a rapid phase of rotation between 50–30 Myr is followed by a slower rotation phase since 30 Myr, while in S06, rotation rate is high throughout the Cenozoic with short pause between 40–30 Myr (Fig. 2.6).

Since S06, the evolution of the intra-oceanic Tonga-Kermadec Trench was also examined in wider regional perspective, by considering it as part of the South Pacific Trench system (e.g. Schellart et al., 2006). The evolution of the Tonga-Kermadec Trench after 40 Myr is similar between S06 and M16-19 with minor differences in trench position and retreat velocity. Some variation in ages along the trench between 40–20 Myr stems from changes in the updated history of Phoenix Plate fragmentation. Post 90 Myr, the spreading ridges between the Pacific and the Manihiki and Hikurangi fragments

ceased, resulting in the formation of single large Pacific Plate. The intersection of these extinct ridges arrived at the Tonga-Kermadec Trench at ∼20 Myr, resulting in younger ages close to the ridges and older ages between them.

Finally, the Sunda-Java Trench evolution in M16-19 mainly differs from that in S06 in the evolution of trench shape due to updates in the evolution of the various basins in the South-East Asian part of the overriding Eurasian Plate (Zahirovic et al., 2014; Bai et al., 2015). In particular, M19 includes significant back-arc extension between 50–20 Myr, and a more significant trench advance of the northern end of the Sumatran Trench post 20 Myr.

In summary, these changes in trench evolution between the different reconstructions reflect both evolving constraints and insights and inherent uncertainties. In particular for intra-oceanic plate boundaries, trench locations are often uncertain by several 100 km. In addition, the timing and magnitude of rotations can be highly uncertain, as these rely on limited evidence, like preserved volcanic arcs, together with other global constraints for making a complete plate reconstruction.

2.4.3 Velocity and age trends

We examined global subduction behaviour by reviewing trench and plate motions globally in M16-19, following a similar analysis of S06 by Goes et al. (2011). Such an analysis can shed light on the main subduction driving forces. Studies of models of single plate subduction indicate that if local slab pull is a dominant driving force (as indicated by e.g. Conrad and Lithgow-Bertelloni, 2002; Schellart, 2004b), subducting plate velocity and trench retreat should increase with subducting-plate age (Garel et al., 2014; Agrusta et al., 2017) and trenches would dominantly retreat (Bellahsen et al., 2005; Capitanio et al., 2007). Previous work has indicated that such a correlation exists between ages at the trench and subducting-plate velocities along the main Cenozoic and present-day trenches (Carlson et al., 1983; Lallemand et al., 2005; Sdrolias

and Müller, 2006; Goes et al., 2011). Such observational studies have also shown that trenches mostly retreat, as long as a mantle reference frame that is a reasonable approximation of a global reference and which limits intra-hotspot motions is used. This retreat had also been shown to be consistent with tomographic imaging of slab shapes (Goes et al., 2011; Williams et al., 2015). However, previous work also indicated that the magnitudes and directions of trench motions do not vary simply with age, even for the main trenches (Goes et al., 2011). Here we test whether such trends are present in our newer subduction parameter compilations. We note here that inevitably, some of our analysis may reflect the assumptions used by the GPlates algorithm in interpolating reconstructed plate boundaries and motions. This is more likely to occur at earlier reconstruction times where geological evidence is more scarce.

Fig. 2.7 shows the analysis of the distributions of subducting-plate velocity (V_{sub}) relative to total convergence (V_{con}=V_{sub}+V_{tr}) and trench velocity (V_{tr}) relative to subduction velocity. All velocities are measured in a mantle reference frame, as discussed in Section 2.3.3. We also considered the angle between the trench strike and the direction of motion of the subducting plate (Fig. 2.7A-B). We divided the angles to perpendicular motion (within 30° to trench normal; 54-59% of sampled points), mixed motion (within 30°-60° to trench normal; 29-32% of sampled points) and parallel motion (over 60° to trench normal; 12-14% of sampled points) and excluded from the velocity analysis (Fig. 2.7C-F) any points with parallel motion, to remove non-subducting segments from the analysis of force balance in subduction systems. We show the trends for all trench segments since 120 Myr and highlight those for the main trenches since 60 Myr which are most likely to show the influence of local slab pull. We note that long trenches with relatively uniform behaviour may skew the analysis, an effect which is greater for the analysis of the main trenches.

The majority of subducting plates, 74% of sampled points, move close to perpendicular to the trench (within 45° to the trench normal in Fig. 2.7A-B). This indicates that trench position tends to align with the direction of motion of the subducting plate,

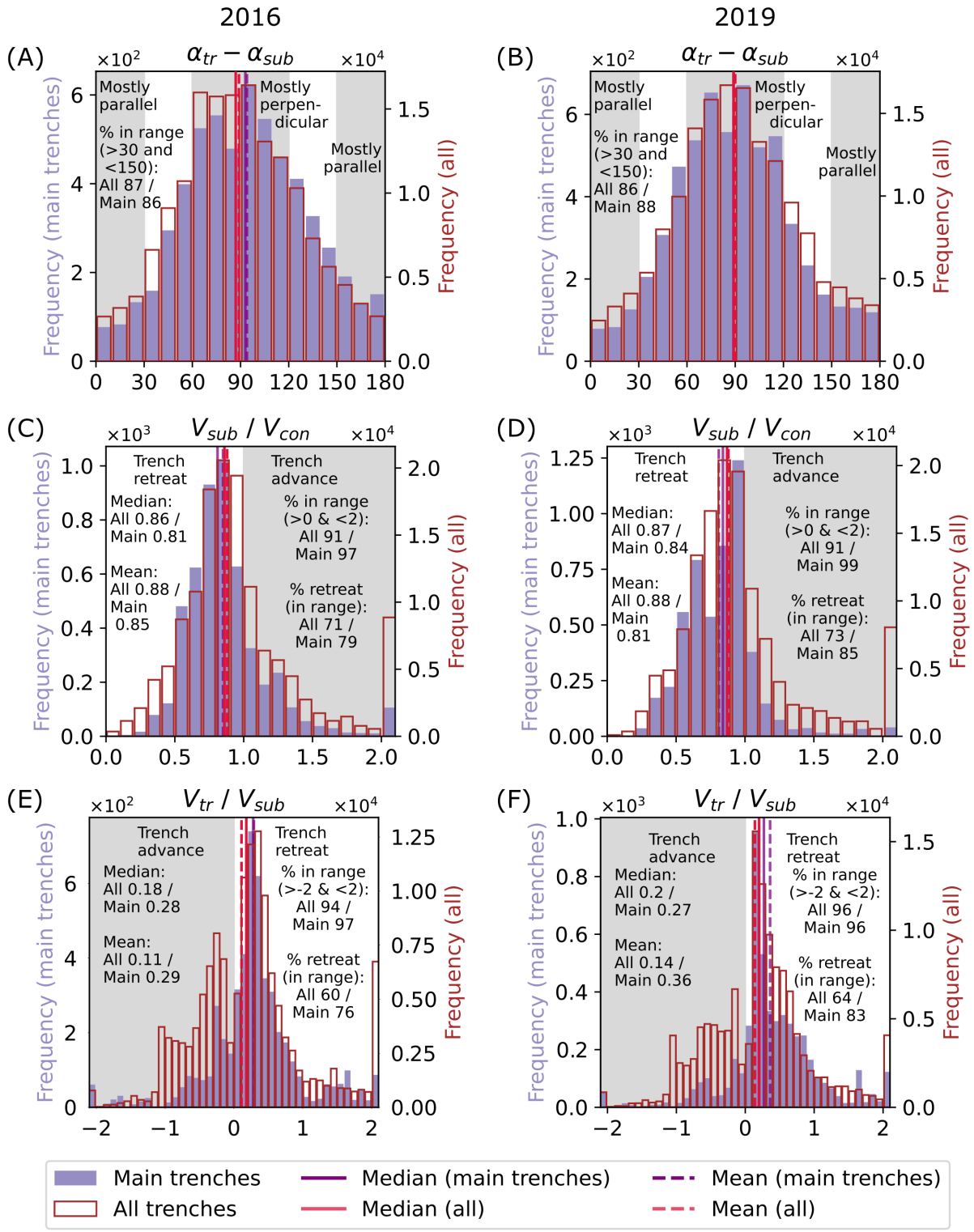


Figure 2.7: Histograms of frequency along the main trenches after 60 Myr (purple) and of all trench segments after 120 Myr (red outlines) with median (solid lines) and mean (dashed lines) values. A) and B) show angle between trench strike and subducting plate motion direction, where 0° and 180° indicate motion parallel to the trench. C) and D) show the ratio of subducting plate to convergence velocity. Points with values >2 are summed in the last bar. E) and F) show the ratio of trench to subducting plate velocity. Points with values <-2 and >2 are summed in the first and last bars. Statistics from M16 are shown in the left panels (A, C and E) and from M19 in the right panels (B, D and F). Points with values below 30° and above 150° in A and B were excluded in C-F. Factor multipliers for the number of points are shown above the y axes on either side of the graphs.

which is expected to be mainly determined by slab pull. Such an alignment of trench normal and plate convergence is as observed in recent subduction models, where initially oblique trenches tend to rotate to align with subducting plate motion (Rudaviciute, 2015; Balázs et al., 2021). The small group of subducting-plate motion parallel trench segments in the compilations are likely the result of secondary factors controlling local trench position. These include three-dimensional effects that lead to local misalignment of trench and subduction orientation, such as the subduction of buoyant features (Miller et al., 2006a,c; Gulick et al., 2007; Seton et al., 2012, see further discussion in Chapter 5).

Similar to Goes et al. (2011), we find that subduction is dominated by subducting-plate motion. Along those segments of the trench where convergence occurs within 60° to the trench normal, between 80–90% of the plate convergence is accomplished by motion of the subducting plate into the trench 2.7C-D). This percentage is higher (86-88%) for the complete compilation than for the main trenches (81-85%). In the overwhelming majority of trench segments, subducting plate velocity is more than twice the magnitude of trench velocity (either retreating or advancing; Fig. 2.7E-F). The observed contribution of subducting-plate advance is higher than in many single-subduction models (see also discussion in Chapter 3). The higher contribution of trench retreat for the main trenches is consistent with what would be expected if along those large trenches, local slab pull is a dominant driving force (Conrad and Lithgow-Bertelloni, 2002).

We also find that retreat dominates trench motion, with retreat occurring for 60-73% of points, with motion within 60° of the trench normal (Fig. 2.7C-F). This trend is much more prominent for the main trenches during the Cenozoic, with 76-85% of the points retreating, as would be expected for the presence of large slabs and an important role of local slab pull. A low trench to subducting-plate velocity ratio and a dominance of trench retreat indicate that the internal strength of the plate (i.e. resistance to bending) is not a major contribution to the force balance (Ribe, 2010), a point which is

discussed further in Chapter 4. Low bending strength allows local slab pull (for major plates) or other external forces (for minor subduction segments) to determine the balance of plate and trench motions. We note that, following the work of Williams et al. (2015) who found that trench retreat is likely to dominate global trench motions in pre-Cenozoic periods, the APM model used in Müller et al. (2019) includes trench retreat as parameter for 'best-fit' optimisations. However, this parameter was not included in the APM model for Müller et al. (2016b), which presented similar trends to Müller et al. (2019) (Fig. 2.7).

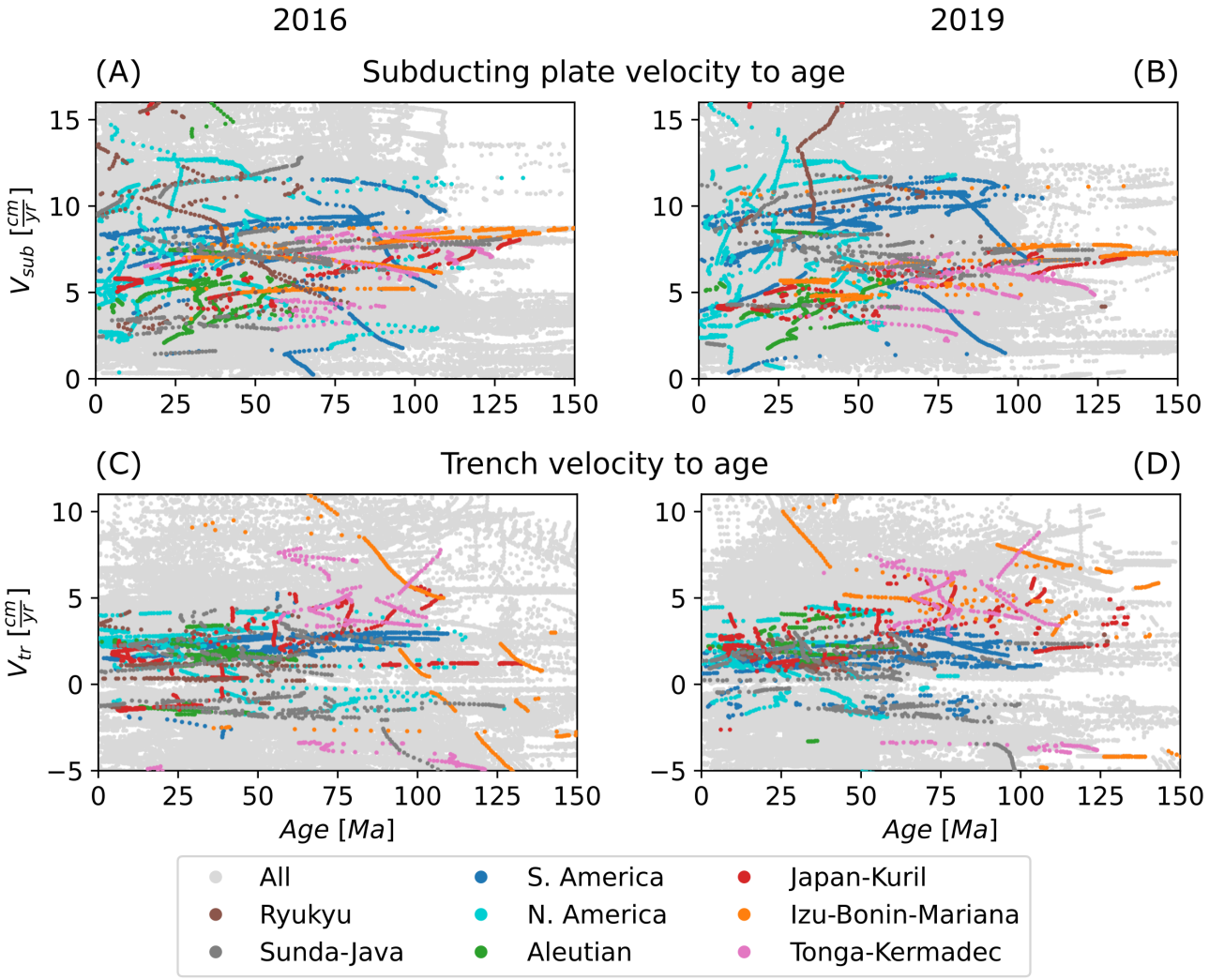


Figure 2.8: Age trends illustrated by: A) and B) subducting plate velocity versus subducting plate age, C) and D) trench velocity versus subducting plate age. Parameters from the main trenches after 60 Myr are shown in colour (warm colours indicate West Pacific trenches and cold colours indicate East Pacific trenches) and those from all trench segments after 120 Myr are shown in the background in grey. Information from M16 in left panels (A and C) and from M19 in right panels (B and D).

We do not find a global correlation between either subducting-plate velocity or trench velocity with the age of the subducting plate at the trench (Fig. 2.8). A mild increase in subducting-plate velocity with age is observed during the Cenozoic in trenches in the West Pacific (Japan-Kuril, IBM system and Tonga-Kermadec; Fig. 2.8A-B). This is consistent with the trend previously inferred from present-day data at the main trenches (Carlson et al., 1983; Doglioni et al., 2007; Goes et al., 2011; Vérard, 2019), and does hint at slab pull being controlled by local age at the trench. However, overall, a correlation between age and subducting-plate velocity, as occurs in models of single-plate subduction (Schellart, 2008; Goes et al., 2011), is not observed. Rather, for the main trenches during the Cenozoic, there is a larger range of subducting-plate velocities for younger plates ($<$80 Ma), although this finding may be a bias due to the small set of trench segments where old plate subducts.

Trench velocity magnitude at the main trenches during the Cenozoic is mostly limited between minor advance (-1 cm/yr) and mild retreat ($\sim$3 cm/yr) (Fig. 2.8C-D), with a somewhat larger range for older ages ($<$100 Ma), although this range is dominated by the large motions of the IBM and Tonga-Kermadec Trenches.

The lack of age trends indicates that in natural subduction zones other factors than slab pull controlled by local age at the trench determine the magnitude of subduction velocity. Even if the dominant force is pull from the slab directly attached to the subducting plate (as indicated by global modelling studies Forsyth and Uyeda, 1975; Becker and O'Connell, 2001; Conrad and Lithgow-Bertelloni, 2002), lateral variations in age and additional buoyancy variations (as those discussed in Chapter 5) may make local age a poor indicator of this pull. In addition, external forces exerted on the plate, such as drag by global mantle flow pattern set up by large slabs (Becker and Faccenna, 2011) or by concentrations of mantle plumes (Lithgow-Bertelloni and Silver, 1998) may play a role. For small trenches, external forces and constraints are likely a much more dominant influence than in the main subduction systems, consistent with the larger scatter of velocities in the global compilation (including all after 120 Myr), compared

with the main trenches during the Cenozoic.

2.5 Tour of regional evolution of the main trenches

In this section, we summarise the evolution of position, subducting-plate age and velocities along the main trenches in M19 in the context of a the global tectonic evolution of the Earth during the last 120 Myr, similar to the analysis done in Sdrolias and Müller (2006).

North and South America Trenches

In M19, at 120 Myr, the Farallon plate subducted below North America from Alaska to Mexico (Fig. 2.3). West of northern South America, the Quebradagrande back-arc basin has started forming, bounded by subduction of the Farallon on the western side, and early stages of subduction of the Proto-Caribbean seafloor along the Greater Arc of the Caribbean (GAC) on the eastern side (Braz et al., 2018; Braszus et al., 2021). Eastward Farallon subduction below what will become Central America ceased at ~100 Myr and restarts at 85 Myr, isolating the Caribbean Plate. At a similar time, the Chazca Plate becomes part of the Farallon as the spreading between the two plates ceased. This results in a long continuous subduction spanning below most of North and South America. At the same time, the Kula Plate separates from the northern Farallon along a new spreading centre.

Fig. 2.9 shows in more detail the subducting-plate age distribution through the Cenozoic. Along the long Farallon Trench, ages of the subducting lithosphere at the start of the Cenozoic broadly increase from north (near the Farallon-Kula ridge) to the south, with a sharp decrease in lithospheric age at the southern part of the South America trench due to the continued spreading along the ridge between the Farallon and the Aluk fragment of the Phoenix Plate (Fig. 2.3).

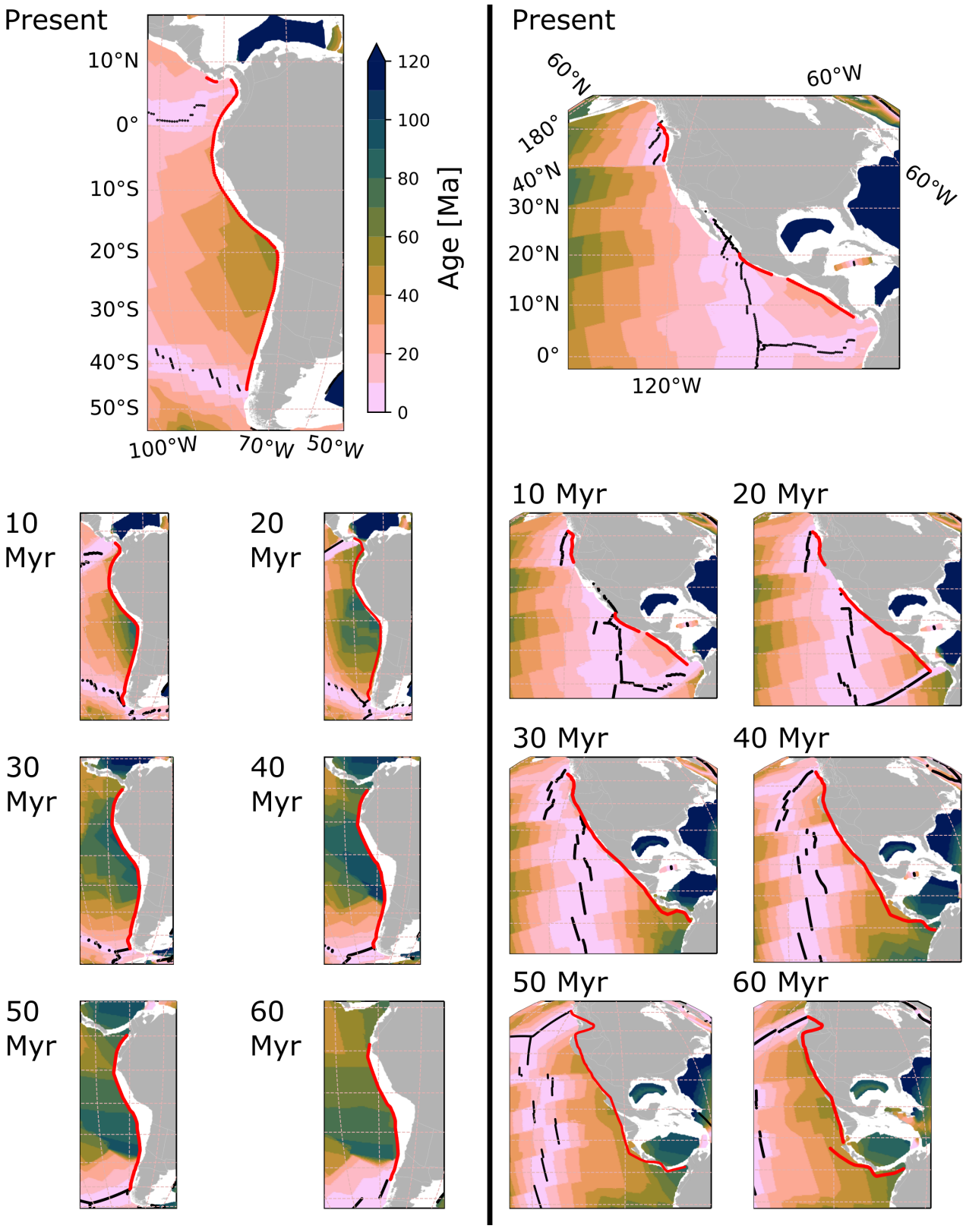


Figure 2.9: Evolution of South America and North America trenches during the Cenozoic, with age grid and reconstructed landmasses, based on Müller et al. (2019).

Further segmentation at the north of the Farallon Plate occurred at ∼53 Myr with the formation of the Vancouver Plate (Fig. 2.3; Wright et al., 2016). The boundary between the Vancouver and Farallon Plate slowly subducts below the North America trench until fully subducted 29 Myr ago. The intersection of the Pacific-Farallon spreading ridge with the North America Trench leads to the formation of the Juan de Fuca Plate and the initiation of the San Andreas transform boundary between the Pacific and North American Plate (Riddihough, 1984; Atwater, 1989). The southern Farallon later fragments into the Cocos and Nazca segments, with a new spreading ridge initiating between them at ∼23 Myr (Lonsdale, 2005). As the distance between the spreading ridge between the Pacific and Farallon fragments and the North and South America Trench decreases through the Cenozoic, the ages of the subducting plates at the trench decrease. At present, the maximum age of the Juan de Fuca at the trench is only 5 Ma, of the Cocos Plate 20–30 Ma and of the Nazca Plate 50 Ma. Throughout the Cenozoic, the oldest part of the Farallon Plate (and later the Nazca Plate) subducts near the centre of the Andean Trench. With the initiation of the Cocos-Nazca spreading ridge, the age-gradients along the trench have become further pronounced.

North Pacific Trenches

In the North Pacific, at 120 Myr, the Izanagi Plate subducted at a long trench stretching along most of the eastern margin of Asia all the way to Alaska (Fig. 2.3). As this plate is consumed by subduction, first the Kula subduction zone grows westwards, subducting below the eastern Aleutians, and from 70 Myr the northern Pacific Plate starts to subduct below the Aleutians. At 55 Myr, when the last remnant of the Izanagi-Pacific Ridge subducted along its full length within a few Myr, Pacific subduction also started below Asia. In these last phases of Izanagi subduction, very young lithosphere and actively spreading ridges subduct rapidly along most of the margin, probably driven by the previously subducted large continuous Izanagi slab (Goes et al., 2008).

Fig. 2.10 shows the Cenozoic evolution of the Aleutian and Japan-Kuril Trenches. Spread-

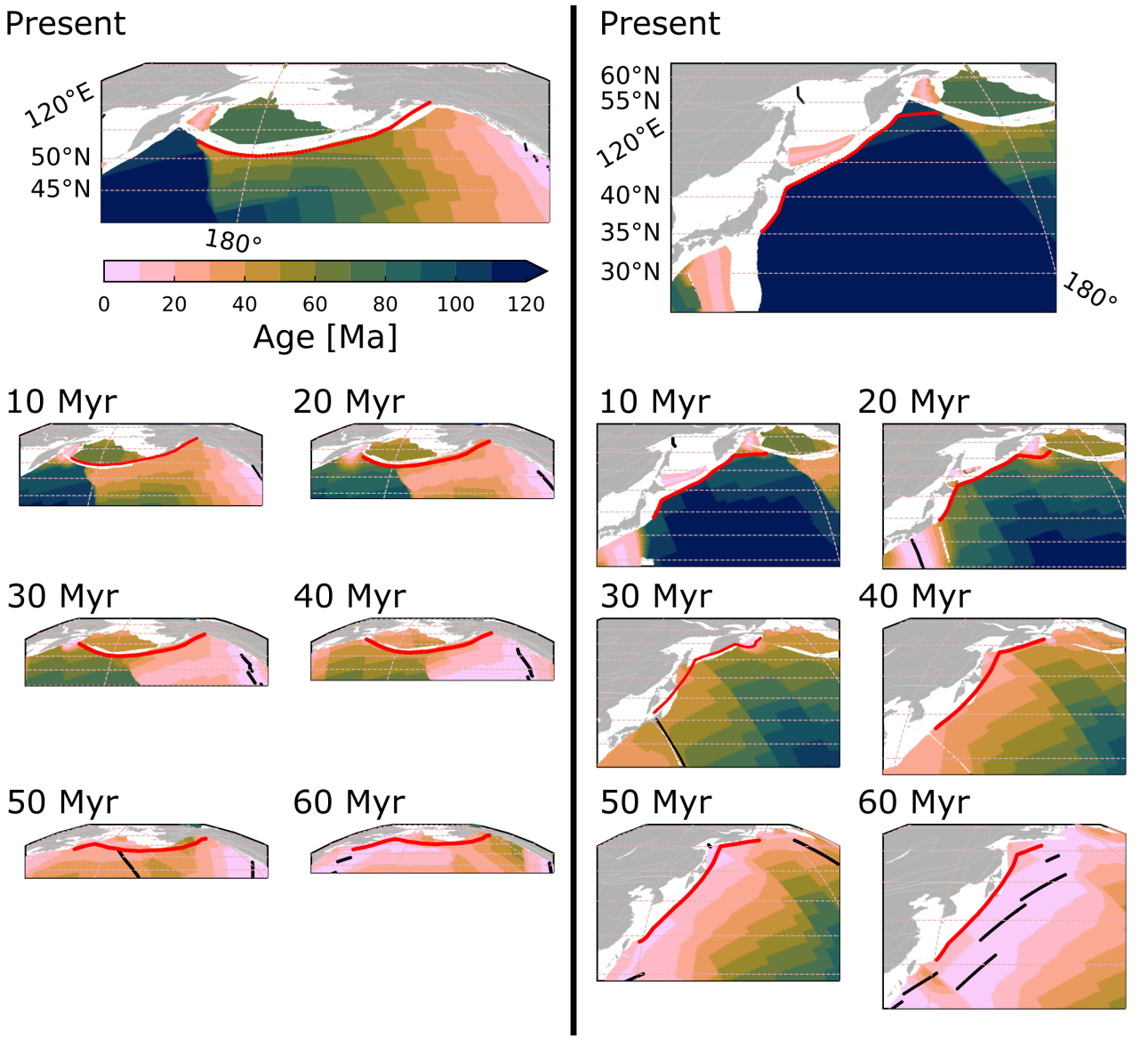


Figure 2.10: Evolution of Aleutian and Japan-Kuril trenches during the Cenozoic, with age grid and reconstructed landmasses, based on Müller et al. (2019).

ing along the Kula Ridge ceased at ~41 Myr (Wright et al., 2016), as part of the EPRE, effectively merging it with the subducting Pacific Plate. The proximity of the extinct ridge to the Aleutian Trench near Alaska, and its continued subduction until ~20 Myr results in the present day young ages near the eastern edge of the Aleutian Trench. Along the central and western segments of the Aleutian Trench, ages are controlled by the ongoing subduction of the Pacific Plate and are therefore older. Along the Japan-Kuril Trench, the subduction of the Izanagi Ridge almost parallel to the trench (Whittaker et al., 2007), resulted in similar ages everywhere along the trench. Fol-

lowing the subduction of the ridge at ∼55 Myr the retreat rate of the trench increases rapidly, resulting in quick ageing all along the trench (Seton et al., 2015). At present, subducting-plate ages at the trench are between 90 Myr, below Kamchatka, and 110–130 Myr, below Honshu.

West Pacific Trenches

The subduction at the IBM and Ryukyu-Nankai Trenches initiated in the Cenozoic and are shown in Fig. 2.11. The evolution of both trenches is dominated by the fast retreat of the Pacific Plate along the IBM Trench following the EPRE (Whittaker et al., 2007; Seton et al., 2015), and are interlinked with the subsequent expansion of the North- and South-PSP back-arc basins (Zahirovic et al., 2014). The subduction of the PSP along the Ryukyu-Nankai and Philippine Trench is also associated with regional plate reorganisation as a result of the westward motion of South East Asia following the India-Asia collision (Hall, 2002). The subducting-plate ages along the two trenches differ substantially. The Ryukyu-Nankai ages at the trench reflect the young ages of the basins making up the PSP, with present-day subducting-plate ages below 60 Ma at the Ryukyu Trench, and around 20 Ma at the Nankai Trough (determined by the timing of activity of the now extinct Shikoku Ridge, which subducts at this part of the trench). On the other hand, the ages at the IBM Trench reflect the oldest ages of the Pacific Plate, due to the fast consumption of the plate as the trench retreated, and presently range from 120 Ma below northern Izu to 160 Ma at the Mariana Trench.

South Pacific and eastern Indian Ocean Trenches

The South Pacific Trench is the first location where subduction of the Pacific Plate initiated ∼120 Myr (Fig. 2.3). The size of the trench grew steadily until 80 Myr ago as the Izanagi Plate, north of the Pacific, and the Hikurangi segment of the Phoenix Plate, south of the Pacific, subducted and shrank in size. The trench grows rapidly

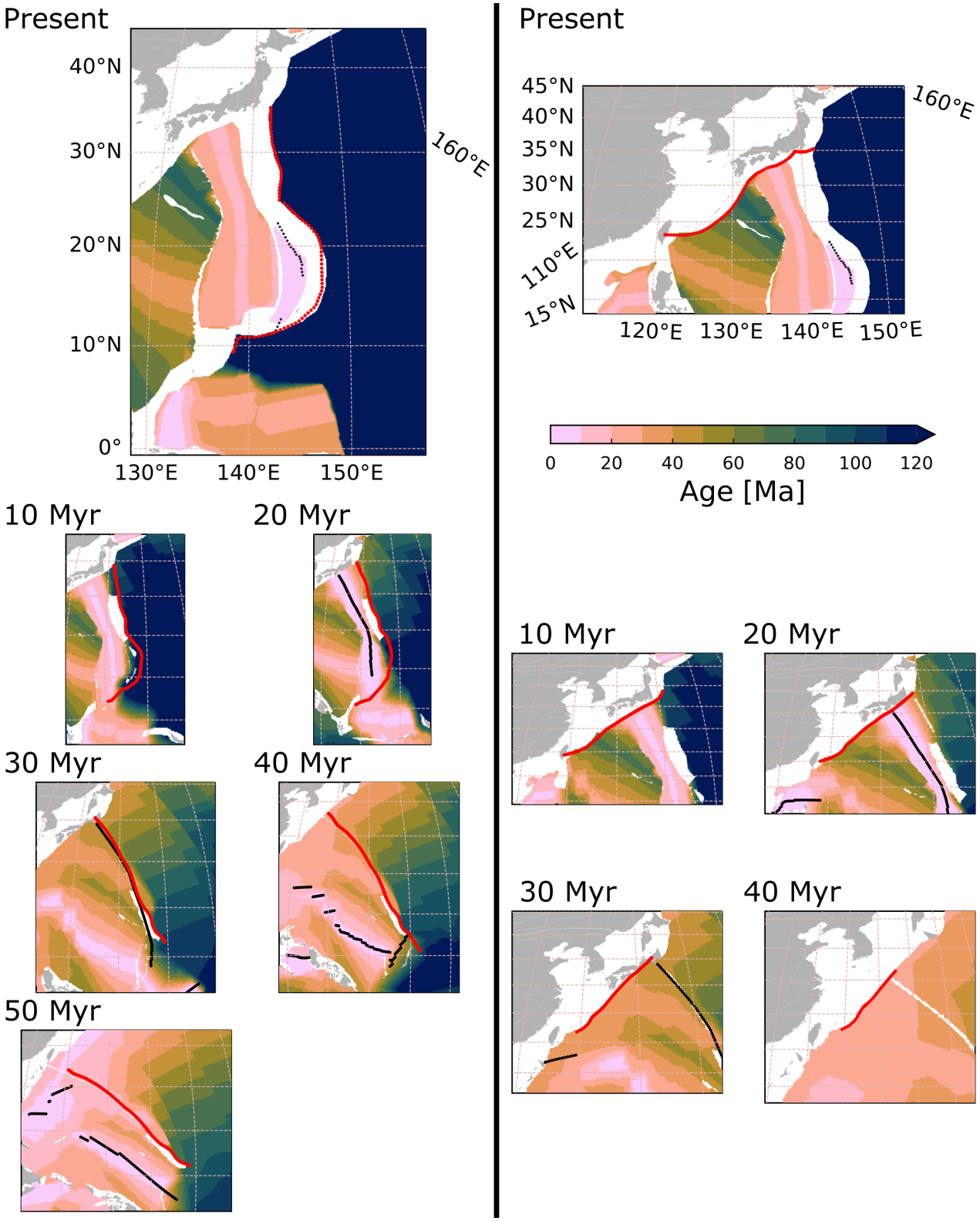


Figure 2.11: Evolution of Izu-Bonin-Mariana and Ryukyu-Nankai trenches during the Cenozoic, with age grid and reconstructed landmasses, based on Müller et al. (2019).

when at around 80 Myr, spreading along the Pacific-Hikurangi-Manihiki ridges ceases and these plates amalgamate into a single larger Pacific Plate. The subduction of the Izanagi Plate and the consequent formation of the PSP and IBM Trenches (Fig. 2.3) define the northern boundary of the trench since 60–50 Myr ago.

By the early Cenozoic, the South Pacific Trench consists of a long continuous trench subducting about 90 Ma Pacific lithosphere in the north, and relatively young lithosphere from the extinct Hikurangi-Pacific spreading ridge, the Osbourne Ridge, in the south. Fig. 2.12 presents the evolution of the South Pacific subduction system as well as that of the neighbouring Sunda-Java Trench in the Indian Ocean. After the EPRE, the morphology of the trench evolved (Whittaker et al., 2007; Sutherland et al., 2017). Rotation of both the trench and Pacific Plate motions led to increasing convergence normal to the trench. The South Pacific Trench maintained a relatively continuous nature until $\sim$20 Myr. Between 20–10 Myr subduction polarity changed along several segments of the trench, where recently-formed back-arc basins within the Australian Plate began subducting beneath the Pacific Plate. This change was likely induced by the arrival at the trench of major buoyant plateaus on the Pacific Plate, most notably the Ontong-Java plateau (OJP) (Mann and Taira, 2004). The change in subduction polarity resulted in fragmentation of the South Pacific Trench, where the southern, central and northern sections separated into the Tonga-Kermadec, New Hebrides and New Britain Trenches, respectively. The reversal of the subduction polarity at the New Hebrides and New Britain Trenches (Mann and Taira, 2004) is the reason for the present-day young ages along these segments, while along the Tonga-Kermadec section, subduction of old Pacific lithosphere continues.

Subduction along the Sunda-Java Trench was part of a long subduction system where several of the plates which composed the Tethys Ocean subducted below Asia. The subduction of the Tethys began during the Mesozoic and concluded in the early Cenozoic, apart from a small remnant sea, the Mediterranean (Rögl, 1999). At 120 Myr ago, $>$100 Ma old Tethys lithosphere subducts along the Sunda-Java Trench, while back-

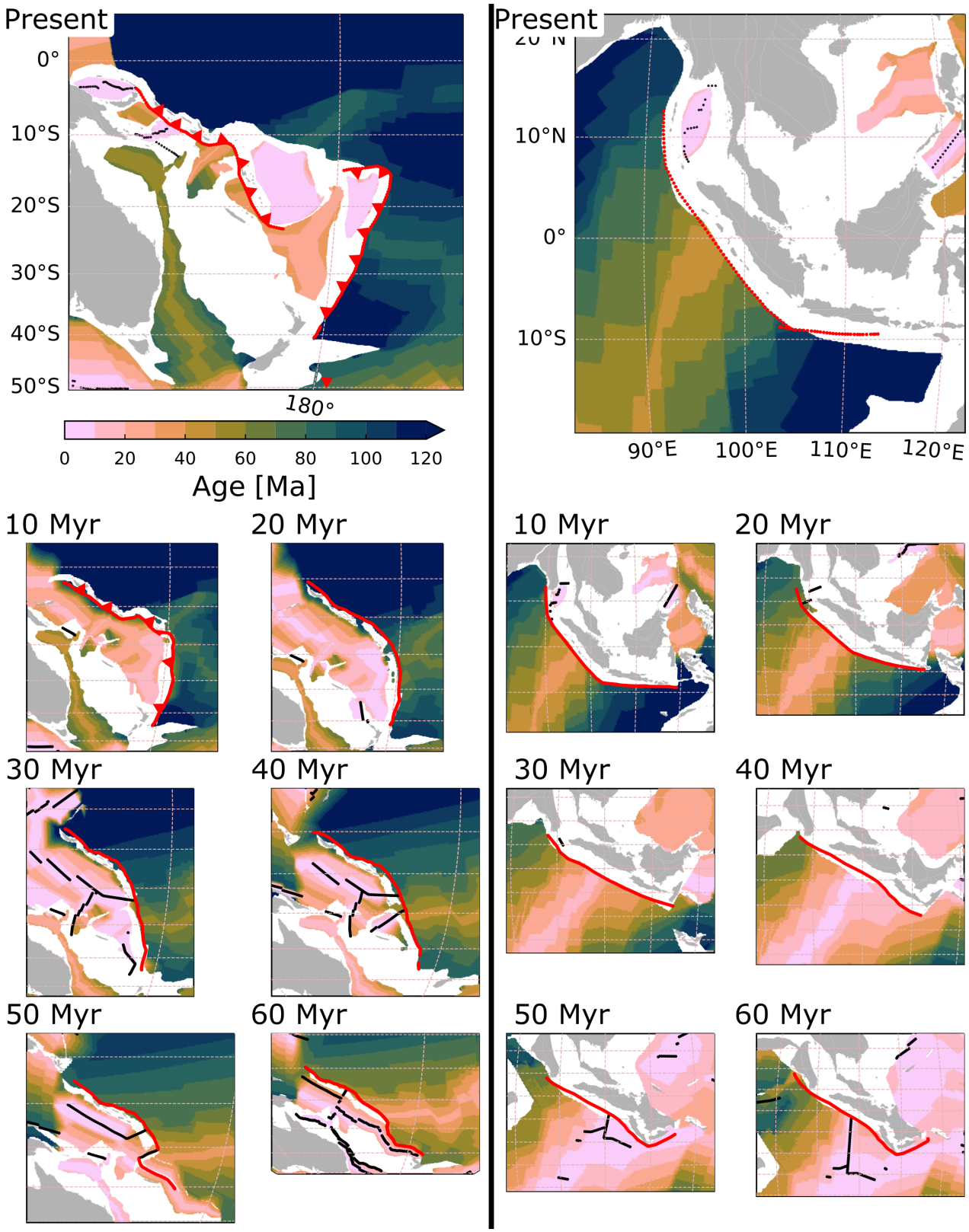


Figure 2.12: Evolution of South Pacific (including Tonga-Kermadec, New Hebrides and New Britain trenches) and Sunda-Java trenches during the Cenozoic, with age grid and reconstructed landmass, based on Müller et al. (2019). Directional triangles are shown where trench segments have different subduction polarity.

arc basins and additional convergence zones form north of the main trench along the southern Asian margin. Spreading ridges separated the shrinking Tethyan seafloor from the growing Indian and Australian plates south of it. By 50 Myr, the last part of the Tethys was consumed and the Wharton Ridge, which accommodated divergence between the Indian Plate and the Australian Plate reaches the Sunda-Java part of the trench.

At ∼45 Myr, after the India-Asia collision, the spreading along the India-Australia Ridge ceased and the India and Australia Plate started moving as an essentially unified plate (Hall, 2002). The intersection of the extinct Wharton Ridge and the Sunda-Java Trench marks the point of youngest ages along the trench, with older ages west and east of the ridge. The ridge-trench intersection point migrates northward throughout the Cenozoic but has remained far from both ends of the trench. During the late Cenozoic from 40–30 Myr ago, South East Asia deformation in response to India-Asia collision (Hall, 2002) and the arrival of the continental Australian Plate at the trench resulted in a period of trench advance at the northern Sumatra section and trench stagnation at the Java section at 30–0 Myr.

2.6 Conclusions

We presented here a compilation of global subduction zone trench parameters based on the GPlates models of Müller et al. (2016b) and Müller et al. (2019) for the past 120 Myr. We detailed how the parameters were extracted for the compilation from the underlying plate reconstruction model, discussed the associated uncertainties and presented some initial analyses. We showed how this compilation compares with the most recent compilation for the Cenozoic by Sdrolias and Müller (2006), the underlying plate reconstruction model by Müller et al. (2008b) and an analysis of age and velocity trends during the Cenozoic by Goes et al. (2011). Finally we presented a summary of how global and regional tectonic events affected trench position and the dis-

tribution of subducting-plate ages along the main trenches in the Pacific and Indian Oceans.

The compilation of subduction parameters presented here can aid the study of subduction zone dynamics and surface expressions as well as other associated fields. In using the parameter compilation, it is important to bear in mind the intrinsic uncertainties. The largest uncertainties are probably associated with the evolution of the location and shape of the trenches and whether they functioned as single or segmented systems. Trends in plate velocities and age of the subducting lithosphere are more certain as they are the outcome of the global plate motion model that over the past 120 Myr is quite well constrained by isochrons and additional geologic data (including palaeontological evidence, sediment accumulation record and gravity and magnetic anomalies; Müller et al., 2019; Vérard, 2019).

The new compilations confirm a number of previously proposed characteristics of natural subduction. Given that the present compilations span double the time of the previous compilation by Sdrolias and Müller (2006), and therefore include more trench and plate reorganisations, these characteristics are more likely to apply to the past few 100 Myr of subduction (at Earth's current thermal regime), and not only to the Cenozoic. In 74% of all sampled points, subduction occurs in a direction close to normal to the trench (within 45° to trench normal). For the set of points with subducting-plate motions within 60° to the trench normal, 76-85% of the sampled points retreat, similar to what was found in an earlier evaluation by Williams et al. (2015). These two signatures are consistent with an important role of local slab pull in the dynamics. Trench motions contribute on average only about 12-19% to plate convergence, with a higher contribution of trench retreat for the subduction in the main trenches, as expected if local slab pull is a more dominant force at larger subduction zones. The relatively small trench motions as well as dominance of trench retreat require that plate resistance to bending is a relatively small force compared to the total driving forces (Ribe, 2010). Yet, we find (consistent with analysis by Vérard, 2019) that there is, at most, a

weak correlation between subduction velocity and age, and only at some of the main trenches during the Cenozoic. This shows that local age at the trench is a poor indicator of the magnitude of slab pull, which instead must be the integrated result of slab buoyancy which varies both laterally and through time.

Our overview of the evolution of the main subduction zones in the M19 compilation highlights that they have often been significantly affected by large scale events, such as the global Eocene plate reorganisation event. This indicates that other forces in the global plate-mantle system, such as those exerted by nearby slabs or large-scale mantle flow or forces constraining the upper plate, appear to play a significant role in shaping subduction evolution, in particular at smaller trenches. The subduction parameter analysis thus underlines the importance of combining insights of subduction dynamics derived from models of a single subducting plate, together with models of 3D plates containing for example buoyant features, as well as models that focus on forces exerted by nearby plates, and models of a global Earth systems of plates and mantle flow.

2.7 Files and access

The Python scripts for generating the compilation and the associated plots, as well as the complete set of extracted parameters in `.csv` file format, can be found at: `https://github.com/lsuchoy/TrSubParametersCompilation`. The `pygplates` and `ptt` Python modules are required for the different functions of the script. The `pygplates` module is an associated python module for GPlates which can be found, together with the GPlates software, at `https://www.gplates.org/download`. The `ptt` (plate tectonics tools) module is a custom-made module for plate tectonics calculations of GPlates plate reconstruction models that was created and maintained by John Cannon and can be found at `https://github.com/EarthByte/PlateTectonicTools`. A copy of the `ptt` module version used for the script can be found with the script files.

The GPlates plate reconstruction model of Müller et al. (2016b) and Müller et al. (2019) can be found in `https://www.earthbyte.org`.

Chapter 3

Effects of basal drag on subduction dynamics from 2D numerical models

3.1 Summary

Subducting slabs are an important driver of plate motions, yet the relative importance of different forces in governing subduction motions and styles remains incompletely understood. Basal drag has been proposed to be a minor contributor to subduction forcing because of the lack of correlation between plate size and velocity in observed and reconstructed plate motions. Furthermore, in single subduction system models, low basal drag leads to subduction behaviour most consistent with the observation that trench migration velocities are generally low compared to convergence velocities. By contrast, analytical calculations and global mantle flow models indicate basal drag can be substantial. In this study, we revisit this problem by examining the drag at the base of the lithosphere, for a single subduction system, in 2D models with a free trench and composite non-linear rheology. We compare the behaviour of short and long plates for a range of asthenospheric and lithospheric rheologies. We reproduce results from previous modelling studies, including low ratios of trench over plate mo-

tions. However, we also find that any combination of asthenosphere and lithosphere viscosity that produces Earth-like subduction behaviour leads to a correlation of velocities with plate size, due to the role of basal drag. By examining Cenozoic plate motion reconstructions, we find that slab age and plate size are positively correlated: higher slab pull for older plates tends to be offset by higher basal drag below these larger plates. This, in part, explains the lack of plate velocity-size correlation in observations, despite the important role of basal drag in the subduction force-balance.

3.2 Introduction

It is widely agreed that the negative buoyancy of subducting slabs provides the main driving force for subduction, as well as for plate motions in general (e.g. Forsyth and Uyeda, 1975; Becker and O'Connell, 2001; Conrad and Lithgow-Bertelloni, 2002; Coltice et al., 2019). This insight has led to first-order models where slabs are treated as Stokes sinkers through a viscous mantle, which successfully produce the main density structure of the mantle and the main patterns of plate motions, assuming that surface plate motions are driven by the resulting mantle flow (e.g. Lithgow-Bertelloni and Richards, 1998; Becker and O'Connell, 2001; Conrad and Lithgow-Bertelloni, 2002). Recent global or plate-scale studies show that in some cases additional forcing by mantle plumes and consequent mantle flow (leading to active drag) may also play a role (e.g. Becker and Faccenna, 2011; Coltice et al., 2019; Stotz et al., 2018). Nonetheless, such large-scale models cannot fully capture the regional force balance governing the dynamics of subduction at plate boundaries (i.e. the interplay between slab pull, plate bending, viscous forces between plates and mantle), in governing plate velocities and morphology. As a result, it is important to improve our understanding of the balance of forces in such a regional system to inform how these forces, or a parameterisation of them, would be best incorporated into larger-scale or global models (e.g. Conrad and Hager, 1999).

The main driving force in a regional subduction system is the pull of the sinking slab (Goes et al., 2011). Resistive forces include viscous drag on the slabs, frictional or viscous resistance at the contact between subducting and overriding plates, visco-plastic resistance of the subducting plates to bending into the trench and when they reach upper-lower mantle boundary (ULMB) at 660 km depth, and viscous drag on the base of the plate (e.g. Forsyth and Uyeda, 1975; Carlson et al., 1983; Conrad and Hager, 1999). For subducting plates, the latter force, basal drag, is assumed to be dominantly resistive, although we note that it can be a driving force (e.g. Becker and Faccenna, 2011; Stotz et al., 2018). A driving basal drag can occur where mantle flow, driven by the global system of sinking slabs and aided by rising plumes, provides additional forcing on a regional plate configuration (Coltice et al., 2019). We will not consider such external forces here. The regional subduction resistive forces counteract up to 90% of slab pull, with the largest contribution from viscous resistance between the subducting slabs and the surrounding mantle (e.g. Schellart, 2004a; Capitanio et al., 2007). It is debated what the relative importance of the resistive forces is, and how their contributions vary between different subduction zones, and how this might contribute to the variability in subduction zone behaviour (e.g. Conrad et al., 2004; Husson et al., 2012).

It has been noted that present-day plates with large subducting slabs attached do not display a correlation between plate size and plate velocity, as might be expected if basal drag played a significant role in the subduction force balance (e.g. Forsyth and Uyeda, 1975; Conrad and Hager, 1999, Fig. 3.1). Conrad and Hager (1999) suggested that high plate viscosity, which would lead to substantial loss of energy in bending of the subducting plate at the trench (i.e. high bending resistance relative to basal drag), might be responsible for this lack of correlation. Their estimate of effective plate viscosity (about two orders of magnitude higher than the asthenosphere, i.e. average effective lithospheric viscosity of about 10^{23} Pa·s for a mantle viscosity of 10^{21} Pa·s) has been confirmed by a range of subsequent studies (e.g. Zhong and Davies, 1999; Buffett, 2006). However, dynamic subduction models with a mobile trench have shown

that plates with such effective viscosities tend to adjust their dips and trench velocities to minimise energy lost in bending thus limiting the effect on plate velocities (e.g. Bellahsen et al., 2005; Capitanio et al., 2007; Ribe, 2010).

Other work, using regional dynamic subduction models, has shown that low basal drag, resulting from low asthenospheric viscosities, may be important for understanding trench motions as observed on Earth (Billen and Arredondo, 2018). Trench motions tend to be only a small fraction of plate convergence velocity (on average, throughout the Cenozoic, about 10%; Lallemand et al., 2005; Sdrolias and Müller, 2006; Goes et al., 2011). On the other hand, the type of free subduction models used to investigate the effects of plate bending can lead to trench motions that are up to 100% of convergence (Capitanio et al., 2007), although models featuring an overriding plate result in smaller relative trench velocities (Garel et al., 2014). Furthermore, although most trenches retreat, 20-35% of trench segments in the past 100 Myr advanced (Goes et al., 2011; Williams et al., 2015). Small variations in the balance between the forces affecting the upper and the subducting plates have been proposed to determine the direction of trench motion (Husson et al., 2012; Capitanio, 2013; Alsaif et al., 2020) and for such a mechanism to be effective, a low asthenospheric viscosity is likely required. Billen and Arredondo (2018) showed that a low-viscosity asthenosphere (with non-linear, strain-rate dependent rheology leading to average asthenospheric viscosities of 10^{19}-10^{20} Pa·s and minimum viscosities as low as 10^{18}-10^{19} Pa·s, relative to maximum lithospheric viscosities of 10^{24} Pa·s) facilitated small trench motions and periods of both trench advance and retreat.

Other 2-D models of convection that approximate plate behaviour by a mechanical top boundary condition and strongly temperature-dependent rheology, albeit with an immobile trench, document how the ratio of lithosphere to asthenosphere viscosity governs to what extent basal drag is a resistive force (Höink and Lenardic, 2008, 2010). In such models, a low enough ratio even leads to a driving (Poiseuille) basal drag. From these results, one would expect that if the trench was free to move, resistive basal drag

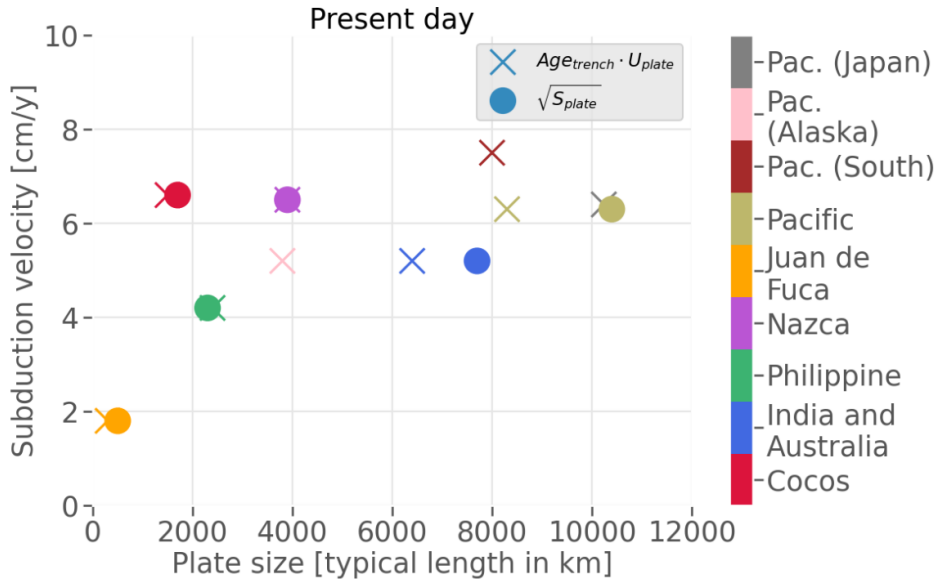


Figure 3.1: Present-day subducting plate velocities, measured at the trench in a lower mantle (plume) reference frame (O'Neill et al., 2005), as a function of plate size, in terms of a typical plate length. Typical plate length is a measure of plate size calculated as the age at the trench (Age_{trench}) multiplied by plate velocity (U_{plate}) (x markers) or as the square root of the plate surface area (S_{plate}, o markers). Velocities data from Sdrolias and Müller (2006) and Schellart et al. (2007) and plate size data from Conrad and Hager (1999).

would lead to trench retreat and driving basal drag would be associated with trench advance, i.e. viscosity ratio near this transition would lead to small trench motions, as found by Billen and Arredondo (2018). This indeed appears to be borne out by correlations found by Husson et al. (2012) between modelled mantle flow patterns and trench motions. Höink and Lenardic (2010) further showed that there is an influence of box size (which simulates plate size in their setup) on the viscosity ratio at which the transition from resisting to driving basal drag occurs. These studies indicate that a low ratio of average asthenosphere to average lithosphere viscosity (around 0.001), i.e. relatively low-magnitude basal drag, puts the system close to the transition from retreating to advancing trench motion and hence may be the most appropriate for understanding natural subduction dynamics.

On the other hand, analytical calculations and global-scale numerical models indicate that basal drag may not be such a negligible force. Basic analytical calculations

(section 6.3 in Turcotte and Schubert, 2002) yield estimates of basal drag that are on the order of 5-10% of slab pull. Observations of seismic anisotropy (Bokelmann and Silver, 2002) have been used to estimate that drag on the base of thick cratonic lithosphere is of a similar magnitude as ridge push, which is about 10% of slab pull and of a similar magnitude as the net slab pull (i.e. the difference between slab pull and viscous resistance to slab sinking). Several other studies have also shown that basal drag can be high in areas of thick continental roots (e.g. Conrad and Lithgow-Bertelloni, 2006; Coltice et al., 2019) and tractions from global mantle flow models yield high cumulative values of basal drag on large plates like the Pacific (Conrad and Lithgow-Bertelloni, 2006). The magnitude of basal drag by global mantle flow has been shown to be important for explaining plate motions (e.g. Becker and O'Connell, 2001; Conrad and Lithgow-Bertelloni, 2002; Becker and Faccenna, 2011; Coltice et al., 2019) and can only be effective if asthenospheric viscosities are not too low.

To better understand the role that basal drag plays in controlling subduction and trench motions, we revisit these issues here using 2D dynamic subduction models with a composite stress- and temperature-dependent rheology and mobile trench and ridge. We test the effects of increased lithosphere viscosity, decreased asthenosphere viscosity and hence variable lithospheric to asthenospheric viscosity ratio. Finally, we re-evaluate relation between subducting plate velocity and plate size on Earth, by examining both present-day plate configurations and reconstructions through the Cenozoic Era.

3.3 Modelling methods

We use a thermo-mechanical model of a single subduction system comprising a subducting and overriding plate in a 2D rectangular box (Fig. 3.2). The finite-element, control-volume code Fluidity (Davies et al., 2011; Kramer et al., 2012; Garel et al., 2014; Le Voci et al., 2014) is used to solve the mass, momentum and energy conservation

equations for Stokes flow under the Boussinesq approximation of incompressibility, for a viscous rheology. An irregular triangular adaptive mesh, with element sizes ranging from 0.4-200 km, yields high resolution in areas of dynamic significance (i.e. in areas of strong gradients of velocity, temperature, viscosity and material volume fraction) and lower resolution elsewhere (Fig. 3.2). Our models utilise the same numerical methodologies and physical properties as those of Garel et al. (2014). A summary of the model set up is given below, and further details, including all model parameters, are provided in Table 3.1.

3.3.1 Governing equations and rheology

We solve flow for incompressible Stokes fluid, under the Boussinesq approximation, assuming mass, momentum and energy conservation equations:

$$\partial_i u_i = 0 \tag{3.1}$$

$$\partial_i \sigma_{ij} + \Delta\rho g = 0 \tag{3.2}$$

$$\frac{\partial T}{\partial t} + U_i \partial_i T - \kappa \partial_i^2 T = 0 \tag{3.3}$$

where u is the velocity, σ is the stress tensor, g is gravity, T is temperature, κ is the thermal diffusivity and $\Delta\rho = -\alpha\rho_s\Delta T$ is the density difference due to temperature, with α the coefficient of thermal expansion, ρ_s the reference (surface) mantle density and ΔT the difference in temperature from the surface. i and j are axes notations.

Viscosity is therefore the ratio of deviatoric stress to strain rate:

$$\eta = \frac{\tau_{ij}}{2\dot{\varepsilon}_{ij}} = \frac{\sigma_{ij} + P\delta_{ij}}{2\dot{\varepsilon}_{ij}} \tag{3.4}$$

where τ is the deviatoric stress, $\dot{\varepsilon}$ is the strain rate, P is the dynamic pressure and δ_{ij} is the delta function. The effective viscosity is calculated in our models using:

$$\eta_{eff} = \left(\frac{1}{\eta_{diff}} + \frac{1}{\eta_{disl}} + \frac{1}{\eta_y} + \frac{1}{\eta_{Pie}} \right)^{-1} \tag{3.5}$$

where η_{diff}, η_{disl}, η_y and η_{Pie} are the viscosities calculated using diffusion creep, dislocation creep, yielding mechanism and simplified Pierels creep, respectively. The viscosities derived from diffusion, dislocation and Pierels creep are calculated using the generalised equation:

$$\eta_{(diff\backslash disl\backslash Pie)} = A^{\frac{-1}{n}} \exp \left(\frac{E + P_l V}{nRT_{ad}} \right)^{-1} \dot{\varepsilon}_{II}^{\frac{1-n}{n}} \tag{3.6}$$

$$P_l = \rho g D \tag{3.7}$$

where A is a prefactor, n is the stress exponent, E and V are the activation energy and volume, respectively, P_l is the lithostatic pressure, R the gas constant, $\dot{\varepsilon}_{II}$ is the second invariant of the strain rate tensor and D is the depth. T_{ad} is the temperature adjusted with an adiabatic gradient of 0.5 K/km in the upper mantle and 0.3 K/km in the lower mantle (Fowler, 2005). The yielding mechanism is calculated as:

$$\eta_y = \frac{\tau_y}{2\dot{\varepsilon}_{II}} = \frac{\min\left(\tau_s + f_c P_l, \tau_{y\ max}\right)}{2\dot{\varepsilon}_{II}} \tag{3.8}$$

where τ_y is the yield stress, τ_s is the surface yield stress, f_c is the friction coefficient and $\tau_{y\ max}$ is the maximum yield stress. The viscosity field is capped by both minimum and maximum values. The yielding viscosity is adjusted within the weak decoupling layer by applying a different friction coefficient:

$$\eta_{y\ weak} = \frac{\min\left(\tau_s + f_{c\ weak} P_l, \tau_{y\ max}\right)}{2\dot{\varepsilon}_{II}} \tag{3.9}$$

The initial temperature field in the lithosphere is calculated using the half-space cool-

ing equation from Turcotte and Schubert (2002):

$$T = T_s + \Delta T \cdot \text{erf}\left(\frac{D}{2\sqrt{\kappa t_{age}}}\right) \tag{3.10}$$

where T_s is the surface temperature and t_{age} is the age.

3.3.2 Model set up

The initial temperature field includes a cold lithosphere, with temperatures calculated using half-space cooling (Turcotte and Schubert, 2002) with a linear age gradient from ridge to trench on both the overriding and subducting plate sides, and a prescribed bent slab down to 220 km depth. We examined both this set up with a prescribed initial slab in the upper 220 km of the box with no initial strain, as well as a set up where we kinematically drive the slab to a comparable depth before continuing the calculations without kinematic constraints. No significant differences in the evolution with the two initial conditions were observed and, accordingly, we present only the results from the former approach.

We use a subducting plate with initial age of 65 Myr and overriding plate with initial age of 20 Myr, both with the same initial length (Fig. 3.2a). The young overriding plate exerts relatively low resistance to trench motion (Garel et al., 2014). In this study we do not vary initial subducting- and upper-plate ages to focus on varying lithospheric and asthenospheric strengths. The top surface is a free surface, which leads to a natural ridge push, and all other sides are free slip. Thermal boundary conditions are insulating on the left, a constant temperature at the top and bottom, and we apply mantle temperature to the right-hand side boundary to force a ridge at the edge of the overriding plate. The trench and the ridge on the subducting side are mobile.

We use a temperature, pressure and strain-rate dependent composite rheology, which naturally results in a strong lithosphere and weaker asthenosphere. Other factors

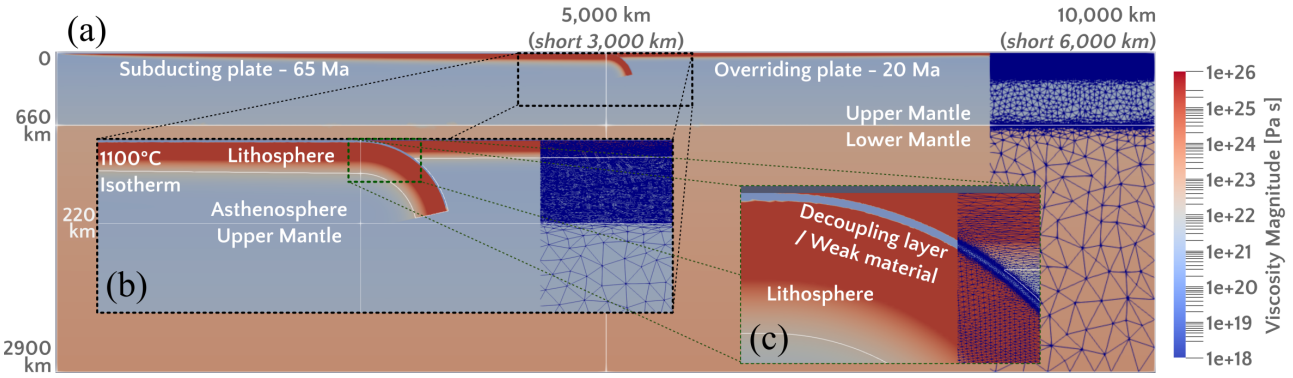


Figure 3.2: Model set up illustrated with the initial viscosity field of the reference long-plate model, with text indicating parameters for the reference short-plate model. Initial trench ages are indicated for the overriding and subducting plates, which have linear age variations between the ridges and the trench. Initial plate temperature is set according to half space cooling (Turcotte and Schubert, 2002). See text for boundary conditions and further information. (a) Full model view, (b) Zoom of initial slab, (c) Zoom of trench and decoupling layer. The irregular adaptive mesh is presented on the right side of each panel. White lines mark the initial location of the trench (vertical line), the ULMB at 660 km, the bottom of the asthenosphere (chosen at 220 km) and the bottom of the lithosphere (at the 1100°C isotherm).

may contribute to the contrast between lithosphere and asthenosphere viscosity, e.g. hydration, partial melt and anisotropy (e.g. Hirth and Kohlstedt, 1995; Korenaga and Karato, 2008; Becker and Kawakatsu, 2011). Here, we consider diffusion and dislocation creep mechanisms, combined with a low-pressure yield-stress mechanism to approximate brittle failure and an approximation of Peierls low-temperature plasticity at high pressure (e.g. Čižková et al., 2002; Garel et al., 2014). The parameterisation of diffusion and dislocation creep mechanisms are consistent with the experimental range derived from olivine deformation (e.g. Hirth and Kohlstedt, 2003) and predict realistic bulk upper mantle viscosities consistent with large-scale observations (Garel et al., 2020). The parameterisation of the Peierls creep is simplified (Garel et al., 2014), but is consistent with first order approximation of the dependency on temperature- and strain-rate (e.g. Kameyama et al., 1999). The yield stress mechanism is derived from Byerlee's law (Eq. 3.8) using rock-deformation experimental data (e.g. Burov, 2011). Such parameterisation of a low yield stress is common in geodynamical modelling (e.g. Mallard et al., 2016) to model surface plate deformation. We vary parameters, as discussed below, to evaluate different relative lithosphere and asthenosphere

viscosities. A 5 km thick weak, or decoupling, layer is included on top of the subducting plate and slab (Fig. 3.2c). The decoupling layer has a relatively low viscosity, which arises from modified rheological parameters (see Table 3.1 for further details) effective only at depths shallower than 200 km.

We examine the effect of basal drag by comparing long and short plates with initial lengths of 5000 and 3000 km from ridge to trench, respectively, adapting both plate size, through the initial thermal field, and box size. We examine the role of asthenospheric and lithospheric strength by adapting their rheology independently from the background rheology using a simple scaling factor. This method allows us to isolate the influence of changing lithosphere or asthenosphere strength without some of the additional feedbacks that arise in a fully dynamically controlled rheology. To do this, we use the 1100°C isotherm to delineate the lithosphere-asthenosphere boundary (LAB) and use passive markers to track the outlines of the subducting lithosphere and differentiate it from the overriding plate. We set the base of the asthenosphere at 220 km depth, which is below the bulk of the modelled minimum in viscosity, and consistent with the seismically imaged depth of the base of the asthenospheric low wave-speed zone (e.g. Dziewonski and Anderson, 1981; French et al., 2013). A 10 km linear transition is set across the boundaries of the lithosphere and the asthenosphere to prevent introducing sharp discontinuities in viscosity. Finally, we test the insights from these systematic models against a model where the relative lithosphere to asthenosphere viscosity contrast is modified self-consistently by changing the rheological parameters.

To model a system with weak asthenosphere we multiply its viscosity by 0.5, so that, with strain-rate feedbacks, it reaches minimum values of 10^{18}-10^{19} Pa·s. These values are consistent with current estimates of minimum asthenospheric viscosities based on postglacial rebound and laboratory experiments (e.g. Korenaga and Karato, 2008; Paulson and Richards, 2009; Billen and Arredondo, 2018). To simulate a strong lithosphere, we multiply its viscosity by factors of 2.0 or 10.0, limiting the strongest litho-

Quantity	Symbol	Units	Value		
			UM (reference)$^{(a)}$	UM (modified self-consistent)$^{(b)}$	LM
Gravity	g	m/s^2	9.8		
Thermal expansivity coef.	α	1/K	$3{\cdot}10^{-5}$		
Thermal diffusivity	κ	m^2/s	10^{-6}		
Reference density	ρ_s	kg/m	3300		
Surface temperature	T_s	K	273		
Mantle temperature	T_m	K	1573		
Gas constant	R	J/(K·mol)	8.3145		
Maximum viscosity (Strong Lith. model)	η_{max}	Pa·s	10^{26}		
Maximum viscosity (Ref. and other models)	η_{max}	Pa·s	10^{25}		
Minimum viscosity	η_{min}	Pa·s	10^{18}		
Diffusion Creep					
Activation energy	E	J/mol	$300{\cdot}10^3$	$335{\cdot}10^3$	$200{\cdot}10^3$
Activation volume	V	m^3/mol	$4{\cdot}10^{-6}$	$5{\cdot}10^{-6}$	$1.5{\cdot}10^{-6}$
Pre-factor	A	1/(Pa^n·s)	$3{\cdot}10^{-11}$	$1.5{\cdot}10^{-9}$	$6{\cdot}10^{-17}$
Stress exponent	n		1		
Dislocation Creep					
Activation energy	E	J/mol	$540{\cdot}10^3$	$472{\cdot}10^3$	$300{\cdot}10^3$
Activation volume	V	m^3/mol	$12{\cdot}10^{-6}$	$11{\cdot}10^{-6}$	$2{\cdot}10^{-6}$
Pre-factor	A	1/(Pa^n·s)	$5{\cdot}10^{-15}$	$1.34{\cdot}10^{-17}$	10^{-42}
Stress exponent	n		3.5	3.472	3.5
Peierls Creep					
Activation energy	E	J/mol	$540{\cdot}10^3$	$540{\cdot}10^3$	$300{\cdot}10^3$
Activation volume	V	m^3/mol	$10{\cdot}10^{-6}$	$10{\cdot}10^{-6}$	$2{\cdot}10^{-6}$
Pre-factor	A	1/(Pa^n·s)	10^{-150}	10^{-145}	10^{-300}
Stress exponent	n		20		
Yield Strength Law					
Surface yield strength	τ_s	Pa	$2{\cdot}10^6$		
Friction coefficient	f_c		0.2		
Friction coefficient (decoupling layer)	$f_{c\ weak}$		0.02	0.07	
Maximum yield strength	$\tau_{y\ max}$	Pa	10^{10}		

Table 3.1: Physical and rheological parameters of all models, following the model set-up used by Garel et al. (2014). (a) Activation parameters and stress exponent are consistent with experimental data on Olivine (e.g. Karato and Wu, 1993; Hirth and Kohlstedt, 1995; Ranalli, 1995; Hirth and Kohlstedt, 2003; Korenaga and Karato, 2008). Lower mantle pre-factor value for dislocation and Peierls creep are set at a low value to ensure diffusion creep-controlled viscosity in the lower mantle (in accordance with Eq. 3.5). (b) Upper mantle values for the modified self-consistent models were determined using optimisation method described in Maunder et al. (2016).

sphere to 10^{25} Pa·s (reference and most other cases) and 10^{26} Pa·s (strong lithosphere cases), which results in average lithospheric viscosity of 10^{24}-10^{25} Pa·s. These values are consistent with the highest estimates of effective lithospheric strength (Conrad and Hager, 1999; Billen and Hirth, 2007; Burov, 2011) where a maximum 10^{26} Pa·s is an upper bound of viscosities for subductable plates. With this range of lithospheric and asthenospheric viscosities, we can generate continuous Earth-like oceanic style subduction while avoiding immediate slab detachments which result from to lithospheric weakening due to high strain rates, or the stalling of subduction due to unattainable forces required for the bending of very strong lithosphere.

Before implementing the design of the models in this study, we ran a set of benchmark tests, including the 2D mantle convection models with a cold thermal boundary at the top and a hot thermal boundary at the bottom from Blankenbach et al. (1989). We also ran other models, not further used below, where we tested how different aspects of our model design affect subduction dynamics. We examined the effect of strength of the decoupling layer by modifying the friction coefficient ($f_{c\ weak}$; Table 3.1) between 0.01 and 0.1. The trends identified in this set agree with the findings in other studies (e.g. Čížková and Bina, 2013). We also examined subduction dynamics in settings where the asthenosphere flows towards the trench faster than the plate, effectively creating basal drag in the trenchward direction. This was accomplished by adding a buoyant hot layer (triggering a mantle plume) under the ridge of the subducting plate. These experiments resulted in a very fast subducting plate motions and significant trench advance. Lastly, we tested a set of models with different boundary conditions where the mid-ocean ridge was fixed to the edge of the box for either the subducting plate or overriding plate side. In these models, trench motion was limited in models with fixed overriding plate ridge, or much more extensive in models with fixed subducting plate ridge.

3.4 Results

3.4.1 Reference model

The long- and short-plate reference models progress in stages, with their temporal evolution shown in Fig. 3.3. The initial stage is characterised by slab sinking through the upper mantle at relatively high subduction velocities. Asthenospheric viscosity and mantle viscosities around the slab are lowered due to high strain rates. This stage ends when the slab reaches the ULMB at 660 km depth. At this point, velocities and strain rates drop and viscosities rise.

The second stage exhibits periodic oscillations in velocity between intermediate and low values (Fig. 3.5a). The oscillations are caused by episodes of flattening and steepening of the slab on the ULMB and may have a surface expression of oscillating trench motion (e.g. Clark et al., 2008; Lee and King, 2011). During this stage, the slab buckles, and the resulting folds are preserved during the descent of the slab into the lower mantle. The amplitude of the buckling decreases with time, such that if the models are run long enough (time is dependent on rheology), the subducting plates evolve to a final stage of more or less steady subduction. This is achieved in the long-plate reference model. The shorter plate has higher subduction velocities than the long plate (Fig. 3.5a), whilst the longer plate exhibits enhanced trench retreat compared to the short-plate case (Fig. 3.5b). These results indicate a significant influence of basal drag. Higher basal drag resistance leads to the slower subduction velocity of the long plate. In an additional feedback, less strain-rate weakening occurs in the asthenosphere under the long plate, as the asthenosphere moves with a similar velocity to the overlaying lithosphere in each model. This results in higher asthenospheric viscosity and resistance and makes subduction by trench retreat energetically preferable over subduction by plate advance over the asthenosphere. Trench advance does not occur at any stage in our reference models.

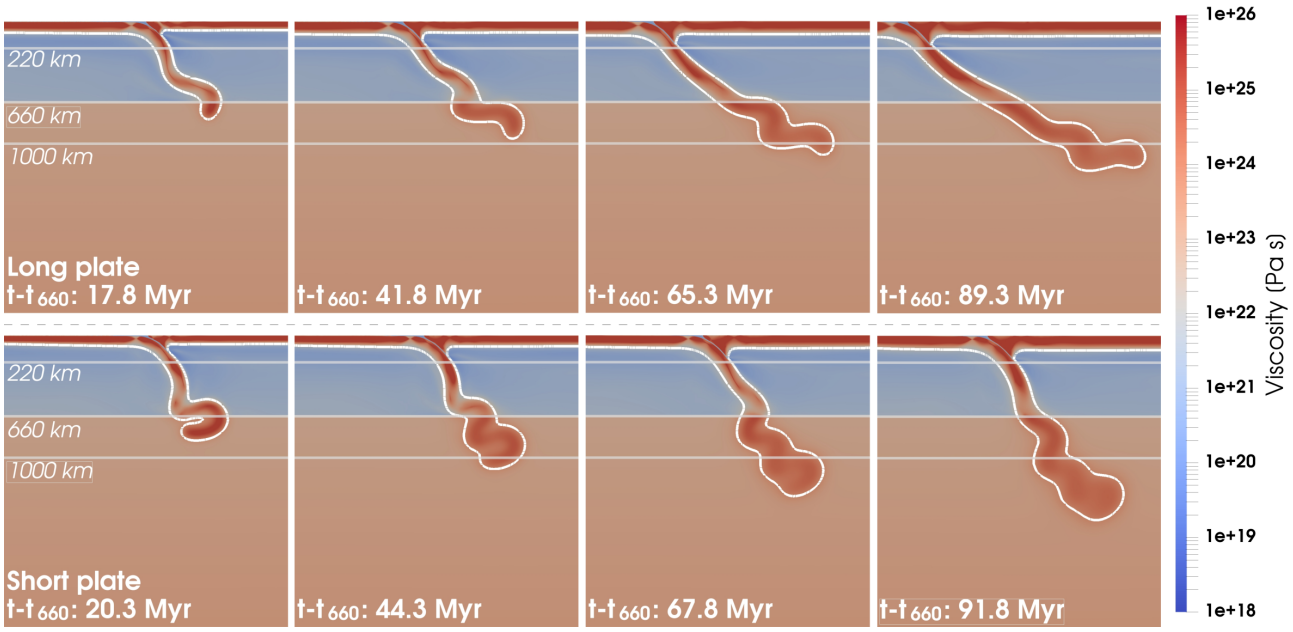


Figure 3.3: Viscosity field evolution at various times for the reference long-plate model (top row) and reference short-plate model (bottom row). White contour marks the 1100°C isotherm as the outline of the lithosphere. The vertical and horizontal spatial scales are identical and only part of the full model domain is shown. Note each model presents a distinct evolution of the slab and trench, which is the result of a difference in basal drag.

To evaluate the relative importance of basal drag in the overall force balance, we estimate basal drag below the subducting plate for each time step in the models, and compare it to the main driving force, slab pull. We do this using the following approximate equations from Section 6.3 in Turcotte and Schubert (2002), yielding forces per unit length out of the model plane:

$$F_{BD} = \frac{2 \cdot \eta_{Ast} \cdot \Delta U}{h_{Ast}} \cdot \left(2 + 3 \cdot \frac{h_{Lit}}{h_{Ast}}\right) \cdot L_{plate} \tag{3.11}$$

$$F_{SP} = \Delta\rho \cdot g \cdot S_{slab} \tag{3.12}$$

where F_{BD} and F_{SP} are the basal drag and slab pull forces respectively, η_{Ast} is the viscosity of the asthenosphere, ΔU velocity difference between the lithosphere and the asthenosphere, h_{Ast} and h_{Lit} the thickness of the asthenosphere and the lithosphere, respectively, L_{plate} is the length of the unsubducted part of the plate, $\Delta\rho$ is the density

difference between the slab and mantle, with a typical value of 40-50 kg/m^3, g is the gravitational acceleration and S_{slab} is the cross-sectional area of the slab. The parameters for basal drag, η_{Ast}, ΔU, h_{Ast} and h_{Lit}, are measured at a representative vertical profile through the subducting plate (Figure 3.4): provided that the profile is taken away from the trench and ridge, there is negligible sensitivity to the profile location. The 1100°C isotherm is used as the LAB in determining h_{Ast} and h_{Lit} and to outline the edge of the slab, for S_{slab}, (see Fig. 3.2). Plate velocity is measured at 20 km and asthenosphere velocity and viscosity at 160 km depth. For the calculation of S_{slab}, the length of the slab is measured as the length of a straight line connecting the trench and the deepest point of the slab, or the coldest point of the slab at the ULMB, and the width of the slab is measured along a horizontal cross section at 220 km depth. These approximate expressions for F_{BD} and F_{SP} are sufficient to understand variations in subduction behaviour between models and through time. Note that the expression for F_{SP} assumes stresses are effectively transmitted from the slab to the plate, which is appropriate because the adaptive grids of our models ensure we always resolve the strong slab core, even when it is quite thin (Garel et al., 2014). Both slab pull and basal drag evolve in our dynamic models (Fig. 3.5d-e). The cyclical nature of the buckling phases is associated with the evolution of the slab pull and basal drag forces. As the slab slows and flattens on top of the ULMB as a result of the increased resistance to sinking at this depth, its dip decreases, and slab pull increases. The higher pull increases the velocity and consequently the basal drag. The increased drag subsequently contributes to the slowing down the plate leading to steepening of the slab, and a reduction of slab pull. The following decrease in subduction velocity leads to lowering of drag. This reduction then allows for increase in slab pull and a new flattening episode.

For the reference models, we find that basal drag averages around 10% of slab pull, ranging from just below 30% in the fast, early stage of subduction to 3-5% in the final stage (Fig. 3.5f). This is similar to the estimated magnitude of ridge push relative to slab pull (e.g. Turcotte and Schubert, 2002). Furthermore, the basal drag ratio (of slab pull) for the short plate is systematically several % lower than the basal drag ratio for

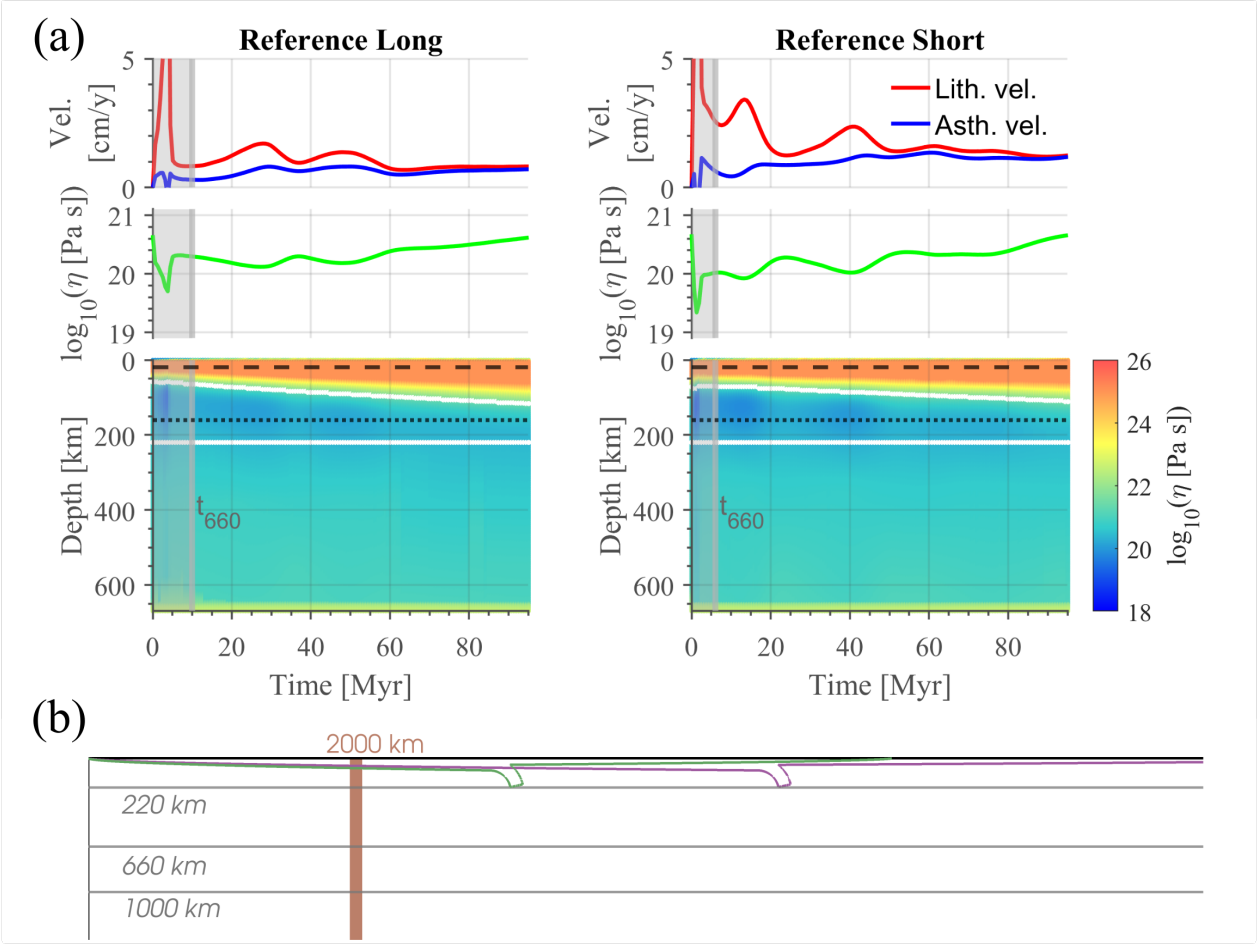


Figure 3.4: (a) Temporal evolution of parameters used for the calculation of basal drag for the long- (left panels) and short- (right panels) plate reference model. Top panel shows the velocities of the lithosphere (red line) and asthenosphere (blue line) (measured along the dashed and dotted lines in the bottom panel, respectively). Middle panel shows the magnitude of the viscosity of the asthenosphere (green line, measured along the dotted line in the bottom panel). Bottom panel shows a vertical profile (0-660 km depth) through the magnitude of the effective viscosity field. White lines mark the base of the lithosphere (1100°C isotherm) and asthenosphere (constant depth of 220 km). Parameters for the lithosphere were measured at 20 km depth (black dashed line) and parameters for the asthenosphere at 160 km depth (black dotted line). Time before $t660$ is shaded and is not shown in Figs. 3.5 and 3.7-3.9. (b) Location of the vertical profile location along which the quantities in (a) are measured (brown line), marked on an outline of the lithosphere at the initial condition of the long- (magenta line) and the short- (green line) plate reference model. The vertical and horizontal spatial scales are identical and only part of the full model domain is shown. Grey lines mark 220 km, 660 km (ULMB) and 1000 km depths.

the long plate (Fig. 3.5e-f). Note that due to the nonlinear feedbacks in the models, there are about 10 Myr right after the plates reach the ULMB (time $t660$) where the short plate experiences a higher drag than the long plate (Fig. 3.5). These relatively

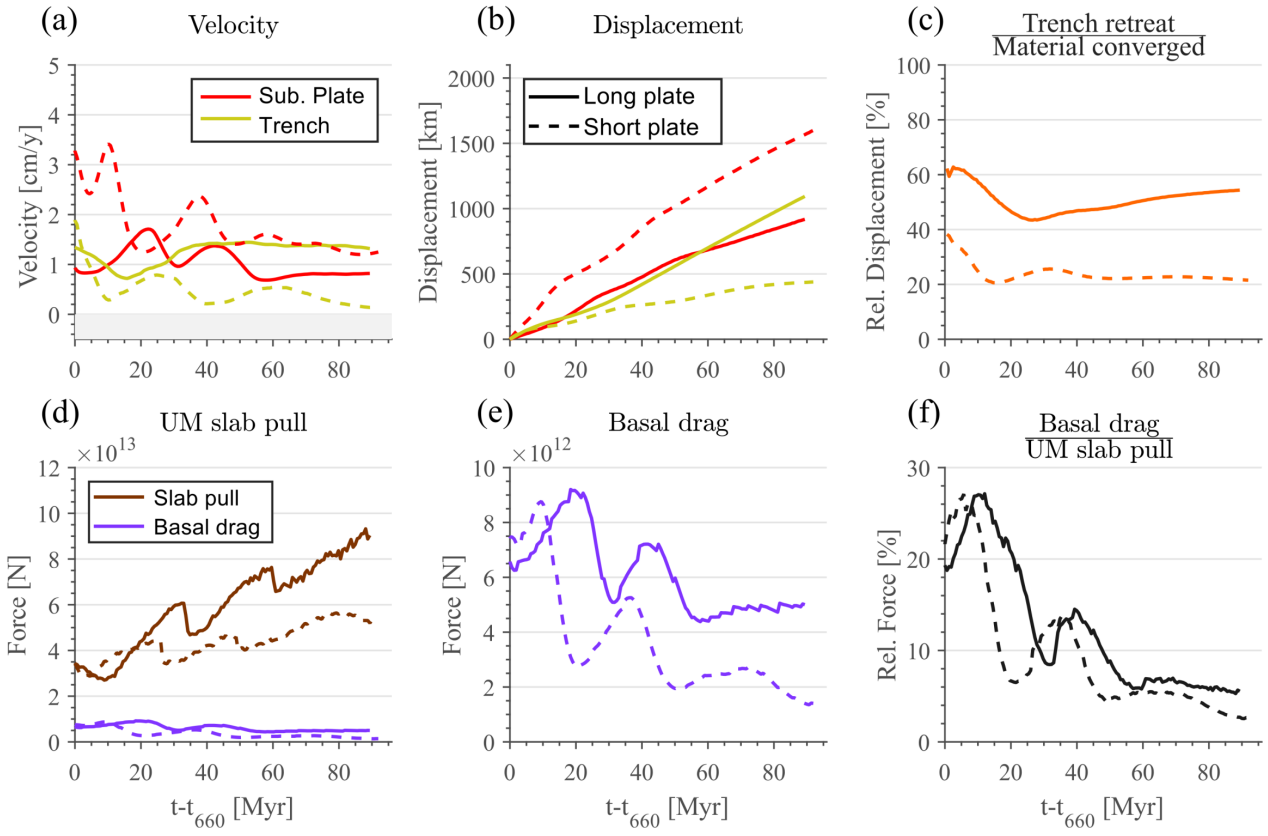


Figure 3.5: Temporal evolution of the long-plate reference model (full lines) and the short-plate reference model (dashed lines). $t - t_{660}$ indicates the time since the initial interaction of the slab with the ULMB. (a) Velocity of the subducting plate (positive towards the upper plate, red) and the trench (positive away from the upper plate, yellow), measured at 2000 km distance from the initial subducting plate ridge. (b) Displacement of the subducting plate (red) and the trench (yellow) relative to the initial condition. (c) Percent of plate convergence (calculated as the sum of trench retreat and plate displacement) achieved by trench retreat. (d) Upper mantle slab pull and basal drag below the subducting plate, calculated as described in the main text. (e) Basal drag force from (d). (f) Ratio of basal drag to upper mantle slab pull force. This shows that basal drag is of a similar magnitude as effective slab pull (i.e. the difference between gravitational pull and the viscous mantle resistance on the slab sides) which is 10% of the upper-mantle slab pull force.

high drag values for the short plate are a consequence of the high velocities that the short plate attains in response to the initially significantly lower drag (Fig. 3.4). The difference in basal drag ratio between the long- and short-plate models is apparently sufficient to change subduction velocity and influence the overall evolution of the morphology of the slab.

3.4.2 Weak asthenosphere

The most direct mechanism to reduce basal drag is to lower the asthenosphere viscosity. A lower basal drag allows for higher subduction velocity to develop, which in turn decreases the asthenospheric viscosity through the feedback effect of increased strain rate. The compound effect of applying the 0.5 reduction factor and consequent strain-rate weakening is an order of magnitude decrease in asthenospheric viscosity compared to the reference models.

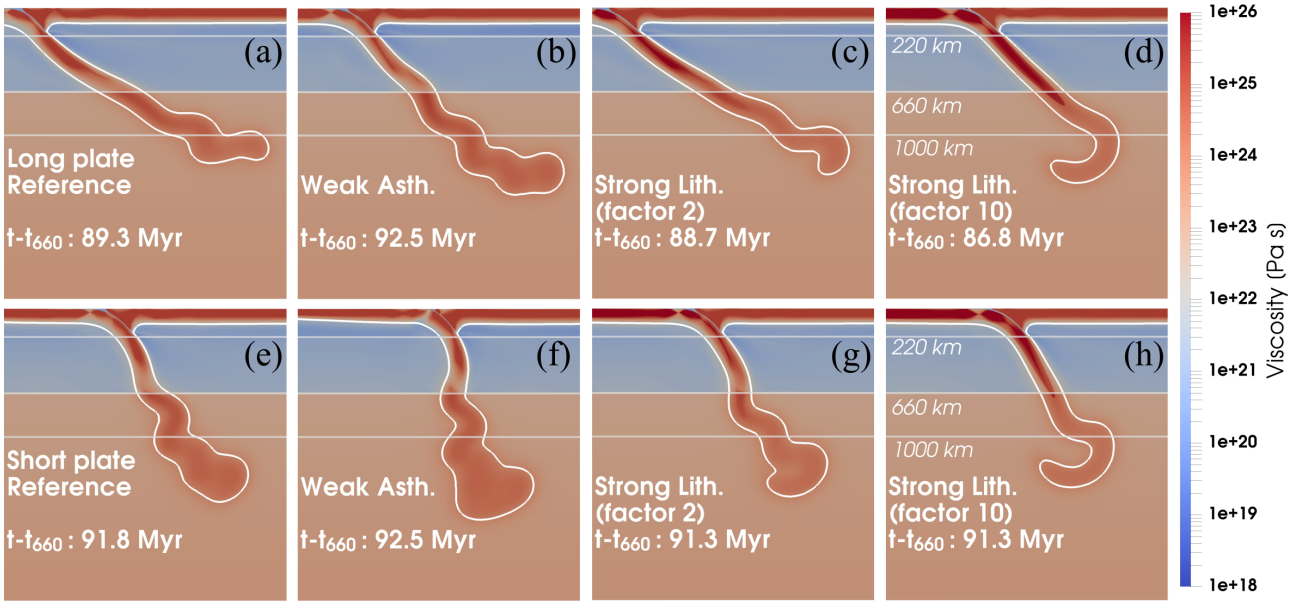


Figure 3.6: Comparison of final slab shapes for different models shown as a snapshot of the viscosity field. Long-plate (top row, (a)–(d)) and short-plate (bottom row, (e)–(h)) cases of Reference models ((a) and (e)), Weak Asthenosphere models ((b) and (f)), and Strong Lithosphere models with strength scaling factors of 2 ((c) and (g)) and 10 ((d) and (h)). White contour marks the 1100°C isotherm as the outline of the lithosphere. The vertical and horizontal spatial scales are identical, with grey lines to mark depths of 220 km, 660 km and 1000 km. For every type of model, the subducting slab in the short-plate model has more buckles and has undergone less trench retreat than in the long-plate model.

Assigning a weak asthenosphere results in an increase in subduction velocity and a reduction in trench retreat, as shown in Fig. 3.6 and Fig. 3.7. However, the reduced basal drag does not remove the plate-length dependence of the subduction evolution; the difference between the displacement of the subducting plate for the long and short plates remains similar even if the total displacement has slightly increased due to the

higher subduction velocities (Fig. 3.7a). The basal-drag ratios are lower than in the reference models and the difference between the long and short plates has increased, with the basal drag ratio for the short plate ranging from about 20% to less than 1% over the evolution of the models (Fig. 3.7d). Although overall ratios of basal drag to slab pull are lower than in the reference model, basal drag still plays a significant role in these low-viscosity asthenosphere cases, as is clear from the difference in the final shapes of the long- and short-plate slabs (Fig. 3.6b and f). The overall contribution of trench retreat to plate convergence is reduced for both the long- and the short-plate models compared with the reference models (Fig. 3.7c).

3.4.3 Strong lithosphere effect (factor 2 and 10)

A second mechanism to reduce the significance of basal drag as a resistive force is to increase the energy cost of bending through increased lithospheric viscosity (Conrad and Hager, 1999). This was implemented by applying the strengthening factor only in the subducting lithosphere and the slab. This process, unlike the reduction in asthenosphere viscosity, does not trigger any strong feedbacks between strain rate and effective viscosity. We therefore tested models where we increase lithospheric viscosity by a factor of 2 or 10 to compare the strengthening mechanism with the prescribed and the effective asthenosphere weakening. The resulting plate strength of the factor 10 experiments was at the upper bound of suggested realistic plate viscosity and at the upper bound of what is subductable in our models.

Increasing the strength of the lithosphere by a factor 2 reduces the amount of material subducted for the short-plate model, relative to the short-plate reference model, much more than it reduces the amount subducted for the long plate compared to the long-plate reference case (i.e. the behaviour of the long and the short plates becomes more similar). Trench retreat for both plates is similar to the reference models. The resulting basal drag ratio is slightly reduced relative to the reference models (by 1-

2%), as shown in Fig. 3.7e-h. Slab shapes at the end of the simulation are similar to the reference models with somewhat less slab deformation and buckling at the ULMB interface because less material has subducted (Fig. 3.6c).

For the factor 10 increase of subducting-lithosphere viscosity, the long- and short-plate models achieve similar amounts of subducted material. The amount of material subducted by the long plate deviates substantially less from the reference than the short plate, while trench retreat is reduced more in the long- than the short-plate model (Fig. 3.7i-j). This is as expected following the work of Conrad and Hager (1999); the resistance to plate bending becomes a more important control on subduction velocity than basal drag if the plate is sufficiently strong. However, we consider this model as an endmember of plate strength, as it is close to what, in our models, is the limit of subductable plates. The basal drag ratio for these strong-plate models is substantially lower than the reference models, with average values of around 5% only, and with a small systematic difference remaining between the long- and short-plate models (Fig. 3.7l). This amount of reduction in basal drag ratio by about 3-5% is sufficient to influence subduction dynamics, as can be observed at the final stages of the models (Fig. 3.6d) where the long- and short-plate models achieve different trench locations and slab shapes than the reference models.

In models where we combined a weaker asthenosphere with a stronger lithosphere (factor 2 and factor 10), the result was a joint effect of what we observed when we changed asthenosphere and lithospheric viscosity individually. The combined models subduct an increased amount of plate but there was less difference between the long- and short-plate models, and trench retreat was reduced. Thus, the models with strong lithosphere and weak asthenosphere exhibit the most Earth-like behaviour in terms of a low contribution of trench motion to convergence and limited sensitivity to plate length. However, this behaviour only appears for the upper bound of plate strength.

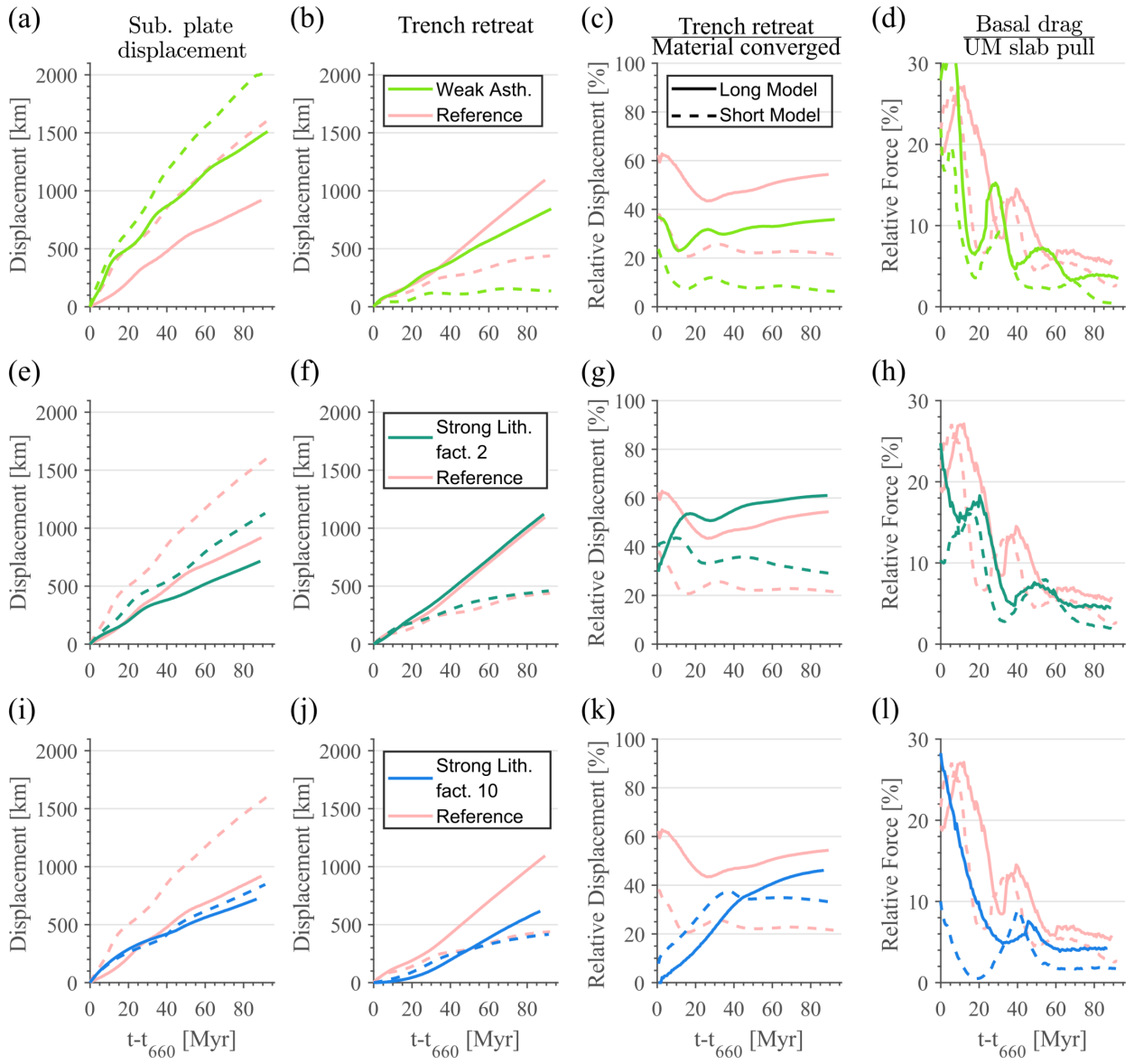


Figure 3.7: Temporal evolution of the long-plate (full lines) and short-plate (dashed lines) models. Rows of graphs are for different types of models, where (a)–(d) are Weak Asthenosphere models, (e)–(h) are Strong Lithosphere (factor 2) models and (i)–(l) are Strong Lithosphere (factor 10) models. The first column, (a), (e) and (i), shows the displacement of the subducting plate from the initial state, the second column, (b), (f), and (j), the amount of trench retreat, the third column, (c), (g) and (k), shows trench retreat significance as percentage of the total material converged, the fourth column, (d), (h) and (l), shows the ratio of basal drag to upper mantle slab pull force. All models are compared with the reference models, shown in light red.

3.4.4 Self-consistent rheology

We tested how a model in which the flow law parameters were modified to produce a self-consistent rheology that yields a stronger lithosphere and weaker asthenosphere

than the reference models. We aimed to achieve the same weakening of the asthenosphere and strengthening of the lithosphere as described in previous sections, but without artificially modifying the effective viscosity. To achieve this, we extracted profiles of temperature, pressure, strain rate and effective viscosity from the model with artificially modified viscosities at 100 Ma (long after t_{660}), 2000 km away from the initial position of the trench on the subducting plate side (as in Fig. 3.4). We used the temperature, pressure and strain-rate fields as inputs and applied the same calculation as done in the model to get the instantaneous effective viscosity for a self-consistent rheology. We then optimised the rheological parameters (activation energy, E, and volume, V, the pre-factor, A, and the stress exponent, n, for diffusion, dislocation and Peierls creep; see Table 3.1) to obtain an effective viscosity profile similar to the profiles with prescribed viscosity increase or decrease. We optimised the rheological parameters within ranges which agree with experimental data, using a similar approach to Maunder et al. (2016). We required that the modified composite rheology still satisfied the set of Earth-like conditions that Garel et al. (2014) imposed. These

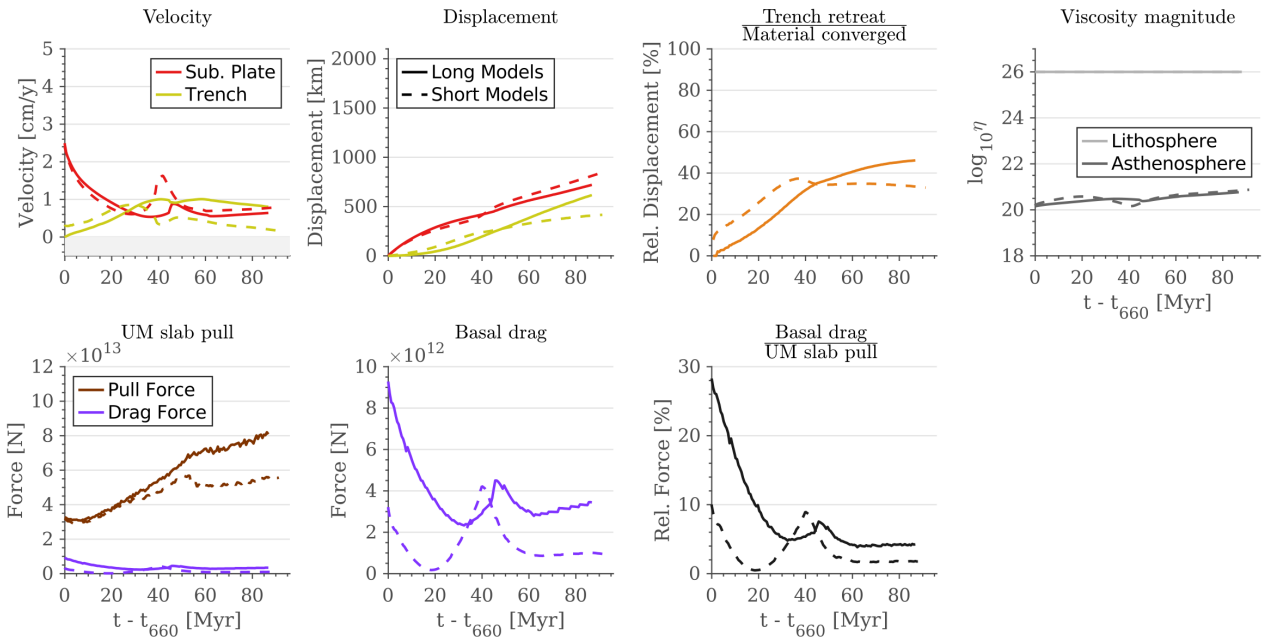


Figure 3.8: Temporal evolution of the long-plate case (full lines) and the short-plate case (dashed lines) for the self-consistent rheology model. Lines and symbols are the same as in Fig. 3.5.

conditions include: (i) that viscosities of the upper mantle and lower mantle will be in a range reasonable for postglacial rebound (Paulson and Richards, 2009), (ii) Peierls low-temperature plasticity is required to control deformation in the lower lithosphere and in the slab once subducted, to account for deep slab weakening, (iii) the transition from dislocation to diffusion creep as the dominant deformation mechanism is required to comply with the depth range inferred from seismic anisotropy (i.e. around 250 km depth in background mantle; Ranalli, 1995), (iv) the lithospheric thickness is similar as in the models with prescribed increase or decrease in viscosity. Table 3.1 lists our preferred set of modified parameters that satisfies all constraints. We then tested that under the new rheology, subduction remained viable. We found that, in addition to adjusting the overall rheological parameters, we needed to increase the strength of the weak decoupling layer to limit subduction velocities (and avoid slab detachment) early in the evolution of the model.

All these conditions together strongly narrow the set of possible rheological parameters that allow strengthening of the lithosphere while weakening the asthenosphere, and we were not able to strengthen the lithosphere as much as in the artificially scaled rheology models without stalling subduction. This is due to the nature of self-

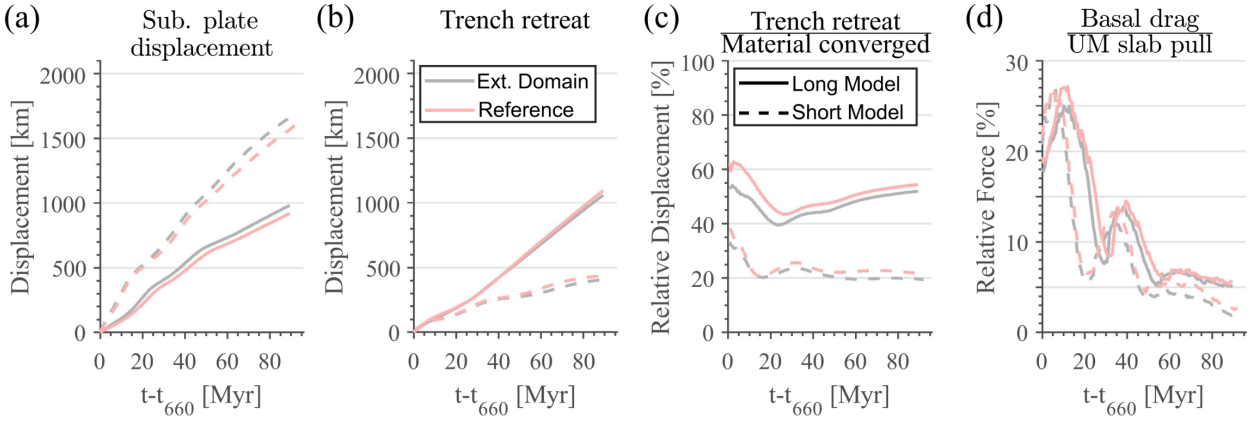


Figure 3.9: Temporal evolution of the long-plate (full lines) and short-plate (dashed lines) extended domain (grey) and reference (light red) models. (a) displacement of the subducting plate from the initial state. (b) amount of trench retreat. (c) trench retreat significance as percentage of the total material converged, (d) ratio of basal drag to upper mantle slab pull force.

consistent rheology, which couples the strength of the plate and its thickness. Any plates with 10 times higher strength were also thicker thus additionally increasing bending resistance and impeding subduction. Fig. 3.8 shows how the evolution of subducting plate morphology and trench retreat are similar to our models where we artificially lower the viscosity of the asthenosphere and increased the viscosity of the lithosphere.

3.4.5 Models with extended domain

In the models discussed above, we changed the size of the model domain together with plate size, so that the models always contained the only two plates with their bounding spreading ridges at the box edge. To test whether box size affects the results, we also ran a set of models where we use an extended and fixed box size but vary the plate size inside the box. We tested both the long- and the short-plate reference cases in a box of 15,000 km length. Compared to the reference models, the box was extended by an additional 5000/9000 km, for the long- and short-plate models respectively, to the left (trailing end) of the subducting plate. The initial condition in the extended section was set to mantle temperature throughout, i.e. the extended section contained no initial lithosphere. The upper plate was set to be the same length as the reference models (i.e. 5000 km and 3000 km for the long plate and short plate models respectively). The top thermal boundary condition allowed for lithosphere to develop in the extended section with time. Comparing with the reference models, these cases display the same trends of plate advance and trench motion, with differences in diagnostic parameters of less than 5% (Fig. 3.9). These differences are minor and indicate that box size does not bias the results.

3.5 Discussion

3.5.1 Trench motion

The trench always retreats in both the long- and short-plate reference models. Although strengthening the lithosphere and weakening the asthenosphere affect trench behaviour, only the short-plate model with the weak asthenosphere displays periods of trench advance. In this model, due to the lowered basal drag, subduction is able to occur through more plate advance, whilst limited periods of trench advance occur during the buckling interaction between the strong slab and lower mantle. These periods occur when, as a result of increased subduction velocity, a colder and stronger slab segment interacts with the ULMB. The interaction between the steep strong slab and the upper mantle, which has lowered viscosity due to strain-rate weakening, does not allow the slab to unbend. Instead, the cold slab attains a rolled-over shape that upon interaction with the higher viscosity lower mantle pushes the plate forward. These episodes end once subduction velocity reduces, as this gives the slab time to heat and weaken, and to regain the ability to unbend. This type of trench advance mechanism can be observed in other models (Bellahsen et al., 2005; Di Giuseppe et al., 2008; Ribe, 2010; Billen and Arredondo, 2018), in particular models where slab strength does not decrease with increasing temperature (i.e. models without a Peierls type plasticity). This type of rolled-over slab is rare on Earth, and has been imaged only below part of the Indian collision front (e.g. review by Goes et al., 2017); below other advancing trenches, slabs are steep but do not have the shape expected for trench advance resulting from the push of a strong slab at the ULMB. So, although the modelled trench advance episodes have magnitudes and rates in the range of observations, other mechanisms for trench advance, such as external forcing by background mantle flow and mantle plumes (as happens in the models from Höink and Lenardic, 2008) or an imbalance between ridge push and slab pull (e.g. Capitanio et al., 2009) may be more likely drivers of trench advance on Earth.

The ability of the upper plate to move plays a significant role in determining the amount of trench motion. A fixed upper plate, for example, can prevent trench motion completely, thus also modifying the shape of the slab (Capitanio et al., 2010; Quinquis et al., 2011; Chertova et al., 2012). Previous studies also show that resistance to motion of the upper plate (due to large thickness or viscosity leading to high basal drag) limits trench motion and may result in trench stagnation (compared to cases where a more mobile upper plate allows continuous trench migration; Sharples et al., 2014; Holt et al., 2015b). In our models, the upper plate is the same length as the subducting plate in both the long- and short-plate models. As a result, in the long-plate models, the energy spent on resisting plate motion by basal drag is increased on both sides of the trench. That is, the overriding plate in the long-plate models is less mobile and thus more strongly resists trench motion. Yet, trench retreat in the long-plate model is increased in both absolute terms and as a share of the convergence velocity (Fig. 3.5a-c). Thus the ability of basal drag to limit the movement on the subducting plate side appears to be more significant than than the increased resistance to the motion of the upper plate side and the expected reduction in trench motion.

3.5.2 Model limitations

The models approximate subduction in a number of ways: we study only a single initial age for subducting and overriding plates and neglect the effect of upper mantle phase transitions. Phase transitions exert a second-order effect on the difference between short- and long-plates, that would mainly enhance the slab buckling and flattening that happens in the models (for review, see e.g. Goes et al., 2017). The effect of plate age was studied by Garel et al. (2014) and Agrusta et al. (2017), who used a similar model set up as we use here but varied the age of subducting and upper plates without varying plate size. These models show that the initial ages of subducting and overriding plates affect the partitioning of plate convergence between trench retreat and subducting plate advance, with a lower contribution of trench retreat for initially

younger subducting plates and initially older overriding plates, resulting in a steeper more buckled slab. The difference in motion partitioning and resulting slab morphology between our short- and long-plate reference models is similar to the difference between subduction of an initially 100 Myr old and an initially 30-50 Myr old plate (Garel et al., 2014). This further emphasises the importance of drag below the plate in the total force balance of our models.

However, one should also bear in mind the limitations of the 2D setup of the models. For 3D plates, there may be more convergent boundary length (and hence slab pull) relative to plate surface area than in the 2D cases. This influences the ratio of slab pull to basal drag, which we investigate with some basic analytical calculations for end-member natural subduction systems in the following section. Furthermore, in a 3D system mantle flow may be at an angle to the plate advance direction, which will affect the component of velocity used to calculate the drag. A more Earth-like 3D system will also include mantle upwelling as well as downwelling flows. Upwelling flow, together with the global system of subduction-driven flow can result in driving drag below some plates (e.g. Colli et al., 2014; Stotz et al., 2018; Coltice et al., 2019), and cannot occur in our model setup. These complications, as well as local phenomena (e.g. the presence of mantle plumes, lateral variations in slab properties, or an imbalance between ridge push and slab pull; Capitanio et al., 2009; Capitanio, 2013) may result in more complex behaviour than presented in our models.

3.5.3 The role of basal drag on Earth

Our set of models clearly shows that basal drag is an important component of the force balance governing subduction dynamics, across the parameter space investigated. This is consistent with simple first-order analytical calculations of basal drag. We demonstrate this, by calculating basal drag and slab pull for the Pacific and Cocos plate as large and small plate end members. We use Eq. 3.11 and 3.12 but for plate

	U [cm/yr]	S_{plate} [10^6 km^2]	V_{slab}		
			L_{slab} [km]	W_{slab} [km]	L_{trench} [10^3 km]
Pacific	6.3	108	700	80	12
Cocos	6.6	3		40	2.5
	η_{Ast} [Pa·s]	$\Delta\rho$ [kg/m^3]	h_{Lit}, h_{Ast} [km]	F_{SP} [10^{19} N]	F_{BD} [10^{19} N]
Pacific	10^{19}	50	100, 150	33.6	11.1
Cocos				3.5	0.3

Table 3.2: Slab pull and basal drag force calculations, with associated parameters, for the Pacific and Cocos plates. U is subduction velocity, S_{plate} is subducting plate surface area, V_{slab} is the slab volume, L_{slab} is the length of the slab in the upper mantle, W_{slab} is the thickness of the slab, contributing to the difference in buoyancy due to slab age, L_{trench} is the length of subduction trench, η_{Ast} is the viscosity of the asthenosphere, $\Delta\rho$ is the density difference between the slab and surrounding mantle and h_{Lit} and h_{Ast} are the thickness of the lithosphere and asthenosphere. F_{SP} and F_{BD} are the slab pull and basal drag forces, calculated using Eq. 3.11 and 3.12.

area S_{plate} rather than length L_{plate} and slab volume $V_{slab} = S_{slab} \times L_{trench}$ rather than slab area $S_{slab} = L_{slab} \times W_{slab}$. We consider only pull from the upper mantle part of the slab. L_{slab} is the length of a slab extending through the whole upper mantle under an average dip of 70° (representative dip from the global compilation of Lallemand et al., 2005). We also assume the observed plate velocity U is a reasonable estimate of the difference in velocity between lithosphere and asthenosphere, ΔU. The properties used for the calculation and the forces calculated are summarised in Table 3.2. The relative basal drag, measured as the ratio of basal drag to slab pull, is around 30% for the Pacific plate, but only around 10% for the Cocos Plate. The analytical values of basal drag are somewhat larger than the values in the second stage of subduction in our models because the Pacific plate is about a factor of two larger than our subducting plate in the long-plate model, and our model velocities are on the low side compared to those observed around the Pacific. So, all evidence points to a role of basal drag that is significant, and the models would predict that unless other factors mask this trend, subduction velocities should vary with plate size.

We re-examine the observations of velocity and plate size throughout the Cenozoic Era, using GPlates (Müller et al., 2018) and the reconstruction of Müller et al. (2016b). This was done for all trenches previously studied by Sdrolias and Müller (2006) who considered the Andean subduction zone, Central-North Farallon subduction systems, subduction below Alaska and the Aleutians, Japan-Kuriles-Kamchatka subduction, Izu-Bonin-Marianas subduction, Tonga-Kermadec subduction and Sunda-Banda arc. To these we added the subduction of the Philippine Sea plate and the final stages of the subduction of the Izanagi and Kula plates. In processing this database, we considered all the Pacific subduction systems (i.e. Alaska-Aleutians, Japan-Kuriles-Kamchatka, Izu-Bonin-Marianas and Tonga-Kermadec) as a single Pacific system (see further details in chapter 2).

The relevant trenches were identified by extracting the global subducted segments of all plate polygons in GPlates (Müller et al., 2018). All trenches were sampled at 50 km intervals, and the coordinates were output and then plotted to select those belonging to the major subducting plate systems listed above. For each selected system, age and velocities along the trench were plotted every 10 Myr to remove any clearly erroneous data and edge points where these were clearly anomalous from the rest of the trench (e.g. because of an anomalous age or convergence direction). We evaluated the point subduction velocity, overriding plate velocity and convergence velocity and direction to select the segments to analyse. Maps showing the trench segments included in our analysis at each stage are shown in Fig. 3.10, where the sampling points along the trenches are also coloured according to absolute subduction velocity (in the moving hotspot reference frame of O'Neill et al., 2005) and age. These maps illustrate the evolving set of subduction systems through the Cenozoic as well as the variability of age and velocity along each trench. Aside from some edge points, we excluded from our analysis the part of the South American trench at 40 and 50 Myr which was south of the Antarctic ridge and the Cocos subduction system at 20 Myr, because according to the plate motion model there is limited convergence along most of the trench at this time. Finally, we considered for our analysis the mean value of the velocities and trench

age for each subducting system, and the standard variation of the mean value as the uncertainty. We average age and velocity of the active subduction systems along each trench at each time step and calculate plate area for the plate polygons that make up the subducting plate at the corresponding time. Resulting trends are similar for the full velocity of the subducting plate and the trench-normal component of it.

The resulting size-velocity trend is shown in Fig. 3.11a. The recent reconstruction shows a similar present-day trend (bold symbols) as the older reconstructions (Fig. 3.1), with a hint of a trend of increasing subduction velocity with increasing plate size for small plates, but a flat trend for plates with a larger than 3000^2 km^2. When all subducting plates through the Cenozoic are considered, no significant trend of velocity with age is present. However, it is also observed (Fig. 3.11b) that, on average, subduction zones with older plates at the trench tend to be bigger, like the present-day Pacific and Indo-Australia plate, than those subducting younger material at the trench, such as the present-day Cocos, Nazca and Juan de Fuca. Previous (thermo-)mechanical models show that the age of the subducting plate strongly affects subduction dynamics. Older plates, i.e. those with older age at the trench, are colder and therefore denser and stronger. Consequently, they exert more pull force and are harder to bend, resulting in higher subduction velocities and higher trench retreat rates (Bellahsen et al., 2005; Capitanio et al., 2007; Stegman et al., 2010b; Garel et al., 2014). A consequence of the observed correlation of average age at the trench and plate size is that plates with a stronger slab pull tend to also have larger surface area and hence a stronger resisting basal drag. This provides a mechanism that offsets the velocity enhancing effect of larger driving forces of old plates, and could explain the observation that velocities of subducting plates on Earth, today and throughout the Cenozoic, do not increase with age but tend to be mostly stable around 8-10 cm/yr (Fig. 3.11, Sdrolias and Müller, 2006; Goes et al., 2011).

Note that the relation between age and size is not a causal relationship, but a feature of the plate configuration that has dominated most of the Cenozoic. Early in the Ceno-

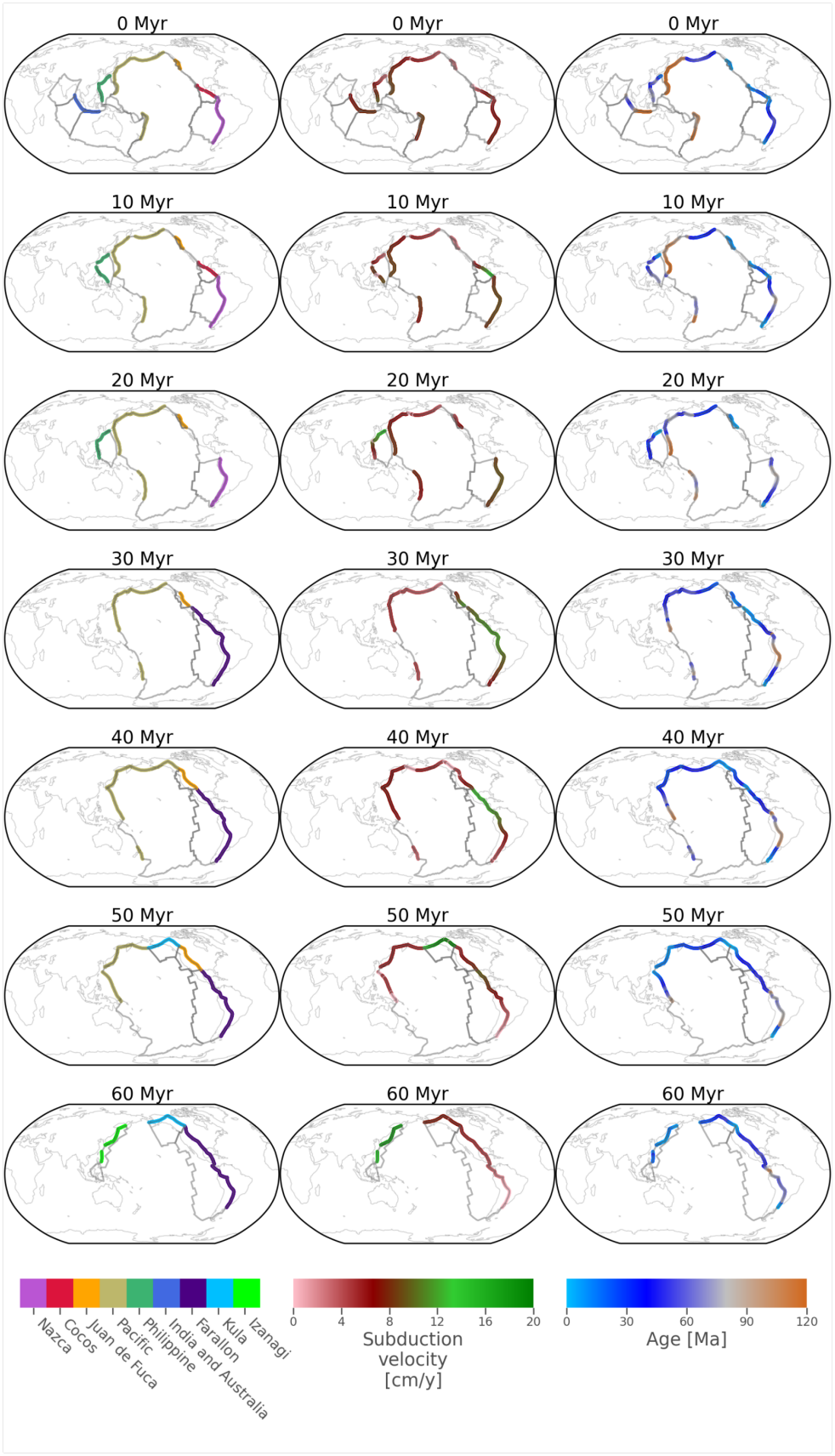


Figure 3.10: Evolution of velocities and ages along the trenches considered in the global analysis of Cenozoic subduction systems, in intervals of 10 Myr. 3 maps are shown for each time interval, displaying the trenches used for the analysis (left), absolute subducting plate velocity in hotspot reference frame (O'Neill et al., 2005, middle) and age at the trench (right). Grey lines represent other boundaries of the subducting plates. The background light grey shows present day global coastlines for reference. Data following Müller et al. (2016b) and processed using GPlates (Müller et al., 2018) and Cartopy (Met Office, 2015).

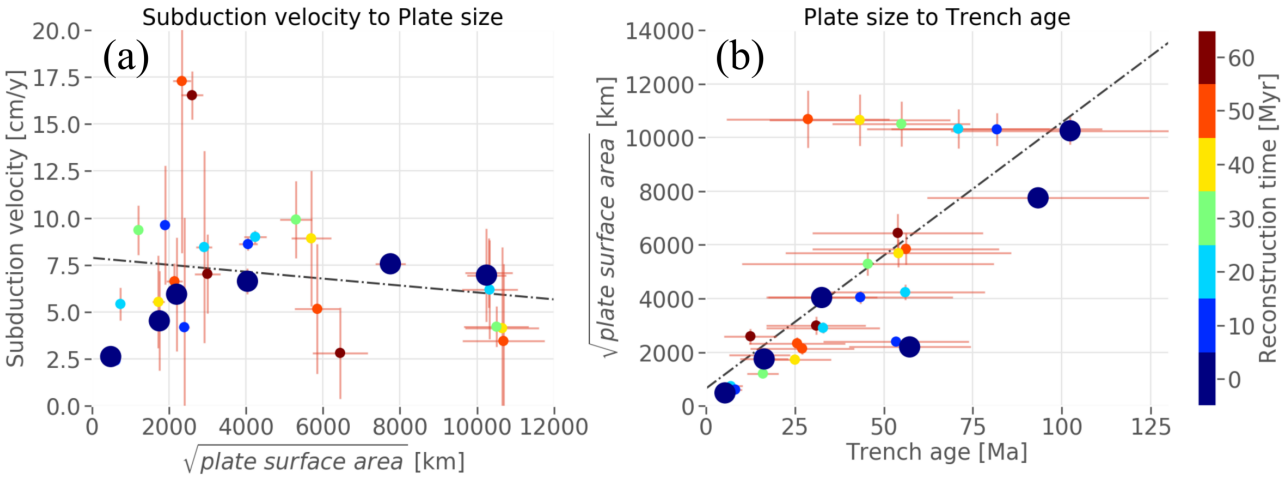


Figure 3.11: (a) Velocity of subducting plates from Müller et al. (2016b) in lower mantle (plume) reference frame (O'Neill et al., 2005) throughout the Cenozoic, as a function of characteristic plate size (measured as the square root of plate surface area). (b) Plate size as a function of age at the trench for subducting plates throughout the Cenozoic. Maps showing the subduction zones at each time are shown in Fig. 3.10. Blue bold circles represent data from present-day subducting plates. Linear regression fits (black lines) show that there is no resolvable trend of velocity with plate size (p-value 0.351, R^2 0.03) while there is a trend of size with age (p value < 0.05 and R^2 of 0.52).

zoic, there are several cases that deviate from the buffered velocity trend. At the start of the Cenozoic, much of the subduction surrounding the Pacific plate consumed relatively young lithosphere, even though the Pacific plate itself was already large in size (horizontally aligned points at the top of the area–age trend in Fig. 3.11b). Other early Cenozoic deviations include very high velocities of the last remnants of the Izanagi and Kula plates (points with area of about 2500^2 km^2 and velocities around 17 cm/yr in Fig. 3.11a) and low velocities of Farallon plate (area about 6000^2 km^2 in Fig. 3.11a).

Previous models documented that older plates tend to drive more trench retreat due to both their larger bending strength and their larger negative buoyancy (e.g. Capitanio et al., 2007; Stegman et al., 2010b; Garel et al., 2014). This has been suggested to help explain the difference between Cenozoic subduction styles along the western Pacific (subducting mainly older plate with significant trench retreat) and eastern Pacific (subducting younger plates with low trench retreat contributions) (Goes et al., 2017). Our results suggest that plate size may further enhance these differences, as the high basal drag exerted on the dominantly westward-subducting large Pacific plate would

favour more trench retreat than for the smaller eastward-subducting Cocos, Nazca and Juan de Fuca plates.

3.6 Conclusions

We presented a set of 2D models to examine the role of basal drag in subduction dynamics. Previous studies have reached contradictory conclusions, with some proposing that drag between the subducting plate and the underlying asthenosphere plays only a small role in dictating the subduction force balance (e.g Conrad and Hager, 1999; Billen and Arredondo, 2018; Wolf and Huismans, 2019), but others invoking a more significant role for basal drag in controlling subduction and plate motions on Earth (e.g. Conrad and Lithgow-Bertelloni, 2006). A low contribution of basal drag could explain the lack of a correlation between plate velocity and size (Conrad and Hager, 1999). Furthermore, the observation that trench migration velocities are mostly low compared to convergence velocities, can be either positive or negative in sign (Billen and Arredondo, 2018), and may be the result of a high ratio of lithosphere to asthenosphere viscosity drag (Conrad and Hager, 1999; Höink and Lenardic, 2008; Billen and Arredondo, 2018), is also suggestive of a low contribution from basal drag.

Our 2D numerical models comprise a single subduction system with a mobile trench and composite non-linear rheology. We consider long and short subducting plate models to evaluate the effect of plate length and the associated basal drag. The set-up of these regional subduction models is similar to those of previous studies, which have been used to elucidate how slab buoyancy, slab strength, slab interaction with the upper-lower mantle boundary or subduction-upper plate interaction influence subduction dynamics (e.g. Bellahsen et al., 2005; Capitanio et al., 2007, 2009; Stegman et al., 2010b; Čížková and Bina, 2013; Garel et al., 2014; Agrusta et al., 2017; Billen and Arredondo, 2018; Wolf and Huismans, 2019). We found that basal drag limits subduction velocities for our reference models and models with a lower asthenospheric vis-

cosity (in a range consistent with likely viscosities on Earth and still allowing for steady subduction, without rapid slab detachment, leading to lithosphere-asthenosphere viscosity ratios of a factor 10^3 to 10^4). Models with a low-viscosity asthenosphere do reduce the contribution of trench motion to plate convergence to more Earth-like values, as observed in previous studies (e.g. Capitanio et al., 2007; Billen and Arredondo, 2018). They also allow for periods of trench retreat and advance (Billen and Arredondo, 2018), although we note that trench advance with reclining/vertical slab geometries as observed in nature probably requires additional forcing (e.g. by upwellings or other forces within the global plate system).

Strengthening the lithosphere can significantly lower the dependency of velocity on plate length but requires strengthening by as much as a factor of 10 (to maximum viscosity of 10^{26} Pa·s), which is an upper bound: our models that incorporate lithospheric strengthening of this magnitude often preclude subduction. Although it has been shown that the relative strength of the lithosphere to asthenosphere is important in controlling the dynamics of subduction (Höink and Lenardic, 2008, 2010; Ribe, 2010), with non-linear rheologies, increasing lithosphere strength and decreasing asthenosphere strength have distinct effects.

Basal drag values in our models range from a few percent of slab pull (in the strongest lithosphere cases) to up to 10-30%. Similar values are estimated in analytical calculations of basal drag to pull ratio assuming a reasonable set of parameters for the Pacific and Cocos plate. This, together with results from global flow models where basal drag by whole mantle flow has been shown to be important to reproduce patterns of plate motion (Lithgow-Bertelloni and Richards, 1998; Becker and O'Connell, 2001; Conrad and Lithgow-Bertelloni, 2006), indicates that basal drag is a substantial contributor towards the subduction force balance, of the same order as effective slab pull (i.e. slab pull minus the viscous resistance to sinking) and ridge push.

Based upon an analysis of a Cenozoic plate motion reconstruction (Müller et al., 2016b), we suggest that the reason that most plates in the past 60 Myr moved at velocities

around 8-10 cm/yr is because the plate configuration during this era was such that plate size correlated with plate age at the trench, i.e., both driving and resisting forces increased together. Note however, that this correlation between size and age is not causal and may not have existed in other times of Earth history. As a result, during the Cenozoic, the increase in basal drag more or less balanced the increase in plate velocity induced by increased slab pull with increasing age. Such co-variations between plate velocity, age and size should be considered in regional models of subduction systems.

Chapter 4

3-D subduction regimes and choice of reference model

4.1 Summary

All models necessarily approximate different aspects of the complex properties of natural subduction. This chapter illustrates the importance of carefully choosing the properties of the model reference case to ensure that model response to variations in plate density, strength and width indeed correspond to those expected for subduction systems in an Earth-like regime. Published numerical and analogue models illustrate that subduction can be either in a 'sinking' regime (where most of the sinking potential energy is dissipated in overcoming the viscous resistance of the mantle) or a 'bending' regime (where the energy spent on bending the plate is an additional significant energy sink). We present here a set of three-dimensional mechanical models with Earth-like parameters and variations in viscosity, density and plate geometry. Although observations indicate most subduction zones on Earth are likely within the 'sinking' regime our models predominantly exhibit 'bending' behaviour. We show how our reference model produces opposite responses to changes in plate properties

to those that occur in models with plates in the 'sinking' regime. Our 3D models further show how the style of subduction is expected to vary along strike due to the effects of toroidal flow along the plate edges. Finally, although some previous studies identified plate stiffness as the main control on subduction style, our models indicate buoyancy is expected to be additionally important for slabs interacting with a higher-viscosity lower mantle. These results are further used to design a new reference model with rheologically layered plates (reducing strength without affecting density) which is in the 'sinking' regime. We use this model set up in our investigation into the effects of buoyant feature subduction in Chapter 5.

4.2 Introduction

The subduction of plates into the Earth is the main driver of plate tectonics. The pull force due to the negative buoyancy of the slabs and the transmission of stresses to the surface is the first order control of subduction and consequent plate motions (e.g. Forsyth and Uyeda, 1975; Becker and O'Connell, 2001; Conrad and Lithgow-Bertelloni, 2002; Goes et al., 2011). While the dynamics of subduction has been the focus of many studies (e.g. Forsyth and Uyeda, 1975; Conrad and Hager, 1999; Funiciello et al., 2003a; Schellart, 2004a; Lallemand et al., 2005; Stegman et al., 2006; Capitanio et al., 2007; Li and Ribe, 2012; Goes et al., 2017), fundamental aspects remain debated. Among these are how subduction dynamics are controlled by strength, density and dimensions of the plate (Bellahsen et al., 2005; Stegman et al., 2006; Di Giuseppe et al., 2008; Schellart, 2008; Fourel et al., 2014; Dasgupta et al., 2021), what the relations are between slab morphology and trench motion (Funiciello et al., 2003a; Faccenna et al., 2007; Funiciello et al., 2008) and what the role is of the viscous mantle that resists subduction (Conrad and Hager, 1999; Funiciello et al., 2006).

Many studies have investigated how subduction styles vary as a function of subduction parameters using models of a single subducting plate in an ambient mantle, i.e.

'free-subduction' (e.g. Funiciello et al., 2003a; Capitanio et al., 2007; Funiciello et al., 2008; Schellart, 2008; Capitanio et al., 2009; Ribe, 2010; Li and Ribe, 2012), while others focused on the system with an upper plate (e.g. Garel et al., 2014; Billen and Arredondo, 2018). Some of these studies predict that increased plate viscosity will lead to an increase in trench advance (e.g Funiciello et al., 2008; Billen and Arredondo, 2018) while others find higher plate viscosity increases trench retreat (e.g Capitanio et al., 2007; Garel et al., 2014; Stegman et al., 2010b). Similarly ambiguous are the results on the role of plate density, where increased trench retreat has been found to be encouraged by high plate density by some (e.g Capitanio et al., 2007; Garel et al., 2014; Stegman et al., 2010b) and by low plate density by others (in combination with high plate strength, e.g. Funiciello et al., 2008; Billen and Arredondo, 2018). A decrease in plate width has been associated with both stronger trench retreat (e.g Schellart et al., 2007) or weaker trench retreat (Stegman et al., 2006, 2010a) or a transition to trench advance (Bellahsen et al., 2005). The question remains which of these predictions is most representative of natural subduction systems on Earth.

Behaviour of free-subduction models can be divided to two regimes: 'bending' and 'sinking' (Ribe, 2010). In both regimes, subduction is driven by the potential energy of the slab, while the main resisting force differs. For the 'sinking' regime, the viscous displacement of the mantle is the dominant resisting force while in the 'bending' regime, the stiffness of the plate and the resulting resistance to bending is the main force hampering subduction (Ribe, 2010; Li and Ribe, 2012). 'Sinking' and 'bending' regimes are distinct in slab geometry, trench behaviour and style of interaction with the upper-lower mantle boundary (ULMB) at 660 km depth, and can be further divided into different modes (Bellahsen et al., 2005; Di Giuseppe et al., 2008; Funiciello et al., 2008; Schellart, 2008; Ribe, 2010; Stegman et al., 2010b; Li and Ribe, 2012, see further details in Fig. 4.1):

- The mode of very weak plates is vertical-folding (VF) where the slab undergoes extensive deformation and folds on itself at the ULMB. Due to poor stress trans-

mission to the surface, plates in vertical-folding mode have minor trench motion which frequently switches from retreat to advance.

- Stronger plates under the 'sinking' regime are in retreat mode in which the trench retreats continuously while the slab either lies flat on the ULMB or penetrates it in an angle significantly lower than 90°. In the weak-retreat (WR) mode, the deep dip angle of the slab (when it reaches the ULMB) is closer to 90° while slabs in strong-retreat (SR) mode have smaller deep dip angles.

- Strong plates in the 'bending' regime develop an initial backwards fold as the tip of the slab reaches the ULMB. Plates which consequently overturn completely evolve in advance (A) mode and will remain overturned as the trench advances. Plates which do not overturn are in folding (F) mode, and can be further divided into fold-and-retreat (FR) and fold-and-advance (FA) modes, depending on trench motion after the initial folding.

Various mechanisms have been proposed to control the transition between these different modes of subduction. The evolution of subduction into the different modes depends on the contact angle between the plate and the ULMB (Torii and Yoshioka, 2007; Schellart, 2008; Li and Ribe, 2012). Contact angles $<90°$ result in 'sinking' regime while angles larger than 90° lead to 'bending' regime (Ribe, 2010). Several studies propose that the main controls on this angle are plate thickness (relative to upper mantle depth) and plate bending strength, with an additional influence of the length of the dipping slab at model initiation (Schellart, 2004a, 2008; Ribe, 2010; Li and Ribe, 2012). These parameters together control the amount of bending during the descend of the slab through the upper mantle (i.e. does it overturn or not) and whether it can unbend before reaching the ULMB. The role of slab buoyancy may be limited, because of its dual affect. High buoyancy increases the force that bends the plate while at the same time increasing the sinking velocity allowing less time to achieve bending (Ribe, 2010). However, some studies found that a combination of slab strength and slab buoyancy is required to predict subduction modes and regimes (Stegman et al., 2010b; Capitanio

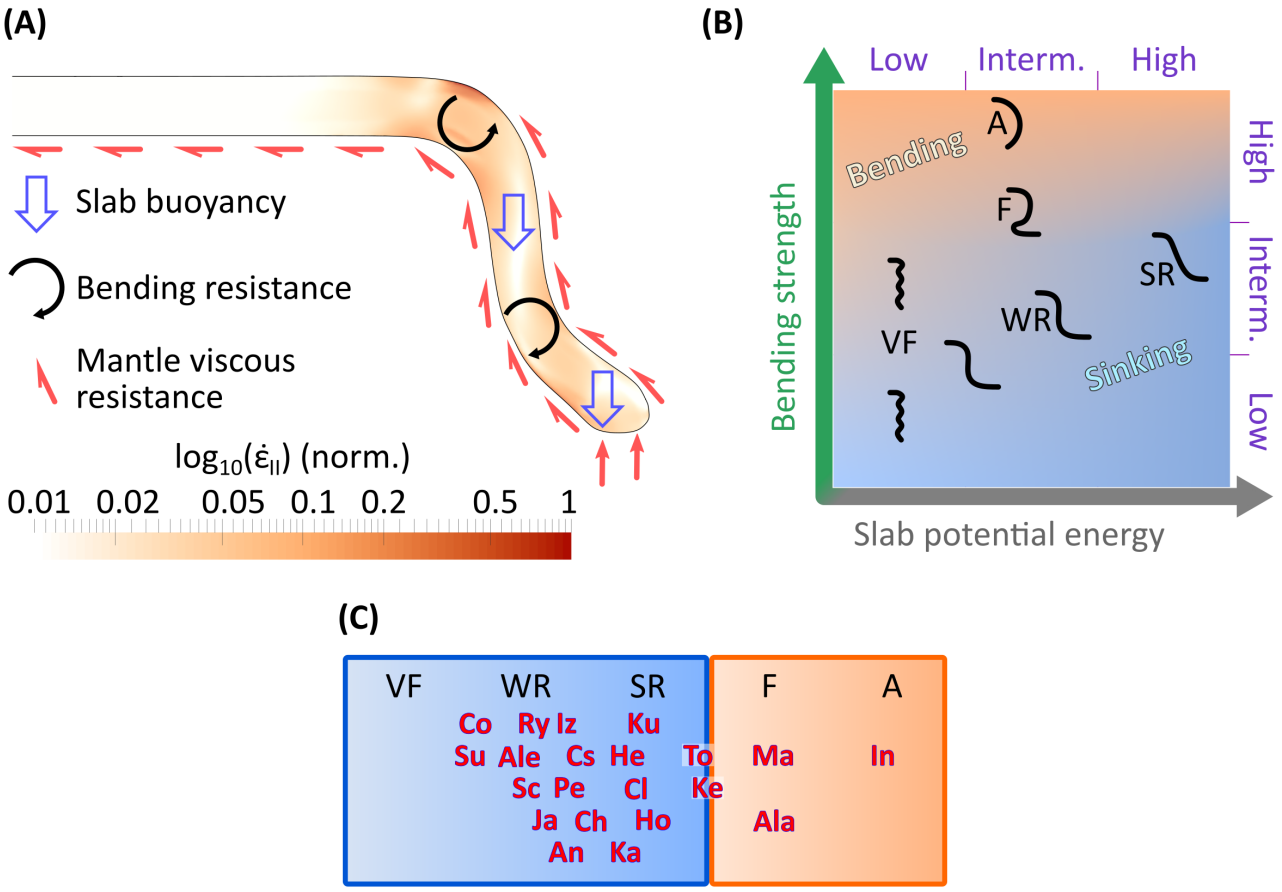


Figure 4.1: (A) outline of subducting plate, coloured by normalised value of the second invariant of the strain rate tensor, $\dot{\varepsilon}_{II}$. Main forces are marked by blue, black and red arrows. (B) Schematic regime diagram of slab shapes (black) in various subduction modes. Orange background indicates 'bending' regime and blue background indicates 'sinking' regime (modified after Goes et al., 2017). (C) Global subduction trench segments sorted by subduction mode based on previous compilation of shapes from seismic tomography and seismicity by Goes et al. (2017). Subduction mode abbreviations (black): A - advance, F - folding, SR - strong retreat, VF - vertical folding and WR - weak retreat. Trench abbreviations (red): Ala - Alaska, Ale - Aleutians, An - Antilles, Ch - Chile, Cl - Calabria, Co - Cocos, Cs - Cascadia, He - Hellenic, Ho - Honshu, In - India, Iz - Izu, Ja - Java, Ka - Kamchatka, Ke - Kermadec, Ku - Kuril, Ma - Mariana, Pe - Peru, Ry - Ryukyu, Sc - Scotia, Su - Sumatra, To - Tonga.

and Morra, 2012; Goes et al., 2017). Such a regime diagram is schematically illustrated in Fig. 4.1B.

A compilation of global slab morphologies and dips indicates that the large majority of subducting slab segments have deep dips $<80^{\circ}$ (Lallemand et al., 2005) and are in weak-retreat mode with no or few observed folds in the upper mantle (Fig 4.1; Ribe, 2010; Stegman et al., 2010b; Goes et al., 2017, and references therein). A few slabs, like

Mariana and Sumatra appear to penetrate through the ULMB vertically and only the Indian slab, under the Himalayan collision zone, is overturned (Goes et al., 2017).

In this chapter, we will use 3-D mechanical numerical models to show how the choice of parameters for a reference model determines its regime and mode. The choice of reference model in turn determines how it is affected by variations in plate viscosity, density and width. We will use these findings to (i) discuss the reasons previous studies came to contradicting conclusions regarding the role of plate strength, width and buoyancy on subduction dynamics, and what should be considered in future models of Earth-like subduction and (ii) to show how variations in mode along strike of our 3D models further complicate subduction style. Finally, we will use our conclusions to design a reference case for further study on the effects of buoyant features on subduction dynamics in the Chapter 5.

4.3 Modelling methods

4.3.1 Modelling system and setup

We design 11 models in a 3-D Cartesian domain. We use a multi-material approach to simulate subduction of a plate into ambient mantle, with no upper plate (i.e. 'free subduction'). We use a multi-material approach to distinguish the subducting lithosphere from the mantle, taking the constant density and viscosity plate to represent the combined impact of the crust and the mantle lithosphere. The absence of an upper plate allows us to analyse the dynamic forcing by the subducting plate which is widely agreed to be the main driver of subduction dynamics and diversity (e.g. Forsyth and Uyeda, 1975; Goes et al., 2017). Our approach neglects the thermal evolution of the slab and associated feedbacks on density and viscosity (e.g. Garel et al., 2014; Suchoy et al., 2021). This simplification enhances numerical efficiency, allowing us to perform a systematic 3-D study across a wide parameter space. Previous studies have

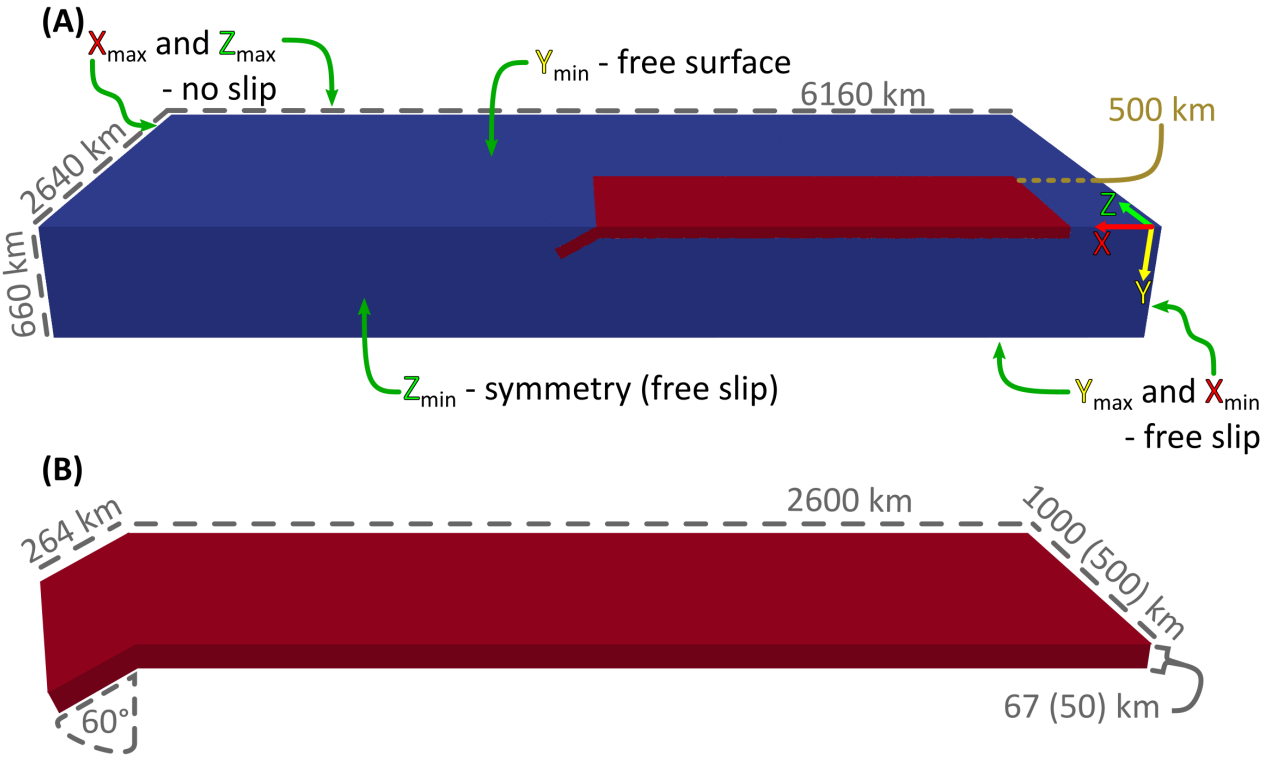


Figure 4.2: Initial condition of (A) model domain and (B) subducting half-plate with geometry and boundary conditions. See table 4.1 for material properties (viscosity and density) of the plate and the mantle. Dimensions modified between models shown in parentheses.

demonstrated that the multi-material, mechanical approach used herein captures the first-order dynamics of subduction (e.g. Bellahsen et al., 2005; Capitanio et al., 2007; Stegman et al., 2010b; Chen et al., 2022b).

We use Fluidity, an adaptive, unstructured mesh, finite-element, control-volume computational modelling framework (e.g. Wilson, 2009; Davies et al., 2011; Kramer et al., 2012, 2021), to solve the conservation equations of mass and momentum for an incompressible fluid under the infinite Prandtl number and Boussinesq approximations:

$$\nabla \cdot u = 0 \tag{4.1}$$

$$\nabla \cdot \left[\mu \left(\vec{\nabla} u + \left(\vec{\nabla} u \right)^T \right) \right] - \vec{\nabla} p = -g \Delta \rho \Gamma \hat{y} \tag{4.2}$$

$$\frac{\partial \Gamma}{\partial t} + \mathbf{u} \cdot \vec{\nabla} \Gamma = 0 \tag{4.3}$$

where u is the velocity, μ is the dynamic viscosity, p is the pressure, g is the acceleration due to gravity, $\Delta\rho$ is the difference in density between different materials, Γ is the material volume fraction ($\Gamma = 1$ within a given material and $\Gamma = 0$ elsewhere) and $\hat{y}$ is a unit vector in the direction of gravity. We utilise an adaptive unstructured mesh of tetrahedral elements, with minimum and maximum element sizes of 1 and 450 km, respectively (Fig. 4.3). This allows us to resolve fine-scale features where the gradients of velocity and viscosity are strong, whilst maintaining computational efficiency (see Davies et al., 2007, 2011, for further detail).

Our model setup consists of a Cartesian domain of 6160×660×2640 km^3 (length × depth × width), and includes half a plate, assuming symmetry at the centre of the plate along the long (i.e. *X*) axis (Fig. 4.2). The symmetry plane (*Z*=0 km), bottom (*Y*=660 km) and back (*X*=0 km) boundaries are prescribed as free slip, while the front (*X*=6160 km) and side (*Z*=2640 km) boundaries are no slip, and the top (*Y*=0 km) boundary is a free surface. The plate is initially placed 500 km away from the back (*X*=0 km) domain boundary (Fig. 4.2). An initial slab tip of 264 km long, dipping at an angle of 60° from the vertical, is prescribed to initiate subduction (similar to Stegman et al., 2010b).

The plate is 2600 km long, and thickness and width are varied for different cases (Table 4.1). Density of the mantle is 3300 kg/m^3, and mantle viscosity is set to either $2{\cdot}10^{20}$ Pa·s or $5{\cdot}10^{20}$ Pa·s, dependent on the case. Plate density and viscosity are varied to evaluate sensitivity of the subduction mode to these parameters. All properties of the models are presented in Tables 4.1 and 4.2.

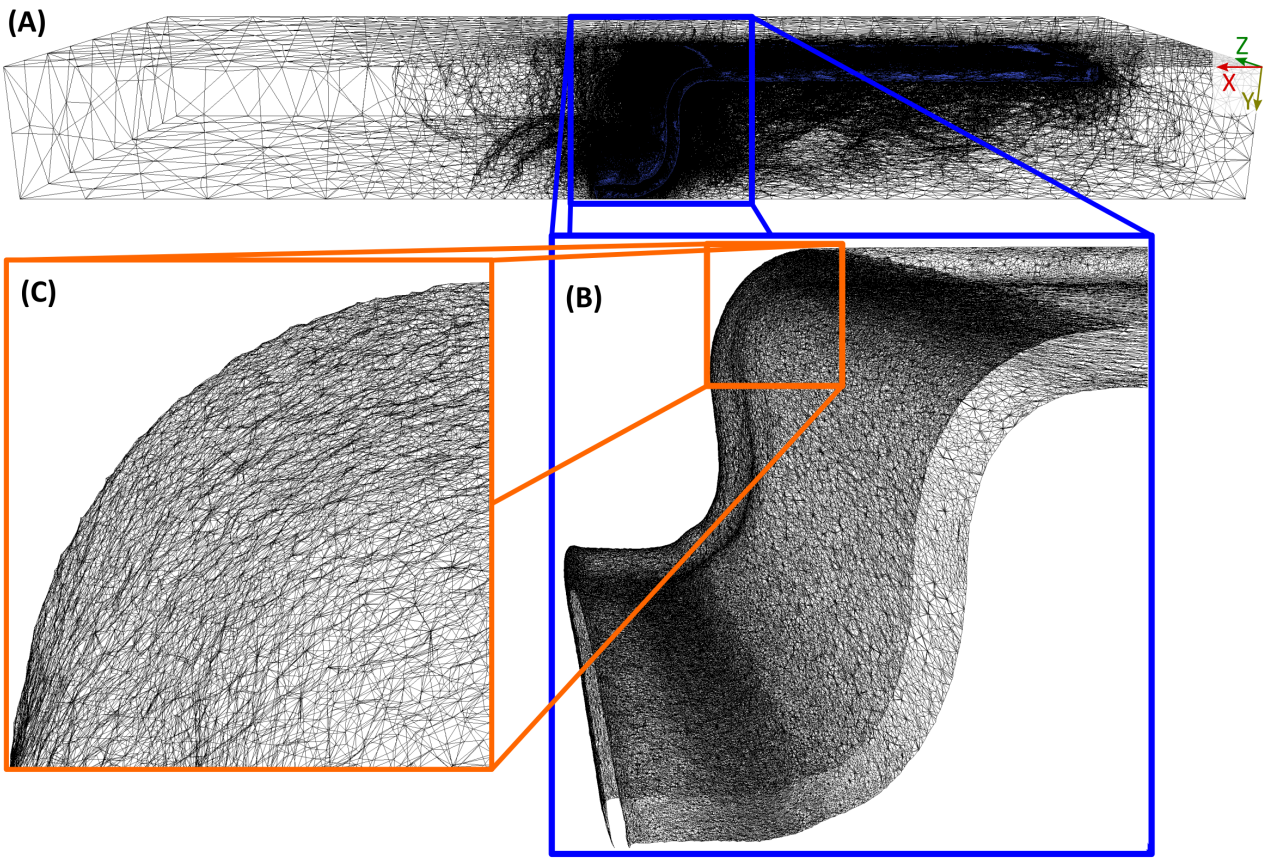


Figure 4.3: Examples of grid cell geometry in (A) full model domain, (B) the front of the plate and (C) at the top of the edge of the trench. The mesh is refined during the evolution of the model to increase resolution in areas of high velocity and viscosity gradients to increase computational efficiency (see also Davies et al., 2007, 2011). The smallest and largest edges of the grid cells, shown in (C) and (A), respectively, are 1 km and 450 km long.

4.3.2 Model Cases

For our reference case Ea, we explore the behaviour of a model where we assigned material properties typical of natural subduction on Earth (Table 4.1). The viscosities of the plate and the mantle are 10^{23} Pa·s and $2{\cdot}10^{20}$ Pa·s, respectively. This choice of viscosities is motivated by previous studies that have concluded that effective plate viscosities are between 10^2-10^3 times that of the underlying mantle (e.g Billen and Hirth, 2007; Schellart, 2008; Ribe, 2010; Stegman et al., 2010b; Li and Ribe, 2012). Plate and mantle densities are set to 3360 kg/m^3 and 3300 kg/m^3, respectively, resulting in

Model Name	$H_P \times W_P$ [km^2]	η [10^{21} Pa·s] Plate	Mantle	Plate-mantle $\Delta\rho$ [kg/m^3]	B_P [10^{13} N/m]
Ea	67×2000	100	0.2	60	8.04
V1	67×2000	200	0.2	60	8.04
V2	67×2000	40	0.2	60	8.04
V3	67×2000	20	0.2	60	8.04
V4	67×2000	100	0.5	60	8.04
D1	67×2000	100	0.2	120	16.08
D2	67×2000	100	0.2	30	4.02
VD	67×2000	100	0.5	120	16.08
T	50×2000	100	0.2	60	6.00
TD	50×2000	100	0.2	80.4	8.04
N	67×1000	100	0.2	60	4.02

Table 4.1: Model variables. Underlined parameters differ from model Ea. H_P is plate thickness, W_P is plate width and B_P is plate buoyancy per unit length. Note the simulated plate width is half the full plate width, W_P, assuming symmetry at the centre (at Z=0 km). B_P is calculated as $\Delta\rho \cdot H \cdot W \cdot g$, and is positive in the direction of gravity.

plate negative buoyancy valid for plates of an age of approximately 80 Myr. Full plate width is 2000 km, similar to the length of many subduction arcs.

Next, we examine 10 cases where viscosity, density, plate thickness and plate width are varied (V, D, T and N type models, respectively; see Table 4.1). The ratio of plate to mantle viscosity in all models is set within the range common on Earth of 10^2-10^3. The range of plate thicknesses and densities is typical of plates on Earth according to plate cooling models which are consistent with surface heatflow and bathymetry (McKenzie et al., 2005), with the exception of the plate densities in cases D1 and VD, which represent a relatively strong sinking-force end member.

In the lead-up to the work discussed in this chapter, we ran a set of benchmark tests of mantle convection in a 3-D box with a top cold thermal boundary and a bottom hot thermal boundary, following the design of cases 1a and 1b in Busse et al. (1994) in which the initial condition resulted in bimodal convection flow. We also reproduced the subduction model described in Stegman et al. (2010b) and in Mériaux et al. (2018)

Parameter	Symbol	Value
Gravitational acceleration	g	10 m/s^2
Domain length	L_{dom}	6160 km
Domain width	W_{dom}	2640 km
Domain depth	D_{dom}	660 km
Plate length	L_{plate}	2600 km
Initial plate trailing edge distance	L_{te}	500 km
Initial slab tip length	L_S	264 km
Initial slab angle from vertical	α_S	60°
Mantle density	ρ_m	3300 kg/m^3

Table 4.2: Parameters common to all simulations. Note the domain is simulating half space, assuming symmetry at Z=0 km.

when we designed the reference model described in Section 4.5.3, which was used as a reference model for the study in Chapter 5.

For analysis purposes, the plate is defined as an iso-surface where the mantle material volume fraction is 0.5. Fig. 4.4 shows each case at the final stage of the simulation, after considerable interaction with the bottom boundary (i.e. the ULMB). The trench is defined as the front of the plate (along the X axis) at 20 km depth. Measurements of plate evolution, as shown in Figs. 4.5-4.11 and 4.13-4.14, were done in 3 points along the trench: 15 km from the symmetry (Z=0 km) boundary, 50 km from the edge of the plate and at a point half way along the trench (denoted as 'symmetry', 'edge' and 'middle', respectively). Red diamonds mark the locations of the measurement at chosen times in Figs. 4.5, 4.7, 4.9, 4.11 and 4.14.

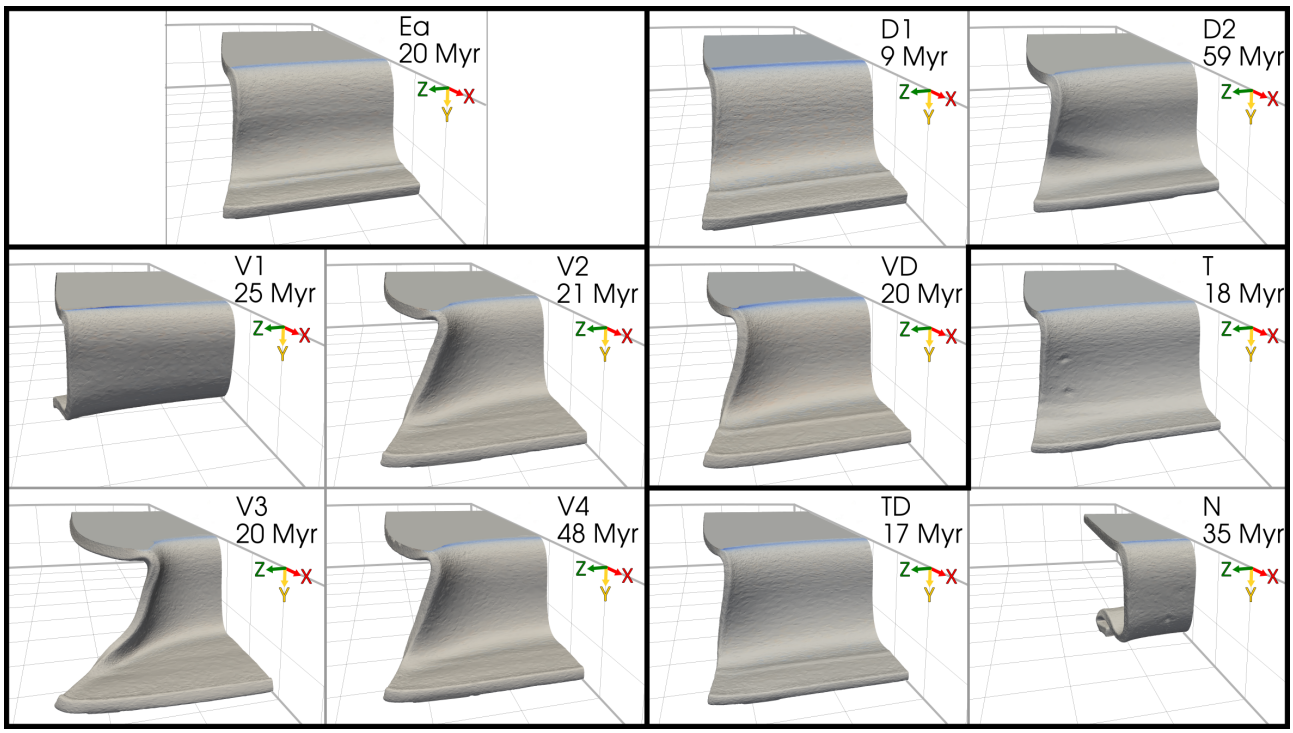


Figure 4.4: Slab geometries at the end of the simulation for all model cases, coloured according to the pressure. Case name and simulation time are shown for each panel. Cell length of the grid cells is 400 km. The symmetry boundary is to the right of the plate in each panel.

4.4 Results

4.4.1 Reference: Case Ea

We first explore the behaviour our case Ea, with parameters that are typical for Earth subduction (Table 4.1). While it might be expected such a model would result in 'weak-retreat' style of subduction, common in most plates on Earth, this is only partially true. Like in other subduction models, the behaviour of the plate is characterised by 2 stages (as initially described by Funiciello et al., 2003a), following an initialisation phase of $\sim$5 Myr where the slab steepens from the initially assigned dip. In the first stage, the slab sinks through the upper mantle, accelerating as the slab lengthens. In the second stage, the slab interacts with the ULMB (bottom of the modelling domain in our case)

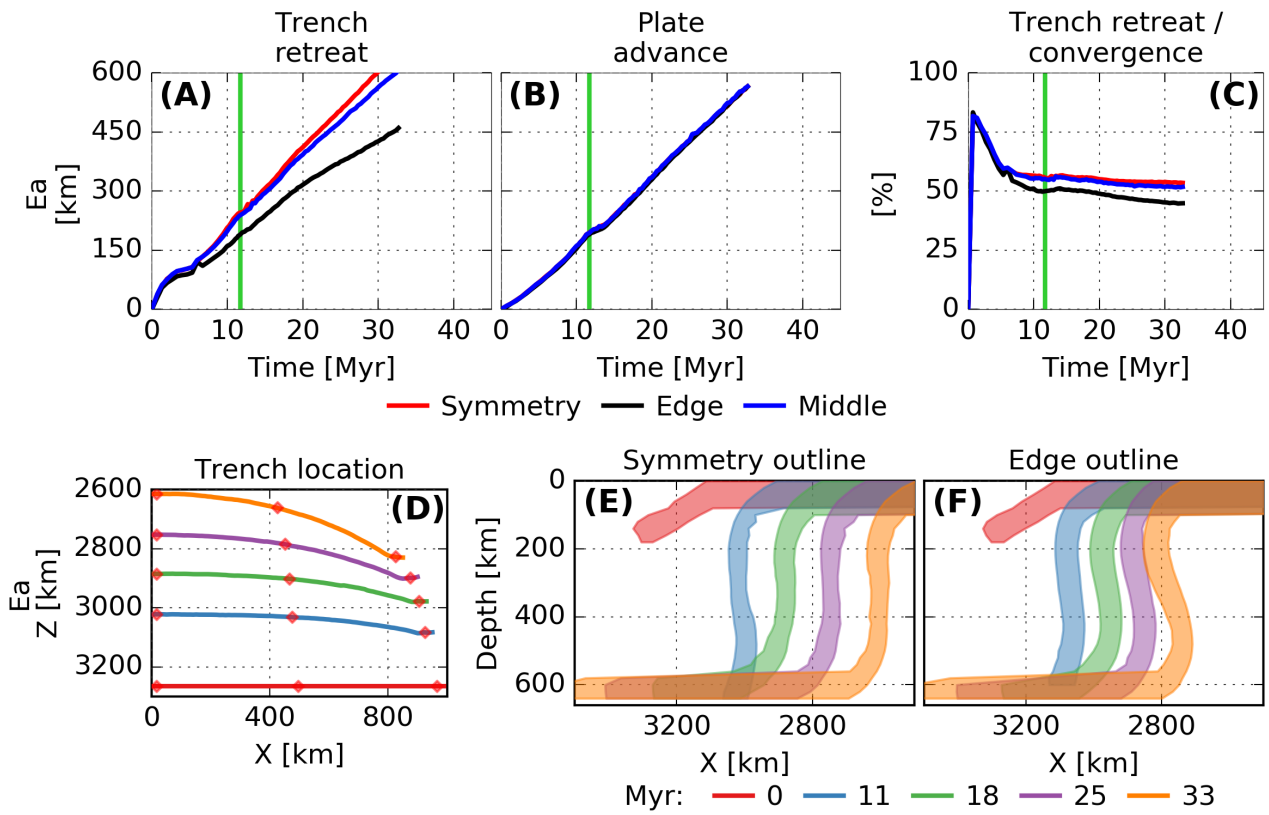


Figure 4.5: Temporal evolution of reference model Ea. (A)-(C) Trench retreat, plate advance and ratio of retreat to convergence, respectively, as a function of time. Red lines are for measurements at the symmetry boundary (i.e. at the centre of the plate), blue lines are for measurements in the middle of the half-plate and black lines for measurements at the edge of the plate. Vertical green lines mark the time that the slab reaches the bottom of the domain (i.e. *t660*). (D)-(F) Evolution of trench shape (top down view), slab shape at the symmetry (cross-section view) and slab shape at the edge, respectively. Red diamonds on (D) mark the location where slab and trench position, motion and velocity were measured, with results displayed in the other panels. Horizontal and vertical axes in (D)-(F) are scaled the same.

and reaches a quasi steady state. The time when the slab first reaches 660 km depth, marking the transition between the first and second stages, is referred to as *t660*.

During the first stage of the subduction, plate convergence velocities of case Ea are similar to moderate convergence velocities observed on Earth, at 2-4 cm/yr. Following the start of interaction with the bottom of the domain at 11 Myr, convergence velocity stabilises at ∼3.5 cm/yr. Trench retreat dominates convergence in both the first and the second stages of subduction. While in the first stage the ratio of retreat to convergence peaks at ∼60%, after *t660* this ratio drops slightly to ∼55%.

The behaviour of the subducting plate changes along strike. While the plate advances at the same rate everywhere, trench retreat is greatest at the centre of the plate (∼470 km by 25 Myr at the symmetry boundary) and smallest at the edge (∼380 km by 25 Myr; Fig. 4.5A-B). This difference is the result of toroidal flow around the edge of the plate (Schellart et al., 2007). This variation leads to a similar along strike variation in the ratio of retreat to convergence. While convergence is always dominated by trench retreat at the centre of the plate, at the edge, convergence at later stages of the simulation is dominated by plate advance, with the ratio of retreat to convergence slightly less than ∼50% (Fig. 4.5C). These variations lead to along strike changes in slab geometry, evolving to a vertical slab at the centre of the plate and an S-shaped slab at the edge (Fig. 4.5E-F).

The along-strike differences in slab geometries and trench retreat are expressions of different modes of subduction. The centre of the slab displays typical weak retreat behaviour, while the shape of the slab at the edge of the plate could be associated with either vertical folding or a fold-and-retreat mode. We classify it as the latter because (i) the plate is strong enough to continue to drive trench motion even during folding, and (ii) this mode is most compatible with the change in subduction behaviour upon increasing plate viscosity, which is discussed in the next section.

The change in mode towards a more bending dominated style at the plate edge is the result of the additional along-strike bending that is introduced by the toroidal flow, dissipating more of the potential energy, as previously noted in the 3-D models of Li and Ribe (2012). This additional dissipation also leads to the lower sinking velocities at the plate edge than at the centre of the plate.

4.4.2 Effects of plate viscosity: Cases V1-V4

We next inspect cases where we vary the viscosity contrast between the plate and the mantle, by either changing the viscosity of the plate (cases V1-V3) or the mantle (case

V4). In all cases, modified viscosities affect final slab and trench shapes (Figs. 4.4 and 4.7), although not necessarily the subduction mode.

Trench retreat after *t660* is much diminished in case V1, with increased plate viscosity, compared to case Ea (Fig. 4.6A). The higher viscosity for the same plate density means that the slab does not have time to unbend before reaching the base of the model. This results in an overturning of the plate at *t660* (Fig. 4.4) which starts at the centre of the plate and propagates to the edge. After *t660*, trench retreat of the overturned plate decreases at the same time as plate advance rate decreases (Fig. 4.6B-C). The tip of the overturned slab is able to slide along the bottom of the domain (Fig. 4.7B-C) facilitated by the low drag associated with the 'free-slip' bottom boundary condition. A high-viscosity lower mantle would be expected to cause trench advance, leading to a similarly overturned plate, as observed in analogue models (Funiciello et al., 2003a; Schellart, 2004a; Bellahsen et al., 2005).

Trench retreat is greater in centre of the plate for the low-viscosity case V2 and the even lower-viscosity case V3 compared with case Ea. At 20 Myr, the trench at centre of the plate has retreated ∼550 km in case V2, compared with ∼570 km in case V3 and only ∼430 km in case Ea (Fig. 4.5A and 4.6D,G). The edges of the trenches in cases V2 and V3 move at higher rates than model Ea, but most of this motion is along-strike, leading to increasing trench curvature with decreasing plate viscosity (Fig. 4.7D,G), and very little trench motion in the direction of plate motion (i.e. X direction) at the plate edges. The shape of the slab in both cases V2 and V3 is close to vertical at the centre of the plate and S-shaped at the edge, similar to case Ea (Figs. 4.5E-F and 4.7B-C, E-F). However, the low trench retreat rate for cases V2 and V3 indicates the edges of these plates may actually be closer to vertical folding than fold-and-retreat mode.

The main effect of the increased mantle viscosity in case V4 is to slow the evolution of the model. This model has the same plate-mantle viscosity contrast as model V2 and displays the same behaviour, however the evolution of model V4 takes ∼2.4 longer (e.g. *t660* at 26 Myr and stable trench retreat rate of 1.2 cm/yr in case V4 compared

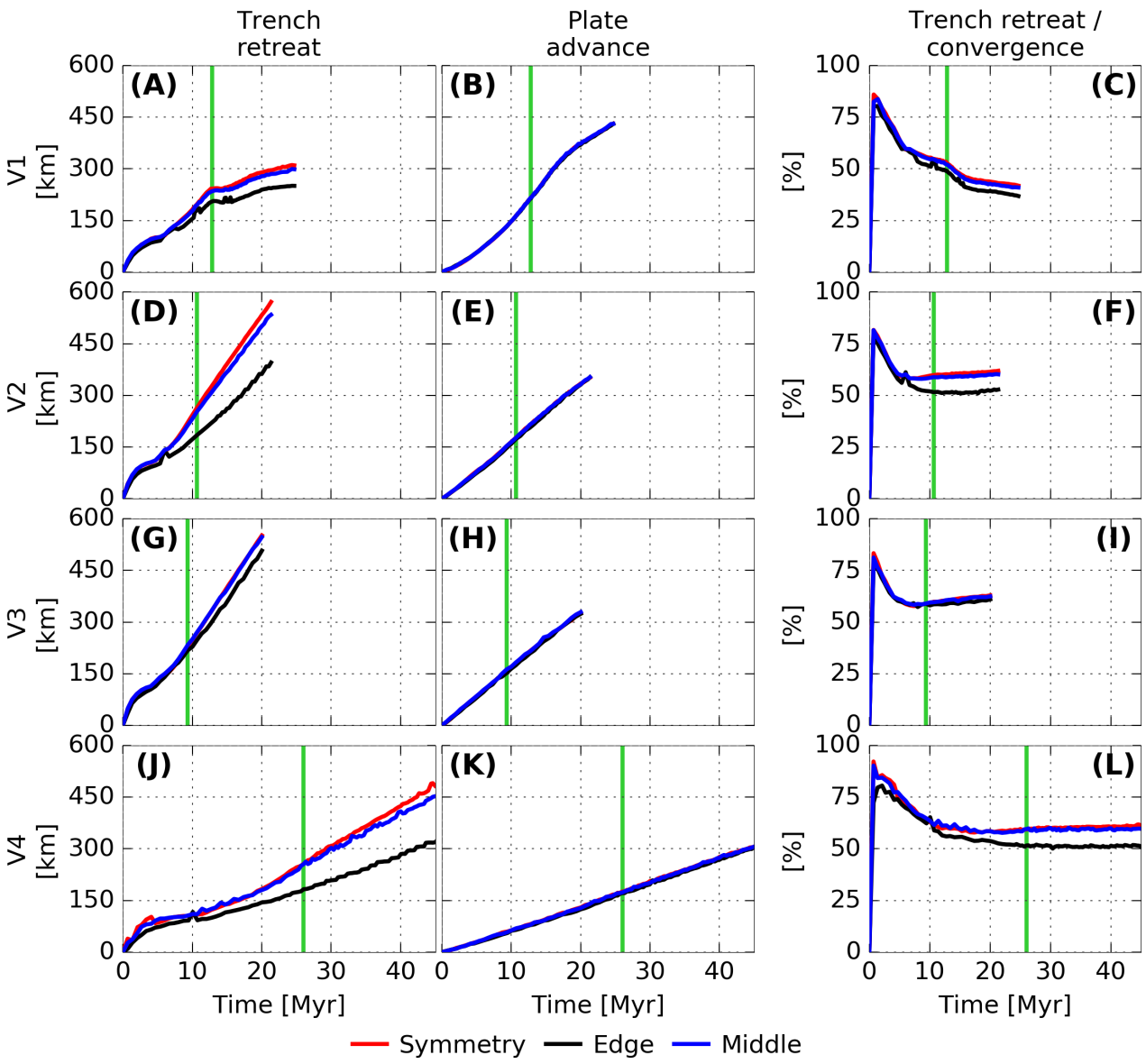


Figure 4.6: Trench retreat, plate advance and ratio of retreat to convergence (left, centre and right columns, respectively), as a function of time for models V1-V4, at the locations marked on Fig. 4.7. Lines styles are the same as in Fig. 4.5A-C.

with 11 Myr and 2.75 cm/yr respectively in case V2; Fig. 4.6D,J). The curvature and amount of trench retreat in cases V4 and V2 is similar after 1.5·*t660* (i.e. at 39 Myr and 15 Myr, respectively). That is, the subduction process is slowed down in proportion to the increase in mantle viscosity. Like in case V2, the slab shape in case V4 ends up almost vertical at the centre of the plate and S-shaped at the edge (Fig. 4.7E-F,K-L).

In summary, the retreat rates are higher and trench curvature stronger than case Ea

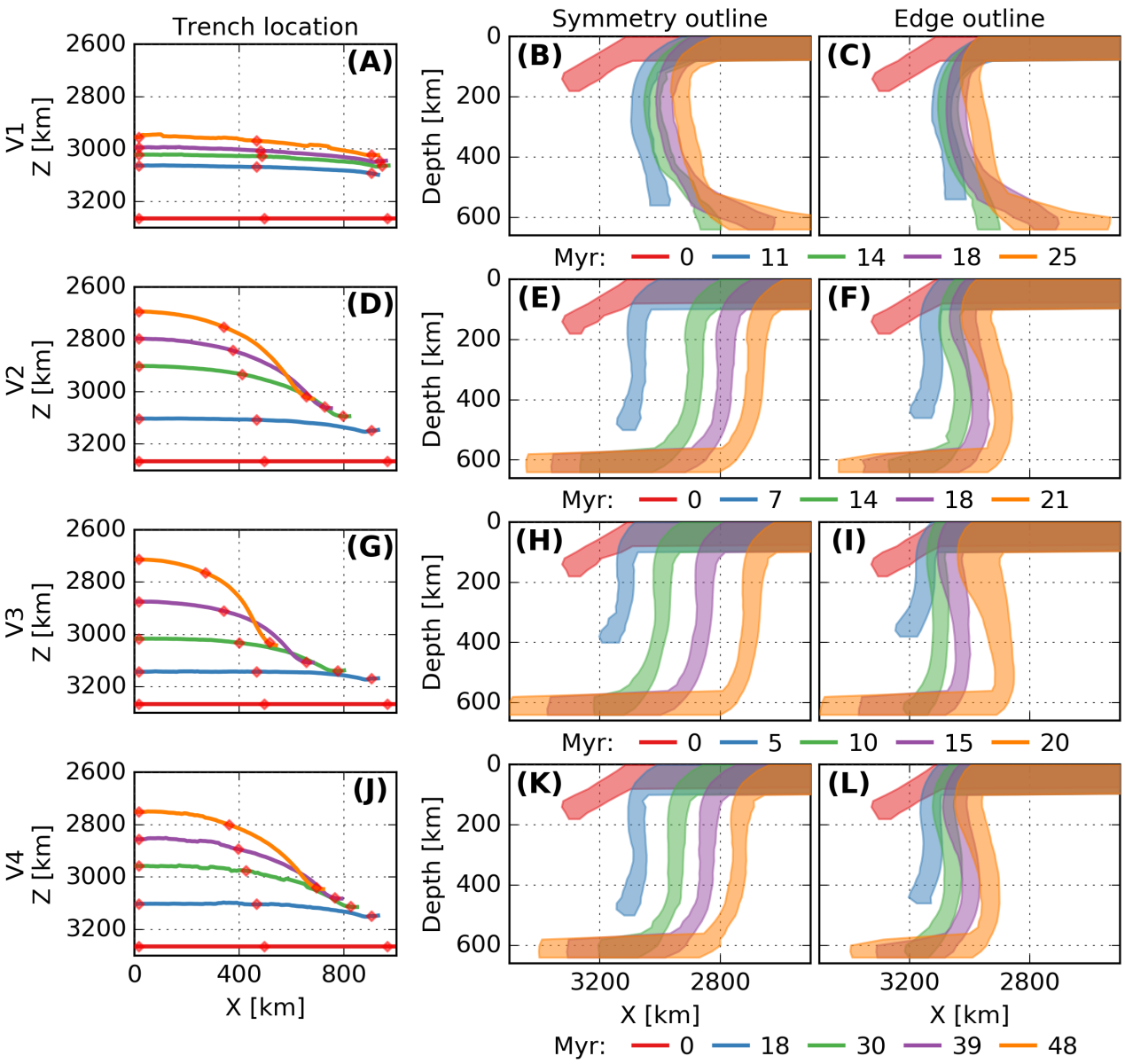


Figure 4.7: Evolution of trench shape (top down view), slab shape at the symmetry (cross-section view) and slab shape at the edge (left, centre and right columns, respectively), for models V1-V4. Markings are the same as in Fig. 4.5D-F. Red diamonds on left column mark the location of measurements, with results displayed in the other columns and in Fig. 4.6.

in the lower plate-mantle viscosity contrast cases V2-V4. However, the mode of subduction in these cases does not change strongly from model Ea. The centre of the plate in models V2-V4 is in weak retreat and the edge may be in vertical folding mode. The strong plate V1 case is in advance mode all along the plate, with little along strike variation in trench motion. Nevertheless, the centre of the plate behaves as if it is stronger than the edge as it overturns slightly earlier.

4.4.3 Effects of plate density: Cases D1, VD and D2

We investigate the role of plate buoyancy on subduction mode by examining cases with modified density contrast between the plate and the mantle. Cases D1 and VD have twice the density contrast, while case D2 has half the density contrast, compared with case Ea. The mantle viscosity in case VD is increased relative to case EA to the same value as in case V4.

The evolution of case D1, with increased plate density, is ∼2.4 faster than model Ea (e.g. *t660* at 5 Myr and a final trench retreat rate of ∼4.6 cm/yr in case D1 compared with 12 Myr and ∼1.9 cm/yr, respectively, in case Ea; Figs. 4.5A and 4.8A). Convergence in case D1 is slightly more dominated by trench retreat than model Ea, peaking at 58% ratio of trench retreat to convergence after *t660* (Fig. 4.8C). The dip of the slab between 200 and 500 km is ∼85° at the centre of the plate and vertical at the edge (rather than overturned as in case Ea) (Fig. 4.9B-C). In this case, the whole plate appears to be marginally in weak retreat mode.

The reduced buoyancy in case D2 results in much longer evolution than in case Ea. Evolution of case D2 is ∼4 times slower than that of case Ea (e.g. *t660* at 41 Myr and final trench retreat rate of ∼0.55 cm/yr in case D2 compared with 12 Myr and ∼1.9 cm/yr respectively in case Ea; Figs. 4.5A and 4.8G). This change in slab properties does not result in a different slab behaviour, although slab shape at the centre is more S-shaped than in case Ea. Subduction mode in both the centre and the edge of the plate appears to shift further towards a fold-and-retreat compared with case Ea.

In case VD, the increased viscosity of the mantle, which slows down subduction, coupled with the higher density contrast, which speeds up subduction, results in overall very similar evolution to case Ea. The net effect is a slightly faster evolving version of model Ea, with *t660* of 11 Myr and a final trench retreat rate of ∼2.4 cm/yr compared with 12 Myr and ∼1.9 cm/yr, respectively, in case Ea (Figs. 4.5A and 4.8D). The shape of the slab in case VD is also similar to that of case Ea, with S-shaped slab at the edge

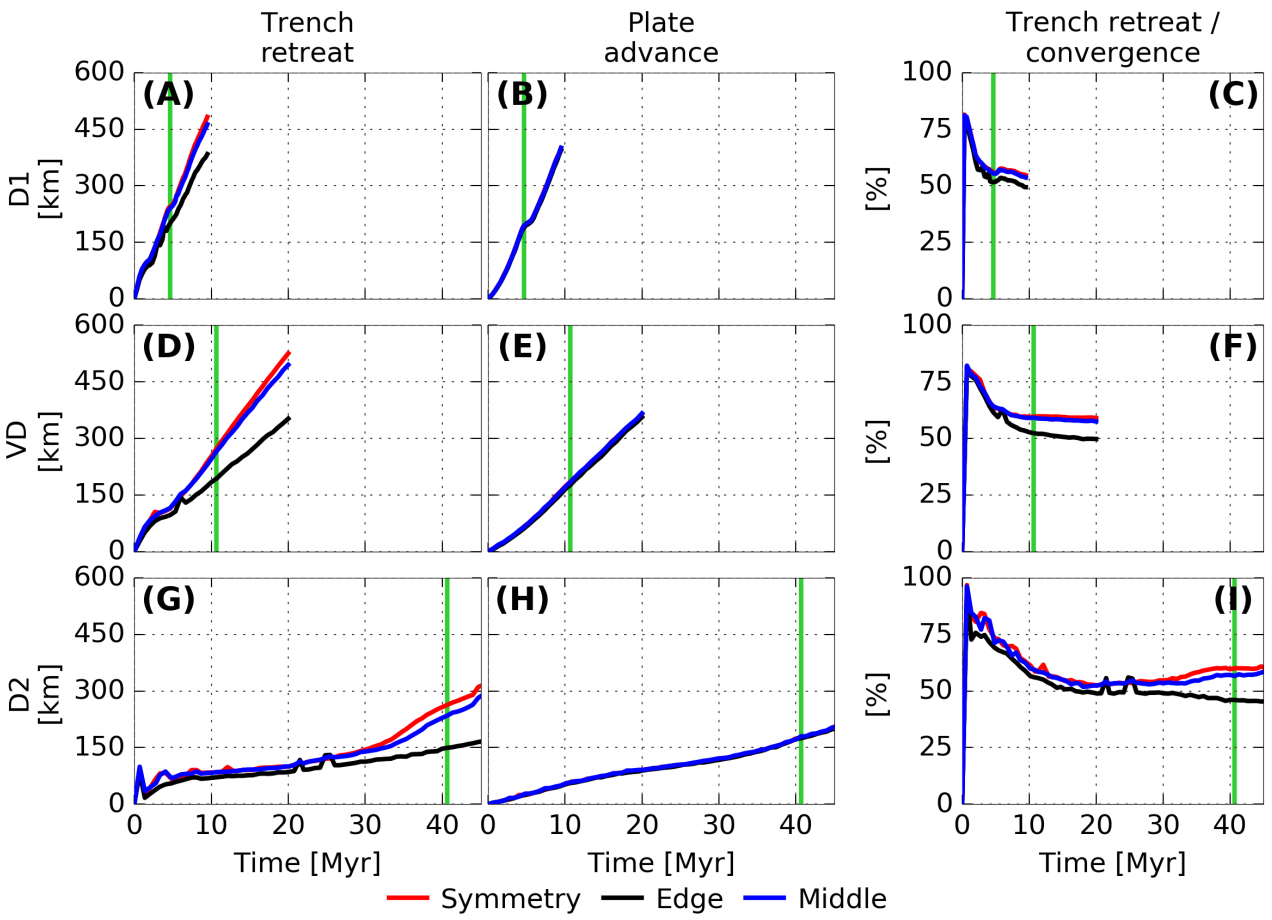


Figure 4.8: Trench retreat, plate advance and ratio of retreat to convergence (left, centre and right columns, respectively), as a function of time for models D1, VD and D2, at the locations marked on Fig. 4.9. Lines styles are the same as in Fig. 4.5A-C.

of the plate and almost vertical slab at the centre (Figs. 4.5E-F and 4.9E-F), indicating fold-and-retreat mode at the edge and slight change towards more weak retreat behaviour at the centre.

4.4.4 Effects of plate dimensions: Cases T, TD and N

Plate thickness affects both sinking force, through slab volume, and bending resistance. We explore how the thickness of the plate determines subduction mode by modelling subduction of thinner plates in cases T and TD, as significantly thicker plates than the reference plate in case Ea are not consistent with plates on Earth. We also consider the effects of plate width by modelling a narrow plate in case N.

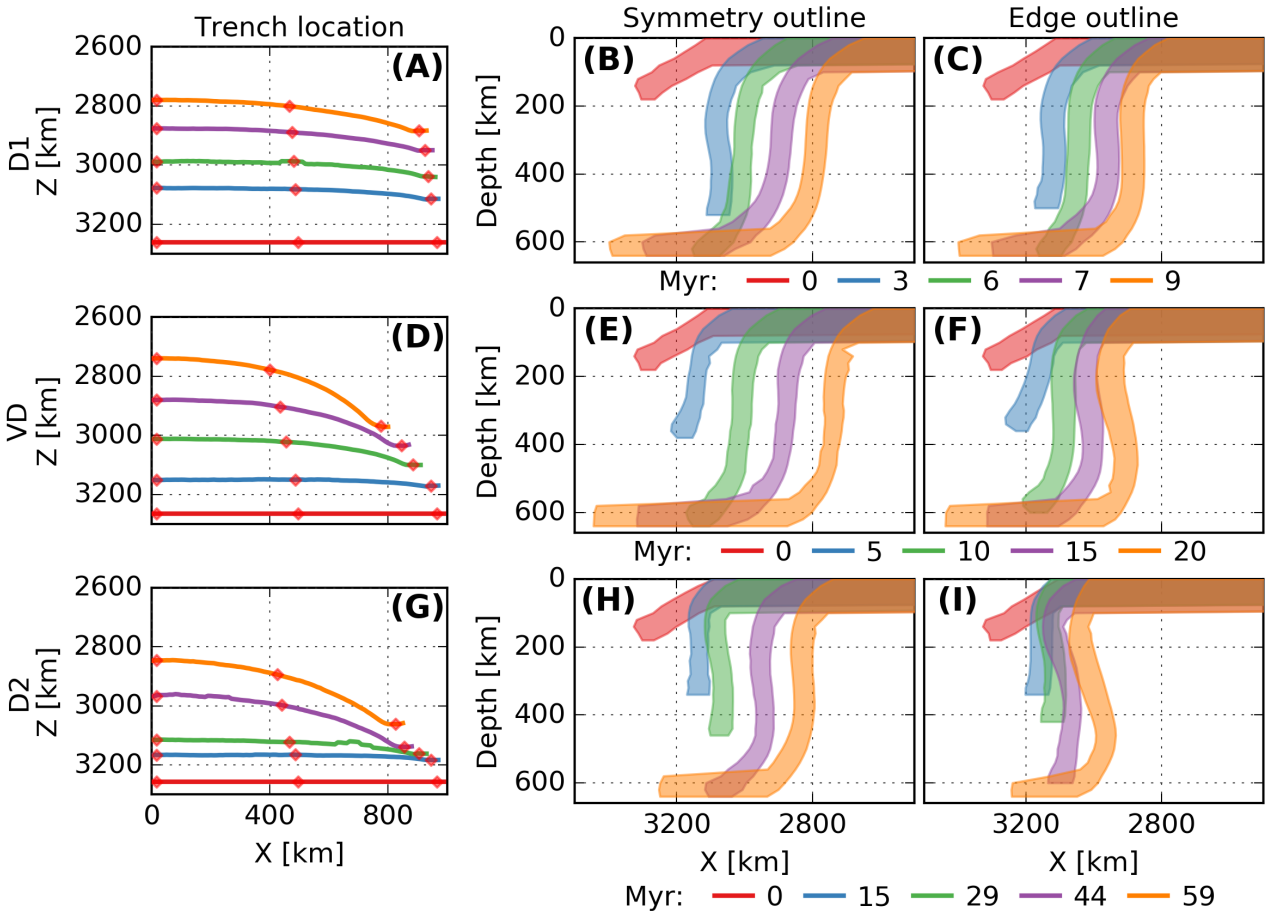


Figure 4.9: Evolution of trench shape (top down view), slab shape at the symmetry (cross-section view) and slab shape at the edge (left, centre and right columns, respectively), for models D1, VD and D2. Markings are the same as in Fig. 4.5D-F. Red diamonds on left column mark the location of measurements, with results displayed in the other columns and in Fig. 4.8.

The combined effects of reduced buoyancy and decreased strength in case T, compared with case Ea, result in slightly slower subduction evolution (*t660* at 15 Myr and final trench retreat rate of ∼1.3 cm/yr in case T, compared with 12 Myr and ∼1.9 cm/yr, respectively, in case Ea; Figs. 4.5A and 4.10A). The slab at the centre of the plate is vertical and S-shaped at the edge, similar to case Ea (Figs. 4.5E-F and 4.11B-C).

Plate thickness in case TD is the same as in case T, while plate buoyancy is adjusted to the value of case Ea. The smaller thickness reduces plate bending strength relative to case Ea without changing plate viscosity. The weaker plate evolves at a similar rate as case V2, with *t660* at 10.5 Myr and final trench retreat rate of ∼2.9 cm/yr, compared with 11 Myr and 2.75 cm/yr respectively in case V2 (Figs. 4.6D and 4.10D). Similarly,

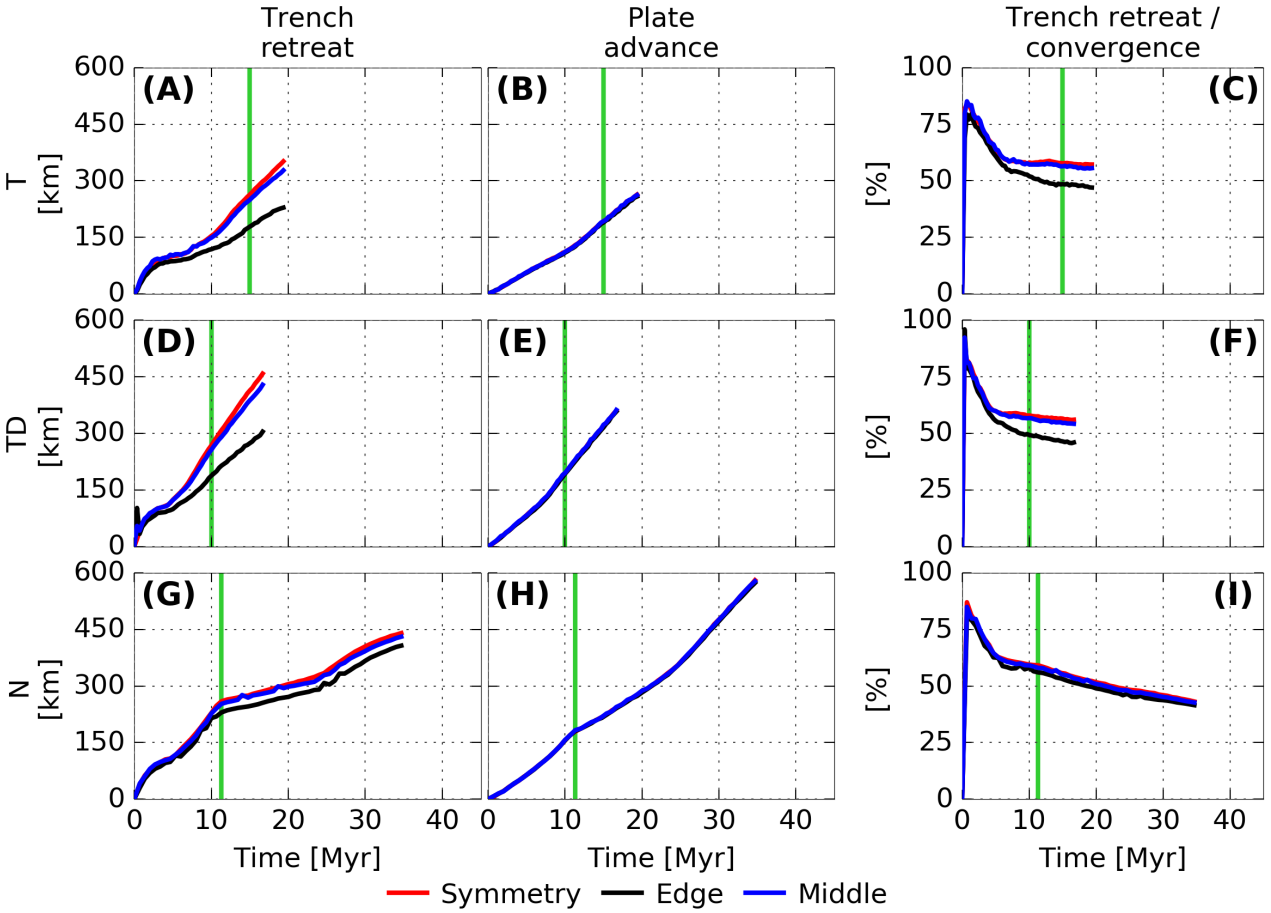


Figure 4.10: Trench retreat, plate advance and ratio of retreat to convergence (left, centre and right columns, respectively), as a function of time for models T, TD and N, at the locations marked on Fig. 4.11. Lines styles are the same as in Fig. 4.5A-C.

the slab in case TD is vertical at the centre of the plate and S-shaped at the edge, as in cases V2 and Ea (Figs. 4.5E-F, 4.7E-F and 4.11E-F). However, the trench curvature of case VD is similar to that of case Ea, and significantly less curved than the trench in case V2 (Figs. 4.5D, 4.7D and 4.11D).

The evolution of the narrow plate in case N is similar to case Ea up until *t660* at which point it overturns, similar to case V1 (Fig. 4.4). As in case V1, the overturning advances from the centre of the plate to the edge (Fig. 4.11H-I), resulting in rapid decline in trench retreat rate (Fig. 4.10G). After ∼15 Myr of minor trench retreat, and due to lack of traction at the bottom of the domain imposed by the boundary condition, the trench resumes retreating, albeit at a lower rate than other cases (∼1.2 cm/yr; Fig. 4.11G). Case N displays fold-and-advance behaviour, where initial folding of the slab

is followed by trench advance. The slab edge in case Ea displays similar behaviour, but is forced into a fold-and-retreat mode due to the retreat at the centre of the plate. Since the centre of the plate in case N is closer to the edge and is more strongly affected by the toroidal flow of the mantle, it retreats less and does not affect the edge the same way as in case Ea. We note that due to the the free slip impenetrable bottom boundary condition in our model, distinguishing between fold-and-retreat and fold-and-advance modes at the plate edge is difficult.

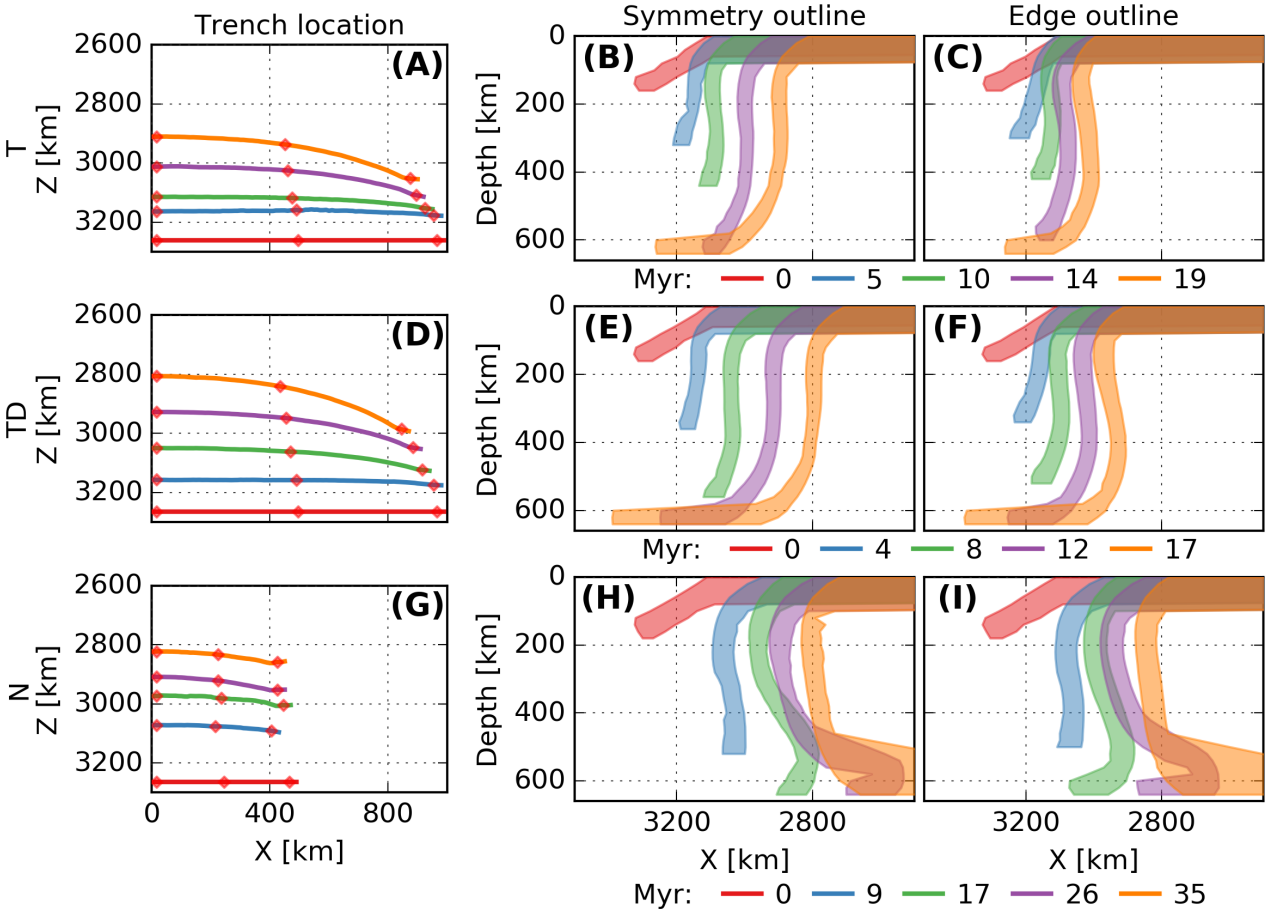


Figure 4.11: Evolution of trench shape (top down view), slab shape at the symmetry (cross-section view) and slab shape at the edge (left, centre and right columns, respectively), for models T, TD and N. Markings are the same as in Fig. 4.5D-F. Red diamonds on left column mark the location of measurements, with results displayed in the other columns and in Fig. 4.10.

4.5 Discussion

4.5.1 Model modes

The design and parameters used in model Ea reflect typical effective properties (viscosity, density, and width) of subducting plates on Earth as estimated in other studies (Zhong and Davies, 1999; Billen et al., 2003; Buffett, 2006; Funiciello et al., 2008; Schellart, 2008; Wu et al., 2008; Ribe, 2010; Stegman et al., 2010b; Li and Ribe, 2012). However, all the models in this study, apart from models D1 and V3, turn out to be fully or partly in a 'bending' subduction regime, i.e. where subduction dynamics is dominated by resistance to bending over Stokes sinking (Table 4.3 and Fig. 4.12). This behaviour is inconsistent with observed behaviour of plates on Earth, as determined by tomography and slab morphology (Fig. 4.1C).

Model	Mode	Model	Mode	
Ea	**WR-FR**	VD	**WR-FR**	Sinking
V1	**A-A**	T	**WR-FR**	Sinking
V2	**WR-VF**	TD	**WR-FR**	
V3	**WR-VF**	N	**FA-FA**	Bending
V4	**WR-VF**	Ly	**VF-VF**	Bending
D1	**WR-WR**	Lm	**WR-WR**	
D2	**FR-FR**	Lo	**SR-SR**	Transition

Table 4.3: Summary table of subduction modes for each case at the centre of the plate (left) and the edge of the plate (right). Case names are coloured by regime of subduction. See Table 4.1 and 4.4 for specific case parameters.

Cases Ea, V2, V4, VD, D2, T and TD are all classified as subducting marginally in weak retreat mode at the centre of the plate and in fold-and-retreat mode at the edge. Case N is classified as fully subducting in a fold-and-advance mode due to observed fold at the tip of the slab, which subsequently overturns. The final slab shape of case N resembles that of case V1, which has no folds. Case V1 is therefore classified as advance mode. Case D1, which has the largest buoyancy contrast between the plate and the mantle

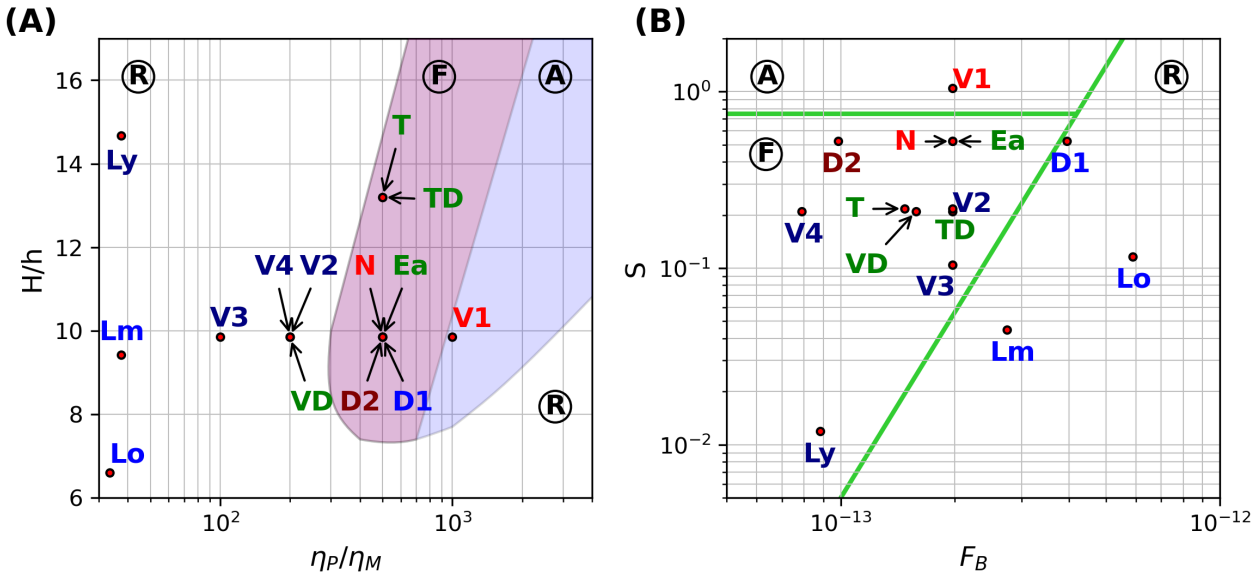


Figure 4.12: All model cases plotted on subduction regime diagram (A) in ratio of plate and mantle thickness to the ratio of plate and mantle viscosity following Li and Ribe (2012) and (B) in plate stiffness to slab negative buoyancy force following Stegman et al. (2010b). Plate stiffness is calculated as $S = \eta_P/\eta_M \cdot (h/H)^3$ and slab buoyancy as $F_B = \Delta\rho \cdot h \cdot g/\eta_M$. Regime abbreviations (in circled black font) are the same as in Fig. 4.1, where our Folding ('F'), Advance ('A'), and Retreat ('R') regimes correspond to regimes V, III and a combined I, II and IV in Stegman et al. (2010b), respectively. Case names are coloured by subduction mode. See Table 4.1 and 4.4 for specific case parameters and Table 4.3 for our mode classification for each model.

of all cases, is the only model fully in weak retreat mode in both the centre and the edge of the plate. The behaviour at the edge of the plate in case V3 resembles fold-and-retreat mode but can also be classified as vertical folding mode because the weak plate allows the development of an increasing trench curvature with little retreat or advance of the slab edge.

Although plate-mantle viscosity ratios in all models are in the range previous studies identified as appropriate to simulate Earth-like subduction, the combination with plate thickness (10% of the domain depth) puts our models mostly in the 'bending' regime. These results agree well with predictions by the regime diagrams proposed by Schellart (2008) and Li and Ribe (2012) (Fig. 4.12A) which explore the parameter space of plate-mantle viscosity ratio and plate-mantle depth ratio. According to this classification, cases Ea, T and TD are in folding mode, case V1 in advance mode and

cases V2-V4 in retreat mode. Variations in density and width, as in cases D1, D2 and N, are not distinguished by this analysis (Fig. 4.12A). The retreat mode field is larger for thinner and much thicker plates than we explored. Since thicker plates are not consistent with plate thermal thicknesses observed on Earth (McKenzie et al., 2005), this indicates that effective plate thickness, i.e. the thickness of the plate which contributes to plate stiffness, must be smaller. We will return to this point in Section 4.5.3.

The parameters of viscosity and thickness ratios, which several studies found are sufficient to classify subduction behaviour (Schellart, 2008; Ribe, 2010; Li and Ribe, 2012), do not provide insights into the differences in subduction mode that we find between cases Ea, D1 and D2. The distinct behaviour of these cases points to an additional dependence of subduction mode on density. This density dependence can be captured by using the parameters of buoyancy and stiffness proposed by Stegman et al. (2010b). Indeed we find that these two parameters can classify the variations in subduction style for all our cases (Fig. 4.12B). Stegman et al. (2010b) characterise buoyancy with a Stokes sinking time (function of density contrast, plate thickness and mantle viscosity) and non-dimensional stiffness (function of plate viscosity and thickness and mantle viscosity and depth). In this parameterisation, mantle and plate viscosities have independent effects, with the former also modulating buoyancy and the latter solely controlling stiffness.

The role of density in modifying the subduction regime is not immediately obvious. In a perfect Stokes flow, buoyancy ($v \sim g\Delta\rho$) increases the driving force but similarly increases the bending force, which entails that greater density contrast is expected to result in similar behaviour at a faster rate. Ribe (2010) proposed that a density dependence of subduction style could be introduced if rheology has non-linear dependency on deformation rates, or in visco-plastic and visco-elastic plates (Stegman et al., 2010b; Capitanio and Morra, 2012). In the presence of such non-linearity, the effect of increased sinking time does not simply offset the increased bending force due to the increase density, as both plate bending resistance and mantle resistance to

slab sinking evolve independently. However, in our models, rheology is linear. The free-surface ($\sigma = 0$) top boundary condition in our models may introduce non-linear impact on velocities. Such impact was not observed in the models of Ribe (2010) and Li and Ribe (2012), which also have a free surface, and which did not display a dependence of mode on plate density. Instead, we propose that our boundary conditions of no-slip ($v = 0$) and free-slip ($v = 0$ in the normal direction) result in non-linear interaction of the mantle flow with the ULMB and other domain boundaries, and introduces an additional dependence of the dynamics on deformation velocities. A recent comparison between subduction in Cartesian and spherical geometry by Chen et al. (2022a) indicates that these boundaries are likely responsible for the non-linear density-dependent effects which impact subduction more as the slab sinks and approaches the lower mantle.

Although side boundaries may not be the optimal approximation of the setting of natural subduction, even if the box size is large, a strong resistance at the ULMB is a more realistic condition than the fully open bottom boundary often used in boundary-element models (Ribe, 2010; Li and Ribe, 2012) and the ULMB would be a factor which, in addition to non-linear rheology, introduce a density dependence of natural subduction styles. Moreover, the dimensions of the box in our models represent Earth-like subduction systems where subduction is limited in space by the spherical geometry of the mantle and other plates. We, therefore, expect that in natural subduction slab buoyancy can affect subduction mode.

Based on the stiffness and buoyancy parameters, most of our cases would be expected to be in folding mode (regime V in Stegman et al., 2010b), consistent with the observed behaviour. To separate the different modes in our models in Fig. 4.12B, the regime boundary of the retreating regime had to be shifted to lower F_B compared to this boundary in Stegman et al. (2010b), possibly reflecting differences in model set up (e.g. plate thickness and rheological layering, and the free-slip bottom boundary). The low viscosity of the upper mantle and the thick plates considered in Stegman et al. (2010b)

result in large Stokes velocities and, in some cases, fast sinking velocities of the order of 10^2 cm/yr, which are much faster than observed on Earth (e.g. Seton et al., 2012). The retreat mode (regime IV in Stegman et al. (2010b)) expands to lower buoyancy for low stiffness values. We argue below that low stiffness values are the plausible reason for the 'sinking' behaviour observed in subduction zones on Earth.

4.5.2 Mode changes with plate parameters

In our model set, stronger and lighter plates lead to decreased trench retreat and increased slab dip (Figs. 4.5, 4.6, 4.7, 4.8 and 4.9). These trends are typical of subduction in a 'bending' regime and were observed in several previous studies (Di Giuseppe et al., 2008; Funiciello et al., 2008; Billen and Arredondo, 2018, and experiments 9 and 14 in Bellahsen et al., 2005). Instead, in models in an Earth-like 'sinking' regime (e.g. Capitanio et al., 2007; Schellart, 2008; Capitanio and Morra, 2012; Li and Ribe, 2012, and most experiments in Bellahsen et al., 2005), trench retreat decreases for *weaker* and lighter plates (and increases for stronger and denser plates). The reduction in plate width in case N results in folded behaviour which indicates higher plate bending resistance and more prominent 'bending' regime behaviour compared with case Ea, as was also observed by Bellahsen et al. (2005). However, the opposite behaviour is observed in models that are in the 'sinking' regime, in which trench motion decreases in *wider* plates (e.g. Schellart et al., 2007; Morra et al., 2012). Thus the choice of reference model parameters and the corresponding subduction regime is key for studying Earth-like subduction behaviour (See Schellart, 2008; Ribe, 2010; Stegman et al., 2010b; Li and Ribe, 2012; Goes et al., 2017).

Other factors will further modulate subduction modes. Strong coupling between the subducting and overriding plates may hamper trench retreat (Čížková and Bina, 2013; Pokorný et al., 2021), as could a strong and thick overriding plate (Capitanio et al., 2009; Guillaume et al., 2009; Capitanio et al., 2010; Garel et al., 2014; Sharples et al., 2014;

Holt et al., 2015b). Higher resistance to sinking at the ULMB may also modify subduction mode by slowing subduction and enhancing the tendency for folding (Garel et al., 2014; Holt et al., 2015a). Models with rheology that allows deep slab weakening (e.g Čižková et al., 2002) accommodate more folding and flattening of the slab at the ULMB than models with strong deep slabs (e.g. Billen and Arredondo, 2018). In models with such added complexity it is important to test that the base models are indeed in an Earth-like 'sinking' regime. Once that is established, additional factors, such as interaction between nearby subducting plates exerting external forcing which can lead to enhanced retreat or advance can be investigated (Čížková and Bina, 2015; Király et al., 2016; Holt and Becker, 2017).

Additional complexities arise in 3-D models. The along-strike plate bending that occurs in 3-D adds to the energy dissipated in plate deformation as previously noted by Li and Ribe (2012); Morra et al. (2012) and Chen et al. (2022b). This adds to the stiffness of the plates, beyond the calculated stiffness in the regime diagrams which depends only on plate-mantle viscosity ratio and plate thickness. As a result, in many of our 3-D plates, the edges of the plates are in modes that indicate stronger bending dissipation than the centre. In models with plates wider than those presented here, more 'bending' style behaviour can also occur in the middle of the plate (Schellart et al., 2007; OzBench et al., 2008; Chen et al., 2022b). The along-strike variation in trench curvatures results in additional energy dissipation in more bent areas, which is likely to come at the expense of the availability of potential energy for sinking. This can explain variations in sinking rates between the edge (lower) and the centre of the trench (higher), observed in 3-D cases by Li and Ribe (2012).

4.5.3 Modelling Earth subduction

Our results reinforce previous work by Conrad and Hager (1999); Buffett (2006); Ribe (2010); Buffett and Becker (2012) and Li and Ribe (2012) which concluded that subducting plates are relatively weak compared to the estimates based on laboratory derived flow laws (e.g. Billen and Hirth, 2007) applied over the full thickness of the plate. Mechanical models often neglect common weakening mechanisms such as brittle failure and strain-dependent weakening which weaken areas of high bending (i.e. areas of high strain rate) along the plate, contributing to a reduction in bending resistance (e.g. OzBench et al., 2008; Buffett and Becker, 2012; Garel et al., 2014) while effective plate viscosity remains unaffected where strain rates are low. In addition, temperature and stress dependent rheologies inferred from experimental data predict that plate strength is concentrated in the core of the plate (Billen and Hirth, 2007; Buffett and Becker, 2012; Garel et al., 2014; Holt and Becker, 2017). Therefore, subducting plates may be better represented by a rheologically layered plate with a strong viscous core sandwiched between top and bottom low-viscosity or visco-plastic layers (e.g. Morra et al., 2006; Capitanio et al., 2007; OzBench et al., 2008; Capitanio et al., 2009; Stegman et al., 2010b). Such a layered rheology reduces bending resistance at the trench and upon interaction with the ULMB, while the strong core allows for efficient transmission of stresses from the slab to the plate (Capitanio et al., 2009; Stegman et al., 2010b; Garel et al., 2014).

The viscous approximation of layered plate rheology may still overestimate bending strength, due to the lack of elastic behaviour in the core of the plate, which facilitates bending and unbending (OzBench et al., 2008; Farrington et al., 2014; Fourel et al., 2014). Wadati-Benioff earthquakes are evidence of such elastic energy storage in plate cores. Therefore, implementations of laboratory derived rheology in a purely viscous model require an additional yielding or viscosity capping mechanism to limit the strength in the core of the plate (e.g. variations of Peierls' creep law have been used for this in Čižková et al., 2002; Agrusta et al., 2014; Garel et al., 2014) allowing

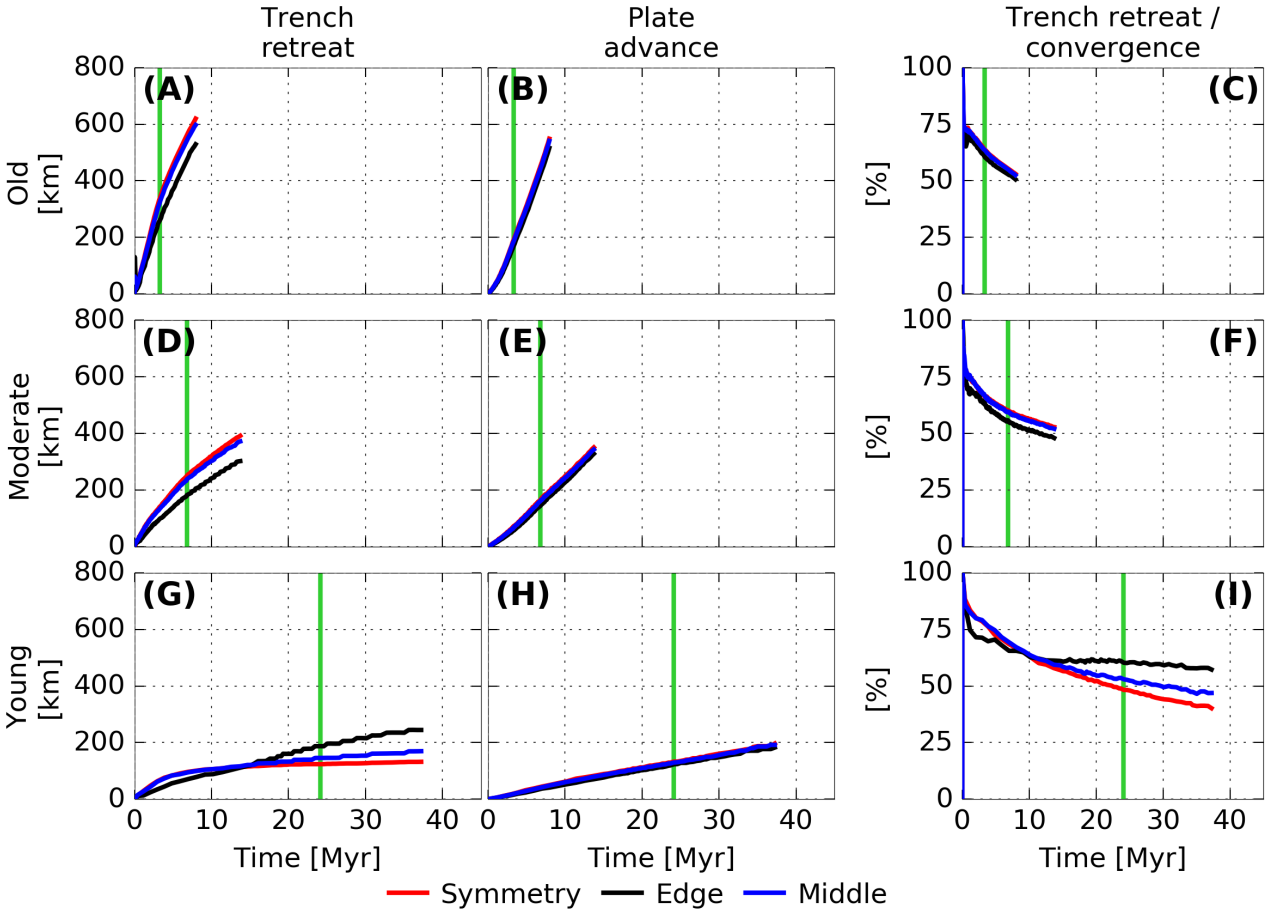


Figure 4.13: Trench retreat, plate advance and ratio of retreat to convergence (left, centre and right columns, respectively), as a function of time for layered models with old, moderate and young plates, at the locations marked on Fig. 4.14. Lines styles are the same as in Fig. 4.5A-C.

plates to have a low enough effective strength such that subduction behaviour is in the 'sinking' regime.

The results from this chapter motivated the model design that was subsequently used by Chen et al. (2022b) and constitutes the reference case for Chapter 5. Our preferred model design includes a three-layer plate with strong viscous core and visco-plastic outer layers. By using core thicknesses ranging from 15 to 40 km within 45 to 100 km plates, respectively (Table 4.4), we are able to account for the full range of Earth-like plate thickness and strength. In this design, we also extend the modelling domain to account for higher-viscosity and penetrable lower mantle to better reflect the resistance plates encounter at the ULMB. We designed three cases representative of the

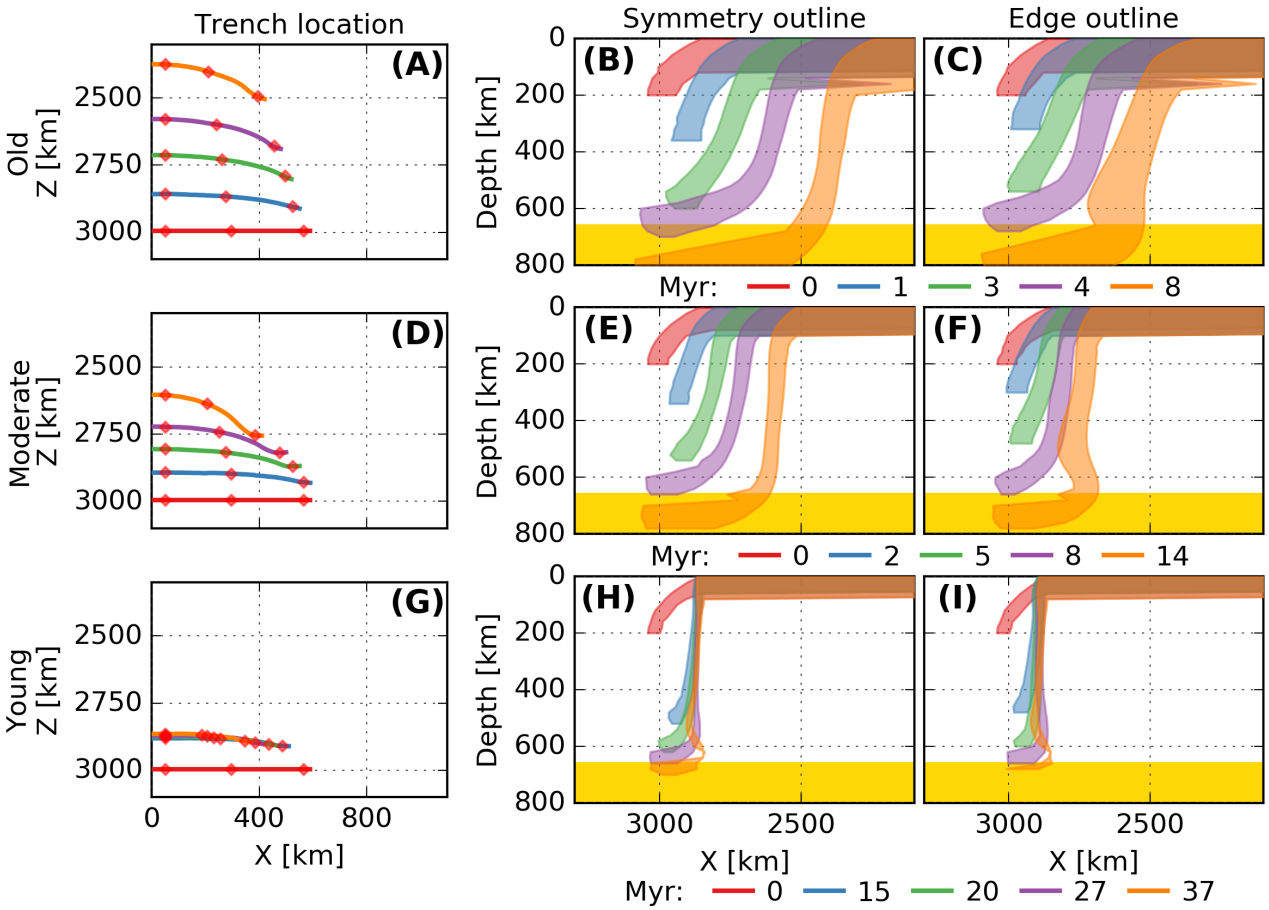


Figure 4.14: Evolution of trench shape (top down view), slab shape at the symmetry (cross-section view) and slab shape at the edge (left, centre and right columns, respectively), for layered models with old, moderate and young plates. Markings are the same as in Fig. 4.5D-F. Red diamonds on left column mark the location of measurements, with results displayed in the other columns and in Fig. 4.13. The lower mantle is depicted on the centre and right columns by yellow semi-transparent rectangle.

buoyancy, thickness and strength of relatively young, moderate-age and old oceanic plates. Parameters chosen are further motivated in the Chapter 5. Figs. 4.13 and 4.14 present the evolution of layered young, moderate and old plate models for 1200 km wide plates from Chen et al. (2022b). These cases display an increase with plate age of trench retreat, trench curvature and slab dip angle (both at the centre of the plate and at the edge), as expected for subduction in a 'sinking' regime. When plotted onto the subduction regime diagrams of Li and Ribe (2012) and Stegman et al. (2010b) (cases Ly, Lm and Lo in Fig. 4.12 and Table 4.3), the old and moderate layered cases fall under retreat mode, while the young layered case is in folding mode. For Chapter 5

Model Name	L×H×W [km^3]	H_C, H_{VP} [km]	η [10^{21} Pa·s] Plate	Mantle	Plate-mantle $\Delta\rho$ [kg/m^3]	B_P [10^{13} N/m]
Ly	2200×45×1200	15, 15	20	0.2	40	2.16
Lm	2200×70×1200	30, 20	20	0.2	80	6.72
Lo	2200×100×1200	40, 40	20	0.2	120	14.40

Table 4.4: Modified model variables. L is plate length in the direction of subduction, H is plate thickness and W is plate width along strike. Note the simulated width is half the full plate width, assuming symmetry at the centre of the plate. H_C and H_{VP} are the thicknesses of the high-viscosity core and the visco-plastic outer layers, respectively. B_P is plate buoyancy per unit length, calculated as $\Delta\rho \cdot W \cdot H \cdot g$, and is positive in the direction of gravity.

where we investigate the effects of the subduction of buoyant ridges, we use models with plates which are 2400 km wide to allow evaluation of lateral variations in subduction dynamics (Schellart et al., 2007; Chen et al., 2022b). In these models, bending resistance dissipates about $<$20% of the potential energy, and slab sinking is achieved mainly through trench retreat.

4.6 Conclusions

Observations of slab morphology and trench motions strongly indicate that typical plates on Earth predominantly subduct according to a 'sinking' regime. Published subduction models in varying subduction regimes have documented different, and sometime opposite, responses to changes in plate density, strength and width. Our set of 3-D numerical models of free-subduction with Earth-like rheological parameters shows that the responses to these subduction parameters depend on the subduction regime, 'sinking' or 'bending', of the reference model. Where the reference model is in Earth-like 'sinking' regime, trench retreat and low upper-mantle slab dips are encouraged by increased plate strength and density, and decreased plate width.

When designing an Earth-like dynamic subduction model, it is important to ensure

that the reference case is in 'sinking' subduction regime. The two key parameters to control this are plate stiffness, or bending resistance, controlled by plate viscosity, thickness and width, and plate sinking potential energy, determined by slab buoyancy and mantle viscosity. There is no one global set of parameters that will achieve the right behaviour for all models. The choice of parameters will depend on specific properties and approximations of the model including the chosen representation of rheology, plate coupling, the presence of an overriding plate, viscosity of the mantle, dimensions of the plate, boundary conditions and initial state. However, regardless of other parameters, Earth-like subduction requires relatively low effective plate strength (ratio of 100-200 between the average viscosity of the plate and mantle, assuming viscous or viscoplastic rheology; Conrad and Hager, 1999; Wu et al., 2008). Furthermore, earth-like subduction is difficult to achieve with iso-viscous plates with natural thicknesses and density contrasts (Stegman et al., 2010b). In mechanical models, Earth-like subduction behaviour is better simulated using a rheologically layered plate with strong core surrounded by weaker material. These insights are implemented to create the reference model for investigating subduction of buoyant ridges in the Chapter 5.

Chapter 5

How buoyant features modify the dynamics of free subduction

5.1 Summary

The subduction of positively buoyant features has been implicated in the development of flat and shallow dipping slabs, the formation of cusps in trench geometry, and the cessation of associated arc magmatism. However, how such buoyant anomalies influence subduction dynamics to produce these different tectonic expressions remains debated. In this chapter, using a series of multi-material 3-D simulations of free subduction, we investigate how linear buoyant ridges modify subduction dynamics, in particular downgoing plate velocities, trench motions and slab morphology. We examine the sensitivity of results to downgoing plate age (affecting buoyancy and strength), ridge buoyancy and ridge location along the trench, finding that buoyant ridges can locally change slab sinking and trench retreat rates, in turn modifying the evolution of slab morphology at depth and trench shape at the surface. In all cases examined, trench retreat is reduced, or switches to trench advance, where the ridge subducts. These effects depend strongly on downgoing plate age: on young, weak plates, the

change in trench shape is more localised than on old, strong plates. Slab shallowing at the ridge only occurs for young plates, while the stronger and more negatively buoyant older plates pull down the ridge at a steeper angle than the rest of the slab. On old plates, ridges located near regions of trench stagnation or advance, which typically develop in wide slabs, have a stronger effect on trench and slab shape. The combined effects of buoyant feature location, subducting plate age and overriding plate properties can result in a range of responses: from mainly trench deformation, through local slab shallowing, to the formation of a flat slab, a variation in expressions also observed on Earth.

5.2 Introduction

Buoyant features are thickened ridges and plateaus on the ocean floor that mark the surface expression of excess mantle melting (Coffin and Eldholm, 1994; Tetreault and Buiter, 2014). Ridges are typically elongated features with a specific orientation, whilst plateaus are often more uniform in their dimensions. Owing to their composition and thickness, they add a component of positive buoyancy to the associated lithosphere and will typically resist the subduction of this lithosphere (Kelleher and McCann, 1976). As a result, the subduction of buoyant features has been implicated in many irregularities of subduction tectonics, including the interruption of arc volcanism on the corresponding overriding plate (e.g. Vogt et al., 1976; Nur and Ben-Avraham, 1983; Mahlburg Kay and Mpodozis, 2002; Hu et al., 2016), uplift and compression in the overriding plate (e.g. Humphreys, 1995; Espurt et al., 2007; O'Driscoll et al., 2009) and either enhancement or suppression of seismic activity (e.g. Nur and Ben-Avraham, 1983; Gutscher et al., 1999, 2000b; Kumar et al., 2016).

Although they have been widely studied, there is currently no consensus on how the subduction of buoyant features modulates subduction dynamics. It was first proposed that buoyant-feature subduction alters the shape of the trench (Vogt, 1973). The main

evidence was the proximity of many features to trench cusps (e.g. the Emperor Chain at the intersection of the Aleutian and Kuril trenches, the Caroline Ridge between the Mariana and Yap trenches and the Ogasawara Ridge between the Mariana and Bonin arcs: Vogt, 1973; Vogt et al., 1976; Miller et al., 2006c; Mason et al., 2010; Rosenbaum and Mo, 2011). A proposed consequence of subduction of buoyant features is the association with low angle (i.e. 'flat'), subduction (Sacks, 1983; Gutscher et al., 2000b). The main examples of flat slab subduction are where the Nazca plate subducts beneath South America: the Nazca ridge is associated with the Peruvian flat slab (Gutscher et al., 2000b), the Juan Fernandez ridge with the Chilean flat slab (Mahlburg Kay and Mpodozis, 2002) and the Carnegie ridge with the Ecuadorian flat slab (Gutscher et al., 1999). The Northeast Pacific hosts an example of a present-day flat slab which is associated with subduction of the plateau-like Yakutat Terrane beneath Alaska (e.g. Gulick et al., 2007). Subduction of the Palau-Kyushu ridge under Japan (Xia et al., 2021) has also been associated with low-angle subduction along the Nankai Trench, and subduction of the Emperor chain with shallow subduction under Kamchatka (Davaille and Lees, 2004). Finally, the subduction of the Shatsky Rise conjugate has been linked to past flat subduction below North America leading to the Laramide Orogeny (Atwater, 1989; Liu et al., 2010).

It is proposed that when a buoyant feature subducts, its buoyancy counteracts downgoing motion of the surrounding negatively buoyant plate, keeping it afloat (Sacks, 1983; Gutscher et al., 1999). When a full flat slab matures and develops a horizontal section that extends several hundred kilometres from the trench, the lack of mantle wedge flow between the slab and overriding plate might cause a shut-down in arc volcanism (Nur and Ben-Avraham, 1981; Isacks, 1988; Atwater, 1989). Furthermore, the release of slab fluids into the thin coupling layer between the plates may reduce seismic activity (Nur and Ben-Avraham, 1983; Kim et al., 2012; Manea et al., 2013) and the induced slab bathymetry may limit the size of large ruptures (Sparkes et al., 2010). Other studies propose that a wide upper-lower plate contact area above a shallow slab increases the potential for large inter-plate earthquakes (Corbi et al., 2017; Muldashev

and Sobolev, 2020).

Although there are a number of observations supportive of a link between the subduction of buoyant features and shallow-angle or flat slab subduction (Vogt et al., 1976; Nur and Ben-Avraham, 1983; Gutscher et al., 1999; Van Hunen et al., 2002), there are also buoyant ridges and plateaus that subduct without affecting slab dip. Skinner and Clayton (2013) observed that some of the largest features subducting in the Pacific (e.g. the Magellan seamounts, Louisville ridge, Caroline ridge) are not correlated with any lower-angle subducting slab. Moreover, for some flat slab segments (most notably, Mexico, and past subduction below the Altiplano-Puna region) no candidate buoyant features have been identified to explain the anomalous subduction angle (Rosenbaum and Mo, 2011; Skinner and Clayton, 2011). In addition, a number of numerical and analogue subduction models indicate that although the subduction of buoyant features may lead to slab shallowing, by themselves they are insufficient to generate a flat slab (Van Hunen et al., 2002; Martinod et al., 2005; Gerya et al., 2009; Manea et al., 2017).

Several other mechanisms have been suggested to cause or contribute to the formation of flat or low-angle slabs. One mechanism is the active overthrusting of the upper plate, which results in forced trench retreat and can lead to a flat slab if the plate is unable to increase its sinking velocity accordingly (van Hunen et al., 2004; Currie and Beaumont, 2011; Liu and Currie, 2016). Episodes of fast convergence ($>$10 cm/yr; Currie and Beaumont, 2011; Manea et al., 2017) have been proposed to have a similar flattening effect. Suction forces in the mantle wedge, although unlikely to lead to flat subduction on their own, generate an upwards force above the slab and can be enhanced by a higher viscosity mantle wedge or thick (cratonic) upper plate (van Hunen et al., 2004; Manea and Gurnis, 2007; O'Driscoll et al., 2009; Roda et al., 2011; Manea et al., 2012; Taramón et al., 2015; Schellart and Strak, 2021), thus encouraging the evolution from a low-angle to a flat slab. Another mechanism suggested to contribute to low-angle subduction is the presence of buoyant mantle support below the slab, as would be expected from a hot upwelling plume (Bishop et al., 2017; Betts et al., 2009),

or as a result of slab tearing (Liu and Stegman, 2012), although this effect may be relatively small (Schellart, 2020). Finally, it has been suggested that long-lived, very wide subduction zones for which the slab is anchored in the lower mantle, can develop a shallow-dipping segment in their centre (e.g. Farallon plate; Schellart, 2020). Most studies suggest that varying combinations of mechanisms, likely involving buoyant features, may be required to explain the observed range of low-angle and flat slab cases (van Hunen et al., 2004; Skinner and Clayton, 2013; Antonijevic et al., 2015; Hu et al., 2016).

While previous studies have modelled the subduction of buoyant features, the majority have done so in 2-D (e.g. Van Hunen et al., 2002; van Hunen et al., 2004; Gerya et al., 2009; Arrial and Billen, 2013; Schellart and Strak, 2021), which is most appropriate for simulating features with large lateral extent. Of the 3-D studies undertaken, some focus on modelling specific subduction zones (Espurt et al., 2008; Mason et al., 2010; Hu et al., 2016). Only a few, analogue modelling, studies have systematically explored how variations in the shape and position of buoyant features affect subduction dynamics with and without overriding plate (Martinod et al., 2005, 2013; Flórez-Rodríguez et al., 2019). These show that the relative buoyancy of a buoyant feature compared to the rest of the slab affects the extent to which it modulates subduction. Several other numerical 3-D models, which did not include buoyant features, examined how overriding plate thickness (Capitanio et al., 2011; Rodríguez-González et al., 2014b; Manea et al., 2012; Taramón et al., 2015) and the width of the subducting plate (Schellart et al., 2007; Schellart, 2020; Chen et al., 2022b) influence slab dip and can possibly cause flat subduction. In this study, we build on and complement previous work, using 3-D numerical models to investigate the effects of the relative buoyancy of buoyant features and their position along the trench. It is the first study which explores the effect of the age-dependent buoyancy and strength of the background subducting slabs. This study uses fully dynamic numerical simulations to simulate a subset of buoyant features, i.e. elongated, trench-perpendicular buoyant ridges, on single-plate subduction (i.e. 'free subduction') to evaluate effects on trench shape and the slab dip angle. We

find that the different modes of ridge subduction, as discussed in Section 5.5.3, help to explain the different expressions of subducting buoyant features around the Pacific and on the Indo-Australian plate.

5.3 Methods

5.3.1 Modelling system and reference setup

We simulate subduction using Fluidity, an adaptive, unstructured mesh, finite-element, control-volume computational modelling framework (e.g. Wilson, 2009; Davies et al., 2011; Kramer et al., 2012, 2021). We designed a series of models of single 3-D mechanical visco-plastic plates (i.e. 'free-subduction') within a Cartesian domain representing the viscous upper and lower mantle. We use a multi-material approach to distinguish the subducting lithosphere from the mantle, taking the density and viscosity plate to represent the combined impact of the crust and the mantle lithosphere. The modelling system is discussed in further detail in Section 4.3 in Chapter 4.

Our reference young and old 'no-ridge' models (Table 5.1) follow two Cartesian model designs from Chen et al. (2022b) (models W2400_young and W2400_ref, respectively). We use a domain of $4000 \times 2890 \times 4000\,\mathrm{km}^3$ (length$\times$depth$\times$width) to simulate half the subducting plate, assuming symmetry at the centre of the plate along the long axis (Z=0; Fig. 5.1).

We apply a free-surface boundary condition at the top of the domain and free-slip boundary conditions at all other boundaries. The initial half-plate is 2200 km long (in the direction of subduction), 1200 km wide (along strike) and 45 or 70 km thick, for young or old plates, respectively. We limit lateral flow from the mantle to the section below the plate by adding a side plate (Fig. 5.1A) with an initial gap of 22 km away from the edge of the subducting plate (e.g. Holt and Becker, 2017). A 600 km gap was

Model Name	H [km]	W_R [km]	H_C,H_P [km]	$\Delta\rho$ [kg/m^3] Plate-Mantle	Ridge-Plate	Ridge location	B_P [10^{13} N/m]
NR_Old	70	-	30, 20	80	-	-	13.44
HB_C_Old	70	200	30, 20	80	-50	Centre	12.74
LB_C_Old	70	200	30, 20	80	-25	Centre	13.09
LB_S_Old	70	2×200	30, 20	80	-25	Side	12.74
NR_Young	45	-	15, 15	40	-	-	4.32
HB_C_Young	45	200	15, 15	40	-75	Centre	3.65
LB_C_Young	45	200	15, 15	40	-37.5	Centre	3.98
LB_S_Young	45	2×200	15, 15	40	-37.5	Side	3.65

Table 5.1: Parameters for all model cases. H - plate thickness, W_R - ridge width (cases with side ridges effectively contain two symmetrical ridges of this width), H_C - thickness of high-viscosity core, H_P - thickness of visco-plastic layers above and below the plate core, $\Delta\rho$ - excess density of plate or ridge, B_P - buoyancy of the plate per unit length, calculated as $(\Delta\rho_{P\text{-}M} \cdot W_P + \Delta\rho_{R\text{-}P} \cdot W_R) \cdot H \cdot g$, and which is positive in the direction of gravity. Model name abbreviations: NR - no-ridge, HB - high positive buoyancy, LB - low positive buoyancy, C - central ridge, S - side ridge. High and low positive buoyancy refer to ridge buoyancy relative to the rest of the plate. Central and side ridge locations pertain to a ridge at the symmetry boundary or at the centre of the half-plate, respectively (see also Fig. 5.1B). Old and young refer to the age of the plate, which is assumed to affect both density and thickness (and thereby strength and buoyancy) of the plate.

prescribed between the trailing edge of the subducting plate and the domain boundary at X=0. The initial slab morphology follows an arc with a radius of 250 km along the top surface, to a dip of 77° (as in Garel et al., 2014; Suchoy et al., 2021), extending to an initial depth of 200 km (Fig. 5.1B).

The subducting plate is composed of 3 layers with a strong isoviscous core in the centre, and visco-plastic layers at the top and bottom. The core has a viscosity 100 times η_{UM}. The visco-plastic layers have this same initial viscosity, but follow a von Mises yield criterion (e.g. OzBench et al., 2008) so that:

$$\eta_P = \begin{cases} \frac{\tau_{II}}{2 \cdot \dot{\varepsilon}_{II}}, & \text{if } \tau_{II} < \tau_y \\ \frac{\tau_y}{2 \cdot \dot{\varepsilon}_{II}}, & \text{if } \tau_{II} \geq \tau_y \end{cases} \tag{5.1}$$

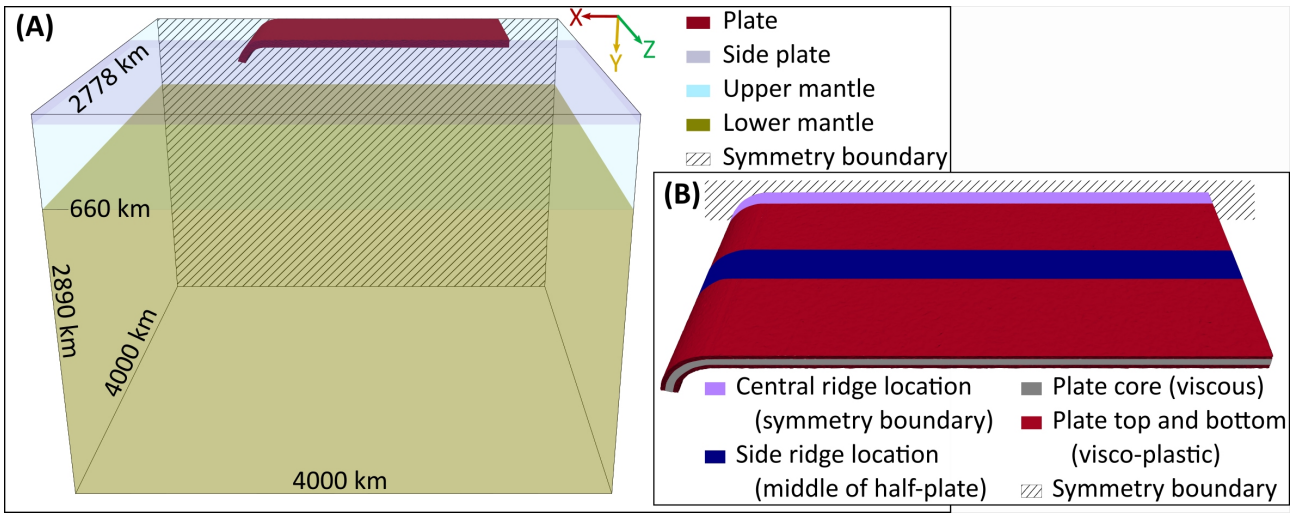


Figure 5.1: Initial conditions of (A) our computational domain and (B) the subducting plate. See text and Table 5.1 and 5.2 for material properties and dimensions. We apply a free-surface boundary condition at the top of the domain, and free-slip boundary conditions elsewhere.

where the second invariant of the stress tensor $\tau_{II} = 2\eta \cdot \dot{\varepsilon}_{II}$, with $\dot{\varepsilon}_{II}$ the second invariant of the strain-rate tensor and τ_y the yield stress. This rheological layering captures the concentration of slab strength in the centre of the dense plate, as expected from temperature and strain-rate dependent mantle rheology (OzBench et al., 2008; Capitanio et al., 2009; Buffett and Becker, 2012). For the old reference plate, the core is 30 km thick and the top and bottom layers are each 20 km thick, while for the young plate each layer is 15 km thick. This results in the old plate being more negatively buoyant and effectively stronger than the young plate. We applied the same density contrast to the full thickness of the plate, i.e. only considering joint buoyancy effects of the crust and mantle lithosphere. The densities and thicknesses of the two background plates yield a range of plate buoyancies similar to that expected for 20 and 120 Myr lithosphere from plate cooling models (e.g. McKenzie et al., 2005). The upper-lower mantle boundary (ULMB) is implemented as a viscosity jump at 660 km depth, with an upper mantle viscosity, η_{UM}, of $2{\cdot}10^{20}$ Pa·s and a lower mantle viscosity, η_{LM}, of $50{\cdot}\eta_{UM}$. The side plate has a viscosity of 1000 times η_{UM}. Material properties common to all simulations are summarised in Table 5.2.

Parameter	Symbol	Value
Gravitational acceleration	g	10 m/s^2
Domain length	L_{dom}	4000 km
Domain width	W_{dom}	4000 km
Domain depth	D_{dom}	2890 km
Plate length	L_{plate}	2200 km
Full plate width	W_{plate}	2400 km
Upper-lower mantle boundary depth	D_{ULMB}	660 km
Initial plate trailing edge distance	L_{te}	600 km
Initial top of slab radius	R_S	250 km
Initial slab maximum angle from horizontal	α_S	77°
Upper mantle viscosity	η_{UM}	$2{\cdot}10^{20}$ Pa·s
Lower mantle viscosity	η_{LM}	$50{\cdot}\ \eta_{UM}$
Plate core viscosity	η_C	$100{\cdot}\ \eta_{UM}$
Side plate viscosity	η_{SP}	$1000{\cdot}\ \eta_{UM}$
Yield stress	τ_y	100 MPa
Mantle density	ρ_m	3300 kg/m^3

Table 5.2: Parameters common to all simulations. Plate length, L_{plate}, is in the direction of subduction and plate width, W_{plate}, is along strike. Note the simulated width is half the full plate width, assuming symmetry at the centre.

5.3.2 Cases with ridges

To examine the effect of buoyant ridges (see Table 5.1), we decrease the density in a trench-perpendicular strip of the subducting plate (Fig. 5.1B). We ran cases with a ridge positioned either at the centre of the plate (i.e. the symmetry edge of the half-plate, at Z=0) or positioned offset from the centre, in the centre of the half plate (initially centred at Z=600 km). The off-centre ridge cases effectively include two ridges (mirrored across the symmetry plane). The distance between these ridges is sufficiently large to allow us to investigate the effect of a single offset ridge. For off-centre ridges, we use a 200 km wide segment. For the central ridges, we use a 100 km wide segment of the plate, to represent half of a 200 km wide symmetrical ridge.

We consider 8 cases (Table 5.1). For each reference plate type (old and young), we ran

a case without any ridges ('NR' or 'no-ridge' models, Table 5.1), as well cases with a central ridge of high and low excess positive buoyancy ('HB' and 'LB' models) relative to the buoyancy of the plate (i.e. counteracting the negative buoyancy of the downgoing plate). We also ran simulations for each plate type with a low positive buoyancy ('LB' cases) ridge at the side of the plate (i.e. at the centre of the half-plate).

We based the properties of ridges in our model on the topography of buoyant ridges on Earth today. Buoyant features in the Pacific and Indian oceans are typically associated with a bathymetric rise of 1-2 km (Table 5.3). Using a typical plate cooling model and assuming isostasy (e.g. McKenzie et al., 2005), such excess topography requires an excess positive buoyancy of between $2.0{\cdot}10^6$ and $4.5{\cdot}10^6$ kg/m^2, irrespective of the age of the background plate. Excess buoyancy can also be calculated from estimates of buoyant feature crustal thickness (following Cloos, 1993; Gutscher et al., 2000b; Rudaviciute, 2015, see Table 5.4). For the shown isostatic calculation, we used a density difference between the lithosphere and the mantle of 77 kg/m^3 and plate thickness of 79 km, typical of 66 Ma plate (following McKenzie et al., 2005). This yields a density difference of 29 and 58 kg/m^3 and excess positive buoyancy of $2.25{\cdot}10^6$ and $4.5{\cdot}10^6$ kg/m^2, for 1 and 2 km rise, respectively, similar to the range of buoyancies estimated using isostasy and plate cooling model above.

Our choice of ridge buoyancies for our high- and low-buoyancy ridge models was based on the calculation above. For our HB cases we used an excess positive buoyancy of $3.5{\cdot}10^6$ kg/m^2, typical of bathymetric rise of 1.5 km. However, we found that this value was already high for our HB_C_Young case and resulted in a ridge which was difficult to subduct using our models. We therefore chose to use an excess positive buoyancy of $1.75{\cdot}10^6$ kg/m^2, typical of bathymetric rise of 0.75 km, for our LB cases to examine the impact of ridges with low positive buoyancy.

To calculate ridge density we distribute the excess positive buoyancy across the 70 km thickness of the 'Old' plate, which yields a density difference of 25 and 50 kg/m^3. For the 45 km thick 'Young' plate models, these same buoyancies yield a density difference

Name	Plate	Surface area [km×km]	Crustal thickness [km]	Rise [km]	Age [Ma]	Reference
Agulhas Plateau	Indian	600×400	20	2.5	100	Parsiegla et al. (2008)
Benham Rise	Philippine	300×400	15	2	48-26	Barretto et al. (2020)
Caribbean Plateau	Caribbean	3500×1000	15-20	-	92-88	Whattam and Stern (2015)
Carnegie Ridge	Cocos (Farallon)	1350×300	19	2	23	Sallarès et al. (2005)
Cocos Ridge	Cocos (Farallon)	1000×250	21	2	25	Walther (2003)
Hess Rise	Pacific	550×1350	15-20	1-2	110-100	Bai et al. (2019)
Manihiki Plateau	Pacific	1000×800	15-25	2-3	125	Timm et al. (2011)
Nazca Ridge	Nazca (Farallon)	1000×200	20	1.5	65	Hampel (2002)
Ninetyeast Ridge	Indo-Australian	5600×200	-	2	77	Krishna et al. (2012)
Ogasawara Plateau	Pacific	300×600	10	2-3	80	Tsuji et al. (2007)
Ontong Java Plateau	Pacific	2300×1100	30	2.5	120	Korenaga (2005)
Roo Rise	Indo-Australian	200×250	11.5	2-2.5	125-155	Kopp et al. (2006)
Shatsky Rise	Pacific	2000×600	30	2-3	128-145	Zhang et al. (2017a)
Tuamotu Plateau	Pacific	1150×1300	21	2-3	50	Patriat et al. (2002)

Table 5.3: Properties of buoyant features in the Pacific and Indian oceans.

of 37.5 kg/m^3 and 75 kg/m^3. The highest positive buoyancy value for the HB_C_Young case results in a ridge which is lighter than the mantle. Our compilation also shows that typical ridge widths are between around 200-300 km (and wider for plateaus and other buoyant features; Table 5.3), i.e. our modelled ridges are on the narrow end of this range.

When calculating subduction diagnostics, the plate-mantle interface was delineated as the iso-surface where the the field of the mantle material volume fraction is 0.5. Snapshots of slab morphologies for all 8 cases, following interaction with the ULMB, are presented in Fig. 5.2. The trench is defined as the front edge of the plate at 20 km depth (Fig. 5.3). We measure the motion and velocity of the trench and the tip of the

	ρ [kg/m^3]	Thickness [km]		
		Plate	1 km rise	2 km rise
Water	1000	2	1	0
Crust	3000	7	13	19
Lithosphere	3377	72	66	60
Asthenosphere	3300	0	1	2
Plate ρ (crust and lithosphere) [kg/m^3]		3344	3315	3286
Ridge-plate $\Delta\rho$ [kg/m^3]			29	58

Table 5.4: Isostatic calculation for 1 and 2 km bathymetric rise for 66 Ma oceanic plate. Plate thickness (lithosphere and crust) assumed to be constant. Lithosphere density and depth following McKenzie et al. (2005). The plate density is the thickness-weighted average density of the crust and lithosphere.

slab at 3 points along strike: 15 km from the symmetry boundary, 50 km from the edge of the plate and at a point half way along the trench (denoted as 'symmetry', 'edge' and 'middle', respectively). The location of the edge and the middle was calculated at each timestep of the simulations to account for temporal changes in trench shape (red diamonds in Fig. 5.3).

5.4 Results

5.4.1 No ridge behaviour

We first discuss the behaviour of the two reference 'no-ridge' models (NR_Old and NR_Young). The evolution of both is consistent with similar 2-D and 3-D models in previous studies (Funiciello et al., 2003a; Schellart, 2005; Capitanio et al., 2007; Stegman et al., 2010b) and includes two phases: initial sinking of the slab through the upper mantle and subsequent interaction of the slab with the lower mantle. We refer to the time of the first slab-ULMB interaction as $t660$.

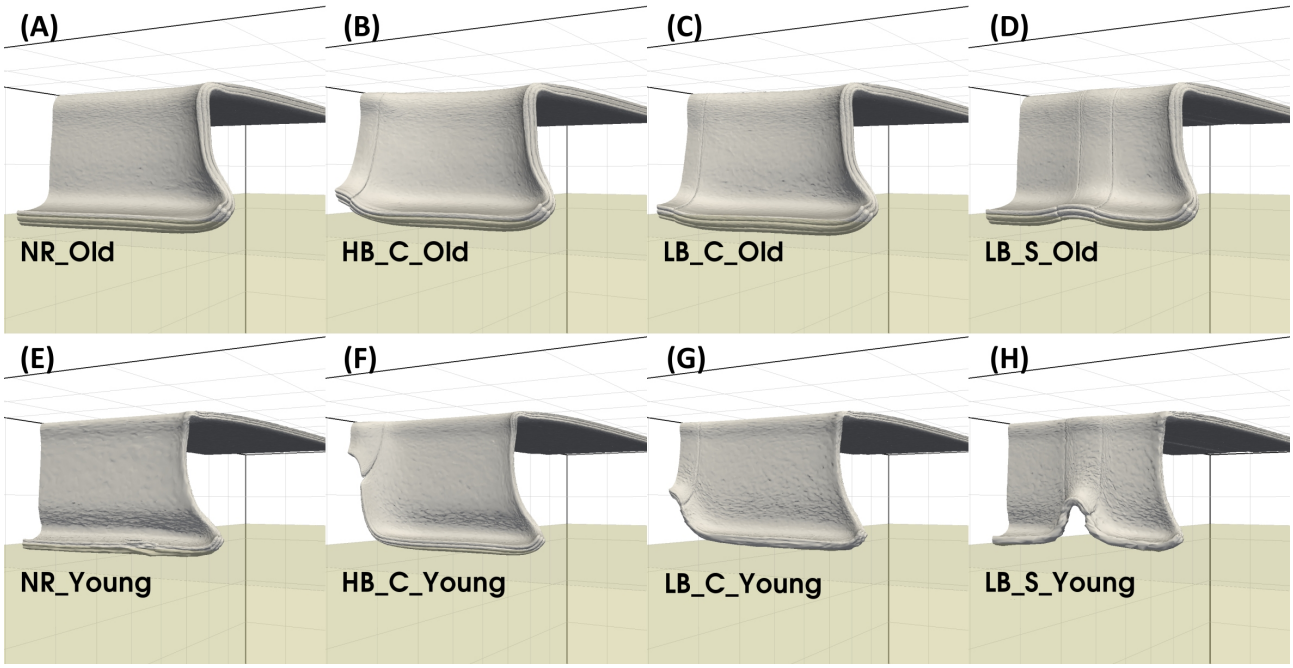


Figure 5.2: Representative slab geometries after plates start interacting with the ULMB for all model cases. Old plate cases are presented in panels (A)-(D) at 10 Myr and young plate cases in panels (E)-(H) at 30 Myr. The lower mantle is depicted by green semi-transparent box. For scale, grey grid cells of 400 km by 400 km are shown on domain boundaries. The ridges are located at the left side (symmetry boundary) of the half-plate in (B)-(C) and (F)-(G) and at the centre of the half-plate (i.e. half way between the symmetry plane and edge of the plate) in (D) and (H).

In case NR_Old, the slab sinks through the upper mantle at an increasing rate, reaching the ULMB after ∼7 Myr (Fig. 5.4A). Over the same period, the trench retreats at rates of between 1 and 3 cm/yr, depending on the position along the trench: the highest rates are at the middle of the half-plate (∼120 km in 7 Myr), with lower rates at the symmetry plane (∼100 km in 7 Myr) and the lowest rate at the slab edge (∼70 km in 7 Myr; Figs. 5.3A and 5.5A). As the slab approaches the ULMB, it flattens due to interaction with the more viscous lower mantle, which reduces the sinking velocity from an average rate of ∼6.5 cm/yr before $t660$ to ∼2.7 cm/yr after $t660$ (Fig. 5.4A). Upon interaction with the ULMB, the trench stagnates and even advances slightly at the edge and at the symmetry boundary (Figs. 5.3A and 5.5A). As a result, the trench develops a 'W'-shape with a stagnation point, where trench motion tends to zero, at the centre (i.e. at the symmetry boundary) surrounded by faster retreating segments, with a maximum in retreat at the middle point of the half-plate (and its symmetrical equivalent).

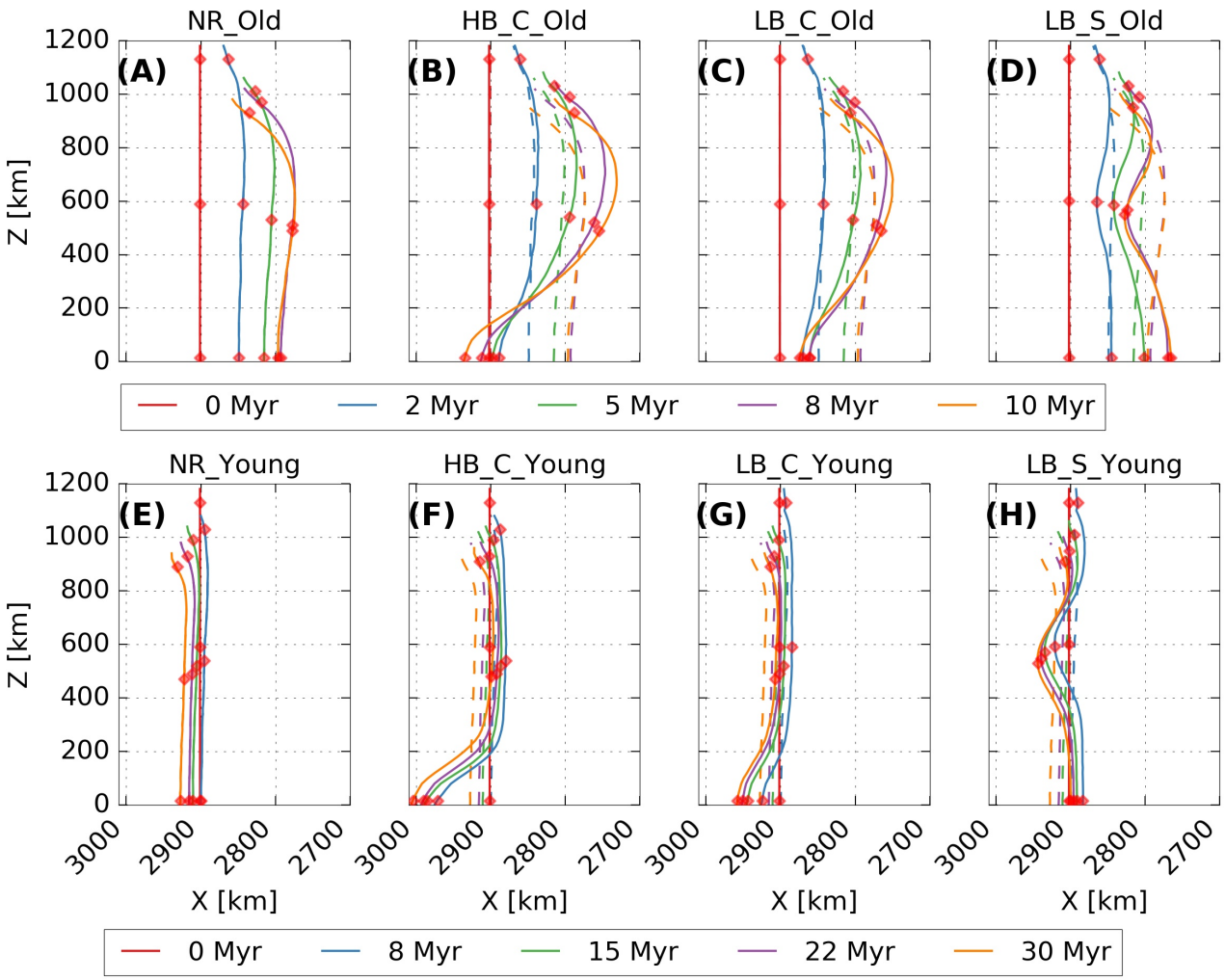


Figure 5.3: Temporal evolution of trench shape, corresponding to the front of the plate measured at 20 km depth, for all models. Dashed lines in panels (B)-(D) and (F)-(H) represent the location of the trench in the corresponding reference models without a ridge (cases NR_Old and NR_Young). Red diamonds mark the location where motion of the trench and slab were measured, with results displayed in Figs. 5.4 and 5.5. Note that the X and Z axes are differently scaled.

In case NR_Young, the slab has less negative buoyancy and, accordingly, sinks at a slower rate of ∼2 cm/yr, reaching the ULMB after 24 Myr. Owing to its reduced thickness, the NR_Young plate is also weaker and, consequently, as the slab approaches the ULMB, it buckles (Fig. 5.2E), as its sinking velocity reduces to ∼0.5 cm/yr (Fig. 5.4E). Both before and after $t660$, the trench slowly advances at a steady rate of 0.1-0.5 cm/yr (Fig. 5.5E). The rate of trench advance is similar everywhere along the trench, resulting in a reasonably straight 'I'-shaped trench (Fig. 5.3E).

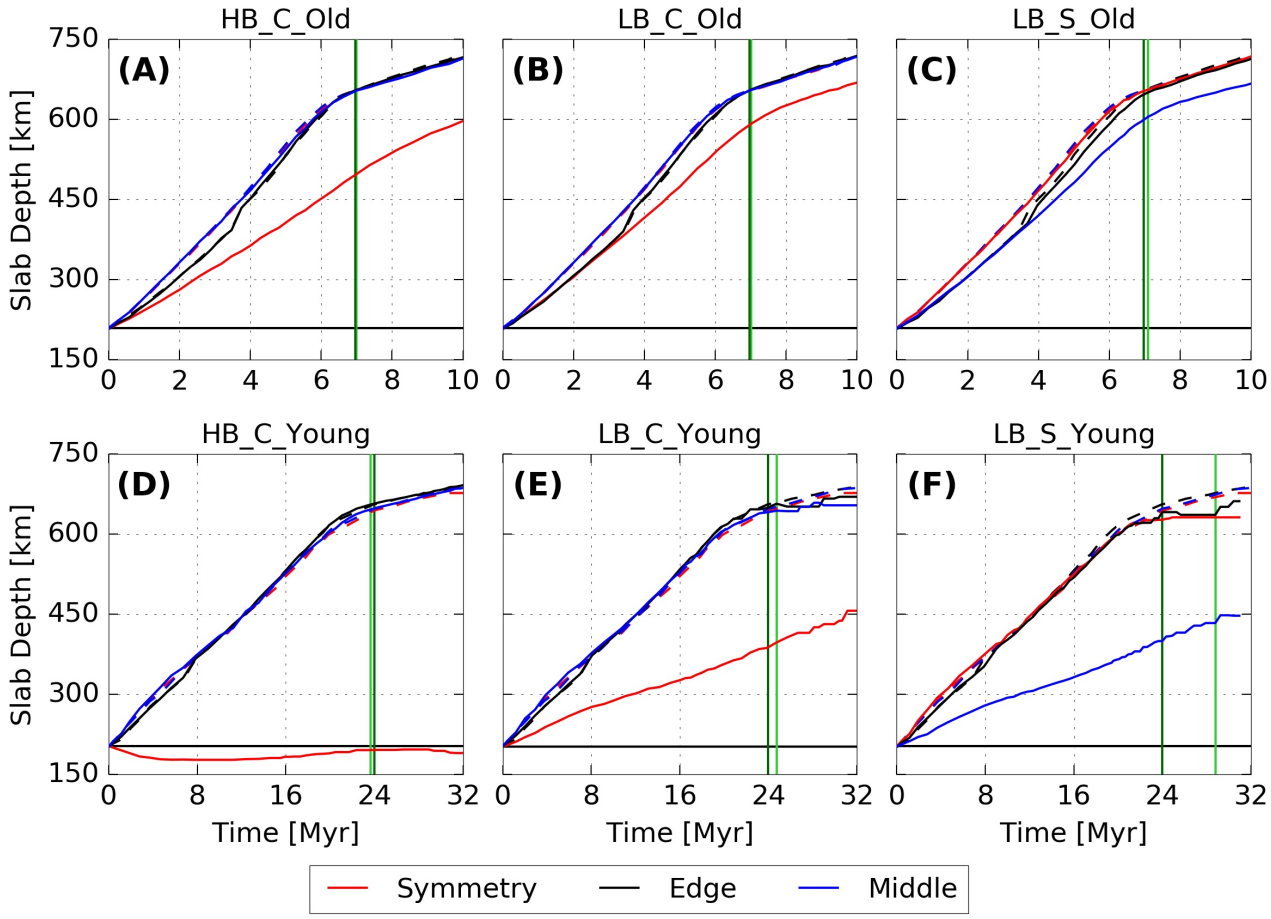


Figure 5.4: Slab depth as a function of time for old plate models in panels (A)-(C) and young plate models in panels (D)-(F). Dashed lines represent motions of the corresponding reference model without a ridge (cases NR_Old and NR_Young). Red lines are for measurements at the symmetry boundary (also ridge location in (A), (B), (D) and (E)), blue lines are for measurements in the middle of the half-plate (also ridge location in (C) and (F)) and black lines for measurements at the edge of the plate. Z-positions (along strike) where sinking was measured are marked on Fig. 5.3. Vertical lines mark the time that the slab reaches ULMB (i.e. $t660$) for the ridge model (light green) and the reference cases (dark green). Solid horizontal black line corresponds to the initial depth of the slab tip at 200 km.

In both the young and old reference models, the shape of the trench is determined by slab-mantle interactions (Schellart et al., 2007). The difference in trench retreat along strike for the old plate is due to return flow caused by slab rollback, which creates toroidal flow cells in the mantle near the edges of the plate. When the toroidal cell is smaller than the width of the half-plate, a stagnation point emerges at the centre of the trench (Schellart et al., 2007; Schellart, 2020). Our reference old plate is wide enough for such a central stagnation point to develop (Chen et al., 2022b), thereby providing

an excellent basis for evaluating the effect of ridge position. Narrower old plates develop a 'C'-shaped trench instead, where the centre of the slab retreats more than its sides. The young plate sinks slower, which provides more time for deformation and bending at the trench. As a result, the young plate sinks almost vertically and drives very little trench motion (e.g. Capitanio et al., 2007). The slight curvature at the edge of the plate is the result of the weak toroidal cell caused by the displacement of mantle material due to plate sinking, and overall the trench stays reasonably straight (Chen et al., 2022b).

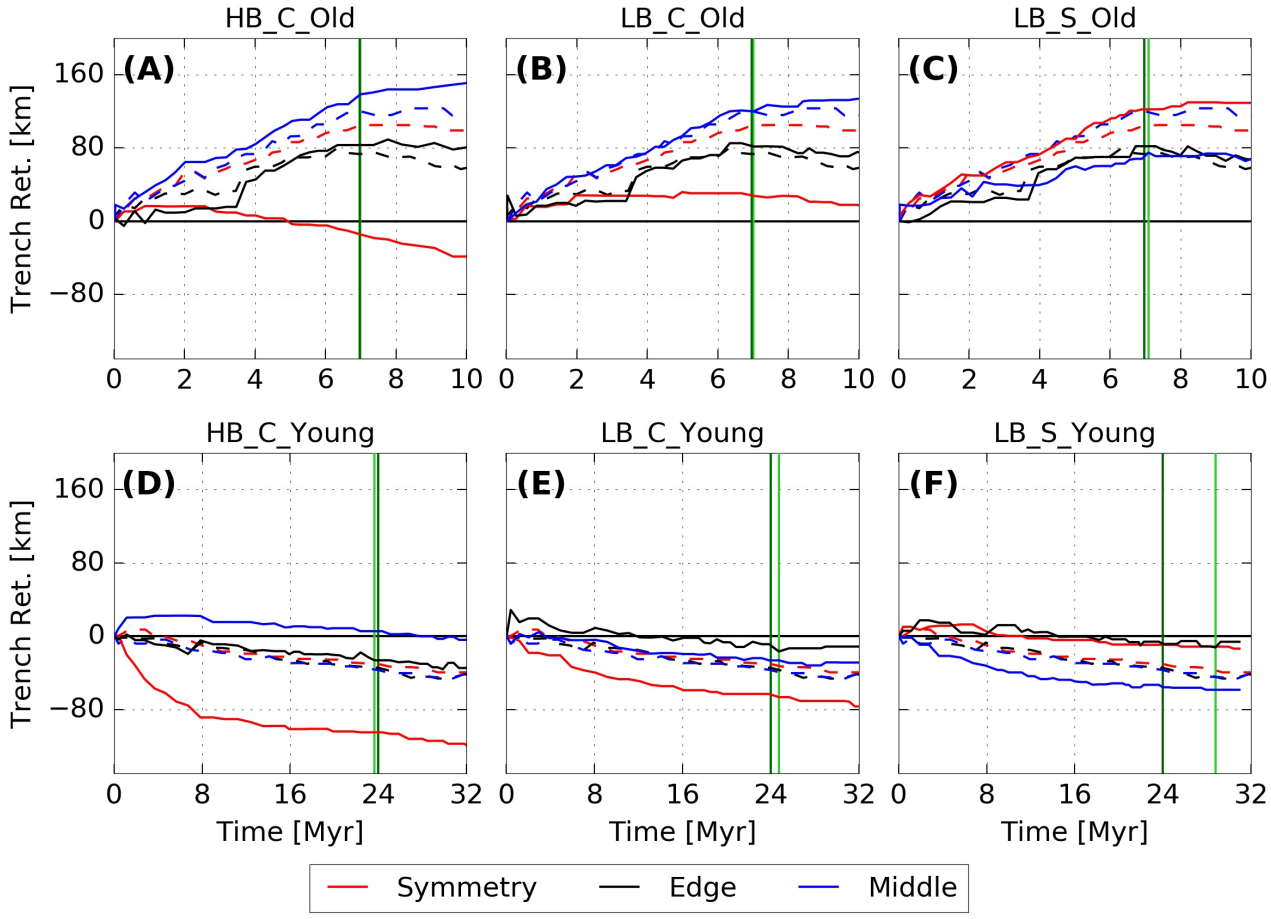


Figure 5.5: Trench motion evolution for old plate models in panels (A)-(C) and young plate models in panels (D)-(F), at the locations marked on Fig. 5.3. Lines styles are as in Fig. 5.4, i.e., solid lines are for the ridge models, and dashed lines for the corresponding reference cases. Vertical lines mark $t660$ for the ridge (light green) and no-ridge (dark green) cases. The initial location of the trench, i.e. 0 km, is marked with solid black horizontal lines.

5.4.2 Ridge buoyancy effects

Next, we examine cases with ridges at the centre of the plate (i.e. at the symmetry plane), with low and high positive buoyancy relative to the downgoing plate: cases HB_C and LB_C. In all cases, the addition of a buoyant ridge results in less trench retreat, or even trench advance, at the location where the ridge intersects with the trench. Compared with the NR_Old reference case, trench retreat at the centre of the plate in case LB_C_Old is reduced from ∼100 km to ∼30 km by $t660$ (Fig. 5.5B), while in case HB_C_Old, the centre of the trench advances ∼15 km by $t660$ (Fig. 5.5A). In the NR_Young reference case, the centre of the trench is already advancing, and the addition of the ridge enhances this advance. For case LB_C_Young, the trench at the centre of the plate advances by ∼70 km by the reference $t660$ compared with ∼30 km in NR_Young case (Fig. 5.5E). For the HB_C_Young case, the trench advances ∼110 km by the reference $t660$ (Fig. 5.5D). In both young and old plate models, trench retreat at locations away from the ridge is increased or trench advance is decreased compared to the corresponding NR case. The hampered motion of the trench at the intersection with the ridge is expected to act as an axis of trench rotation, which is consistent with predictions from models where such motion is possible (i.e. models with full subducting plate and mobile side plates: Mason et al., 2010; Moresi et al., 2014).

The sinking velocity of the slab carrying the ridge is reduced locally due to the added positive buoyancy of the ridge. Particularly in the young plate models, the local plate sinking velocity at the ridge is significantly lower than in the rest of the plate. In model HB_C_Young, the ridge has not sunk at all by the reference $t660$ (Fig. 5.4D). The differential sinking rate in this model is accommodated through thinning of the slab at the ridge-slab intersection, which could facilitate slab tearing under certain rheological parameterisations. In comparison, the less buoyant ridge in model LB_C_Young has sunk ∼200 km, from its initial depth, by the reference $t660$ (Fig. 5.4E). For older plate models, sinking velocity at the ridge deviates less from that in the rest of the plate. The part of the slab with the ridge has sunk ∼300 km for the HB_C_Old case and ∼400 km

for LB_C_Old case (Fig. 5.4A, B). Elsewhere along the slab, the sinking velocity remains similar to the reference case for both young and old plate models.

Previous 2-D models have demonstrated that, in free-subduction, higher slab pull and increased resistance to bending at the trench encourage trench retreat (Capitanio et al., 2007; Ribe, 2010). In our 3-D models, it is the difference between slab pull at the ridge and in the rest of the plate that drives the variable trench retreat, hindered at the ridge and enhanced elsewhere. This differential trench motion increases trench curvature, leading to the formation of a 'W'-shaped trench in the young plate models and a more pronounced 'W'-shape in the old plate, with more retreat at the edge of the plate than at the symmetry boundary (Fig. 5.3B, C, F, G). Due to the low resistance to bending in young plates, such a 'W'-shaped trench is difficult to generate by young plate subduction without along-strike buoyancy variations (Chen et al., 2022b). The differential sinking between the ridge and rest of the plate also creates along-strike tension in the plate. The higher plate strength of the old plates facilitates stress transmission along strike. As a result, old plates can pull the ridge more effectively into the mantle, resulting in less along-strike variations in sinking and a smoother trench and slab shape in comparison to the corresponding young plates with ridges (Figs. 5.2B, C, F, G and 5.3B, C, F, G).

5.4.3 Ridge location effects

We evaluate the impact of ridge location by comparing results from models LB_C and LB_S. As for the models with a central ridge, subduction of a ridge on the side of the plate results in locally reduced trench retreat and, sometimes, induces a small amount of trench advance (Fig. 5.3D, H). Although the side ridge cases effectively contain two ridges, there is no indication from the resulting trench shapes (Fig. 5.3D, H) that there is an interference due to superposition of the influence of the two ridges, so these models can be used to study the effect of the subduction of a ridge offset from the slab

centre.

The along-strike changes in trench motion compared to the reference cases are less for the cases with a side ridge than for the cases with a central ridge. For case LB_S_Old, the reduction in trench retreat by $t660$ is ∼50 km, compared to a reduction of ∼80 km for case LB_C_Old (Fig. 5.5B, C). This is likely because the impact of the ridge in LB_S_Old is concentrated at the point where a ridge-free trench (case NR_Old) would retreat the most. Therefore, in this case, ridge subduction reduces the overall curvature of the trench in comparison to the reference case (Fig. 5.3A, D). For case LB_S_Young, the increase in trench advance relative to case NR_Young by the reference $t660$ is ∼20 km, compared with ∼35 km for case LB_C_Young (Fig. 5.5E, F). All young plate cases with a ridge deform the trench from the straight reference shape of the NR_Young case to a curved trench with a cusp (Fig. 5.3E, G, H).

As for cases with central ridges, the sinking velocity is reduced relative to the corresponding NR cases where the side ridge is subducted. The local reduction in sinking velocity is smaller for the LB_S cases than for the LB_C cases. The ridge in case LB_S_Old has sunk ∼410 km by the reference $t660$, compared with ∼400 km for case LB_C_Old (Fig. 5.4B, C). Similarly, in LB_S_Young, the ridge has subducted ∼70 km deeper by the reference $t660$ than case LB_C_Young at the same time (Fig. 5.4E, F). The side-ridge cases, that effectively contain two ridges, also demonstrate that a subducting buoyant ridge can lower the overall sinking velocity of the plate if the ridge adds enough positive buoyancy. The reduction in overall sinking velocity is small, resulting in a delay of ∼0.2 Myr in $t660$ in model LB_S_Old. In LB_C_Old, where the change in buoyancy is only half of that in the LB_S_Old case, the $t660$ delay is half as small, ∼0.1 Myr. The effect is somewhat larger for the LB_S_Young case, where $t660$ is delayed by ∼5 Myr compared with the reference NR_Young case (Fig. 5.4F).

As in the cases with central ridges, a side ridge's main effect is to locally reduce trench retreat and sinking velocity. These effects are both diminished when the ridge subducts along a part of the trench that is otherwise strongly retreating. When the ridge im-

pacts at the side, the composite trends of the plate's tendency to retreat and the reduced trench retreat of the ridge leads to less along-strike variation in trench shape. The lower amount of along-strike bending in the LB_S cases may explain the slightly higher sinking velocities for the side ridges compared to the central ridges, as less potential energy is lost in plate deformation. Thus, our results imply that ridges that subduct along parts of the trench where trench motion is already hampered by other factors impact subduction more.

5.5 Discussion

5.5.1 Buoyant feature subduction and the morphology of the trench and slab

While 2-D models can elucidate some of the effects of buoyant feature subduction, they overestimate the buoyancy force exerted by the feature, due to the implicit assumption of infinite feature width. The full effects of the subduction of buoyant features of limited along-strike extent can therefore only be investigated using 3-D models.

All our ridge-subduction cases lead to trench deformation, with decreased trench retreat, trench stagnation or increased trench advance where the buoyant ridges subduct. Previous 3-D models that investigated the effect of buoyant feature subduction (Martinod et al., 2005; Mason et al., 2010; Flórez-Rodríguez et al., 2019) also found that trench retreat was impeded where the buoyant feature subducts, leading to differential retreat along strike. This observation was independent of size, shape and orientation and applied to both buoyant ridges and plateaus (Martinod et al., 2005, 2013). The resulting formation of trench cusps can be offset from the position of ridge impact at the trench if the feature subducts obliquely (Martinod et al., 2013). We show that significant trench deformation occurs in both old and young plates. Plate strength

and the relative buoyancy of the ridges compared to the underlying plate determine how pronounced trench deformation is. That is, trenches where a weaker young plate subducts are deformed more locally than those where a stronger old plate subducts, for the same excess ridge buoyancy.

We also find that the position of buoyant ridges along the trench affects the response of the trench and resulting slab morphology. In older plates, ridges near intrinsic trench stagnation points accentuate along-strike variations in trench shape while ridges intersecting the trench at other locations lead to less pronounced curvature. Schellart (2020), in 3-D models without buoyant features, found that the central trench stagnation point can, at a late stage of subduction zone evolution, facilitate local slab shallowing. Our results suggest that the subduction of a buoyant ridge at or near such a stagnation point would further enhance such behaviour. We note that trench stagnation points can also form in response to other factors, for example at the edge of a subducting plate, due to interaction with a side plate or existence of a triple junction, and by interaction with a thick upper plate (Capitanio et al., 2011; Jadamec and Billen, 2012).

Although it is commonly assumed that the subduction of buoyant ridges leads to a decreased slab dip (e.g. Gutscher et al., 2000b), our models display a range of behaviour (Fig. 5.6). In old plate cases (Fig. 5.6A-D), the slab is steepened where the ridge subducts, while the dip of the slab along the rest of the plate is slightly lower than in the reference case without a ridge. Although buoyant ridges act to inhibit sinking, the older subducting plates are sufficiently strong that the pull from the rest of the plate leads to a steeper slab where the buoyant feature enters the subduction zone. In this case, the lowest dips occur where the trench retreats most. In contrast, ridges on young plates develop shallower dip angles than the surrounding plate, and the shallowing is stronger for ridges with a higher positive buoyancy (Fig. 5.6E-H). In these cases, the rest of the plate is weak, and is not negatively buoyant enough to pull down the segment with the ridge. Martinod et al. (2005) found that their slabs shallowed

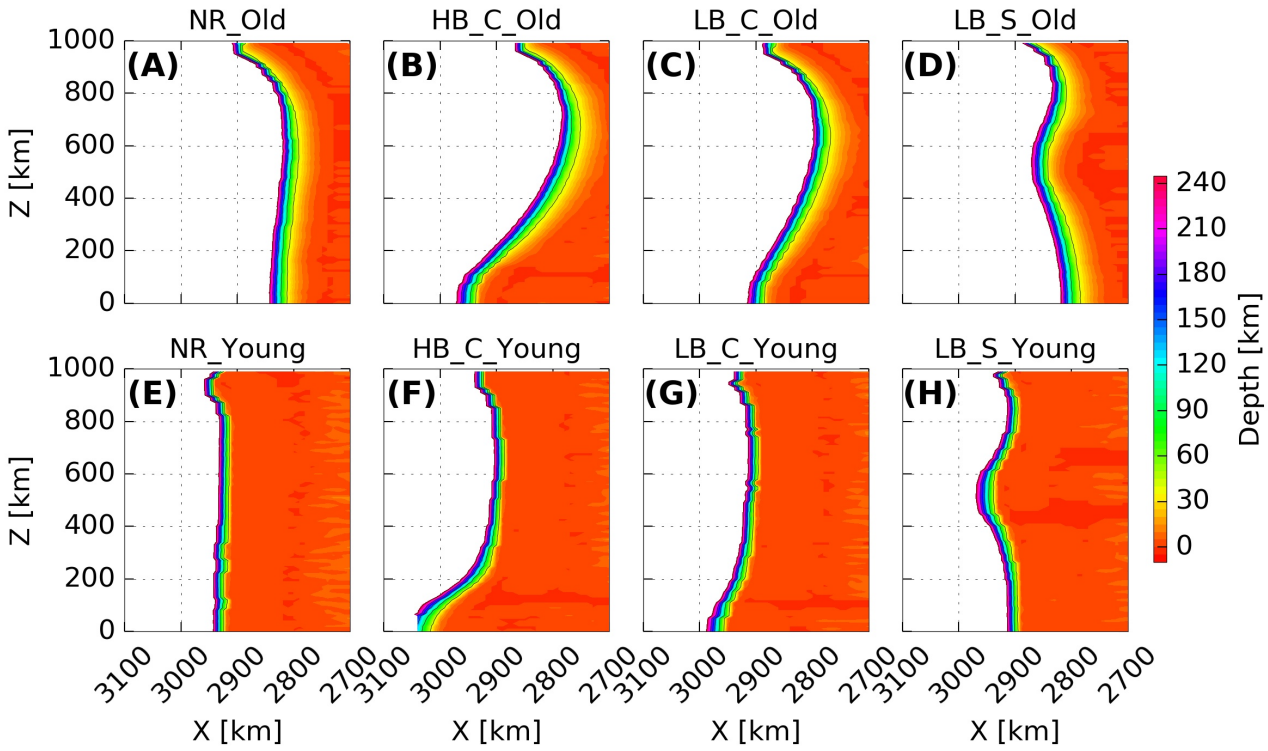


Figure 5.6: Top-down view of final plate top surface depth above 250 km of all models, coloured by depth, thereby providing an illustration of the along-strike variations in slab dip. Note that the X and Z axes are scaled differently.

where the buoyant feature was subducting but steepened below. Flórez-Rodríguez et al. (2019) found yet another variation in their 3-D analogue models of subduction of buoyant ridges on relatively narrow plates, where the slab shallows in the centre of the ridge but steepens on its sides. In a spherical geometry, effective resistance to plate bending at the trench is higher than in equivalent Cartesian plates (Morra et al., 2006; Mahadevan et al., 2010; Chamolly and Ribe, 2021; Chen et al., 2022b). Models of spherical plates display trench and slab deformation in response to along-strike variations in slab buoyancy comparable to Cartesian models (Morra et al., 2006), and are therefore likely to respond to subduction of buoyant ridge similarly. The differences in model behaviour illustrate that the effect of buoyant features on slab dip varies depending on plate strength and relative feature buoyancy, and a range of responses are possible.

5.5.2 Buoyant ridges and low-angle subduction

Our results confirm that ridge subduction alone is insufficient to generate a flat slab, a finding that is consistent with other 3-D free-subduction models (Martinod et al., 2005; Flórez-Rodríguez et al., 2019). Even in 2-D models (van Hunen et al., 2004; Gerya et al., 2009), where the buoyant features are essentially infinite in their along-strike dimension, the subduction of buoyant features alone does not generate a fully flattened slab. Instead, a number of studies have now confirmed that slab flattening requires additional mechanisms such as an upper plate that (by external forcing) overrides the lower plate faster than it can subduct (Van Hunen et al., 2002; Arcay et al., 2008; Currie and Beaumont, 2011; Martinod et al., 2013; Liu and Currie, 2016) or a thick upper plate that generates an upward suction force in the relatively high viscosity mantle wedge, which can pull a shallow-angle slab into a flat-slab geometry (Gerya et al., 2009; O'Driscoll et al., 2009; Manea et al., 2012; Rodríguez-González et al., 2012, 2014b; Taramón et al., 2015; Schellart and Strak, 2021).

While upper plate forcing or thickness can result in a flat slab in the absence of buoyant feature subduction, these mechanisms have clear limitations (Hu et al., 2016). Overthrusting requires a highly forced upper plate velocity (3-5 cm/yr, e.g. van Hunen et al., 2004; Currie and Beaumont, 2011) and would usually apply to the entire upper plate, failing to localise flat subduction in bounded regions of several hundred kilometres, as is observed on Earth at present. A similar issue arises for a thickened upper plate which needs to be of a craton-like thickness (O'Driscoll et al., 2009; Manea et al., 2012; Taramón et al., 2015). While cratons comprise limited parts of the upper plate (e.g. Wyoming Craton in North America; Amazonia Craton in South America), they extend over scales of 1000 kilometres (e.g. Kusky et al., 2014, and references therein) and, therefore, can only explain very wide flat slabs. Conversely, modelling studies demonstrate that the subduction of buoyant features can aid flat slab formation, by locally reducing trench motion and slab dip (van Hunen et al., 2004; Gerya et al., 2009; Martinod et al., 2013). Thus the contribution of buoyant ridge subduction can help to

explain the limited lateral extent and temporal duration of flat slabs.

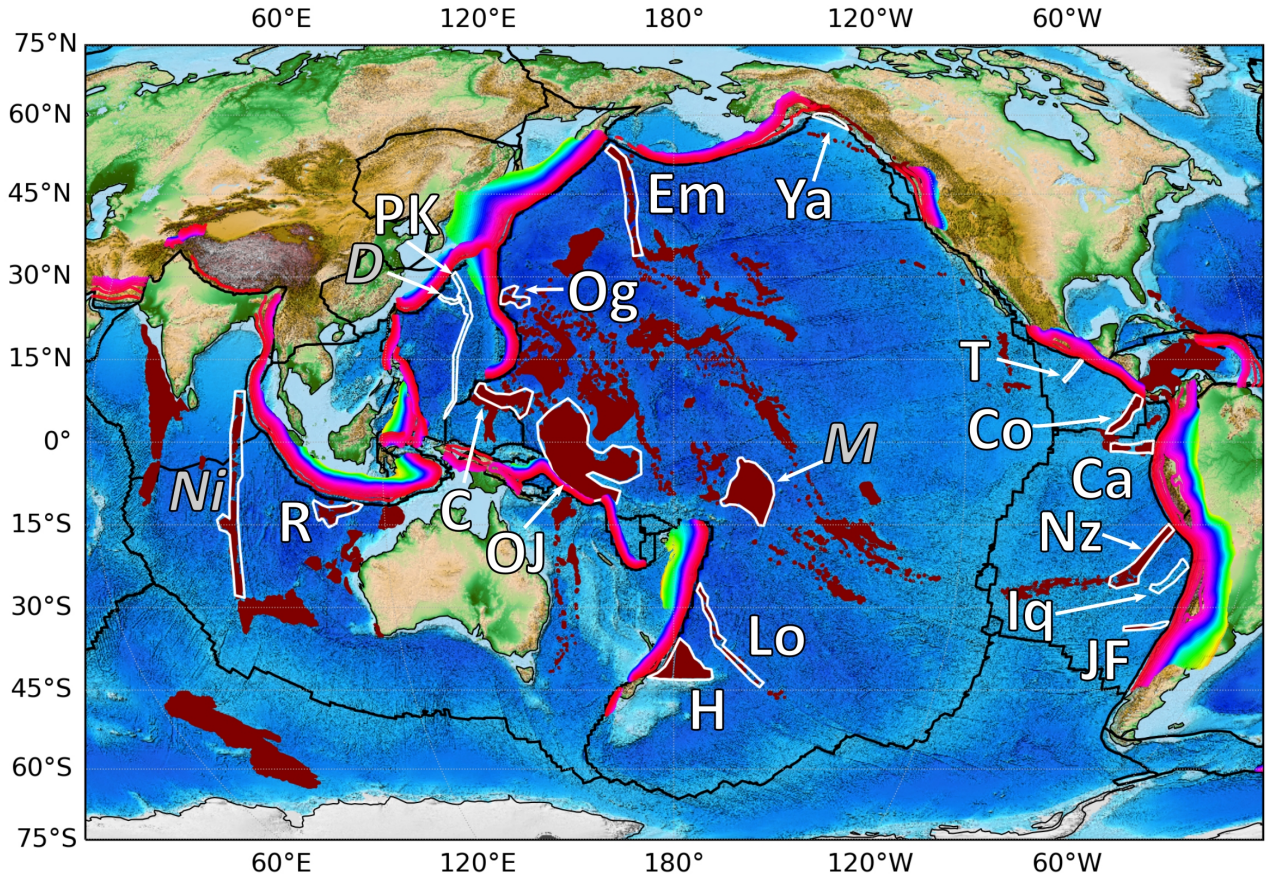


Figure 5.7: Map of buoyant features (white outlined polygons) interacting with subduction zones in the Pacific and Indian oceans. Maroon surfaces indicate oceanic large igneous provinces (LIPs) and volcanic island chains. Slab depth contours are marked in RBG colours. Black lines indicate plate boundaries. Abbreviations for buoyant features discussed in the main text (white text): C - Caroline ridge, Ca - Carnegie ridge, Co - Cocos ridge, Em - Emperor ridge, H - Hikurangi plateau, Iq - Iquique ridge, JF - Juan-Fernandez ridge, Lo - Louisville ridge, Nz - Nazca ridge, OJ - Ontong Java plateau, Og - Ogasawara plateau, PK - Palau-Kyushu ridge, R - Roo rise, T - Tehuantepec ridge, Ya - Yakutat block. Other features (italic grey text): D - Daito ridge, M - Manihiki plateau, Ni - Ninetyeast ridge. Data from Coffin et al. (2006); Skinner and Clayton (2011); Tetreault and Buiter (2014), plate boundaries after Bird (2003), bathymetric data from Amante and Eakins (2008) and slab depth data from Hayes et al. (2018).

5.5.3 Buoyant feature subduction styles on Earth

Together with published dynamic models, our results illustrate a number of different responses to buoyant feature subduction, both ridges and plateaus, are possible.

These include three types: (1) a 'trench deforming' response is an end-member in which subduction of a buoyant feature mainly deforms the trench with minor slab steepening or contortion. Our results demonstrate that this occurs when the positive buoyancy force of a buoyant ridge is low compared with overall plate strength. The upper plate in a 'trench deforming' subduction style is typically thin or weak and therefore does not impede trench deformation; (2) a 'slab deforming' response, in which subduction of the buoyant feature reduces slab dip locally whilst also deforming the trench. This happens when the buoyancy force associated with the feature is strong enough to locally decrease slab dip while any forcing by the upper plate does not play a significant role; (3) a 'slab flattening' response, an end-member in which the slab is flattened at shallow depth over a distance of up to several hundred kilometres. This response occurs when the positive buoyancy of a feature is substantial, and it subducts under a thick, possibly advancing, upper plate. Observations of buoyant features subducting at the plate boundaries of the Pacific and Indian Oceans reflect these different expressions (see Fig. 5.7 and Table 5.5), although many subduction zones do have additional complexities.

The best example of 'trench-deforming' buoyant-feature subduction occurs along the Izu-Bonin-Mariana (IBM) system. The two main buoyant features interacting with the IBM subduction system and impeding retreat of the Mariana trench are both located near major cusps (i.e. the Caroline ridge near the Mariana-Yap junction and the Ogasawara ridge near Bonin-Mariana junction) and these cusps are inferred to have developed when these buoyant features began interacting with the trench (Miller et al., 2006a,c; Seton et al., 2012; Xia et al., 2020). The slab below the Ogasawara Plateau is slightly steeper than adjacent slab segments subducting north and south of it (Miller et al., 2006c; Hayes et al., 2018). The Caroline Island Ridge at the southern end of Mariana is located at a clear cusp where it has reduced convergence velocity significantly and blocked subduction (Miller et al., 2006a; Xia et al., 2021). The slab on the side of the Caroline Ridge, subducting below the southern Mariana trench (Miller et al., 2006a; Zhu et al., 2019) is steep, while the part of the slab along the Yap trench may have de-

Name	Slab shape affected	Trench deforming	Upper plate type	Subducting plate age	Comments
Hikurangi Plateau	Dip decreased above 100 km and increased below 100 km[1,2]	Yes[13,14]	Continental	Old	Near slab edge[1]
Louisville Ridge	Minor shallow dip decrease, deep contortion[1,3]	Minor[13]	Island arc	Old	Oblique sub.[3]
Ontong Java Plateau	Unsubductable[4]	Yes[4,14]	Island arc	Old	Collision resulted in subduction polarity reversal[4]
Caroline Ridge	Not subducting, S. Mariana slab steepened[5]	Yes[5]	Island arc	Old	Collison with the Yap Arc at $\sim$20 Ma[20]
Ogasawara Plateau	Slab steepened and deformed[6]	Yes[6]	Island arc	Old	
Palau-Kyushu Ridge	Dip decreased north of ridge[1,7]	Minor[14]	Island arc	Young	Near the Boso triple junction and possible slab tear[7]
Emperor Ridge	Dip decreased[1,8]	Yes[15]	Island arc or Young oceanic	Old	Near possible slab tear[8]
Yakutat Block	Flat slab[1,9]	Yes[14]	Continental	Young	Near slab edge[1]
Tehuantepec Ridge	Flat slab[1]	Minor[16]	Continental	Young	Flat slab segment much bigger than ridge[1]
Cocos Ridge	Dip decreased significantly[10]	Minor[10]	Continental	Young	Near slab edge[1]
Carnegie Ridge	Flat slab[1,11]	Unknown	Continental	Young	Near slab edge and near the northern end of the Peruvian flat slab[1]
Nazca Ridge	Flat slab[1,11]	No[1]	Continental	Moderate	Near the southern end of the Peruvian flat slab[11]
Iquique Ridge	No effect[1]	Unknown	Continental	Moderate	
Juan-Fernandez Ridge	Flat slab[1,11]	No[1]	Continental	Moderate	
Roo Rise	Not yet subducted[1,12]	Minor[17,18]	Island arc	Old	Previous sub. of similar features implicated in slab tear[12]
Investigator Frac. Zone and Wharton Ridge	Minor local shallowing and slab contortion[1]	Minor[19]	Island Arc	Moderate	Near possible slab tear[19]

Table 5.5: Properties of buoyant features discussed in the main text. Superscripts refer to information source: 1 - Hayes et al. (2018), 2 - Reyners et al. (2011), 3 - Bonnardot et al. (2007), 4 - Mann and Taira (2004), 5 - Miller et al. (2006a), 6 - Miller et al. (2006c), 7 - Xia et al. (2021), 8 - Davaille and Lees (2004), 9 - Gulick et al. (2007), 10 - Morell (2015), 11 - Gutscher et al. (2000b), 12 - Hall and Spakman (2015), 13 - Schellart and Spakman (2012), 14 - Seton et al. (2012), 15 - Rosenbaum and Mo (2011), 16 - Suárez (2021), 17 - Kopp et al. (2006), 18 - Shulgin et al. (2011), 19 - Jacob et al. (2014), 20 - Lee (2004)

tached in response to impingement of the Caroline Ridge (Zhang and Zhang, 2020). Another example of 'trench-deforming' buoyant-feature subduction is at the southern end of the Tonga trench, where the Hikurangi Plateau appears to have served as a pivot for the rotation and migration of the Tonga-Kermadec system (Schellart and Spakman, 2012; Seton et al., 2012). Although there is some shallowing of the Hikurangi-southern Kermedec slab above 100 km, this shallowing occurs mainly north of the plateau, while below 100 km depth, the slab is steeper than further north (Reyners et al., 2011; Hayes et al., 2018). These examples all display the expected behaviour for old plates with sufficient slab pull to carry buoyant features into the trench. Rosenbaum and Mo (2011) previously noted that this behaviour is typical of the western Pacific, where subduction of buoyant features often leads to locally hampered trench retreat and to slab steepening rather than slab shallowing.

Several other buoyant features in the Pacific and Indian Oceans are associated with 'slab deforming' subduction, in which both a cusp in the trench and local shallowing of the slab dip is observed. Some cases correspond to smaller features on plates of young or intermediate age (as in our young plate models), and others to larger features on older plates (similar to the models of Flórez-Rodríguez et al., 2019). The most straightforward example of 'slab deforming' buoyant-feature subduction may be the Cocos ridge, which coincides with a cusp and shallowing of the slab (Morell, 2015). Subduction of the Louisville Ridge below the Tonga trench introduces a minor cusp and some slab shallowing and contortion along the downdip projection of the obliquely subducting ridge (Bonnardot et al., 2007; Hayes et al., 2018). The Tonga-Kermadec trench is of moderate length, and might be expected to evolve to a 'C' shaped trench (Schellart et al., 2007). However, the present-day shape of the Tonga-Kermadec trench is relatively straight, which may be due to early interaction between the middle of the trench, where it would have had the largest curvature, and the Louisville Ridge. This process would also account for the small size of the observed cusp where the ridge currently interacts with the Tonga-Kermadec trench. The cusp between the Japan and Kurile trench near Hokkaido is also associated with shallow slab below the island (Miller

et al., 2006b; Kennett and Furumura, 2010; Hayes et al., 2018). Although there is no buoyant feature evident on the incoming plate, it has all the signatures of a recently subducted feature.

The interaction of the Ontong Java Plateau (OJP) with the South Pacific Trench is probably an extreme example of 'slab deforming' style of interaction. The OJP separated from the Hikurangi plateau at ∼120 Myr and from the Manihiki plateau at ∼100 Myr (Taylor, 2006; Chandler et al., 2012; Seton et al., 2012) to reach the South Pacific trench at ∼20 Myr (Mann and Taira, 2004; Seton et al., 2012). The impinging of the OJP on the trench hampered trench retreat and deformed the trench which, until that time, had a typical concave shape similar to the present-day Japan trench (Mann and Taira, 2004; Seton et al., 2012). The large extent of the OJP made it too buoyant to subduct, perhaps acting similarly to the ridge in model HB_C_Young. As a result, subduction in the region ceased and eventually reversed polarity (Mann and Taira, 2004).

Slab deformation due to buoyant-feature subduction may expose parts of the slab to increased stresses, which result in slab tears (e.g. models by Mason et al., 2010). This may be the case for the subduction of the Emperor ridge at the cusp between the Kamchatka and Aleutian trench, which is associated with a low slab dip angle and a possible tear (Davaille and Lees, 2004). However, this cusp may predate subduction of the Emperor chain (Seton et al., 2012), and its formation may instead have been associated with the subduction of previous, arc-related, buoyant features (e.g. Vaes et al., 2019). Another example is the Palau-Kyushu ridge, located at the cusp between the Ryukyu and Nankai trenches, which has been proposed to contribute to shallow subduction along Nankai trench, possibly with a tear near the subducting ridge (Wu et al., 2016; Pownall et al., 2017; Xia et al., 2021). The low dip of the Nankai slab may also be affected by the fact that its northern end lies at the Boso triple junction, where trench motion is limited by interaction between the Nankai, Izu and Japan trenches. In the Indian ocean, subduction of the Investigator Fracture Zone and the extinct Wharton spreading ridge coincide with a cusp in the Sumatra trench, a local slab 'kink' and

possible slab tear (Hall and Spakman, 2015). The excess buoyancy is likely due to subduction of the Wharton ridge, as oceanic fracture zones like Investigator are not usually associated with changes to plate buoyancy (e.g. Jacob et al., 2014). Along the Java trench, where the Roo rise is starting to deform the trench (Kopp et al., 2006; Shulgin et al., 2011), it has been suggested that past subduction of similar buoyant features is responsible for a slab tear within the Java slab (Hall and Spakman, 2015).

Flat subduction is currently observed in several subduction zones in the Eastern Pacific, under Alaska, Mexico, and South America. In all cases, the strong westward motion of the Americas over the subducting Pacific, Cocos and Nazca plates may facilitate slab flattening (Van Hunen et al., 2002; Manea et al., 2017). In Alaska, the subduction of the Yakutat terrane occurs at a major cusp at the eastern end of the Aleutian trench and is associated with subduction of a narrow flat slab segment (Gulick et al., 2007). The Yakutat terrane subducts under a continental plate, although not of cratonic thickness, with a possible tear on the side (e.g. Daly et al., 2021). In South America, the Ecuador-Peru flat slab is associated with the subduction of the Carnegie and Nazca Ridges (which bound it from north and south) and the Chilean flat slab is associated with subduction of the Juan-Fernandez Ridge (Gutscher et al., 1999, 2000b; Skinner and Clayton, 2013; Kumar et al., 2016; Bishop et al., 2017; Manea et al., 2017). The upper South American plate comprises several old platforms which may all have had thick roots, although not all persist to the present day (Feng et al., 2007). Although the Carnegie ridge interacts with the edge of the trench, where the trench motion is expected to be limited (Schellart et al., 2007), the associated Ecuador-Peru flat slab is located closer to the centre of the trench, as is the Chilean flat slab. Below the major cusp in the Andean trench, at the Bolivian Orocline, the slab is relatively steep. Although the cusp is in front of the subducting Iquique Ridge at present, it was formed before the arrival of the ridge to the trench, at 40-25 Ma (Allmendinger et al., 1997; Schepers et al., 2017). It may have formed above a previous flat slab segment which has been proposed to have existed between 40-20 Ma (Ramos and Folguera, 2009; Skinner and Clayton, 2013). A previously subducted buoyant feature may have formed the older

flat slab and, aided by its location close to the centre of a long trench, have induced slab flattening. Capitanio et al. (2011) proposed that, in contrast to most trenches whose shape appears to be determined by subducting plate forcing, the recent (<20 Ma) rise of the Andes and corresponding shape of the South American trench may be controlled by variations in thickness of the upper plate. Finally, flat subduction below Mexico is generally thought to be too wide to be induced by the buoyant Tehuantepec ridge that subducts at its southern end (Gutscher et al., 2000b; Skinner and Clayton, 2011). Factors that may contribute to the formation of the Mexican flat slab include the subduction of a spreading ridge near the northern end of the plateau, a continental overriding plate, and the flat slab location just north of the boundary between the North and South American plates, where shearing due to differential movement between the Americas may result in fast moving upper plate over slow and young subducting plate.

5.6 Conclusions

We performed a set of 3-D multi-material numerical models of free subduction carrying a buoyant ridge, to investigate the role of plate age, ridge buoyancy and ridge location on trench shape and slab morphology for lower-plate controlled subduction (i.e. cases where the upper plate is young, thin or weak). Our models are the first to illustrate systematically that age-dependent slab density and viscosity can lead to different expressions of the subduction of buoyant features.

Our old-plate cases with buoyant ridges induce significant trench deformation and some steepening (rather than shallowing) of the dip angle of the subducting slab at the ridge. A similar type of 'trench-deforming' response is observed in several Western Pacific subduction zones (e.g. Ogasawara Plateau on the old Pacific plate). Our young-plate cases with buoyant features generate both trench deformation and local shallowing of the subducting plate. This style of 'slab-deforming' response is observed

at several other locations around the Pacific, where the buoyant features are substantial enough that the background plate's pull and strength is insufficient to override the effect of local buoyancy (e.g. Cocos Ridge on the young Cocos plate). Finally, the position of the buoyant features relative to the natural slab shape, which is governed by slab width (Schellart et al., 2007; Schellart, 2020), may lead to a stronger or more subdued expression of ridge subduction. For example, the subduction of the Louisville ridge near the centre of the Tonga-Kermadec trench may explain the relatively mild expression of this ridge in slab dip and the relative straightness of the Tonga trench.

Our results, considered alongside previously published 3-D models that investigated other combinations of subducting plate buoyancy, strength and width, as well as buoyant features of various sizes and densities (Martinod et al., 2005; Mason et al., 2010; Flórez-Rodríguez et al., 2019), illustrate that a range of responses are possible for different subducting plate ages, and it is not expected that all subducting features lead to a shallowing of slab dip (Rosenbaum and Mo, 2011; Skinner and Clayton, 2011). Other studies have shown that the upper plate, if comprised of sufficiently thick continental lithosphere, can lead to further modulation of the expressions of buoyant feature subduction including the formation of flat slab segments (Manea et al., 2012; Rodríguez-González et al., 2012; Taramón et al., 2015). Our results suggest that buoyant features can play an important and varied role in shaping subduction dynamics and, particularly, on the evolution of plate boundaries, where local hampering of trench motion can induce boundary rotations and segmentation.

Chapter 6

Conclusions

6.1 Overview

In this dissertation, I examined how several of the key properties of the plate and underlying mantle contribute to global subduction variability. I used 2-D and 3-D numerical models as well as reconstructed plate age and velocity data to examine this question. I first examined how subduction variability is expressed in age and velocity trends along the evolving global trench system in two different plate reconstruction models. I then focused my investigation on the effects that plate size has on subduction dynamics in 2-D thermo-mechanical models. I also explored how the choice of a set of buoyancy and strength parameters for the plate, within the range observed on Earth, can modify the observed subduction mode in 3-D mechanical models. I built upon these results to examine, in 3-D, the impact of the location and buoyancy of buoyant features carried by either old or young subducting plates, on the evolution of trench and slab shape. Together these studies shed new light on some of the main mechanisms behind the large diversity of subduction behaviour observed on Earth.

In Chapter 2, I examined the variability in subduction parameters in a global compilation of subduction zone parameters based on the GPlates models of Müller et al.

(2016b) and Müller et al. (2019) for the past 120 Myr. This compilation illustrates how age and velocity of the subducting plate at the trench changed both spatially, between different subduction zones, and temporally, at the same trench. It also highlights differences between small and large subduction zones, with the behaviour of the latter somewhat correlated with the properties of the subducting plate, and the former more impacted by external factors such as the motion of adjacent plates. The variation in subduction parameters appears to be bounded in a limited range. I found that the overall majority, 74% of the sampled points, move in a direction close to normal to the trench (within 45° to trench normal). Of the points where subduction occurs within 60° of the trench normal, 76-85% display trench retreat, emphasising how local slab pull controls subduction dynamics, in particular for large trenches. Where large plates subduct in the Pacific and Indian Oceans during the Cenozoic, I found that trench motion ranged from minor advance (1 cm/yr) to mild retreat (5 cm/yr). This observation of relatively small trench motion forms part of the motivation for the models and analysis in Chapter 3. The discussion of the evolution of different subduction zones indicates that some are mostly impacted by local subducting-plate properties, while others are influenced by along-strike variations in properties e.g. due to buoyant features on the subducting plate, and a third group seems significantly affected by external forces that are likely the result of feedback between different plates and global-scale mantle flow. The effect of local plate properties is discussed in Chapter 4 and that of buoyant features was analysed further in Chapter 5

In Chapter 3, I analysed how one force, the drag of the mantle at the base of the plate (i.e. 'basal drag'), can impact subducting plate velocity. Observations of the relative small contribution of trench motions to plate convergence, and the presence of both trench advance and trench retreat has previously been proposed to be caused by low basal drag (Billen and Arredondo, 2018). A low contribution of basal drag has also been suggested to cause the absence of a trend between plate size and plate velocity in subduction models and on Earth (e.g Conrad and Hager, 1999; Billen and Arredondo, 2018; Wolf and Huismans, 2019). In contrast, several global mantle flow models indi-

cate that there is a large contribution of basal drag in determining global plate motion patterns (e.g. Conrad and Lithgow-Bertelloni, 2006). In this chapter, I showed how, in 2-D models of single subduction zone with non-linear rheology, which produced a low-viscosity asthenosphere (and hence relatively low drag), trench motions are indeed low. However at the same time, in our models, long plates were consistently subducting at a lower rate than short plates. This effect only diminished, although not completely, in models with plate strength at a value near or above what is considered an upper bound for subducting plates on Earth. When re-analysing observations on Earth at the present-day and through the Cenozoic, I found that there is covariance of plate size and age, and as a result, there was no observed trend of increased velocity with plate age or decreased velocity with plate size. Rather than indicating a minor role of basal drag, the absence of these trends means that significant resistance of basal drag to plate motion (for larger plates), is likely balanced by an increased driving force, through older and more negatively buoyant slabs. My models with low-viscosity asthenosphere of 10^{19}–10^{21} thus reconcile low trench motions with a significant role of basal drag.

Variations in subducting-plate parameters have been proposed to explain at least some of the observed subduction variability (e.g. Capitanio et al., 2007; Funiciello et al., 2008). In Chapter 4, I explored the variability of behaviour in subduction models, for the purpose of finding an Earth-like set of model parameters for Chapter 5. Studies of previous subduction models of a single plate into the mantle (i.e. 'free subduction') have observed contradictory changes in behaviour in response to changes to plate density, strength and width. My 3-D mechanical models of free subduction indicate how these contradicting behaviours are linked to the dominant resistive force in the reference model. Increased trench advance with increased plate viscosity or increased trench retreat with reduced plate density were both found in models where the main resistive force is the resistance to bending of the plate (called 'bending' regime), while the opposite trends occur in models where subduction is mainly resisted by the viscous resistance of the mantle to plate sinking (i.e. 'sinking' regime). While both types

of behaviour are possible in subduction models, observations of slab shapes and subduction parameter trends on Earth show that the overall majority of subducting plates are in the sinking regime. To achieve this behaviour in 3-D subduction models, I further examined a set of models where plate strength is concentrated in a thin core. The use of such rheologically layered plates with Earth-like density and thickness, together with an extended model domain to include a high-viscosity penetrable lower mantle, resulted in similar behaviour as observed on Earth. This design was then use for the models in Chapter 5.

In the study in Chapter 5, I investigated how subduction of buoyant features (ridges and plateaus) impacts subduction dynamics. Such features are common on all the major subducting plates on Earth, but so far had not been studied much using 3-D subduction models. I explored how the buoyancy and location of an elongated ridge modify trench shape and slab dip when included in either a young or old subducting plate. While some previous studies indicated that buoyant feature subduction is likely to cause slab shallowing, I found that in the models of old plates (which are strong and have a high negative buoyancy) subduction of buoyant features causes steepening above 250 km as well as significant trench deformation. In models of young plates, slab shallowing together with trench deformation are observed near the location of the buoyant feature. In combining the results of the models with observations of the subduction of buoyant features on Earth, I observed three distinct buoyant-feature subduction regimes. The first 'trench deforming' regime, deforms the trench accompanied by minor slab steepening or contortion and is typical of old subducting plates carrying buoyant features that have a relatively low positive buoyancy force, under thin overriding oceanic plates. The second 'slab deforming' regime, results in local reduction of the slab dip angle and deformation of the trench, and is associated with the subduction of buoyant features with an intermediate to strong positive buoyancy force relative to the underlying plate, below a weak or thin upper plate. In the third 'slab flattening' regime, subduction of the buoyant feature results in a flat slab at shallow depth, over a distance of several 100 km, and is associated with the subduction

of buoyant features with a very strong positive buoyancy force below a thick, and possibly advancing, upper plate.

In summary, the work in this dissertation illustrates that although subduction on Earth shares some common traits, including that it occurs mostly in 'sinking' mode, with a relatively small contribution of trench motion to the total convergence, there is significant variability in styles (Chapter 2). Part of this variability can be explained by the variation in local downgoing plate properties (Chapter 4). However, lateral variations in downgoing plate buoyancy can significantly modify subduction behaviour and explain quite a few cases of complex subduction evolution on Earth (Chapter 5). Low basal drag, due to a low-viscosity asthenosphere, explains the observed small trench motions, yet when integrated over large plates exerts a significant influence on plate motions (Chapter 3), and thus also facilitates large-scale interactions between plates and mantle flow.

6.2 Future Work

There are still many outstanding questions on the dynamics of subduction, which future numerical models, in particular in 3D and spherical geometries, can help shed light on.

Intra-plate stress regime near subducting buoyant features

Further insights in the role of buoyant ridges on modifying subduction behaviour might be gained by studying earthquakes that reflect intra-plate stress. In 2021, a magnitude 7.3 earthquake occurred offshore East Cape, New Zealand, in which shallow trench-normal extension was observed alongside deep trench-parallel compression (Okuwaki et al., 2021). The earthquake's deformation only partially reflects the

expected stress regime due to plate bending into the trench, which for a linear trench, should be trench-normal, with extension in the top and compression in the bottom of the plate. The rotation of the compressional stress direction away from the trench normal was attributed to plate warping (Okuwaki et al., 2021) in response to lateral variations in plate buoyancy due to the proximity of the Hikurangi Plateau or a subducted seamount.

Initial analysis of the stress directions in the models in Chapter 5 reveals a similar rotation in stress near the subducting ridge which are more apparent in the models with older subducting plates. I am now investigating whether there are other examples of such intra-plate stress rotation on Earth by examining the focal mechanisms from the Global CMT catalogue (Dziewonski et al., 1981; Ekström et al., 2012) of previous earthquakes near subducting buoyant features at major subduction zones subducting old lithosphere (e.g. West Pacific) and young lithosphere (e.g. Nazca and Cocos Plates).

Outlook

The models in Chapters 4 and 5 clearly illustrate the role that 3-D variations in forcing, and specifically of slab pull, can have on controlling the evolution of subduction dynamics. Several other outstanding questions also require 3-D modelling. These include the impact of slab tearing and the subduction of 'slab windows', which can result from the subduction of spreading ridges (parallel to the trench, as in the case of the Izanagi subduction, or perpendicular to the trench, as in the case of the Cocos-Nazca subduction). The development of tears and gaps are common processes resulting from or causing plate boundary evolution.

Another important avenue for future investigation would be adding an overriding plate. Quite a few models comprising both subducting and upper plate, in 2-D and 3-D, exist for specific scenarios of subduction. These models investigate the plausibility of a specific factor in governing local trench history (e.g. the development of flat slabs be-

neath South America due to subduction of buoyant ridges; Manea et al., 2012; Hu et al., 2016). Some systematic studies on the effects of the upper plate have been done in 2-D (e.g. van Hunen et al., 2004; Capitanio et al., 2010; Roda et al., 2011; Rodríguez-González et al., 2012; Holt et al., 2015b) but only a few in 3-D, mostly due to computational challenges (e.g. Butterworth et al., 2012; Sharples et al., 2014; Rodríguez-González et al., 2016). Systematic examination in 3-D of the impact of the overriding plate on subduction dynamics has remained an important avenue to progress our understanding of the variations in subduction dynamics.

The models in Chapter 3 illustrate the feedback mechanisms that occur when numerical models include thermally dependent rheology. Such complex rheology is so far mostly limited to 2-D models (e.g. Čižková et al., 2002; Garel et al., 2014), with only few 3-D models incorporating it (e.g. Crameri et al., 2017), due to computational limitations. Implementing thermally dependent rheology in 3-D models will be an important next step in order to better understand, for example, the interplay between rising mantle plumes and subduction dynamics (e.g. Gurnis et al., 2000; Becker and Faccenna, 2011) and capture thermally governed variations in buoyancy and viscosity.

The compilation of subduction parameters presented in Chapter 2 illustrates that interactions between adjacent subduction zones can have a significant impact on subduction evolution. Modelling the interactions between neighbouring plates and the main subducting plate will allow for investigation of the interactions between several subducting plates. Only a few studies investigated two or more plate systems, e.g. on two plates subducting in the same direction (as in the Izu-Bonin-Mariana and Ryukyu-Nankai subduction zones; Mishin et al., 2008; Čížková and Bina, 2015; Holt et al., 2017), or two neighbouring slabs subducting in opposing directions (Zhang et al., 2017b; Peral et al., 2020). When larger systems are studied, it will be important to set up the models in spherical geometry (Chen et al., 2022a).

The studies presented in this dissertation demonstrate the potential of numerical models to advance our understanding of the dynamics of subduction and its expressions

at the surface.

Bibliography

Agrusta, R., Goes, S., and van Hunen, J. (2017). Subducting-slab transition-zone interaction: Stagnation, penetration and mode switches. *Earth and Planetary Science Letters* 464, 10–23. doi:10.1016/j.epsl.2017.02.005

Agrusta, R., Van Hunen, J., and Goes, S. (2014). The effect of metastable pyroxene on the slab dynamics. *Geophysical Research Letters* 41, 8800–8808. doi:10.1002/2014GL062159

Allmendinger, R. W., Jordan, T. E., Kay, S. M., and Isacks, B. L. (1997). The evolution of the Altiplano-Puna plateau of the Central Andes. *Annual Review of Earth and Planetary Sciences* 25, 139–174. doi:10.1146/annurev.earth.25.1.139

Alsaif, M., Garel, F., Gueydan, F., and Davies, D. R. (2020). Upper plate deformation and trench retreat modulated by subduction-driven shallow asthenospheric flows. *Earth and Planetary Science Letters* 532. doi:10.1016/j.epsl.2019.116013

Amante, C. and Eakins, B. (2008). Etopo1 1 arc-minute global relief model: Procedures, data sources and analysis, national geophysical data center, nesdis, noaa, us dept. *Commerce, Boulder, CO, USA*

Antonijevic, S. K., Wagner, L. S., Kumar, A., Beck, S. L., Long, M. D., Zandt, G., et al. (2015). The role of ridges in the formation and longevity of flat slabs. *Nature* 524, 212–215. doi:10.1038/nature14648

Arcay, D., Lallemand, S., and Doin, M. P. (2008). Back-arc strain in subduction zones:

Statistical observations versus numerical modeling. *Geochemistry, Geophysics, Geosystems* 9. doi:10.1029/2007GC001875

Arrial, P. A. and Billen, M. I. (2013). Influence of geometry and eclogitization on oceanic plateau subduction. *Earth and Planetary Science Letters* 363, 34–43. doi:10.1016/j.epsl.2012.12.011

Atwater, T. (1989). Plate tectonic history of the northeast Pacific and western North America. In *The Eastern Pacific Ocean and Hawaii,* eds. E. L. Winterer, D. M. Hussong, and R. W. Decker (Geological Society of America), vol. N. 0. doi:10.1130/DNAG-GNA-N.21

Bai, Y., Gui, Z., Li, M., Dong, D., Wu, S., and Wang, Z. (2019). Crustal thickness over the NW Pacific and its tectonic implications. *Journal of Asian Earth Sciences* 185, 104050. doi:10.1016/j.jseaes.2019.104050

Bai, Y., Wu, S., Liu, Z., Müller, R. D., Williams, S. E., Zahirovic, S., et al. (2015). Full-fit reconstruction of the South China Sea conjugate margins. *Tectonophysics* 661, 121–135. doi:10.1016/j.tecto.2015.08.028

Balázs, A., Faccenna, C., Ueda, K., Funiciello, F., Boutoux, A., Blanc, E. J., et al. (2021). Oblique subduction and mantle flow control on upper plate deformation: 3D geodynamic modeling. *Earth and Planetary Science Letters* 569, 117056. doi:10.1016/j.epsl.2021.117056

Barretto, J., Wood, R., and Milsom, J. (2020). Benham Rise unveiled: Morphology and structure of an Eocene large igneous province in the West Philippine Basin. *Marine Geology* 419, 106052. doi:10.1016/j.margeo.2019.106052

Becker, T. W. and Faccenna, C. (2011). Mantle conveyor beneath the Tethyan collisional belt. *Earth and Planetary Science Letters* 310, 453–461. doi:10.1016/j.epsl.2011.08.021

Becker, T. W. and Kawakatsu, H. (2011). On the role of anisotropic viscosity for plate-scale flow. *Geophysical Research Letters* 38. doi:10.1029/2011GL048584

Becker, T. W. and O'Connell, R. J. (2001). Predicting plate velocities with mantle circulation models. *Geochemistry, Geophysics, Geosystems* 2. doi:10.1029/2001GC000171

Běhounková, M. and Čížková, H. (2008). Long-wavelength character of subducted slabs in the lower mantle. *Earth and Planetary Science Letters* 275, 43–53. doi:10.1016/j.epsl.2008.07.059

Bellahsen, N., Faccenna, C., and Funiciello, F. (2005). Dynamics of subduction and plate motion in laboratory experiments: Insights into the "plate tectonics" behavior of the Earth. *Journal of Geophysical Research: Solid Earth* 110, 1–15. doi:10.1029/2004JB002999

Bellahsen, N., Faccenna, C., Funiciello, F., Daniel, J., and Jolivet, L. (2003). Why did Arabia separate from Africa? Insights from 3-D laboratory experiments. *Earth and Planetary Science Letters* 216, 365–381. doi:10.1016/S0012-821X(03)00516-8

Best, M. G. (2002). *Igneous and Metamorphic Petrology* (Malden, MA: Wiley-Blackwell), 2nd edn.

Betts, P. G., Giles, D., Foden, J., Schaefer, B. F., Mark, G., Pankhurst, M. J., et al. (2009). Mesoproterozoic plume-modified orogenesis in eastern Precambrian Australia. *Tectonics* 28, 1–28. doi:10.1029/2008TC002325

Bilek, S. L. and Lay, T. (2018). Subduction zone megathrust earthquakes. *Geosphere* 14, 1468–1500. doi:10.1130/GES01608.1

Billen, M. I. and Arredondo, K. M. (2018). Decoupling of plate-asthenosphere motion caused by non-linear viscosity during slab folding in the transition zone. *Physics of the Earth and Planetary Interiors* 281, 17–30. doi:10.1016/j.pepi.2018.04.011

Billen, M. I., Gurnis, M., and Simons, M. (2003). Multiscale dynamics of the Tonga—Kermadec subduction zone. *Geophysical Journal International* 153, 359–388. doi:10.1046/j.1365-246X.2003.01915.x

Billen, M. I. and Hirth, G. (2007). Rheologic controls on slab dynamics. *Geochemistry, Geophysics, Geosystems* 8, Q08012. doi:10.1029/2007GC001597

Bird, P. (2003). An updated digital model of plate boundaries. *Geochemistry, Geophysics, Geosystems* 4. doi:10.1029/2001GC000252

Bishop, B. T., Beck, S. L., Zandt, G., Wagner, L., Long, M., Antonijevic, S. K., et al. (2017). Causes and consequences of flat-slab subduction in southern Peru. *Geosphere* 13, 1392–1407. doi:10.1130/GES01440.1

Blankenbach, B., Busse, F., Christensen, U., Cserepes, L., Gunkel, D., Hansen, U., et al. (1989). A benchmark comparison for mantle convection codes. *Geophysical Journal International* 98, 23–38. doi:10.1111/j.1365-246X.1989.tb05511.x

Bokelmann, G. H. and Silver, P. G. (2002). Shear stress at the base of shield lithosphere. *Geophysical Research Letters* 29, 61–64. doi:10.1029/2002GL015925

Bonnardot, M. A., Régnier, M., Ruellan, E., Christova, C., and Tric, E. (2007). Seismicity and state of stress within the overriding plate of the Tonga-Kermadec subduction zone. *Tectonics* 26, 1–15. doi:10.1029/2006TC002044

Boschman, L. M., van Hinsbergen, D. J., Torsvik, T. H., Spakman, W., and Pindell, J. L. (2014). Kinematic reconstruction of the Caribbean region since the Early Jurassic. *Earth-Science Reviews* 138, 102–136. doi:10.1016/j.earscirev.2014.08.007

Boutelier, D. A. and Cruden, A. R. (2008). Impact of regional mantle flow on subducting plate geometry and interplate stress: insights from physical modelling. *Geophysical Journal International* 174, 719–732. doi:10.1111/j.1365-246X.2008.03826.x

Braszus, B., Goes, S., Allen, R., Rietbrock, A., Collier, J., Harmon, N., et al. (2021). Subduction history of the Caribbean from upper-mantle seismic imaging and plate reconstruction. *Nature Communications* 12. doi:10.1038/s41467-021-24413-0

Braz, C., Seton, M., Flament, N., and Müller, R. D. (2018). Geodynamic reconstruction

of an accreted Cretaceous back-arc basin in the Northern Andes. *Journal of Geodynamics* 121, 115–132. doi:10.1016/j.jog.2018.09.008

Buffett, B. A. (2006). Plate force due to bending at subduction zones. *Journal of Geophysical Research: Solid Earth* 111, 1–9. doi:10.1029/2006JB004295

Buffett, B. A. and Becker, T. W. (2012). Bending stress and dissipation in subducted lithosphere. *Journal of Geophysical Research: Solid Earth* 117, 1–10. doi:10.1029/2012JB009205

Burov, E. B. (2011). Rheology and strength of the lithosphere. *Marine and Petroleum Geology* 28, 1402–1443. doi:10.1016/j.marpetgeo.2011.05.008

Busse, F. H., Christensen, U., Clever, R., Cserepes, L., Gable, C., Giannandrea, E., et al. (1994). 3D convection at infinite Prandtl number in Cartesian geometry — a benchmark comparison. *Geophysical and Astrophysical Fluid Dynamics* 75, 39–59. doi:10.1080/03091929408203646

Butterworth, N. P., Quevedo, L., Morra, G., and Müller, R. D. (2012). Influence of overriding plate geometry and rheology on subduction. *Geochemistry, Geophysics, Geosystems* 13. doi:10.1029/2011GC003968

Capitanio, F., Stegman, D., Moresi, L., and Sharples, W. (2010). Upper plate controls on deep subduction, trench migrations and deformations at convergent margins. *Tectonophysics* 483, 80–92. doi:10.1016/j.tecto.2009.08.020

Capitanio, F. A. (2013). Lithospheric-age control on the migrations of oceanic convergent margins. *Tectonophysics* 593, 193–200. doi:10.1016/j.tecto.2013.03.003

Capitanio, F. A., Faccenna, C., Zlotnik, S., and Stegman, D. R. (2011). Subduction dynamics and the origin of Andean orogeny and the Bolivian orocline. *Nature* 480, 83–86. doi:10.1038/nature10596

Capitanio, F. A. and Morra, G. (2012). The bending mechanics in a dynamic subduction system: Constraints from numerical modelling and global compilation analysis. *Tectonophysics* 522-523, 224–234. doi:10.1016/j.tecto.2011.12.003

Capitanio, F. A., Morra, G., and Goes, S. (2007). Dynamic models of downgoing plate-buoyancy driven subduction: Subduction motions and energy dissipation. *Earth and Planetary Science Letters* 262, 284–297. doi:10.1016/j.epsl.2007.07.039

Capitanio, F. A., Morra, G., and Goes, S. (2009). Dynamics of plate bending at the trench and slab-plate coupling. *Geochemistry, Geophysics, Geosystems* 10, Q04002. doi:10.1029/2008GC002348

Carlson, R. L., Hilde, T. W. C., and Uyeda, S. (1983). The driving mechanism of plate tectonics: Relation to age of the lithosphere at trenches. *Geophysical Research Letters* 10, 297–300. doi:10.1029/GL010i004p00297

Chamolly, A. and Ribe, N. M. (2021). Fluid mechanics of free subduction on a sphere. Part 1. The axisymmetric case. *Journal of Fluid Mechanics* 929, 1–32. doi:10.1017/jfm.2021.871

Chandler, M. T., Wessel, P., Taylor, B., Seton, M., Kim, S. S., and Hyeong, K. (2012). Reconstructing Ontong Java Nui: Implications for Pacific absolute plate motion, hotspot drift and true polar wander. *Earth and Planetary Science Letters* 331-332, 140–151. doi:10.1016/j.epsl.2012.03.017

Chen, F., Davies, D. R., Goes, S., Suchoy, L., and Kramer, S. C. (2022a). Comparing the Dynamics of Free Subduction in Cartesian and Spherical Domains. ESSOAr [Preprint]. Available at: `https://www.essoar.org/doi/10.1002/essoar.10512692.1`; Access date: 09/11/2022. doi: 10.1002/essoar.10512692.1

Chen, F., Davies, D. R., Goes, S., Suchoy, L., and Kramer, S. C. (2022b). How Slab Age and Width Combine to Dictate the Dynamics and Evolution of Subduction Systems: A 3-D Spherical Study. *Geochemistry, Geophysics, Geosystems* 23, 1–21. doi:10.1029/2022GC010597

Chertova, M. V., Geenen, T., van den Berg, A., and Spakman, W. (2012). Using open sidewalls for modelling self-consistent lithosphere subduction dynamics. *Solid Earth* 3, 313–326. doi:10.5194/se-3-313-2012

Christensen, U. R. (1996). The influence of trench migration on slab penetration into the lower mantle. *Earth and Planetary Science Letters* 140, 27–39. doi:10.1016/0012-821X(96)00023-4

Christensen, U. R. and Yuen, D. A. (1984). Interaction of a Subducting Lithospheric Slab With a Chemical or Phase Boundary. *Journal of Geophysical Research* 89, 4389–4402. doi:10.1029/JB089iB06p04389

Čížková, H. and Bina, C. R. (2013). Effects of mantle and subduction-interface rheologies on slab stagnation and trench rollback. *Earth and Planetary Science Letters* 379, 95–103. doi:10.1016/j.epsl.2013.08.011

Čížková, H. and Bina, C. R. (2015). Geodynamics of trench advance: Insights from a Philippine-Sea-style geometry. *Earth and Planetary Science Letters* 430, 408–415. doi:10.1016/j.epsl.2015.07.004

Čížková, H., van Hunen, J., van den Berg, A. P., and Vlaar, N. J. (2002). The influence of rheological weakening and yield stress on the interaction of slabs with the 670 km discontinuity. *Earth and Planetary Science Letters* 199, 447–457. doi:10.1016/S0012-821X(02)00586-1

Clark, S. R., Stegman, D., and Müller, R. D. (2008). Episodicity in back-arc tectonic regimes. *Physics of the Earth and Planetary Interiors* 171, 265–279. doi:10.1016/j.pepi.2008.04.012

Cloos, M. (1993). Lithospheric buoyancy and collisional orogenesis: subduction of oceanic plateaus, continental margins, island arcs, spreading ridges, and seamounts. *Geological Society of America Bulletin* 105, 715–737. doi:10.1130/0016-7606(1993)105<0715:LBACOS>2.3.CO;2

Coffin, M. F., Duncan, R. A., Eldholm, O., Fitton, J. G., Frey, F. A., Larsen, H. C., et al. (2006). Large igneous provinces and scientific ocean drilling: Status quo and a look ahead. *Oceanography* 19, 150–160. doi:10.5670/oceanog.2006.13

Coffin, M. F. and Eldholm, O. (1994). Large igneous provinces: Crustal structure, dimensions, and external consequences. *Reviews of Geophysics* 32, 1–36. doi:10.1029/93RG02508

Colli, L., Stotz, I., Bunge, H. P., Smethurst, M., Clark, S., Iaffaldano, G., et al. (2014). Rapid South Atlantic spreading changes and coeval vertical motion in surrounding continents: Evidence for temporal changes of pressure-driven upper mantle flow. *Tectonics* 33, 1304–1321. doi:10.1002/2014TC003612

Coltice, N., Husson, L., Faccenna, C., and Arnould, M. (2019). What drives tectonic plates? *Science Advances* 5. doi:10.1126/sciadv.aax4295

Conrad, C. P. and Behn, M. D. (2010). Constraints on lithosphere net rotation and asthenospheric viscosity from global mantle flow models and seismic anisotropy. *Geochemistry, Geophysics, Geosystems* 11, n/a–n/a. doi:10.1029/2009GC002970

Conrad, C. P., Bilek, S., and Lithgow-Bertelloni, C. (2004). Great earthquakes and slab pull: Interaction between seismic coupling and plate-slab coupling. *Earth and Planetary Science Letters* 218, 109–122. doi:10.1016/S0012-821X(03)00643-5

Conrad, C. P. and Hager, B. H. (1999). Effects of plate bending and fault strength at subduction zones on plate dynamics. *Journal of Geophysical Research: Solid Earth* 104, 17551–17571. doi:10.1029/1999jb900149

Conrad, C. P. and Hager, B. H. (2001). Mantle convection with strong subduction zones. *Geophysical Journal International* 144, 271–288. doi:10.1046/j.1365-246x.2001.00321.x

Conrad, C. P. and Lithgow-Bertelloni, C. (2002). How Mantle Slabs Drive Plate Tectonics. *Science* 298, 207–210. doi:10.1126/science.1074161

Conrad, C. P. and Lithgow-Bertelloni, C. (2006). Influence of continental roots and asthenosphere on plate-mantle coupling. *Geophysical Research Letters* 33. doi: 10.1029/2005GL025621

Corbi, F., Herrendörfer, R., Funiciello, F., and van Dinther, Y. (2017). Controls of seismogenic zone width and subduction velocity on interplate seismicity: Insights from analog and numerical models. *Geophysical Research Letters* 44, 6082–6091. doi: 10.1002/2016GL072415

Courtillot, V., Davaille, A., Besse, J., and Stock, J. (2003). Three distinct types of hotspots in the Earth's mantle. *Earth and Planetary Science Letters* 205, 295–308. doi:10.1016/S0012-821X(02)01048-8

Cox, A. and Hart, R. B. (2009). *Plate Tectonics: How It Works* (Germany: Wiley), 2nd edn.

Crameri, F., Lithgow-Bertelloni, C., and Tackley, P. (2017). The dynamical control of subduction parameters on surface topography. *Geochemistry, Geophysics, Geosystems* 18, 1661–1687. doi:10.1002/2017GC006821

Crameri, F., Tackley, P. J., Meilick, I., Gerya, T. V., and Kaus, B. J. P. (2012). A free plate surface and weak oceanic crust produce single-sided subduction on Earth. *Geophysical Research Letters* 39. doi:10.1029/2011GL050046

Cruciani, C., Carminati, E., and Doglioni, C. (2005). Slab dip vs. lithosphere age: No direct function. *Earth and Planetary Science Letters* 238, 298–310. doi:10.1016/j.epsl.2005.07.025

Currie, C. A. and Beaumont, C. (2011). Are diamond-bearing Cretaceous kimberlites related to low-angle subduction beneath western North America? *Earth and Planetary Science Letters* 303, 59–70. doi:10.1016/j.epsl.2010.12.036

Daly, K. A., Abers, G. A., Mann, M. E., Roecker, S., and Christensen, D. H. (2021). Subduction of an Oceanic Plateau Across Southcentral Alaska: High-Resolution Seismicity. *Journal of Geophysical Research: Solid Earth* 126, 1–18. doi:10.1029/2021JB022809

Dasgupta, R., Sen, J., and Mandal, N. (2021). Bending curvatures of subducting plates: Old versus young slabs. *Geophysical Journal International* 225, 1963–1981. doi:10.1093/gji/ggab070

Davaille, A. and Lees, J. M. (2004). Thermal modeling of subducted plates: tear and hotspot at the Kamchatka corner. *Earth and Planetary Science Letters* 226, 293–304. doi:10.1016/j.epsl.2004.07.024

Davies, D. R., Davies, J. H., Hassan, O., Morgan, K., and Nithiarasu, P. (2007). Investigations into the applicability of adaptive finite element methods to two-dimensional infinite Prandtl number thermal and thermochemical convection. *Geochemistry, Geophysics, Geosystems* 8. doi:10.1029/2006GC001470

Davies, D. R., Wilson, C. R., and Kramer, S. C. (2011). Fluidity: A fully unstructured anisotropic adaptive mesh computational modeling framework for geodynamics. *Geochemistry, Geophysics, Geosystems* 12. doi:10.1029/2011GC003551

Davies, G. F. (1995). Penetration of plates and plumes through the mantle transition zone. *Earth and Planetary Science Letters* 133, 507–516. doi:10.1016/0012-821X(95)00039-F

De Franco, R., Govers, R., and Wortel, R. (2007). Numerical comparison of different convergent plate contacts: subduction channel and subduction fault. *Geophysical Journal International* 171, 435–450. doi:10.1111/j.1365-246X.2006.03498.x

Di Giuseppe, E., Faccenna, C., Funiciello, F., van Hunen, J., and Giardini, D. (2009). On the relation between trench migration, seafloor age, and the strength of the subducting lithosphere. *Lithosphere* 1, 121–128. doi:10.1130/L26.1

Di Giuseppe, E., Van Hunen, J., Funiciello, F., Faccenna, C., and Giardini, D. (2008). Slab stiffness control of trench motion: Insights from numerical models. *Geochemistry, Geophysics, Geosystems* 9, 1–19. doi:10.1029/2007GC001776

Dobson, D. P., Meredith, P. G., and Boon, S. A. (2002). Simulation of Subduction Zone

Seismicity by Dehydration of Serpentine. *Science* 298, 1407–1410. doi:10.1126/science.1075390

Doglioni, C., Carminati, E., Cuffaro, M., and Scrocca, D. (2007). Subduction kinematics and dynamic constraints. *Earth-Science Reviews* 83, 125–175. doi:10.1016/j.earscirev.2007.04.001

Domeier, M. and Torsvik, T. H. (2014). Plate tectonics in the late Paleozoic. *Geoscience Frontiers* 5, 303–350. doi:10.1016/j.gsf.2014.01.002

Dutkiewicz, A., Müller, R. D., Cannon, J., Vaughan, S., and Zahirovic, S. (2019). Sequestration and subduction of deep-sea carbonate in the global ocean since the Early Cretaceous. *Geology* 47, 91–94. doi:10.1130/G45424.1

Dvorkin, J., Nur, A., Mavko, G., and Ben-Avraham, Z. (1993). Narrow subducting slabs and the origin of backarc basins. *Tectonophysics* 227, 63–79. doi:10.1016/0040-1951(93)90087-Z

Dziewonski, A. M. and Anderson, D. L. (1981). Preliminary reference Earth model. *Physics of the Earth and Planetary Interiors* 25, 297–356. doi:10.1016/0031-9201(81)90046-7

Dziewonski, A. M., Chou, T. A., and Woodhouse, J. H. (1981). Determination of earthquake source parameters from waveform data for studies of global and regional seismicity. *Journal of Geophysical Research: Solid Earth* 86, 2825–2852. doi:10.1029/JB086iB04p02825

Ekström, G., Nettles, M., and Dziewoński, A. (2012). The global CMT project 2004–2010: Centroid-moment tensors for 13,017 earthquakes. *Physics of the Earth and Planetary Interiors* 200-201, 1–9. doi:10.1016/j.pepi.2012.04.002

Elsasser, W. M. (1971). Sea-floor spreading as thermal convection. *Journal of Geophysical Research* 76, 1101–1112. doi:10.1029/JB076i005p01101

Espurt, N., Baby, P., Brusset, S., Roddaz, M., Hermoza, W., Regard, V., et al. (2007). How does the Nazca Ridge subduction influence the modern Amazonian foreland basin? *Geology* 35, 515–518. doi:10.1130/G23237A.1

Espurt, N., Funiciello, F., Martinod, J., Guillaume, B., Regard, V., Faccenna, C., et al. (2008). Flat subduction dynamics and deformation of the South American plate: Insights from analog modeling. *Tectonics* 27, TC3011. doi:10.1029/2007TC002175

Faccenna, C., Heuret, A., Funiciello, F., Lallemand, S., and Becker, T. W. (2007). Predicting trench and plate motion from the dynamics of a strong slab. *Earth and Planetary Science Letters* 257, 29–36. doi:10.1016/j.epsl.2007.02.016

Faccenna, C., Holt, A. F., Becker, T. W., Lallemand, S., and Royden, L. H. (2018). Dynamics of the Ryukyu/Izu-Bonin-Marianas double subduction system. *Tectonophysics* 746, 229–238. doi:10.1016/j.tecto.2017.08.011

Farrington, R. J., Moresi, L.-N., and Capitanio, F. A. (2014). The role of viscoelasticity in subducting plates. *Geochemistry, Geophysics, Geosystems* 15, 4291–4304. doi:10.1002/2014GC005507

Feng, M., van der Lee, S., and Assumpção, M. (2007). Upper mantle structure of South America from joint inversion of waveforms and fundamental mode group velocities of Rayleigh waves. *Journal of Geophysical Research: Solid Earth* 112, 1–16. doi:10.1029/2006JB004449

Ficini, E., Zilio, L. D., Doglioni, C., and Gerya, T. V. (2017). Horizontal mantle flow controls subduction dynamics. *Scientific Reports* 7, 1–7. doi:10.1038/s41598-017-06551-y

Flament, N., Gurnis, M., Müller, R. D., Bower, D. J., and Husson, L. (2015). Influence of subduction history on South American topography. *Earth and Planetary Science Letters* 430, 9–18. doi:10.1016/j.epsl.2015.08.006

Flórez-Rodríguez, A. G., Schellart, W. P., and Strak, V. (2019). Impact of Aseismic Ridges

on Subduction Systems: Insights From Analog Modeling. *Journal of Geophysical Research: Solid Earth* 124, 5951–5969. doi:10.1029/2019JB017488

Forsyth, D. and Uyeda, S. (1975). On the Relative Importance of the Driving Forces of Plate Motion. *Geophysical Journal of the Royal Astronomical Society* 43, 163–200. doi:10.1111/j.1365-246X.1975.tb00631.x

Fourel, L., Goes, S., and Morra, G. (2014). The role of elasticity in slab bending. *Geochemistry, Geophysics, Geosystems* 15, 4507–4525. doi:10.1002/2014GC005535

Fowler, C. (2005). *The Solid Earth An Introduction to Global Geophysics* (Cambridge: Cambridge University Press), 2 edn.

French, S., Lekic, V., and Romanowicz, B. (2013). Waveform tomography reveals channeled flow at the base of the oceanic asthenosphere. *Science* 342, 227–230. doi:10.1126/science.1241514

Funiciello, F., Faccenna, C., Giardini, D., and Regenauer-Lieb, K. (2003a). Dynamics of retreating slabs: 2. Insights from three-dimensional laboratory experiments. *Journal of Geophysical Research: Solid Earth* 108, 1–16. doi:10.1029/2001jb000896

Funiciello, F., Faccenna, C., Heuret, A., Lallemand, S., Di Giuseppe, E., and Becker, T. W. (2008). Trench migration, net rotation and slab-mantle coupling. *Earth and Planetary Science Letters* 271, 233–240. doi:10.1016/j.epsl.2008.04.006

Funiciello, F., Moroni, M., Piromallo, C., Faccenna, C., Cenedese, A., and Bui, H. A. (2006). Mapping mantle flow during retreating subduction: Laboratory models analyzed by feature tracking. *Journal of Geophysical Research: Solid Earth* 111, 1–16. doi:10.1029/2005JB003792

Funiciello, F., Morra, G., Regenauer-Lieb, K., and Giardini, D. (2003b). Dynamics of retreating slabs: 1. Insights from two-dimensional numerical experiments. *Journal of Geophysical Research: Solid Earth* 108, 2206. doi:10.1029/2001JB000898

Garel, F., Goes, S., Davies, D. R., Davies, J. H., Kramer, S. C., and Wilson, C. R. (2014). Interaction of subducted slabs with the mantle transition-zone: A regime diagram from 2-D thermo-mechanical models with a mobile trench and an overriding plate. *Geochemistry, Geophysics, Geosystems* 15, 1739–1765. doi:10.1002/2014GC005257

Garel, F., Thoraval, C., Tommasi, A., Demouchy, S., and Davies, R. (2020). Using thermo-mechanical models of subduction to constrain effective mantle viscosity. *Earth and Planetary Science Letters* 539, 116243. doi:10.1016/j.epsl.2020.116243

Garfunkel, Z., Anderson, C. A., and Schubert, G. (1986). Mantle circulation and the lateral migration of subducted slabs. *Journal of Geophysical Research: Solid Earth* 91, 7205–7223. doi:10.1029/JB091iB07p07205

Gerya, T. V., Fossati, D., Cantieni, C., and Seward, D. (2009). Dynamic effects of aseismic ridge subduction: numerical modelling. *European Journal of Mineralogy* 21, 649–661. doi:10.1127/0935-1221/2009/0021-1931

Gibbons, A., Zahirovic, S., Müller, R., Whittaker, J., and Yatheesh, V. (2015). A tectonic model reconciling evidence for the collisions between India, Eurasia and intra-oceanic arcs of the central-eastern Tethys. *Gondwana Research* 28, 451–492. doi:10.1016/j.gr.2015.01.001

Goes, S., Agrusta, R., van Hunen, J., and Garel, F. (2017). Subduction-transition zone interaction: A review. *Geosphere* 13, 644–664. doi:10.1130/GES01476.1

Goes, S., Capitanio, F. A., and Morra, G. (2008). Evidence of lower-mantle slab penetration phases in plate motions. *Nature* 451, 981–984. doi:10.1038/nature06691

Goes, S., Capitanio, F. A., Morra, G., Seton, M., and Giardini, D. (2011). Signatures of downgoing plate-buoyancy driven subduction in Cenozoic plate motions. *Physics of the Earth and Planetary Interiors* 184, 1–13. doi:10.1016/j.pepi.2010.10.007

Govers, R. and Wortel, M. (2005). Lithosphere tearing at STEP faults: response to edges of subduction zones. *Earth and Planetary Science Letters* 236, 505–523. doi:10.1016/j.epsl.2005.03.022

Grellet, C. and Dubois, J. (1982). The depth of trenches as a function of the subduction rate and age of the Lithosphere. *Tectonophysics* 82, 45–56. doi:10.1016/0040-1951(82)90087-7

Guillaume, B., Martinod, J., and Espurt, N. (2009). Variations of slab dip and overriding plate tectonics during subduction: Insights from analogue modelling. *Tectonophysics* 463, 167–174. doi:10.1016/j.tecto.2008.09.043

Gulick, S. P., Lowe, L. A., Pavlis, T. L., Gardner, J. V., and Mayer, L. A. (2007). Geophysical insights into the transition fault debate: Propagating strike slip in response to stalling Yakutat block subduction in the Gulf of Alaska. *Geology* 35, 763–766. doi:10.1130/G23585A.1

Gurnis, M., Ritsema, J., Van Heijst, H.-J., and Zhong, S. (2000). Tonga slab deformation: The influence of a lower mantle upwelling on a slab in a young subduction zone. *Geophysical Research Letters* 27, 2373–2376. doi:10.1029/2000GL011420

Gurnis, M., Turner, M., Zahirovic, S., DiCaprio, L., Spasojevic, S., Müller, R., et al. (2012). Plate tectonic reconstructions with continuously closing plates. *Computers and Geosciences* 38, 35–42. doi:10.1016/j.cageo.2011.04.014

Gutscher, M.-A. (2002). Andean subduction styles and their effect on thermal structure and interplate coupling. *Journal of South American Earth Sciences* 15, 3–10. doi:10.1016/S0895-9811(02)00002-0

Gutscher, M. A., Malavieille, J., Lallemand, S., and Collot, J. Y. (1999). Tectonic segmentation of the North Andean margin: Impact of the Carnegie Ridge collision. *Earth and Planetary Science Letters* 168, 255–270. doi:10.1016/S0012-821X(99)00060-6

Gutscher, M.-A., Maury, R., Eissen, J.-P., and Bourdon, E. (2000a). Can slab melting be caused by flat subduction? *Geology* 28, 535–538. doi:10.1130/0091-7613(2000)028<0535:CSMBCB>2.3.CO;2

Gutscher, M.-A., Spakman, W., Bijwaard, H., and Engdahl, E. R. (2000b). Geodynamics

of flat subduction: Seismicity and tomographic constraints from the Andean margin. *Tectonics* 19, 814–833. doi:10.1029/1999TC001152

Hall, R. (2002). Cenozoic geological and plate tectonic evolution of SE Asia and the SW Pacific: computer-based reconstructions, model and animations. *Journal of Asian Earth Sciences* 20, 353–431. doi:10.1016/S1367-9120(01)00069-4

Hall, R. and Spakman, W. (2015). Mantle structure and tectonic history of SE Asia. *Tectonophysics* 658, 14–45. doi:10.1016/j.tecto.2015.07.003

Hampel, A. (2002). The migration history of the Nazca Ridge along the Peruvian active margin: A re-evaluation. *Earth and Planetary Science Letters* 203, 665–679. doi:10.1016/S0012-821X(02)00859-2

Handy, M. R., M. Schmid, S., Bousquet, R., Kissling, E., and Bernoulli, D. (2010). Reconciling plate-tectonic reconstructions of Alpine Tethys with the geological–geophysical record of spreading and subduction in the Alps. *Earth-Science Reviews* 102, 121–158. doi:10.1016/j.earscirev.2010.06.002

Hayes, G. P., Moore, G. L., Portner, D. E., Hearne, M., Flamme, H., Furtney, M., et al. (2018). Slab2, a comprehensive subduction zone geometry model. *Science* 362, 58–61. doi:10.1126/science.aat4723

Hayes, G. P., Wald, D. J., and Johnson, R. L. (2012). Slab1.0: A three-dimensional model of global subduction zone geometries. *Journal of Geophysical Research: Solid Earth* 117. doi:10.1029/2011JB008524

Heuret, A., Conrad, C. P., Funiciello, F., Lallemand, S., and Sandri, L. (2012). Relation between subduction megathrust earthquakes, trench sediment thickness and upper plate strain. *Geophysical Research Letters* 39. doi:10.1029/2011GL050712

Heuret, A. and Lallemand, S. (2005). Plate motions, slab dynamics and back-arc deformation. *Physics of the Earth and Planetary Interiors* 149, 31–51. doi:10.1016/j.pepi.2004.08.022

Hilton, D. R., Fischer, T. P., and Marty, B. (2002). Noble Gases and Volatile Recycling at Subduction Zones. *Reviews in Mineralogy and Geochemistry* 47, 319–370. doi: 10.2138/rmg.2002.47.9

Hirth, G. and Kohlstedt, D. L. (1995). Experimental constraints on the dynamics of the partially molten upper mantle: Deformation in the diffusion creep regime. *Journal of Geophysical Research* 100, 1981–2001. doi:10.1029/94JB02128

Hirth, G. and Kohlstedt, D. L. (2003). Rheology of the Upper Mantle and the Mantle Wedge: A View from the Experimentalists. In *Inside the Subduction Factory*, ed. J. Eiler (American Geophysical Union), chap. 6. 83–15. doi:10.1029/138GM06

Höink, T. and Lenardic, A. (2008). Three-dimensional mantle convection simulations with a low-viscosity asthenosphere and the relationship between heat flow and the horizontal length scale of convection. *Geophysical Research Letters* 35. doi:10.1029/2008GL033854

Höink, T. and Lenardic, A. (2010). Long wavelength convection, Poiseuille-Couette flow in the low-viscosity asthenosphere and the strength of plate margins. *Geophysical Journal International* 180, 23–33. doi:10.1111/j.1365-246X.2009.04404.x

Holt, A. F. and Becker, T. W. (2017). The effect of a power-law mantle viscosity on trench retreat rate. *Geophysical Journal International* 208, 491–507. doi:10.1093/gji/ggw392

Holt, A. F., Becker, T. W., and Buffett, B. A. (2015a). Trench migration and overriding plate stress in dynamic subduction models. *Geophysical Journal International* 201, 172–192. doi:10.1093/gji/ggv011

Holt, A. F., Buffett, B. A., and Becker, T. W. (2015b). Overriding plate thickness control on subducting plate curvature. *Geophysical Research Letters* 42, 3802–3810. doi: 10.1002/2015GL063834

Holt, A. F., Royden, L. H., and Becker, T. W. (2017). The Dynamics of Double Slab Subduction. *Geophysical Journal International* 209, ggw496. doi:10.1093/gji/ggw496

Holt, A. F., Royden, L. H., Becker, T. W., and Faccenna, C. (2018). Slab interactions in 3-D subduction settings: The Philippine Sea Plate region. *Earth and Planetary Science Letters* 489, 72–83. doi:10.1016/j.epsl.2018.02.024

Hu, J., Liu, L., Hermosillo, A., and Zhou, Q. (2016). Simulation of late Cenozoic South American flat-slab subduction using geodynamic models with data assimilation. *Earth and Planetary Science Letters* 438, 1–13. doi:10.1016/j.epsl.2016.01.011

Humphreys, E. D. (1995). Post-Laramide removal of the Farallon slab, western United States. *Geology* 23, 987–990. doi:10.1130/0091-7613(1995)023<0987:PLROTF>2.3.CO;2

Husson, L., Guillaume, B., Funiciello, F., Faccenna, C., and Royden, L. H. (2012). Unraveling topography around subduction zones from laboratory models. *Tectonophysics* 526-529, 5–15. doi:10.1016/j.tecto.2011.09.001

Irvine, D. N. and Schellart, W. P. (2012). Effect of plate thickness on bending radius and energy dissipation at the subduction zone hinge. *Journal of Geophysical Research: Solid Earth* 117, 1–14. doi:10.1029/2011JB009113

Isacks, B. L. (1988). Uplift of the central Andean Plateau and bending of the Bolivian Orocline. *Journal of Geophysical Research* 93, 3211–3231. doi:10.1029/JB093iB04p03211

Jacob, J., Dyment, J., and Yatheesh, V. (2014). Revisiting the structure, age, and evolution of the Wharton Basin to better understand subduction under Indonesia. *Journal of Geophysical Research: Solid Earth* 119, 169–190. doi:10.1002/2013JB010285

Jadamec, M. A. and Billen, M. I. (2012). The role of rheology and slab shape on rapid mantle flow: Three-dimensional numerical models of the Alaska slab edge. *Journal of Geophysical Research: Solid Earth* 117, B02304. doi:10.1029/2011JB008563

Jarrard, R. D. (1986). Relations among subduction parameters. *Reviews of Geophysics* 24, 217–284. doi:10.1029/RG024i002p00217

Kameyama, M., Yuen, D. A., and Karato, S.-i. (1999). Thermal-mechanical effects of low-temperature plasticity (the Peierls mechanism) on the deformation of a viscoelastic shear zone. *Earth and Planetary Science Letters* 168, 159–172. doi: 10.1016/S0012-821X(99)00040-0

Karato, S.-i. and Wu, P. (1993). Rheology of the Upper Mantle: A Synthesis. *Science* 260, 771–778. doi:10.1126/science.260.5109.771

Karig, D. E. (1970). Ridges and basins of the Tonga-Kermadec Island Arc System. *Journal of Geophysical Research* 75, 239–254. doi:10.1029/JB075i002p00239

Kaus, B. J., Mühlhaus, H., and May, D. A. (2010). A stabilization algorithm for geodynamic numerical simulations with a free surface. *Physics of the Earth and Planetary Interiors* 181, 12–20. doi:10.1016/j.pepi.2010.04.007

Kelleher, J. and McCann, W. (1976). Buoyant zones, great earthquakes, and unstable boundaries of subduction. *Journal of Geophysical Research* 81, 4885–4896. doi:10.1029/JB081i026p04885

Kelleher, J., Sykes, L., and Oliver, J. (1973). Possible criteria for predicting earthquake locations and their application to major plate boundaries of the Pacific and the Caribbean. *Journal of Geophysical Research* 78, 2547–2585. doi:10.1029/JB078i014p02547

Kennett, B. L. and Furumura, T. (2010). Tears or thinning? Subduction structures in the Pacific plate beneath the Japanese Islands. *Physics of the Earth and Planetary Interiors* 180, 52–58. doi:10.1016/j.pepi.2010.03.001

Kim, Y., Miller, M. S., Pearce, F., and Clayton, R. W. (2012). Seismic imaging of the Cocos plate subduction zone system in central Mexico. *Geochemistry, Geophysics, Geosystems* 13, 1–16. doi:10.1029/2012GC004033

Kincaid, C. and Olson, P. (1987). An experimental study of subduction and slab migration. *Journal of Geophysical Research: Solid Earth* 92, 13832–13840. doi: 10.1029/jb092ib13p13832

King, S. D. (2001). Subduction zones: observations and geodynamic models. *Physics of the Earth and Planetary Interiors* 127, 9–24. doi:10.1016/S0031-9201(01)00218-7

Király, Á., Capitanio, F. A., Funiciello, F., and Faccenna, C. (2016). Subduction zone interaction: Controls on arcuate belts. *Geology* 44, 715–718. doi:10.1130/G37912.1

Kopp, H., Flueh, E. R., Petersen, C. J., Weinrebe, W., Wittwer, A., and Scientists, M. (2006). The Java margin revisited: Evidence for subduction erosion off Java. *Earth and Planetary Science Letters* 242, 130–142. doi:10.1016/j.epsl.2005.11.036

Korenaga, J. (2005). Why did not the Ontong Java Plateau form subaerially? *Earth and Planetary Science Letters* 234, 385–399. doi:10.1016/j.epsl.2005.03.011

Korenaga, J. and Karato, S.-I. (2008). A new analysis of experimental data on olivine rheology. *Journal of Geophysical Research: Solid Earth* 113. doi:10.1029/2007JB005100

Kramer, S. C., Davies, D. R., and Wilson, C. R. (2021). Analytical solutions for mantle flow in cylindrical and spherical shells. *Geoscientific Model Development* 14, 1899–1919. doi:10.5194/gmd-14-1899-2021

Kramer, S. C., Wilson, C. R., and Davies, D. R. (2012). An implicit free surface algorithm for geodynamical simulations. *Physics of the Earth and Planetary Interiors* 194-195, 25–37. doi:10.1016/j.pepi.2012.01.001

Krishna, K. S., Abraham, H., Sager, W. W., Pringle, M. S., Frey, F., Gopala Rao, D., et al. (2012). Tectonics of the Ninetyeast Ridge derived from spreading records in adjacent oceanic basins and age constraints of the ridge. *Journal of Geophysical Research: Solid Earth* 117, 1–19. doi:10.1029/2011JB008805

Kumar, A., Wagner, L. S., Beck, S. L., Long, M. D., Zandt, G., Young, B., et al. (2016). Seismicity and state of stress in the central and southern Peruvian flat slab. *Earth and Planetary Science Letters* 441, 71–80. doi:10.1016/j.epsl.2016.02.023

Kusky, T. M., Windley, B. F., Wang, L., Wang, Z., Li, X., and Zhu, P. (2014). Flat slab subduction, trench suction, and craton destruction: Comparison of the North China, Wyoming, and Brazilian cratons. *Tectonophysics* 630, 208–221. doi:10.1016/j.tecto.2014.05.028

Lallemand, S., Heuret, A., and Boutelier, D. (2005). On the relationships between slab dip, back-arc stress, upper plate absolute motion, and crustal nature in subduction zones. *Geochemistry, Geophysics, Geosystems* 6. doi:10.1029/2005GC000917

Lallemand, S., Peyret, M., Rijsingen, E., Arcay, D., and Heuret, A. (2018). Roughness Characteristics of Oceanic Seafloor Prior to Subduction in Relation to the Seismogenic Potential of Subduction Zones. *Geochemistry, Geophysics, Geosystems* 19, 2121–2146. doi:10.1029/2018GC007434

Larson, K. M., Freymueller, J. T., and Philipsen, S. (1997). Global plate velocities from the Global Positioning System. *Journal of Geophysical Research: Solid Earth* 102, 9961–9981. doi:10.1029/97JB00514

Lawver, L. A., Dalziel, I. W., Norton, I. O., Gahagan, L. M., and Davis, J. (2015). *The PLATES 2014 Atlas of Plate Reconstructions (550 Ma to Present Day), PLATES Progress Report No. 374-0215*. Tech. Rep. Technical Report No. 201, University of Texas

Lay, T. (2015). The surge of great earthquakes from 2004 to 2014. *Earth and Planetary Science Letters* 409, 133–146. doi:10.1016/j.epsl.2014.10.047

Lay, T. and Kanamori, H. (1981). An Asperity Model of Large Earthquake Sequences. In *Earthquake Prediction - An International Review*, eds. D. W. Simpson and P. G. Richards (American Geophysical Union). 579–592. doi:10.1029/ME004p0579

Le Voci, G., Davies, D. R., Goes, S., Kramer, S. C., and Wilson, C. R. (2014). A systematic 2-D investigation into the mantle wedge's transient flow regime and thermal structure: Complexities arising from a hydrated rheology and thermal buoyancy. *Geochemistry, Geophysics, Geosystems* 15, 28–51. doi:10.1002/2013GC005022

Lee, C. and King, S. D. (2011). Dynamic buckling of subducting slabs reconciles geological and geophysical observations. *Earth and Planetary Science Letters* 312, 360–370. doi:10.1016/j.epsl.2011.10.033

Lee, S. M. (2004). Deformation from the convergence of oceanic lithosphere into Yap trench and its implications for early-stage subduction. *Journal of Geodynamics* 37, 83–102. doi:10.1016/j.jog.2003.10.003

Li, S., Li, X., Wang, G., Liu, Y., Wang, Z., Wang, T., et al. (2019). Global Meso-Neoproterozoic plate reconstruction and formation mechanism for Precambrian basins: Constraints from three cratons in China. *Earth-Science Reviews* 198, 102946. doi:10.1016/j.earscirev.2019.102946

Li, Z. H. and Ribe, N. M. (2012). Dynamics of free subduction from 3-D boundary element modeling. *Journal of Geophysical Research: Solid Earth* 117. doi:10.1029/2012JB009165

Lithgow-Bertelloni, C. and Richards, M. A. (1998). The dynamics of cenozoic and mesozoic plate motions. *Reviews of Geophysics* 36, 27–78. doi:10.1029/97RG02282

Lithgow-Bertelloni, C. and Silver, P. G. (1998). Dynamic topography, plate driving forces and the African superswell. *Nature* 395, 269–272. doi:10.1038/26212

Liu, L., Gurnis, M., Seton, M., Saleeby, J., Müller, R. D., and Jackson, J. M. (2010). The role of oceanic plateau subduction in the Laramide orogeny. *Nature Geoscience* 3, 353–357. doi:10.1038/ngeo829

Liu, L. and Stegman, D. R. (2012). Origin of Columbia River flood basalt controlled by propagating rupture of the Farallon slab. *Nature* 482, 386–389. doi:10.1038/nature10749

Liu, S. and Currie, C. A. (2016). Farallon plate dynamics prior to the Laramide orogeny: Numerical models of flat subduction. *Tectonophysics* 666, 33–47. doi:10.1016/j.tecto.2015.10.010

Lonsdale, P. (2005). Creation of the Cocos and Nazca plates by fission of the Farallon plate. *Tectonophysics* 404, 237–264. doi:10.1016/j.tecto.2005.05.011

Madsen, J., Thorkelson, D., Friedman, R., and Marshall, D. (2006). Cenozoic to Recent plate configurations in the Pacific Basin: Ridge subduction and slab window magmatism in western North America. *Geosphere* 2, 11. doi:10.1130/GES00020.1

Magni, V., Faccenna, C., van Hunen, J., and Funiciello, F. (2014). How collision triggers backarc extension: Insight into Mediterranean style of extension from 3-D numerical models. *Geology* 42, 511–514. doi:10.1130/G35446.1

Mahadevan, L., Bendick, R., and Liang, H. (2010). Why subduction zones are curved. *Tectonics* 29, 1–10. doi:10.1029/2010TC002720

Mahatsente, R. (2017). Global Models of Ridge-Push Force, Geoid, and Lithospheric Strength of Oceanic plates. *Pure and Applied Geophysics* 174, 4395–4406. doi:10.1007/s00024-017-1647-2

Mahlburg Kay, S. and Mpodozis, C. (2002). Magmatism as a probe to the Neogene shallowing of the Nazca plate beneath the modern Chilean flat-slabs. *Journal of South American Earth Sciences* 15, 39–57. doi:10.1016/S0895-9811(02)00005-6

Malinverno, A. and Ryan, W. B. F. (1986). Extension in the Tyrrhenian Sea and shortening in the Apennines as result of arc migration driven by sinking of the lithosphere. *Tectonics* 5, 227–245. doi:10.1029/TC005i002p00227

Mallard, C., Coltice, N., Seton, M., Müller, R. D., and Tackley, P. J. (2016). Subduction controls the distribution and fragmentation of Earth's tectonic plates. *Nature* 535, 140–143. doi:10.1038/nature17992

Manea, V. and Gurnis, M. (2007). Subduction zone evolution and low viscosity wedges and channels. *Earth and Planetary Science Letters* 264, 22–45. doi:10.1016/j.epsl.2007.08.030

Manea, V. C., Manea, M., and Ferrari, L. (2013). A geodynamical perspective on the subduction of Cocos and Rivera plates beneath Mexico and Central America. *Tectonophysics* 609, 56–81. doi:10.1016/j.tecto.2012.12.039

Manea, V. C., Manea, M., Ferrari, L., Orozco, T., Valenzuela, R. W., Husker, A., et al. (2017). A review of the geodynamic evolution of flat slab subduction in Mexico, Peru, and Chile. *Tectonophysics* 695, 27–52. doi:10.1016/j.tecto.2016.11.037

Manea, V. C., Marta, P. G., and Manea, M. (2012). Chilean flat slab subduction controlled by overriding plate thickness and trench rollback. *Geology* 40, 35–38. doi:10.1130/G32543.1

Mann, P. and Taira, A. (2004). Global tectonic significance of the Solomon Islands and Ontong Java Plateau convergent zone. *Tectonophysics* 389, 137–190. doi:10.1016/j.tecto.2003.10.024

Martinod, J., Funiciello, F., Faccenna, C., Labanieh, S., and Regard, V. (2005). Dynamical effects of subducting ridges: Insights from 3-D laboratory models. *Geophysical Journal International* 163, 1137–1150. doi:10.1111/j.1365-246X.2005.02797.x

Martinod, J., Guillaume, B., Espurt, N., Faccenna, C., Funiciello, F., and Regard, V. (2013). Effect of aseismic ridge subduction on slab geometry and overriding plate deformation: Insights from analogue modeling. *Tectonophysics* 588, 39–55. doi:10.1016/j.tecto.2012.12.010

Mason, W. G., Moresi, L., Betts, P. G., and Miller, M. S. (2010). Three-dimensional numerical models of the influence of a buoyant oceanic plateau on subduction zones. *Tectonophysics* 483, 71–79. doi:10.1016/j.tecto.2009.08.021

Matthews, K. J., Maloney, K. T., Zahirovic, S., Williams, S. E., Seton, M., and Müller, R. D. (2016). Global plate boundary evolution and kinematics since the late Paleozoic. *Global and Planetary Change* 146, 226–250. doi:10.1016/j.gloplacha.2016.10.002

Maunder, B., van Hunen, J., Magni, V., and Bouilhol, P. (2016). Relamination of mafic

subducting crust throughout Earth's history. *Earth and Planetary Science Letters* 449, 206–216. doi:10.1016/j.epsl.2016.05.042

McGeary, S., Nur, A., and Ben-Avraham, Z. (1985). Spatial gaps in arc volcanism: The effect of collision or subduction of oceanic plateaus. *Tectonophysics* 119, 195–221. doi:10.1016/0040-1951(85)90039-3

McKenzie, D., Jackson, J., and Priestley, K. (2005). Thermal structure of oceanic and continental lithosphere. *Earth and Planetary Science Letters* 233, 337–349. doi:10.1016/j.epsl.2005.02.005

Meade, C. and Jeanloz, R. (1991). Deep-Focus Earthquakes and Recycling of Water into the Earth's Mantle. *Science* 252, 68–72. doi:10.1126/science.252.5002.68

Menant, A., Sternai, P., Jolivet, L., Guillou-Frottier, L., and Gerya, T. (2016). 3D numerical modeling of mantle flow, crustal dynamics and magma genesis associated with slab roll-back and tearing: The eastern Mediterranean case. *Earth and Planetary Science Letters* 442, 93–107. doi:10.1016/j.epsl.2016.03.002

Merdith, A. S., Landgrebe, T. C. W., Dutkiewicz, A., and Müller, R. D. (2013). Towards a predictive model for opal exploration using a spatio-temporal data mining approach. *Australian Journal of Earth Sciences* 60, 217–229. doi:10.1080/08120099.2012.754793

Mériaux, C. A., May, D. A., Mansour, J., Chen, Z., and Kaluza, O. (2018). Benchmark of three-dimensional numerical models of subduction against a laboratory experiment. *Physics of the Earth and Planetary Interiors* 283, 110–121. doi:10.1016/j.pepi.2018.07.009

[Dataset] Met Office (2015). Cartopy: a cartographic python library with a Matplotlib interface

Miller, M. S., Gorbatov, A., and Kennett, B. L. N. (2006a). Three-dimensional visualization of a near-vertical slab tear beneath the southern Mariana arc. *Geochemistry, Geophysics, Geosystems* 7. doi:10.1029/2005GC001110

Miller, M. S., Kennett, B. L., and Gorbatov, A. (2006b). Morphology of the distorted subducted Pacific slab beneath the Hokkaido corner, Japan. *Physics of the Earth and Planetary Interiors* 156, 1–11. doi:10.1016/j.pepi.2006.01.007

Miller, M. S., Kennett, B. L. N., and Toy, V. G. (2006c). Spatial and temporal evolution of the subducting Pacific plate structure along the western Pacific margin. *Journal of Geophysical Research: Solid Earth* 111. doi:10.1029/2005JB003705

Mishin, Y. A., Gerya, T. V., Burg, J.-P., and Connolly, J. A. (2008). Dynamics of double subduction: Numerical modeling. *Physics of the Earth and Planetary Interiors* 171, 280–295. doi:10.1016/j.pepi.2008.06.012

Morell, K. D. (2015). Late Miocene to recent plate tectonic history of the southern Central America convergent margin. *Geochemistry, Geophysics, Geosystems* 16, 3362–3382. doi:10.1002/2015GC005971

Moresi, L., Betts, P. G., Miller, M. S., and Cayley, R. A. (2014). Dynamics of continental accretion. *Nature* 508, 245–248. doi:10.1038/nature13033

Morra, G., Quevedo, L., and Müller, R. D. (2012). Spherical dynamic models of top-down tectonics. *Geochemistry, Geophysics, Geosystems* 13, n/a–n/a. doi:10.1029/2011GC003843

Morra, G., Regenauer-Lieb, K., and Giardini, D. (2006). Curvature of oceanic arcs. *Geology* 34, 877–880. doi:10.1130/G22462.1

Muldashev, I. A. and Sobolev, S. V. (2020). What Controls Maximum Magnitudes of Giant Subduction Earthquakes? *Geochemistry, Geophysics, Geosystems* 21. doi:10.1029/2020GC009145

Müller, R., Dutkiewicz, A., Seton, M., and Gaina, C. (2013). Seawater chemistry driven by supercontinent assembly, breakup, and dispersal. *Geology* 41, 907–910. doi:10.1130/G34405.1

Müller, R. D., Cannon, J., Qin, X., Watson, R. J., Gurnis, M., Williams, S., et al. (2018). GPlates: Building a Virtual Earth Through Deep Time. *Geochemistry, Geophysics, Geosystems* 19, 2243–2261. doi:10.1029/2018GC007584

Müller, R. D., Flament, N., Matthews, K. J., Williams, S. E., and Gurnis, M. (2016a). Formation of Australian continental margin highlands driven by plate-mantle interaction. *Earth and Planetary Science Letters* 441, 60–70. doi:10.1016/j.epsl.2016.02.025

Müller, R. D., Sdrolias, M., Gaina, C., and Roest, W. R. (2008a). Age, spreading rates, and spreading asymmetry of the world's ocean crust. *Geochemistry, Geophysics, Geosystems* 9, n/a–n/a. doi:10.1029/2007GC001743

Müller, R. D., Sdrolias, M., Gaina, C., Steinberger, B., and Heine, C. (2008b). Long-Term Sea-Level Fluctuations Driven by Ocean Basin Dynamics. *Science* 319, 1357–1362. doi:10.1126/science.1151540

Müller, R. D., Seton, M., Zahirovic, S., Williams, S. E., Matthews, K. J., Wright, N. M., et al. (2016b). Ocean Basin Evolution and Global-Scale Plate Reorganization Events Since Pangea Breakup. *Annual Review of Earth and Planetary Sciences* 44, 107–138. doi:10.1146/annurev-earth-060115-012211

Müller, R. D., Zahirovic, S., Williams, S. E., Cannon, J., Seton, M., Bower, D. J., et al. (2019). A Global Plate Model Including Lithospheric Deformation Along Major Rifts and Orogens Since the Triassic. *Tectonics* 38, 1884–1907. doi:10.1029/2018TC005462

Nur, A. and Ben-Avraham, Z. (1981). Volcanic gaps and the consumption of aseismic ridges in South America. In *Nazca Plate: Crustal Formation and Andean Convergence*, eds. L. V. D. Kulm, J. Dymond, E. J. Dasch, D. M. Hussong, and R. Roderick (Geological Society of America), vol. 154. 0. doi:10.1130/MEM154-p729

Nur, A. and Ben-Avraham, Z. (1983). Volcanic gaps due to oblique consumption of aseismic ridges. *Tectonophysics* 99, 355–362. doi:10.1016/0040-1951(83)90112-9

O'Driscoll, L. J., Humphreys, E. D., and Saucier, F. (2009). Subduction adjacent to

deep continental roots: Enhanced negative pressure in the mantle wedge, mountain building and continental motion. *Earth and Planetary Science Letters* 280, 61–70. doi:10.1016/j.epsl.2009.01.020

Okuwaki, R., Hicks, S. P., Craig, T. J., Fan, W., Goes, S., Wright, T. J., et al. (2021). Illuminating a Contorted Slab With a Complex Intraslab Rupture Evolution During the 2021 Mw 7.3 East Cape, New Zealand Earthquake. *Geophysical Research Letters* 48, 1–13. doi:10.1029/2021GL095117

O'Neill, C., Müller, D., and Steinberger, B. (2005). On the uncertainties in hot spot reconstructions and the significance of moving hot spot reference frames. *Geochemistry, Geophysics, Geosystems* 6. doi:10.1029/2004GC000784

OzBench, M., Regenauer-Lieb, K., Stegman, D. R., Morra, G., Farrington, R., Hale, A., et al. (2008). A model comparison study of large-scale mantle-lithosphere dynamics driven by subduction. *Physics of the Earth and Planetary Interiors* 171, 224–234. doi:10.1016/j.pepi.2008.08.011

Parsiegla, N., Gohl, K., and Uenzelmann-neben, G. (2008). The Agulhas Plateau: Structure and evolution of a Large Igneous Province. *Geophysical Journal International* 174, 336–350. doi:10.1111/j.1365-246X.2008.03808.x

Patriat, M., Klingelhoefer, F., Aslanian, D., Contrucci, I., Gutscher, M. A., Talandier, J., et al. (2002). Deep crustal structure of the Tuamotu plateau and Tahiti (French Polynesia) based on seismic refraction data. *Geophysical Research Letters* 29. doi:10.1029/2001GL013913

Paulson, A. and Richards, M. A. (2009). On the resolution of radial viscosity structure in modelling long-wavelength postglacial rebound data. *Geophysical Journal International* 179, 1516–1526. doi:10.1111/j.1365-246X.2009.04362.x

Peacock, S. M. (1996). Thermal and Petrologic Structure of Subduction Zones. In *Geophysical Monograph Series*, ed. J. P. P. Gray E. Bebout, David W. Scholl, Stephen H. Kirby (American Geophysical Union), vol. 96. 119–133. doi:10.1029/GM096p0119

Peral, M., Ruh, J., Zlotnik, S., Funiciello, F., Fernàndez, M., Vergés, J., et al. (2020). Analog and Numerical Experiments of Double Subduction Systems With Opposite Polarity in Adjacent Segments. *Geochemistry, Geophysics, Geosystems* 21, 1–22. doi:10.1029/2020GC009035

Pilger, R. H. (1981). Plate reconstructions, aseismic ridges, and low-angle subduction beneath the Andes. *Geological Society of America Bulletin* 92, 448. doi:10.1130/0016-7606(1981)92<448:PRARAL>2.0.CO;2

Pokorný, J., Čížková, H., and van den Berg, A. (2021). Feedbacks between subduction dynamics and slab deformation: Combined effects of nonlinear rheology of a weak decoupling layer and phase transitions. *Physics of the Earth and Planetary Interiors* 313. doi:10.1016/j.pepi.2021.106679

Pownall, J. M., Lister, G. S., and Spakman, W. (2017). Reconstructing subducted oceanic lithosphere by "reverse-engineering" slab geometries: The northern Philippine Sea Plate. *Tectonics* 36, 1814–1834. doi:10.1002/2017TC004686

Quinquis, M. E., Buiter, S. J., and Ellis, S. (2011). The role of boundary conditions in numerical models of subduction zone dynamics. *Tectonophysics* 497, 57–70. doi:10.1016/j.tecto.2010.11.001

Ramos, V. A. and Folguera, A. (2009). Andean flat-slab subduction through time. *Geological Society Special Publication* 327, 31–54. doi:10.1144/SP327.3

Ranalli, G. (1995). *Rheology of the Earth* (London: Springer Science and Business Media), 2nd edn. doi:10.1016/s0040-1951(96)00042-x

Rea, D. K. and Ruff, L. J. (1996). Composition and mass flux of sediment entering the world's subduction zones: Implications for global sediment budgets, great earthquakes, and volcanism. *Earth and Planetary Science Letters* 140, 1–12. doi:10.1016/0012-821X(96)00036-2

Reyners, M., Eberhart-Phillips, D., and Bannister, S. (2011). Tracking repeated subduction of the Hikurangi Plateau beneath New Zealand. *Earth and Planetary Science Letters* 311, 165–171. doi:10.1016/j.epsl.2011.09.011

Ribe, N. M. (2010). Bending mechanics and mode selection in free subduction: A thin-sheet analysis. *Geophysical Journal International* 180, 559–576. doi:10.1111/j.1365-246X.2009.04460.x

Ricard, Y., Doglioni, C., and Sabadini, R. (1991). Differential rotation between lithosphere and mantle: A consequence of lateral mantle viscosity variations. *Journal of Geophysical Research* 96, 8407. doi:10.1029/91JB00204

Riddihough, R. (1984). Recent movements of the Juan de Fuca Plate System. *Journal of Geophysical Research: Solid Earth* 89, 6980–6994. doi:10.1029/JB089iB08p06980

Riguzzi, F., Panza, G., Varga, P., and Doglioni, C. (2010). Can Earth's rotation and tidal despinning drive plate tectonics? *Tectonophysics* 484, 60–73. doi:10.1016/j.tecto.2009.06.012

Roda, M., Marotta, A. M., and Spalla, M. I. (2011). The effects of the overriding plate thermal state on the slab dip in an ocean-continent subduction system. *Comptes Rendus - Geoscience* 343, 323–330. doi:10.1016/j.crte.2011.01.005

Rodríguez-González, J., Billen, M. I., and Negredo, A. M. (2014a). Non-steady-state subduction and trench-parallel flow induced by overriding plate structure. *Earth and Planetary Science Letters* 401, 227–235. doi:10.1016/j.epsl.2014.06.013

Rodríguez-González, J., Billen, M. I., and Negredo, A. M. (2014b). Non-steady-state subduction and trench-parallel flow induced by overriding plate structure. *Earth and Planetary Science Letters* 401, 227–235. doi:10.1016/j.epsl.2014.06.013

Rodríguez-González, J., Billen, M. I., Negredo, A. M., and Montesi, L. G. (2016). Along-strike variation in subducting plate velocity induced by along-strike variation in overriding plate structure: Insights from 3D numerical models. *Journal of Geodynamics* 100, 175–183. doi:10.1016/j.jog.2016.02.006

Rodríguez-González, J., Negredo, A. M., and Billen, M. I. (2012). The role of the overriding plate thermal state on slab dip variability and on the occurrence of flat subduction. *Geochemistry, Geophysics, Geosystems* 13, 1–21. doi:10.1029/2011GC003859

Rögl, F. (1999). Mediterranean and paratethys. Facts and hypotheses of an Oligocene to Miocene Paleogeography (short overview). *Geologica Carpathica* 50, 339–349

Rosenbaum, G. and Mo, W. (2011). Tectonic and magmatic responses to the subduction of high bathymetric relief. *Gondwana Research* 19, 571–582. doi:10.1016/j.gr.2010.10.007

Rowley, D. B. (1996). Age of initiation of collision between India and Asia: A review of stratigraphic data. *Earth and Planetary Science Letters* 145, 1–13. doi:10.1016/S0012-821X(96)00201-4

Rudaviciute, K. (2015). *On the role of variable buoyant ridge width and obliquity on subduction*. Msci thesis, Imperial College London, London

Ruff, L. and Kanamori, H. (1980). Seismicity and the subduction process. *Physics of the Earth and Planetary Interiors* 23, 240–252. doi:10.1016/0031-9201(80)90117-X

Ruff, L. J. (1989). Do trench sediments affect great earthquake occurrence in subduction zones? *Pure and Applied Geophysics PAGEOPH* 129, 263–282. doi:10.1007/BF00874629

Sacks, I. S. (1983). The subduction of young lithosphere. *Journal of Geophysical Research: Solid Earth* 88, 3355–3366. doi:10.1029/JB088iB04p03355

Sallarès, V., Charvis, P., Flueh, E. R., Bialas, J., Agudelo, W., Anglade, A., et al. (2005). Seismic structure of the Carnegie ridge and the nature of the Galápagos hotspot. *Geophysical Journal International* 161, 763–788. doi:10.1111/j.1365-246X.2005.02592.x

Schellart, W., Lister, G., and Toy, V. (2006). A Late Cretaceous and Cenozoic reconstruction of the Southwest Pacific region: Tectonics controlled by subduction and

slab rollback processes. *Earth-Science Reviews* 76, 191–233. doi:10.1016/j.earscirev.2006.01.002

Schellart, W. P. (2004a). Kinematics of subduction and subduction-induced flow in the upper mantle. *Journal of Geophysical Research: Solid Earth* 109. doi:10.1029/2004JB002970

Schellart, W. P. (2004b). Quantifying the net slab pull force as a driving mechanism for plate tectonics. *Geophysical Research Letters* 31, n/a–n/a. doi:10.1029/2004GL019528

Schellart, W. P. (2005). Influence of the subducting plate velocity on the geometry of the slab and migration of the subduction hinge. *Earth and Planetary Science Letters* 231, 197–219. doi:10.1016/j.epsl.2004.12.019

Schellart, W. P. (2008). Kinematics and flow patterns in deep mantle and upper mantle subduction models: Influence of the mantle depth and slab to mantle viscosity ratio. *Geochemistry, Geophysics, Geosystems* 9. doi:10.1029/2007GC001656

Schellart, W. P. (2020). Control of Subduction Zone Age and Size on Flat Slab Subduction. *Frontiers in Earth Science* 8, 26. doi:10.3389/feart.2020.00026

Schellart, W. P., Freeman, J., Stegman, D. R., Moresi, L., and May, D. (2007). Evolution and diversity of subduction zones controlled by slab width. *Nature* 446, 308–311. doi:10.1038/nature05615

Schellart, W. P. and Spakman, W. (2012). Mantle constraints on the plate tectonic evolution of the Tonga–Kermadec–Hikurangi subduction zone and the South Fiji Basin region. *Australian Journal of Earth Sciences* 59, 933–952. doi:10.1080/08120099.2012.679692

Schellart, W. P. and Strak, V. (2021). Geodynamic models of short-lived, long-lived and periodic flat slab subduction. *Geophysical Journal International* 226, 1517–1541. doi:10.1093/gji/ggab126

Schepers, G., Van Hinsbergen, D. J., Spakman, W., Kosters, M. E., Boschman, L. M., and McQuarrie, N. (2017). South-American plate advance and forced Andean trench retreat as drivers for transient flat subduction episodes. *Nature Communications* 8, 1–9. doi:10.1038/ncomms15249

Schmeling, H., Babeyko, A., Enns, A., Faccenna, C., Funiciello, F., Gerya, T., et al. (2008). A benchmark comparison of spontaneous subduction models—Towards a free surface. *Physics of the Earth and Planetary Interiors* 171, 198–223. doi: 10.1016/j.pepi.2008.06.028

Scholl, D. W., Kirby, S. H., von Huene, R., Ryan, H., Wells, R. E., and Geist, E. L. (2015). Great (Mw8.0) megathrust earthquakes and the subduction of excess sediment and bathymetrically smooth seafloor. *Geosphere* 11, 236–265. doi:10.1130/GES01079.1

Scholz, C. H. and Campos, J. (1995). On the mechanism of seismic decoupling and back arc spreading at subduction zones. *Journal of Geophysical Research: Solid Earth* 100, 22103–22115. doi:10.1029/95JB01869

Scotese, C. R. and Schettino, A. (2017). Chapter 3 - Late Permian-Early Jurassic Paleogeography of Western Tethys and the World. In *Permo-Triassic salt provinces of Europe, North Africa and the Atlantic margins : tectonics and hydrocarbon potential*, eds. J. I. Soto, J. Flinch, and G. Tari (Amsterdam: Elsevier), chap. 3. 57–95. doi: 10.1016/B978-0-12-809417-4.00004-5

Sdrolias, M. and Müller, R. D. (2006). Controls on back-arc basin formation. *Geochemistry, Geophysics, Geosystems* 7. doi:10.1029/2005GC001090

Seton, M., Flament, N., Whittaker, J., Müller, R. D., Gurnis, M., and Bower, D. J. (2015). Ridge subduction sparked reorganization of the Pacific plate-mantle system 60–50 million years ago. *Geophysical Research Letters* 42, 1732–1740. doi: 10.1002/2015GL063057

Seton, M., Müller, R. D., Zahirovic, S., Gaina, C., Torsvik, T., Shephard, G., et al. (2012).

Global continental and ocean basin reconstructions since 200Ma. *Earth-Science Reviews* 113, 212–270. doi:10.1016/j.earscirev.2012.03.002

Sharples, W., Jadamec, M. A., Moresi, L. N., and Capitanio, F. A. (2014). Overriding plate controls on subduction evolution. *Journal of Geophysical Research: Solid Earth* 119, 6684–6704. doi:10.1002/2014JB011163

Shulgin, A., Kopp, H., Mueller, C., Planert, L., Lueschen, E., Flueh, E. R., et al. (2011). Structural architecture of oceanic plateau subduction offshore Eastern Java and the potential implications for geohazards. *Geophysical Journal International* 184, 12–28. doi:10.1111/j.1365-246X.2010.04834.x

Simkin, T., Tilling, R. I., Vogt, P. R., Kirby, S. H., Kimberly, P., Stewart, D. B., et al. (2006). This dynamic planet: World map of volcanoes, earthquakes, impact craters, and plate tectonics. *U.S. Geological Survey Geologic Investigations Series Map I-2800*

Skinner, S. M. and Clayton, R. W. (2011). An evaluation of proosed mechanisms of slab flattening in central mexico. *Pure and Applied Geophysics* 168, 1461–1474. doi:10.1007/s00024-010-0200-3

Skinner, S. M. and Clayton, R. W. (2013). The lack of correlation between flat slabs and bathymetric impactors in South America. *Earth and Planetary Science Letters* 371-372, 1–5. doi:10.1016/j.epsl.2013.04.013

Sparkes, R., Tilmann, F., Hovius, N., and Hillier, J. (2010). Subducted seafloor relief stops rupture in South American great earthquakes: Implications for rupture behaviour in the 2010 Maule, Chile earthquake. *Earth and Planetary Science Letters* 298, 89–94. doi:10.1016/j.epsl.2010.07.029

Stadler, G., Gurnis, M., Burstedde, C., Wilcox, L. C., Alisic, L., and Ghattas, O. (2010). The Dynamics of Plate Tectonics and Mantle Flow: From Local to Global Scales. *Science* 329, 1033–1038. doi:10.1126/science.1191223

Stampfli, G. and Borel, G. (2002). A plate tectonic model for the Paleozoic and Mesozoic

constrained by dynamic plate boundaries and restored synthetic oceanic isochrons. *Earth and Planetary Science Letters* 196, 17–33. doi:10.1016/S0012-821X(01)00588-X

Stegman, D., Schellart, W., and Freeman, J. (2010a). Competing influences of plate width and far-field boundary conditions on trench migration and morphology of subducted slabs in the upper mantle. *Tectonophysics* 483, 46–57. doi:10.1016/j.tecto.2009.08.026

Stegman, D. R., Farrington, R., Capitanio, F. A., and Schellart, W. P. (2010b). A regime diagram for subduction styles from 3-D numerical models of free subduction. *Tectonophysics* 483, 29–45. doi:10.1016/j.tecto.2009.08.041

Stegman, D. R., Freeman, J., Schellart, W. P., Moresi, L., and May, D. (2006). Influence of trench width on subduction hinge retreat rates in 3-D models of slab rollback. *Geochemistry, Geophysics, Geosystems* 7, n/a–n/a. doi:10.1029/2005GC001056

Steinberger, B. and Torsvik, T. H. (2008). Absolute plate motions and true polar wander in the absence of hotspot tracks. *Nature* 452, 620–623. doi:10.1038/nature06824

Stern, R. J. (2002). Subduction Zones. *Reviews of Geophysics* 40, 3–1–3–38. doi:10.1029/2001RG000108

Stotz, I. L., Iaffaldano, G., and Davies, D. R. (2018). Pressure-Driven Poiseuille Flow: A Major Component of the Torque-Balance Governing Pacific Plate Motion. *Geophysical Research Letters* 45, 117–125. doi:10.1002/2017GL075697

Suárez, G. (2021). Large earthquakes in the Tehuantepec subduction zone: evidence of a locked plate interface and large-scale deformation of the slab. *Journal of Seismology* 25, 449–460. doi:10.1007/s10950-020-09969-6

Suchoy, L., Goes, S., Maunder, B., Garel, F., and Davies, R. (2021). Effects of basal drag on subduction dynamics from 2D numerical models. *Solid Earth* 12, 79–93. doi:10.5194/se-12-79-2021

Sutherland, R., Collot, J., Bache, F., Henrys, S., Barker, D., Browne, G. H., et al. (2017). Widespread compression associated with Eocene Tonga-Kermadec subduction initiation. *Geology* 45, 355–358. doi:10.1130/G38617.1

Syracuse, E. M. and Abers, G. A. (2006). Global compilation of variations in slab depth beneath arc volcanoes and implications. *Geochemistry, Geophysics, Geosystems* 7, n/a–n/a. doi:10.1029/2005GC001045

Tao, W. C. and O'connell, R. J. (1992). Ablative subduction: A two-sided alternative to the conventional subduction model. *Journal of Geophysical Research* 97, 8877. doi:10.1029/91JB02422

Tao, W. C. and O'Connell, R. J. (1993). Deformation of a weak subducted slab and variation of seismicity with depth. *Nature* 361, 626–628. doi:10.1038/361626a0

Taramón, J. M., Rodríguez-González, J., Negredo, A. M., and Billen, M. I. (2015). Influence of cratonic lithosphere on the formation and evolution of flat slabs: Insights from 3-D time-dependent modeling. *Geochemistry, Geophysics, Geosystems* 16, 2933–2948. doi:10.1002/2015GC005940

Taylor, B. (2006). The single largest oceanic plateau: Ontong Java-Manihiki-Hikurangi. *Earth and Planetary Science Letters* 241, 372–380. doi:10.1016/j.epsl.2005.11.049

Tetley, M. G., Williams, S. E., Gurnis, M., Flament, N., and Müller, R. D. (2019). Constraining Absolute Plate Motions Since the Triassic. *Journal of Geophysical Research: Solid Earth* 124, 7231–7258. doi:10.1029/2019JB017442

Tetreault, J. L. and Buiter, S. J. (2014). Future accreted terranes: A compilation of island arcs, oceanic plateaus, submarine ridges, seamounts, and continental fragments. *Solid Earth* 5, 1243–1275. doi:10.5194/se-5-1243-2014

Timm, C., Hoernle, K., Werner, R., Hauff, F., van den Bogaard, P., Michael, P., et al. (2011). Age and geochemistry of the oceanic Manihiki Plateau, SW Pacific: New evidence for a plume origin. *Earth and Planetary Science Letters* 304, 135–146. doi:10.1016/j.epsl.2011.01.025

Torii, Y. and Yoshioka, S. (2007). Physical conditions producing slab stagnation: Constraints of the Clapeyron slope, mantle viscosity, trench retreat, and dip angles. *Tectonophysics* 445, 200–209. doi:10.1016/j.tecto.2007.08.003

Torsvik, T. H., Müller, R. D., Van Der Voo, R., Steinberger, B., and Gaina, C. (2008). Global plate motion frames: Toward a unified model. *Reviews of Geophysics* 46. doi:10.1029/2007RG000227

Torsvik, T. H., Rousse, S., Labails, C., and Smethurst, M. A. (2009). A new scheme for the opening of the South Atlantic Ocean and the dissection of an Aptian salt basin. *Geophysical Journal International* 177, 1315–1333. doi:10.1111/j.1365-246X.2009.04137.x

Torsvik, T. H., Steinberger, B., Gurnis, M., and Gaina, C. (2010). Plate tectonics and net lithosphere rotation over the past 150 My. *Earth and Planetary Science Letters* 291, 106–112. doi:10.1016/j.epsl.2009.12.055

Tsuji, T., Nakamura, Y., Tokuyama, H., Coffin, M. F., and Koda, K. (2007). Oceanic crust and Moho of the Pacific Plate in the eastern Ogasawara Plateau region. *Island Arc* 16, 361–373. doi:10.1111/j.1440-1738.2007.00589.x

Turcotte, D. L. and Schubert, G. (2002). *Geodynamics* (Cambridge: Cambridge University Press), 2nd edn. doi:10.1017/CBO9780511807442

Uyeda, S. and Kanamori, H. (1979). Back-arc opening and the mode of subduction. *Journal of Geophysical Research* 84, 1049. doi:10.1029/JB084iB03p01049

Vaes, B., van Hinsbergen, D. J., and Boschman, L. M. (2019). Reconstruction of Subduction and Back-Arc Spreading in the NW Pacific and Aleutian Basin: Clues to Causes of Cretaceous and Eocene Plate Reorganizations. *Tectonics* 38, 1367–1413. doi:10.1029/2018TC005164

Van Hunen, J., Van Den Berg, A. P., and Vlaar, N. J. (2002). On the role of subducting oceanic plateaus in the development of shallow flat subduction. *Tectonophysics* 352, 317–333. doi:10.1016/S0040-1951(02)00263-9

van Hunen, J., van den Berg, A. P., and Vlaar, N. J. (2004). Various mechanisms to induce present-day shallow flat subduction and implications for the younger Earth: A numerical parameter study. *Physics of the Earth and Planetary Interiors* 146, 179–194. doi:10.1016/j.pepi.2003.07.027

Vérard, C. (2019). Plate tectonic modelling: review and perspectives. *Geological Magazine* 156, 208–241. doi:10.1017/S0016756817001030

Vogt, P. R. (1973). Subduction and Aseismic Ridges. *Nature* 241, 189–191. doi:10.1038/241189a0

Vogt, P. R., Lowrie, A., Bracey, D. R., and Hey, R. (1976). *Subduction of aseismic oceanic ridges: Effects on shape, seismicity, and other characteristics of consuming plate boundaries*, vol. 172 (Geological Society of America)

Walther, C. H. E. (2003). The crustal structure of the Cocos ridge off Costa Rica. *Journal of Geophysical Research: Solid Earth* 108, 1–21. doi:10.1029/2001jb000888

Whattam, S. A. and Stern, R. J. (2015). Late Cretaceous plume-induced subduction initiation along the southern margin of the Caribbean and NW South America: The first documented example with implications for the onset of plate tectonics. *Gondwana Research* 27, 38–63. doi:10.1016/j.gr.2014.07.011

Whittaker, J. M., Afonso, J. C., Masterton, S., Müller, R. D., Wessel, P., Williams, S. E., et al. (2015). Long-term interaction between mid-ocean ridges and mantle plumes. *Nature Geoscience* 8, 479–483. doi:10.1038/ngeo2437

Whittaker, J. M., Müller, R. D., Leitchenkov, G., Stagg, H., Sdrolias, M., Gaina, C., et al. (2007). Major Australian-Antarctic Plate Reorganization at Hawaiian-Emperor Bend Time. *Science* 318, 83–86. doi:10.1126/science.1143769

Williams, S., Flament, N., Dietmar Müller, R., and Butterworth, N. (2015). Absolute plate motions since 130 Ma constrained by subduction zone kinematics. *Earth and Planetary Science Letters* 418, 66–77. doi:10.1016/j.epsl.2015.02.026

Wilson, C. R. (2009). *Modelling multiple-material flows on adaptive unstructured meshes*. Doctoral dissertation, Imperial College London. doi:10.25560/5526

Wolf, S. G. and Huismans, R. S. (2019). Mountain Building or Backarc Extension in Ocean-Continent Subduction Systems: A Function of Backarc Lithospheric Strength and Absolute Plate Velocities. *Journal of Geophysical Research: Solid Earth* 124, 7461–7482. doi:10.1029/2018JB017171

Wright, N. M., Seton, M., Williams, S. E., and Müller, R. D. (2016). The Late Cretaceous to recent tectonic history of the Pacific Ocean basin. *Earth-Science Reviews* 154, 138–173. doi:10.1016/j.earscirev.2015.11.015

Wu, B., Conrad, C. P., Heuret, A., Lithgow-bertelloni, C., and Lallemand, S. (2008). Reconciling strong slab pull and weak plate bending: The plate motion constraint on the strength of mantle slabs. *Earth and Planetary Science Letters* 272, 412–421. doi:10.1016/j.epsl.2008.05.009

Wu, J., Suppe, J., Lu, R., and Kanda, R. (2016). Philippine Sea and East Asian plate tectonics since 52 Ma constrained by new subducted slab reconstruction methods. *Journal of Geophysical Research: Solid Earth* 121, 4670–4641. doi:10.1002/2016JB012923

Xia, C., Zheng, Y., Liu, B., Hua, Q., Ma, L., Li, X., et al. (2021). Tectonic implications of the subduction of the Kyushu-Palau Ridge beneath the Kyushu, southwest Japan. *Acta Oceanologica Sinica* 40, 70–83. doi:10.1007/s13131-021-1711-8

Xia, C. L., Zheng, Y. P., Liu, B. H., Hua, Q. F., Liu, K., Ma, L., et al. (2020). Geological and geophysical differences between the north and south sections of the Yap trench-arc system and their relationship with Caroline Ridge subduction. *Geological Journal* 55, 7775–7789. doi:10.1002/gj.3903

Yamato, P., Husson, L., Braun, J., Loiselet, C., and Thieulot, C. (2009). Influence of surrounding plates on 3D subduction dynamics. *Geophysical Research Letters* 36, n/a–n/a. doi:10.1029/2008GL036942

Yanagisawa, T., Yamagishi, Y., Hamano, Y., and Stegman, D. R. (2010). Mechanism for generating stagnant slabs in 3-D spherical mantle convection models at Earth-like conditions. *Physics of the Earth and Planetary Interiors* 183, 341–352. doi:10.1016/j.pepi.2010.02.005

Zahirovic, S., Seton, M., and Müller, R. D. (2014). The Cretaceous and Cenozoic tectonic evolution of Southeast Asia. *Solid Earth* 5, 227–273. doi:10.5194/se-5-227-2014

Zhang, J., Sager, W. W., and Durkin, W. J. (2017a). Morphology of Shatsky Rise oceanic plateau from high resolution bathymetry. *Marine Geophysical Research* 38, 169–185. doi:10.1007/s11001-016-9272-5

Zhang, J. and Zhang, G. (2020). Geochemical and chronological evidence for collision of proto-Yap arc/Caroline plateau and rejuvenated plate subduction at Yap trench. *Lithos* 370-371, 105616. doi:10.1016/j.lithos.2020.105616

Zhang, Q., Guo, F., Zhao, L., and Wu, Y. (2017b). Geodynamics of divergent double subduction: 3-D numerical modeling of a Cenozoic example in the Molucca Sea region, Indonesia. *Journal of Geophysical Research: Solid Earth* 122, 3977–3998. doi:10.1002/2017JB013991

Zhong, S. and Davies, G. F. (1999). Effects of plate and slab viscosities on the geoid. *Earth and Planetary Science Letters* 170, 487–496. doi:10.1016/S0012-821X(99)00124-7

Zhong, S. and Gurnis, M. (1995). Mantle Convection with Plates and Mobile, Faulted Plate Margins. *Science* 267, 838–843. doi:10.1126/science.267.5199.838

Zhu, G., Yang, H., Lin, J., Zhou, Z., Xu, M., Sun, J., et al. (2019). Along-strike variation in slab geometry at the southern Mariana subduction zone revealed by seismicity through ocean bottom seismic experiments. *Geophysical Journal International* 218, 2122–2135. doi:10.1093/gji/ggz272